AFOSR-TR- 78-0856 AD A053640

Department of AERONAUTICS and ASTRONAUTICS
STANFORD UNIVERSITY

SUDAAR NO. 508

EFFECT OF CHORDWISE FORCES AND DEFORMATIONS AND DEFORMATIONS DUE TO STEADY LIFT ON WING FLUTTER

by

William Newsome Boyd

December 1977

This research was supported by the Air Force Office of Scientific Research under Contract No. AFOSR-74-2712.

Department of Aeronautics and Astronautics
Stanford University
Stanford, California

EFFECT OF CHORDWISE FORCES AND DEFORMATIONS AND DEFORMATION DUE TO STEADY LIFT ON WING FLUTTER

by

William Newsome Boyd

SUDAAR NO. 508

December 1977

This research was supported by the Air Force Office of Scientific Research under Contract No. AFOSR-74-2712.

ABSTRACT

This investigation explores the effects of chordwise forces and deformations and steady-state deformation due to lift on the static and dynamic aeroelastic stability of a uniform cantilever wing. Results of this analysis are believed to have practical applications for high-performance sailplanes and certain RPV's.

The airfoil cross section is assumed to be symmetric and camber bending is neglected. Motions in vertical bending, fore-and-aft bending, and torsion are considered. A differential equation model is developed, which includes the nonlinear elastic bending-torsion coupling that accompanies even moderate deflections. A linearized expansion in small time-dependent perturbation deflections is made about a steady flight condition. The stability determinant of the linearized system then contains coefficients that depend on steady displacements. Loads derived from two-dimensional incompressible aerodynamic theory are used to obtain the majority of the results, but cases using three-dimensional subsonic compressible theory are also studied.

The stability analysis is carried out in terms of the dynamically uncoupled natural modes of vibration of the uniform cantilever. Dynamic stability in the case of incompressible strip-theory airloads is determined in two ways. One is the "V-g method" familiar to aeroelasticians. When steady deformations are present this method requires an iterative matching of flutter speeds with estimated speed. The second approach involves determination of the complex eigenvalues of the aeroelastic modes at any desired flight condition. The aerodynamic loads are expressed in terms of the generalized Theodorsen function; eigenvalues of the aeroelastic system are located with a gradient search technique.

The effect of steady drag on flutter of nonlifting wings using incompressible strip-theory is studied and shown to correlate with previously known results. Next, the influence of steady lifting deformations on flutter is investigated, and flutter modes are found that involve fore-and-aft bending motions. The significance of unsteady leading edge suction forces, which are predicted by the two-dimensional incompressible aerodynamic theory, is then examined. Two idealized examples based upon existing sailplanes are analyzed.

Steady drag loads lower the flutter speed for larger aspect ratios but increase it for aspect ratios less than a certain value. Divergence speed is more sensitive to steady drag, and for very high aspect ratio wings it can fall below the bending-torsion flutter speed. Steady deformations due to lift always decrease the flutter speed by an amount dependent upon the aspect ratio and the fore-and-aft bending stiffness. Leading-edge suction forces increase flutter speed.

Three-dimensional steady and unsteady airloads are introduced into the V-g flutter analysis scheme, and for a Mach number of zero the role of steady lifting deformations and unsteady leading-edge suction forces is more accurately determined. The behavior predicted using strip theory loads is again observed, and the suction forces are confirmed to contribute a significant stabilizing effect. Further calculations using high subsonic Mach numbers reveal only mild effects due to compressibility (disregarding unsteady chordwise loads of viscous origin).

ACKNOWLEDGMENTS

The author wishes to express his deepest gratitude to his advisor, Professor Holt Ashley, for his expert advice and guidance throughout the course of the research. Thanks are also due Professor Arthur E. Bryson, Jr. and Professor Milton D. Van Dyke for taking their valuable time to provide helpful comments and suggestions. Finally for the trying job of typing sincere thanks go to Dorothy Gundy.

Support for this work was provided by the National Aeronautics and Space Administration under contract NGL 05-020-243.

TABLE OF CONTENTS

LIST OF FIGURES

LIST OF TABLES

LIST OF SYMBOLS

$A = 1/2 + a$	elastic axis location parameter
A_w	structural cross-sectional area of wing
a	distance in semichords elastic axis is aft of midchord
$a_{\nu\mu}^{(j)}$	pressure series coefficient for jth mode, equation (7-1)
B_j	modal property defined by equation (A-4)
b	semichord
$C \equiv \frac{C_D}{2\pi}$	drag parameter
C_D	drag coefficient
$C(k)$	Theodorsen function
$C(\bar{s})$	generalized Theodorsen function
C_F	leading edge pressure singularity strength
$\Delta Cp(x,y,t)$	pressure coefficient distribution on planform
$\Delta Cp_j(x,y)$	pressure coefficient distribution for jth mode per q_j
$\Delta Cp_\alpha^\circ(x,y)$	steady pressure coefficient distribution for rigid pitch per radian
$\Delta Cp_{\phi_\nu}^\circ(x,y)$	steady pressure coefficient distribution for νth torsion mode per $q_{\phi_\nu}^\circ$
$\Delta Cp_{w_j}(x,y)$, $\Delta Cp_{\phi_j}(x,y)$	oscillating pressure coefficient distributions for jth bending and torsion modes
D	drag force
D_p	chordwise component of potential airloads
E	modulus of elasticity
e_a	area centroid-elastic axis offset
$\underset{\sim}{F}$	matrix notation for nonlinear steady equations in (C-2)

$F_s(y,t)$	leading edge suction force
F_x, F_z	applied forces in x and z directions
F_j^o	leading edge steady pressure singularity strength parameter for jth mode, defined in (7-18)
F_j	leading edge oscillatory pressure singularity strength parameter for jth mode, defined in (7-19)
F_α^o	leading edge steady pressure singularity strength parameter for rigid pitch per α
$F_{\phi_\nu}^o$	leading edge steady pressure singularity strength parameter for νth torsion mode per $q_{\phi_\nu}^o$
F_{w_j}, F_{ϕ_j}	leading edge oscillatory pressure singularity strength parameters for jth bending and torsion modes
$f^{(\nu)}(y)$	spanwise assumed pressure distribution, defined in (7-2)
$f_{\phi_i}, f_{w_i}, f_{v_i}$	assumed modes, defined in Appendix A
G	shear modulus of elasticity
g	structural damping
$g^{(\mu)}(x)$	chordwise assumed pressure distribution, defined in (4-7)
$H_{\nu j\mu}$	modal integral defined in (4-7)
h	z-displacement, positive downwards
I_d	area polar moment of inertia defined in (3-11)
I_x	area moment of inertia defined in (3-10)
I_z	area moment of inertia defined in (3-9)
I_{ij}	modal integral defined in (2-13)
$I_{ij}^{(1)}, I_{ij}^{(2)}, I_{ij}^{(3)}$	modal integrals defined in (2-21)

$i_\alpha \equiv \frac{J}{mb^2}$	radius of gyration parameter
i	$\sqrt{-1}$
J	mass moment of inertia defined in (3-14)
$\mathcal{J}$	Jacobian matrix (Appendix C)
$K_n(\bar{s})$	modified Bessel function of the third kind of order n
K_s	$3n \times 3n$ stiffness matrix, Fig. 4-3
$k = \frac{\omega b}{V}$	reduced frequency
L_a	aerodynamic lift
L_{a_C}, $L_{a_{NC}}$	circulatory and noncirculatory parts, respectively, of lift given in (4-14)
L_ϕ, L_w	expressions defined in (2-4)
$\bar{L}_\phi, \bar{L}_w$	expressions defined in (5-3)
ℓ	semispan
$M \equiv \frac{m}{\Pi \rho b^2}$	mass ratio parameter
$\bar{M}$	number of downwash stations on a downwash chord
M_a	Mach number
M_ϕ, M_w	expressions defined in (2-4)
$\bar{M}_\phi, \bar{M}_w$	expressions defined in (5-3)
M_s	$3n \times 3n$ mass matrix, Fig. 4-3
M_x	stress moment defined in (3-10)
M_z	moment of applied drag loads defined in (2-2), also, stress moment defined in (3-9)
M_{z_o}	steady moment defined in (3-33)
M_{z_1}	unsteady moment defined in (3-39)

m	wing mass per unit span
m_a	aerodynamic moment
m_y	applied moment about y-axis
N_j	modal quantitiy defined in Appendix A
$\bar{N}$	number of downwash chords on the semispan
n	number of assumed modes in each degree of freedom
$P \equiv \frac{EI_x b^2}{GI_d \ell^2}$	aspect ratio parameter
ΔP_j	pressure distribution for jth mode per q_j
$p \equiv \ell\sqrt{\frac{J}{GI_d}}$	dimensionless Laplace transform variable
$Q_{j,i}$	3n x 3n generalized force matrix for simple harmonic airloads (2n x 2n in Chapter II)
$\bar{Q}_{j,i}$	3n x 3n generalized force matrix, Laplace domain
$\underset{\sim}{Q}^{o}_{j,i}$	3n x 3n+1 generalized force matrix for steady subsonic 3-D airloads; zeroth column for rigid body pitching mode
$\underset{\sim}{Q}_{j,i}$	3n x 3n generalized force matrix for simple harmonic subsonic 3-D airloads, defined in (7-30)
$\underset{\sim}{Q}^{s}_{j,i}$	sectional generalized force defined in (7-29)
q_j	generalized displacement (steady or simple harmonic time dependency)
$q_{\phi_j}, q_{w_j}, q_{f_j}$	simple harmonic generalized displacements
$\bar{q}_{\phi_j}, \bar{q}_{w_j}, \bar{q}_{v_j}$	Laplace domain generalized displacements
$q^{o}_{\phi_j}, q^{o}_{w_j}, q^{o}_{v_j}$	steady generalized displacements
$\underset{\sim}{q}^{o}$	vector of generalized displacement, defined in (C-1)

$R_{ij\nu\mu}$	modal integral defined in (4-8)
$S \equiv \frac{s_e}{bm}$	mass centroid offset parameter
$S_{\tilde{y}}$	stress torque defined in (3-11)
$s = \sigma + i\omega$	Laplace transform variable
$\tilde{s} = \frac{sb}{V}$	Reduced Laplace transform variable
s_e	mass center offset defined in (3-14)
T	spanwise tension
$\mathcal{T}$	kinetic energy
t	time
$U = \frac{V\ell}{b}\sqrt{\frac{J}{GI_d}}$	dimensionless flight speed
U_e	estimated speed for calculation of steady deformations
$\mathcal{U}$	potential energy
u_x, u_y, u_z	displacements shown in Fig. 3-1
V	flight speed
V_y	stress resultant defined in (3-8)
$v = u_x$	displacement in x-direction, positive downstream
$\mathcal{W}$	virtual work of applied loads
$w = u_z$	displacement in z-direction, positive upwards
x	chordwise spatial coordinate
$\tilde{x} = \frac{x}{y}$	dimensionless chordwise coordinate
$Y_{i\nu j}$	modal integral defined in (5-19)
y	spanwise spatial coordinate
$\tilde{y} = \frac{y}{b}$	dimensionless spanwise coordinate
$Z \equiv (1+ig)\Omega^2$	dimensionless complex frequency
z	vertical spatial coordinate

$z_s(x,y,t)$	displacement of wing planform normal to x-y plane
α	angle of attack of wing root, positive nose up
β	quantity defined in (3-38)
γ	distributed vorticity on airfoil chord
δ	flutter phase angle by which bending displacement leads torsion at wingtip
δ_{ij}	delta function
$\varepsilon_{yy}, \varepsilon_{y\xi}, \varepsilon_{y\eta}$	engineering strains
ζ	damping ratio
η	airfoil major principal axis coordinate
ξ	airfoil minor principal axis coordinate
ρ	atmospheric density
ρ_s	density of wing structure
σ	real part of s
$\sigma_{yy}, \sigma_{y\xi}, \sigma_{y\eta}$	stresses
$\tau = \frac{EI_z}{EI_x}$	bending stiffness ratio
ϕ	torsional displacement, positive leading edge up
$\Omega \equiv \omega\ell\sqrt{\frac{J}{GI_d}}$	dimensionless frequency
ω	frequency
$\omega_{w_j}, \omega_{\phi_j}$	modal natural frequencies (Appendix A)
$A\!\!\!R$	aspect ratio

SUPERSCRIPTS

'	spanwise spatial differentiation
˙	time differentiation
¯	Laplace transformation
~	simple harmonic time dependence

SUBSCRIPTS

D	divergence
F	flutter
0	steady
1	unsteady

ABBREVIATIONS

Cj	j'th chordwise bending normal mode of free vibration
Tj	j'th torsional normal mode of free vibration
Vj	j'th vertical bending normal mode of free vibration
VT	vertical bending/torsion
VCT	vertical bending/chordwise bending/torsion

Chapter I

INTRODUCTION

Aerodynamic loads and deformations parallel to the chord are usually neglected during studies of aeroelastic stability of lifting surfaces. Furthermore, dynamic stability is usually analyzed without regard for the influence of steady deformations due to steady-state lift.

Very little literature exists which treats chordwise forces and bending in an aeroelastic analysis. A substantial study of the effects of drag loads on divergence of a cantilever wing is made by Petre (Ref. 2, pp. 449-487). Here it is clearly demonstrated that the interaction of drag with bending deformations due to lifting loads can significantly reduce divergence speeds. Goetz (Ref. 17) considered this same drag-bending deformation divergence mechanism, specialized to the case of a rigid lifting surface at the end of a beam-rod. This work involved supersonic flow past a surface having a blunt leading edge, and the resulting sizeable drag forces caused a significant reduction of the classical divergence speed.

One example of an aeroelastic study in which chordwise deformations of a straight cantilever wing are accounted for is the work in the area of tilting proprotor aircraft by Wayne Johnson. The cruising flight condition (Ref. 27) is modeled using a proprotor with axial flow mounted at the tip of a cantilever wing. The additional degrees of freedom associated with the individual elastic rotor blades and the aerodynamic and inertial effects of the proprotor result in a much more complex and specialized aeroelastic analysis than is considered here.

The effect which steady chordwise forces can have upon dynamic stability was explored by Petre (Ref. 3) and Petre and Ashley (Ref. 1) using two-dimensional incompressible unsteady lifting airloads. The latter work presents extensive calculations regarding the effect of steady drag on bending-torsion flutter of a uniform cantilever wing. It serves as the starting point for the work pursued in this thesis.

The objectives of this thesis are as follows:

1. To check and interpret the predicted effect of steady drag on the flutter behavior of a nonlifting wing discovered in Ref. 1, using a modal approach instead of a collocation approach.
2. To generalize the equations of motion to include consistently fore-and-aft bending motions, adequately accounting for the elastic coupling among the three degrees of freedom.
3. To include steady-state lifting deformations in the dynamic stability analysis by considering small time-dependent perturbation deflections about a steady displacement solution.
4. To allow for unsteady leading-edge-suction forces in the chordwise direction predicted by two-dimensional incompressible unsteady potential flow theory.
5. To improve the representation of both steady and unsteady airloads by use of a three-dimensional subsonic kernel function program, from which leading-edge suction and induced drag can also be obtained.

Items 2, 3, and 4 are interrelated and together represent a consistent extension over previous research in the modeling of the physical system. For example, when steady lateral bending deformations are present, unsteady chordwise loads can induce twisting motions which significantly affect dynamic stability. The main purpose here will be to establish trends and gain fundamental insight into the influence of chordwise forces and steady deformations, hopefully shedding light on their importance in practical aerospace problems.

Certain assumptions are adhered to throughout this thesis. Since the emphasis is upon working from the equations of motion in differential form in order to include certain nonlinear elastic coupling terms, it is convenient to restrict this study to straight cantilever wings having mass and stiffness properties uniform with span. The wing is taken to be a one-dimensional structure in the sense that all deformations are described as functions of the spanwise variable y. Camber bending is neglected and the simple Euler-Bernoulli beam stress-strain assumptions are used. The platform is rectangular, and the steady and unsteady flow fields are always assumed to be superposable; unsteady loads are computed for the undeformed geometry and applied to the deformed wing. Although these assumptions would be restrictive for the purpose of modeling actual structures, they are acceptable here since only the relative influences of chordwise loads and steady deformations are of interest.

In Chapter II a vertical-bending/torsion model basic to the system of Ref. 1 is developed and modal equations are derived to permit flutter calculations for zero steady lift with steady drag included. Assumed mode solutions are then compared with results of Ref. 1. A linear steady-state version of the modal equations is then examined to allow computation of divergence speeds as affected by steady drag.

In Chapter III a model central to this thesis is developed that includes vertical bending, chordwise bending, and torsion. Nonlinear steady and linearized unsteady differential equations are then deduced, and they are analytically compared with the model in Chapter II.

In Chapter IV the modal forms of these steady and linearized unsteady equations are set up to include lifting airloads deduced from incompressible steady and unsteady strip-theory. A scheme based on the so-called V-g method of flutter analysis is used to determine neutral dynamic stability conditions, and results are checked against those of Chapter II.

In Chapter V a generalization to the case of arbitrary motion in time is presented through Laplace transformation of the modal equations, which requires incompressible unsteady two-dimensional airloads valid for non-periodic motions of the wing.

A determinant iteration procedure is used to determine the aeroelastic eigenvalues for flight speeds above and below the flutter speed. Finally, the effect of unsteady leading-edge suction forces predicted by incompressible strip theory is included in the linearized unsteady stability system.

In Chapter VI all results for incompressible strip-theory airloads are assembled and systematically presented, concluding with two examples based upon actual sailplanes.

In Chapter VII the flutter speed prediction scheme of Chapter IV is modified to use three-dimensional subsonic steady and unsteady lifting airloads. Results are presented to indicate the effects of three-dimensional aerodynamics, unsteady drag, and compressibility.

In Chapter VIII the principal conclusions of this thesis are presented.

Chapter II

DRAG EFFECTS ON FLUTTER AND DIVERGENCE; DEFORMATION IN VERTICAL BENDING AND TORSION ONLY

A. The Vertical Bending/Torsion Equations

In the Petre and Ashley work (Ref. 1) the effect of drag on flutter of cantilever wings is studied assuming only vertical bending and torsion about the elastic axis. The equations are cast into integral form, and solutions are obtained by collocation of the integral equations at ten stations across the span. Here we check the results of Ref. 1 using an entirely different, modal approach. The results also serve as examples with which to compare solutions found with the more general system, developed in the following chapter, which includes chordwise bending.

The differential equations of bending and torsion, as given in Ref. 1 and adapted to the present notation and coordinate system (as in Fig. 2-1), are

$$\text{(2-1a)} \qquad \frac{\partial^2}{\partial y^2}\left[EI_x \frac{\partial^2 w}{\partial y^2}\right] + m\frac{\partial^2 w}{\partial t^2} - s_e \frac{\partial^2 \phi}{\partial t^2} - L_a(w,\phi) + \frac{\partial^2}{\partial y^2}(M_z \phi) = 0$$

$$\text{(2-1b)} \qquad \frac{\partial}{\partial y}\left[GI_G \frac{\partial \phi}{\partial y}\right] - J\frac{\partial^2 \phi}{\partial t^2} + s_e \frac{\partial^2 w}{\partial t^2} + m_a(w,\phi) - M_z \frac{\partial^2 w}{\partial y^2} = 0$$

The quantity M_z is a function of y given by

$$(2\text{-}2)\qquad M_z = -\int_y^{\ell} D(\eta)(\eta-y)d\eta$$
$$= -D\,\tfrac{1}{2}[\ell-y]^2$$

where it is assumed that the running drag force D has constant magnitude across the span. M_z can be recognized as the total moment about the vertical axis applied at station y by all drag acting outboard of this station. Mean values of the twist and bending displacement are assumed to be zero.

Equations (2-1) are linear and are coupled inertially by the third term in each; these terms arise from the offset of the center of mass of the airfoil section from the elastic axis. A second coupling effect is due entirely to drag, introduced through the terms containing M_z . All remaining terms in the equations represent the conventional elastic, inertial, and unsteady lifting aerodynamic load contributions.

The manner in which the drag loads have been introduced into the system is discussed by Petre (pp. 449-487, Ref. 2) and can be explained by the following physically oriented argument. The drag coupling term in the bending equation arises from the resultant bending moment $m_x(y)$ applied at station y due to drag forces outboard of y . As shown in Fig. 2-1, a drag force acting outboard of station y has a component $D\phi(y)$ perpendicular to the airfoil's principal axis of vertical bending, giving a resultant moment at y about the principal direction of

$$m_x(y) = \phi(y)D\int_y^{\ell}(\eta-y)d\eta$$
$$= \phi(y)D\,\tfrac{1}{2}(\ell-y)^2$$
$$= -M_z\phi$$

The moment-curvature relation for the beam,

$$\frac{\partial^2 w}{\partial y^2} = \frac{m_x}{EI_x}$$

together with moment-shear equilibrium

$$\frac{\partial^2 m_x}{\partial y^2} = q(y)$$

(here $q(y)$ is the positive-upward running load in the principal direction of the section) allows the drag effect to be expressed in equilibrium with the elastic term as

$$\frac{\partial^2}{\partial y^2}\left[EI_x \frac{\partial^2 w}{\partial y^2}\right] + \frac{\partial^2}{\partial y^2}\left[M_z \phi\right] = 0$$

This is the same drag coupling term appearing in (2-1).

A similar derivation reveals the origin of the drag term in the torsion equation. Looking at the front view of the wing (Fig. 2.2) one can see that a drag load at η gives rise to a twisting moment at y by acting through the moment arm given by distance e ,

$$e = w(\eta) - \left[w(y) + \frac{\partial w}{\partial y}(y)(\eta - y)\right]$$

The resultant torque applied at station y by all drag forces acting outboard is given by

$$T_y(y) = D \int_y^{\ell} [w(\eta) - w(y) - \frac{\partial w}{\partial y}(y)\ (\eta - y)]d\eta$$

Differentiating with respect to y ,

$$\frac{dTy(y)}{dy} = D \int_y^\ell \left[- \frac{\partial^2 w(y)}{dy^2} (\eta - y) - \frac{\partial w}{\partial y} + \frac{\partial w}{\partial y} \right] d\eta$$

$$= - D \frac{\partial^2 w}{\partial y^2} \tfrac{1}{2}(\ell - y)^2$$

$$= M_z \frac{\partial^2 w}{\partial y^2}$$

Elastic equilibrium for a rod loaded with applied torsion $Ty(y)$ is given by

$$\frac{\partial}{\partial y}\left[GI_d \frac{\partial \phi}{\partial y} \right] - \frac{\partial Ty(y)}{\partial y} = 0$$

The drag coupling term of equation (2-1) can then be identified in the result

$$\frac{\partial}{\partial y}\left[GI_d \frac{\partial \phi}{\partial y} \right] - M_z \frac{\partial^2 w}{\partial y^2} = 0$$

B. Solution By Assumed Modes

When structural dynamics problems yield solutions whose frequencies are within the range of the structure's lowest normal mode natural frequencies and the latter have a sufficiently sparse distribution, modal analysis methods prove to be effective. Primary bending-torsion flutter of cantilever wings, under study here, is a classic example in aeroelasticity of such a system. Inclusion of steady drag effects should have only a small effect on the range of frequencies over which flutter solutions occur and, by this reasoning, should not adversely affect the convergence of modal solutions. Petre in Ref. 1 expresses the opinion that methods relying on the assumption of a few prescribed deformation modes constrain the flutter mode shape and should be avoided. This opinion is tested herein by actually studying modal convergence.

Solutions of (2-1) are sought using superposition of the dynamically uncoupled natural modes of free vibration in bending and torsion of a uniform cantilever beam. These assumed modes, with their relevant properties, are described in Appendix A. Although not true normal modes of the inertially-coupled structure, they can be considered as "pseudo-orthogonal" since integrals of the type

$$\int_0^1 m\, f_{w_i}\, f_{w_j}\, d\tilde{y} = 0 \qquad i \neq j$$

$$\int_0^1 J\, f_{\phi_i}\, f_{\phi_j}\, d\tilde{y} = 0 \qquad i \neq j$$

lead to uncoupled elastic behavior and hence a diagonal stiffness matrix in the matrix eigenvalue problem. Use of the actual normal modes would require that they be calculated for each wing configuration studied. Since the assumed modes satisfy the natural boundary conditions at the free end of the cantilever as well as the geometric boundary conditions at its clamped root, Galerkin's method can be applied to the differential equations (Ref. 4, p. 218) to obtain the system in terms of modal generalized coordinates.

To find the velocity for neutral stability (the flutter velocity), the V-g method (p. 381, Ref. 5), common in aeroelastic stability analyses, in employed. With simple harmonic motion of frequency ω the unsteady, incompressible, strip-theory lifting airloads are expressible as [(4-123) and (4-124) of Ref. 5]

$$L_a(w,\phi;t) = -\Pi\,\rho\,b^3\,\omega^2\{-L_w\frac{\tilde{w}}{b} + [L_\phi - (\tfrac{1}{2}+a)L_w]\tilde{\phi}\}e^{i\omega t} \tag{2-3a}$$

$$m_a(w,\phi;t) = \Pi\,\rho\,b^4\,\omega^2\{-[M_w - (\tfrac{1}{2}+a)L_w]\frac{\tilde{w}}{b} \tag{2-3b}$$

$$+ [M_\phi - (\tfrac{1}{2}+a)(L_\phi + M_w) + (\tfrac{1}{2}+a)^2\,L_w]\tilde{\phi}\}e^{i\omega t}$$

where

$$\begin{cases} L_w = 1 - \frac{2i}{k}\,C(k) & M_w = \frac{1}{2} \\ L_\phi = \frac{1}{2} - \frac{i}{k}\,[1 + 2C(k)] - \frac{2}{k^2}\,C(k) & M_\phi = \frac{3}{8} - \frac{i}{k} \end{cases} \tag{2-4}$$

Here $C(k)$ is the familiar Theodorsen function of reduced frequency $k = \frac{\omega b}{V}$.

The drag coupling terms in (2-1) can be treated as applied loads in developing the modal equations, by defining total applied force and moment in the bending and torsion equations as

$$F_z(y,t) = L_a(w,\phi,t) - \frac{\partial^2}{\partial y^2}(M_z\phi) \tag{2-5a}$$

$$m_y(y,t) = m_a(w,\phi,t) - M_z\frac{\partial^2 w}{\partial y^2} \tag{2-5b}$$

Incorporation of artificial structural damping g by allowing a complex elastic modulus produces the system

$$EI_x(1+ig)\frac{\partial^4 w}{\partial y^4} + m\frac{\partial^2 w}{\partial t^2} - s_e\frac{\partial^2\phi}{\partial t^2} = F_z(y,t) \tag{2-6a}$$

$$GI_d(1+ig)\frac{\partial^2\phi}{\partial y^2} - J\frac{\partial^2\phi}{\partial t^2} + s_e\frac{\partial^2 w}{\partial t^2} = -m_y(y,t) \tag{2-6b}$$

Formal development of the modal equations begins with substitution of the series expansions for w and ϕ in terms of the assumed mode shape functions and generalized coordinates. With the same number n of bending and torsion modes always used, the system order will be $2n$. Generalized displacements are assumed to have simple harmonic time dependence, giving

$$\text{(2-7a)} \qquad w(y,t) = \sum_{i=1}^{n} f_{w_i}(y)\, q_{w_i}\, e^{i\omega t}$$

$$\text{(2-7b)} \qquad \phi(y,t) = \sum_{i=1}^{n} f_{\phi_i}(y)\, q_{\phi_i}\, e^{i\omega t}$$

Generalized displacements for bending modes have units of length, where as for torsion they are dimensionless.

Galerkin's method involves substitution of (2-7) into the system represented by (2-1), (2-2), (2-3), and (2-4) and then multiplication of each term in the bending equation by f_{w_j} and each in the torsion equation by f_{ϕ_j}, followed by integration across the half span. With $e^{i\omega t}$ cancelled the resulting system is

$$\text{(2-8a)} \qquad EI_x(1+ig) \int_0^{\ell} \sum_{i=1}^{n} f''''_{w_i}\, f_{w_j}\, q_{w_i}\, dy - m\omega^2 \int_0^{\ell} \sum_{i=1}^{n} f_{w_i}\, f_{w_j}\, q_{w_i}\, dy$$

$$+ \omega^2 s_e \int_0^{\ell} \sum_{i=1}^{n} f_{\phi_i}\, f_{w_i}\, q_{\phi_i}\, dy = \frac{1}{e^{i\omega t}} \int_0^{\ell} F_z(\phi,w;t) f_{w_j}\, dy$$

$(1 \leq j \leq n)$

$$\text{(2-8b)} \qquad GI_d(1+ig) \int_0^{\ell} \sum_{i=1}^{n} f''_{\phi_i}\, f_{\phi_j}\, q_{\phi_i}\, dy + J\omega^2 \int_0^{\ell} \sum_{i=1}^{n} f_{\phi_i}\, f_{\phi_j}\, q_{\phi_i}\, dy$$

$$- \omega^2 s_e \int_0^{\ell} \sum_{i=1}^{n} f_{w_i}\, f_{\phi_j}\, q_{w_i}\, dy = -\frac{1}{e^{i\omega t}} \int_0^{\ell} m_y(\phi,w;t) f_{\phi_j}\, dy$$

The generalized forces can be arranged in terms of dimensionless unit generalized forces Q_{ji} through the following definitions:

$$\text{(2-9a)} \qquad \int_0^\ell F_z(\phi,w;t) f_{w_j}\, dy = \Pi\rho\omega^2 b^3 \ell \left[\sum_{i=1}^{n} Q_{j,i} \frac{q_{w_i}}{b} + \sum_{i=1}^{n} Q_{j,i+n} q_{\phi_i} \right] e^{i\omega t}$$

$$\text{(2-9b)} \qquad \int_0^\ell m_y(\phi,w;t) f_{\phi_j}\, dy = \Pi\rho\omega^2 b^4 \ell \left[\sum_{i=1}^{n} Q_{j+n,i} \frac{q_{w_i}}{b} + \sum_{i=1}^{n} Q_{j+n,i+n} q_{\phi_i} \right] e^{i\omega t}$$

The modal integral in the first term of (2-8a), integrated by parts twice and with application of cantilever boundary conditions, yields

$$\int_0^\ell f''''_{w_i} f_{w_j}\, dy = \int_0^\ell f''_{w_i} f''_{w_j}\, dy$$

$$= 0 \text{ for } i \neq j$$

From Appendix A, the $i=j$ term can be expressed in terms of the natural frequency of the jth assumed bending mode by the substitution

$$\text{(2-10)} \qquad EI_x \int_0^\ell (f''_{w_j})^2 dy = m\omega^2_{w_j} \int_0^\ell f^2_{w_j}\, dy = m\omega^2_{w_j} \ell$$

Similarly, integrating the first term in (2-8b) by parts and introducing the natural frequency ω_{ϕ_j} of the jth assumed torsion mode leads to

$$\text{(2-11)} \qquad GI_d \int_0^\ell f''_{\phi_i} f_{\phi_j}\, dy = \begin{cases} 0 & (i \neq j) \\ -\tfrac{1}{2} J\omega^2_{\phi_j} \ell & (i = j) \end{cases}$$

Insertion of (2-9), (2-10), and (2-11) into (2-8) and further use of modal orthogonality properties gives

$$(2\text{-}12a) \qquad \frac{m}{\Pi\rho b^2}(1+ig)\frac{\omega_{w_j}^2}{\omega^2}\frac{q_{w_j}}{b} - \frac{m}{\Pi\rho b^2}\frac{q_{w_j}}{b} + \frac{s_e}{bm}\frac{m}{\Pi\rho b^2}\sum_{i=1}^{n} I_{ij}\, q_{\phi_i}$$

$$+ \sum_{i=1}^{n} Q_{j,i}\frac{q_{w_i}}{b} + \sum_{i=1}^{n} Q_{j,i+n}\, q_{\phi_i} = 0$$

$(1 \leq j \leq n)$

$$(2\text{-}12b) \qquad \tfrac{1}{2}\frac{m}{\Pi\rho b^2}\frac{J}{mb^2}\frac{I_d}{J}\frac{\omega_\phi^2}{\omega^2}\, q_{\phi_j} - \tfrac{1}{2}\frac{m}{\Pi\rho b^2}\frac{J}{mb^2}\, q_{\phi_j}$$

$$+ \frac{s_e}{bm}\frac{m}{\Pi\rho b^2}\sum_{i=1}^{n} I_{ij}\frac{q_{w_i}}{b} + \sum_{i=1}^{n} Q_{j+n,i}\frac{q_{w_i}}{b} + \sum_{i=1}^{n} Q_{j+n,i+n}\, q_{\phi_i} = 0$$

where the bending equation has been divided through by $\Pi\rho\omega^2 b^3 \ell$ and the torsion equation by $\Pi\rho\omega^2 b^4 \ell$. Inertial coupling, a consequence of nonorthogonality between bending and torsion assumed modes, produces terms in the modal integrals

$$(2\text{-}13) \qquad I_{ij} \equiv \int_0^1 f_{w_i}(\tilde{y})\, f_{\phi_j}(\tilde{y})\, d\tilde{y}$$

For now it is convenient to reference ω to the first assumed torsion mode natural frequency ω_{ϕ_1} . Assumed mode natural frequencies (Appendix A) are

$$(2\text{-}14) \qquad \begin{cases} \omega_{\phi_j}^2 = \dfrac{2_j-1}{2}\,\dfrac{\Pi^2}{\ell^2}\,\dfrac{GI_d}{J} \\[2ex] \omega_{w_j}^2 = N_j\,\dfrac{4\Pi^4}{\ell^4}\,\dfrac{EI_x}{m} \end{cases}$$

Ratios that are useful are then

$$(2\text{-}15)\quad \left\{\begin{aligned} \frac{\omega^2_{w_j}}{\omega^2_{\phi_j}} &= \frac{N_j^4\Pi^2}{4}\,\frac{EI_x b^2}{GI_d \ell^2}\,\frac{J}{mb^2} \\[2ex] \frac{\omega^2_{\phi_j}}{\omega^2_{\phi_1}} &= (2j-1)^2 \end{aligned}\right.$$

The transcendental N_j are given in Appendix A for $1 \leq j \leq 5$.

The equations can be nondimensionalized through the following dimensionless parameters, chosen to be as consistent as possible with Ref. 1 notation.

$$(2\text{-}16)\quad \left\{\begin{aligned} M &\equiv \frac{m}{\Pi\rho b^2} & \qquad S &\equiv \frac{s_e}{bm} \\[2ex] P &\equiv \frac{EI_x b^2}{GI_d \ell^2} & \qquad i_\alpha &\equiv \frac{J}{mb^2} \end{aligned}\right.$$

Frequency is nondimensionalized as in Ref. 1 by defining the frequency parameter

$$(2\text{-}17)\qquad Z \equiv (1+ig)\Omega^2 \equiv (1+ig)\frac{GI_d}{J\ell^2\omega^2} = \frac{4}{\Pi^2}\,\frac{\omega^2_{\phi_1}}{\omega^2}\,(1+ig)$$

Substitution of (2-15), (2-16), and (2-17) into (2-12) yields the modal equations in a suitable form for computation.

$$(2\text{-}18a)\qquad \{M - N_j^4\Pi^4 MPi_\alpha Z\}\frac{q_{w_j}}{b} + \sum_{i=1}^{n} Q_{j,i}\,\frac{q_{w_i}}{b} + \sum_{i=1}^{n}\{MSI_{ji} + Q_{j,i+n}\}q_{\phi_i} = 0$$

$$(1 \leq j \leq n)$$

$$(2\text{-}18b) \qquad \sum_{i=1}^{n} \{- MSI_{ij} + Q_{j+n,i}\} \frac{q_{w_i}}{b} + \{\tfrac{1}{2} M_{I_\alpha}[1 - \Pi^2(j-\tfrac{1}{2})^2 Z]\} q_{\phi_j}$$

$$+ \sum_{i=1}^{n} Q_{j+n,i+n}\, q_{\phi_i} = 0$$

The flutter determinant, of order $2n$, results as a necessary condition for a nontrivial solution and leads to a complex eigenvalue problem to determine Z .

Next, the unit generalized forces Q_{ij} must be expressed to allow numerical computation. Combining (2-3), (2-4), and (2-7) into (2-9) leads to

$$(2\text{-}19a) \qquad - \Pi\rho b^3\omega^2 \{ - \int_0^\ell L_w \sum_{i=1}^{n} f_{w_i}(y) f_{w_j}(y) \frac{q_{w_i}}{b} dy + \int_0^\ell [L_\phi - (\tfrac{1}{2}+a)L_w] \cdot$$

$$\cdot \sum_{i=1}^{n} f_{\phi_i}(y) f_{w_j}(y) q_{\phi_i} dy\} + \int_0^\ell \frac{\partial^2}{\partial y^2} [\frac{\rho}{2} V^2 b C_D (\ell - y)^2 \sum_{i=1}^{n} f_{\phi_i}(y) q_{\phi_i}] \cdot$$

$$(1 \leq j \leq n) \qquad \cdot f_{w_j}(y) dy = \Pi\rho\omega^2 b^3 \ell [\sum_{i=1}^{n} Q_{j,i} \frac{q_{w_i}}{b} + \sum_{i=1}^{n} Q_{j,i+n}\, q_{\phi_i}]$$

$$(2\text{-}19b) \qquad \Pi\rho b^4\omega^2\{ \int_0^\ell [-M_w + (\tfrac{1}{2}+a)L_w] \sum_{i=1}^{n} f_{w_i}(y) f_{\phi_j}(y) \frac{q_{w_i}}{b} dy$$

$$+ \int_0^\ell [M_\phi - (\tfrac{1}{2}+a)(L_\phi + M_w) + (\tfrac{1}{2}+a)^2 L_w] \sum_{i=1}^{n} f_{\phi_i}(y) f_{\phi_j}(y) q_{\phi_i} dy\}$$

$$+ \int_0^\ell \tfrac{1}{2}\rho V^2 b^2 (\ell - y)^2 C_D \sum_{i=1}^{n} f''_{w_i}(y) f_{\phi_j}(y) \frac{q_{w_i}}{b} dy$$

$$= \Pi\rho\omega^2 b^4 \ell [\sum_{i=1}^{n} Q_{j+n,i} \frac{q_{w_i}}{b} + \sum_{i=1}^{n} Q_{j+n,i+n}\, q_{\phi_i}]$$

After further reduction, with

$$V^2 = \frac{\omega^2 b^2}{k^2}$$

and carrying out remaining differentiations in y , (2-19) becomes:

$$(2\text{-}20a) \qquad \sum_{i=1}^{n} \{L_w \int_0^1 f_{w_i}(\tilde{y}) f_{w_j}(\tilde{y}) d\tilde{y}\} \frac{q_{w_i}}{b} + \sum_{i=1}^{n} \{[-L_\phi + (\tfrac{1}{2}+a)L_w] \cdot$$

$$\cdot \int_0^1 f_{\phi_i}(\tilde{y}) f_{w_j}(\tilde{y}) d\tilde{y} + \frac{C_D}{2\pi k^2}[2 \int_0^1 f_{\phi_i}(\tilde{y}) f_{w_j}(\tilde{y}) d\tilde{y} - 4 \int_0^1 (1-\tilde{y}) \cdot$$

$$(1 \leq j \leq n) \qquad \cdot f'_{\phi_i}(\tilde{y}) f_{w_j}(\tilde{y}) d\tilde{y} + \int_0^1 (1-\tilde{y})^2 f''_{\phi_i}(\tilde{y}) f_{w_j}(\tilde{y}) d\tilde{y}]\} q_{\phi_i}$$

$$= \sum_{i=1}^{n} Q_{j,i} \frac{q_{w_i}}{b} + \sum_{i=1}^{n} Q_{j,i+n}\, q_{\phi_i}$$

$$(2\text{-}20b) \qquad \sum_{i=1}^{n} \{-M_w + (\tfrac{1}{2}+a)L_w] \int_0^1 f_{w_j}(\tilde{y}) f_{\phi_j}(\tilde{y}) d\tilde{y}$$

$$+ \frac{C_D}{2\pi k^2} \int_0^1 (1-\tilde{y})^2 f''_{w_i}(\tilde{y}) f_{\phi_j}(\tilde{y}) d\tilde{y}\} \frac{q_{w_i}}{b} + \sum_{i=1}^{n} \{[M_\phi - (\tfrac{1}{2}+a)(L_\phi + M_w)$$

$$+ (\tfrac{1}{2}+a)^2 L_w] \int_0^1 f_{\phi_i}(\tilde{y}) f_{\phi_j}(\tilde{y}) d\tilde{y}\} q_{\phi_i}$$

$$= \sum_{i=1}^{n} Q_{j+n,i} \frac{q_{w_i}}{b} + \sum_{i=1}^{n} Q_{j+n,i+n}\, q_{\phi_i}$$

Here, integrals in the spanwise variable y have been nondimensionalized. Four different types of modal integrals are encountered, including the I_{ij} previously identified. The three new forms arise from the drag coupling terms and are

$$(2\text{-}21) \qquad \begin{cases} I_{ij}^{(1)} = \int_0^1 (1-\tilde{y})^2 f''_{w_i}(\tilde{y}) f_{\phi_j}(\tilde{y}) d\tilde{y} \\ I_{ij}^{(2)} = \int_0^1 (1-\tilde{y}) f'_{\phi_i}(\tilde{y}) f_{w_j}(\tilde{y}) d\tilde{y} \\ I_{ij}^{(3)} = \int_0^1 (1-\tilde{y})^2 f''_{\phi_i}(\tilde{y}) f_{w_j}(\tilde{y}) d\tilde{y} \end{cases}$$

The modal integrals in (2-13) and (2-21) were numerically computed to twelve significant digits for $1 \leq i,j \leq 5$.

Two additional dimensionless parameters can be introduced, again drawn from Ref. 1.

$$(2\text{-}22) \qquad A = \tfrac{1}{2} + 2 \qquad\qquad C = \frac{C_D}{2\pi}$$

The drag parameter C is defined as the applied steady sectional drag coefficient divided by the sectional lift curve slope (2π for incompresible strip theory).

After (2-20), (2-21), and (2-22) are combined with orthogonal modal integrals recognized, the unit generalized forces are found to be

$$(2\text{-}23) \quad \left\{ \begin{array}{lll} Q_{j,i} & = & \begin{cases} L_w & (i=j) \\ 0 & (i \neq j) \end{cases} \\ Q_{j,i+n} & = & -\,[L \;-\; AL_w]I_{ij} + \frac{C}{k^2}\,[2I_{ij} - 4\,I_{ij}^{(2)} + I_{ij}^{(3)}] \\ Q_{j+n,i} & = & -\,[M_w - AL_w]I_{ij} + \frac{C}{k^2}\,I_{ij}^{(1)} \\ Q_{j+n,i+n} & = & \begin{cases} \tfrac{1}{2}[M_\phi - A(L_\phi + M_w) + A^2 L_w] & (i=j) \\ 0 & (i \neq j) \end{cases} \end{array} \right.$$

The Q_{ij} depend only upon k, A, and C . Actual computation of the Theodorsen function is accomplished by direct use of the ascending power series of the modified Bessel functions K_o and K_1 , as explained in Appendix B.

Equations (2-4), (2-18), and (2-23) together supply the flutter determinant for the VT system using assumed modes, given in matrix form in (2-24). Solutions can be found using from one to five assumed modes in each of bending and torsion, and the maximum order of the determinant will be 10.

$$\left|\begin{array}{ccc|ccc}
M[1-(N_1\Pi)^4 P i_\alpha Z]+Q_{11} & & 0 & -MSI_{11}+Q_{1,n+1} & \cdots & -MSI_{1n}+Q_{1,2n} \\
 & \ddots & & \vdots & & \vdots \\
0 & & M[1-(N_n\Pi)^4 P i_\alpha Z]+Q_{n,n} & -MSI_{n1}+Q_{n,n+1} & \cdots & -MSI_{nn}+Q_{n,2n} \\
\hline
-MSI_{11}+Q_{n+1,1} & \cdots & -MSI_{n1}+Q_{n+1,n} & \frac{1}{2}Mi_\alpha[1-\frac{\Pi^2}{4}Z]+Q_{n+1,n+1} & & 0 \\
\vdots & & \vdots & & \ddots & \\
-MSI_{1n}+Q_{2n,1} & \cdots & -MSI_{nn}+Q_{2n,n} & 0 & & \frac{1}{2}Mi_\alpha[1-(n-\ )^2\Pi^2]+Q_{2n,2n}
\end{array}\right| = 0 \tag{2-24}$$

In seeking solutions, values for M, P, i_α, A, and S must first be chosen to specify the wing configuration. Then, for any desired value of C and an estimate of reduced frequency k, complex eigenvalues Z can be found from (2-24) via linear matrix eigenvalue techniques.

A computer program is used to solve for flutter conditions as follows. With a first estimate of k chosen large enough so that the structural damping,

$$g = \frac{\mathrm{Im}(Z)}{\mathrm{Re}(Z)} \tag{2-25}$$

is negative for all $2n$ eigenvalues, successively smaller values of k are assigned and eigenvalues computed until a positive g is obtained for the eigenvalue corresponding to the aeroelastic mode which encounters flutter. Then a zero-finding subroutine locates k for which $g=0$ for the flutter mode. Dimensionless speed and frequency, defined by

$$U \equiv \frac{V\ell}{b}\sqrt{\frac{J}{GI_d}}$$

(2-26)

$$\Omega \equiv \omega\ell\sqrt{\frac{J}{GI_d}}$$

can easily be computed for the flutter eigenvalue by

$$\Omega = \frac{1}{\sqrt{\mathrm{Re}\,(Z)}}$$

(2-27)

$$U = \frac{\Omega}{k}$$

The flutter mode shape is also found, since it is related to the eigenvector of the eigenvalue yielding the flutter condition.

C. Comparison of Modal with Collocation Results

A rather thorough study was carried out in Ref. 1, covering a wide range of practical combinations of the dimensionless parameters. The present objective is not to recalculate all of the same data but rather to evaluate the effectiveness of the assumed-mode approach. Consequently, (2-24) has been solved at conditions parallel to ones for which results are published in Ref. 1 to offer direct comparison. Also (2-24) is used to verify the performance of the VCT system developed in the next chapter.

A comparison of assumed mode calculations with Ref. 1 results is presented in Table 2.1 for three different configurations. Of these, cases (a) and (c) represent a stubby low-aspect-ratio wing (with P = .4) whereas case (b) is the opposite extreme of large aspect ratio. A typical ratio $\frac{EI_x}{GI_d} = 1.6$, for example, would fix the aspect ratio of cases (a) and (c) at 2 and of case (b) at 20 . The mass ratio parameter of cases (a), (b) is in the regime encountered by sailplanes whereas in (c) it is representative of conventional aircraft. Finally, the steady drag parameter is zero in the first two cases but has the extremely large value $C = 0.04$ in (c) .

In all cases $n=3$ already yields adequate modal convergence. For the large aspect ratio case the use of one assumed mode $(n=1)$ gives a significant error, yet $n=2$ produces good accuracy. This suggests that the second bending mode is an important factor in flutter of high-aspect-ratio wings, a phenomenon discussed in Chapter 6.

Additional comparisons between flutter speeds and frequencies found by the two methods are offered in Table 2.2, emphasizing their relative accuracy as steady drag is increased to the very high value $C = 0.04$. Evidently good agreement is maintained in the presence of drag.

The mode shape at flutter for two of the preceding cases is presented in Table 2.3 for wings of small and large aspect ratio, each with $C = 0.04$. Amplitudes of the ten generalized displacements are normalized with respect to $|q_{\phi_1}|$, and the phase angles are referenced to the phase of this torsion mode. For $P = 0.4$ only q_{ϕ_1} and q_{w_1} have appreciable magnitude, whereas the large-aspect-ratio example displays a significant contribution by q_{w_2} as well.

These flutter mode shapes can be compared to the Ref. 1 results, with some effort, as follows. In Ref. 1, the tangent of the angle by which the torsional displacement at the wingtip leads bending displacement in the flutter mode is tabulated; it is converted here to an angle in degrees. The spanwise shape of the bending portion of the mode at flutter for the two Table 2.3 cases is illustrated in Fig. 5 of Ref. 1. Since the flutter mode's bending displacement obtained in that treatment was complex, its amplitude at each spanwise station was taken, phase differences being neglected in the figure.

For the present solutions a similar assumption is made to display the bending mode shape of the $P = 0.004$ case in Table 2.3. Contributions of q_{w_1} and q_{w_2} have been added vectorically at points along the span to allow comparison of bending amplitudes with the Ref. 1 figure. For $\rho = 0.4$, of course, only the first bending mode contributes significantly and phase differences are negligible.

The comparison of bending flutter mode shapes appears in Fig. 2-3, where amplitudes are normalized to unit torsional displacement at the tip. Phase angles δ between bending and torsion at the tip are also compared. At low aspect ratio excellent agreement for phase angles and mode shapes is observed, with mild disagreement in the bending mode amplitudes. In the $P = 0.004$ case, for which the Ref. 1 solution was made using only five spanwise collocation points, a significant disagreement in mode shapes and tip phase angles is observed. In spite of this discrepancy, the respective flutter speeds differ by only 0.82%. For all large-aspect-ratio cases compared this sort of discrepancy in flutter mode shapes is observed, where the second bending mode plays a significant role and causes appreciable phase differences in bending deflections along the span. Mode shapes at flutter are analyzed in more detail in Chapter 6.

D. Divergence Including the Effects of Drag

One further application of the VT linear model is predicting the effect of drag forces, steady in direction and magnitude and uniform across the span, on static aeroelastic stability. Removal of all time-dependent terms in (2-1) and insertion of simple strip-theory steady incompressible aerodynamic loads gives

$$EI_x \frac{\partial^4 w_o}{\partial y^4} - 2\Pi\rho V^2 b\phi_o + \frac{\partial^2}{\partial y^2}(M_z\phi_o) = 0 \qquad \text{(2-28a)}$$

$$GI_d \frac{\partial^2 \phi_o}{\partial y^2} + 2\Pi\rho V^2 b^2 A\phi_o - M_z \frac{\partial^2 w_o}{\partial y^2} = 0 \qquad \text{(2-28b)}$$

Subscripts emphasize that deflections are static quantities.

As in the foregoing dynamic analysis, deflections are represented by assumed modes and a system of 2n modal equations is derived, which has a nontrivial solution only if the determinant of the matrix of coefficients is zero which yields the divergence speed with drag effects included. For brevity, since the manipulations involved are quite straightforward, the final form of the stability determinant is presented here.

$$\text{(2-29)} \quad \left|\begin{array}{ccc:ccc}
\Pi^4 N_1^4 P i_\alpha M \frac{1}{U_D^2} & & 0 & -\left[\begin{array}{l}2(1+C)I_{11} \\ + CI^{(3)}_{11} - 4CI^{(2)}_{11}\end{array}\right] & \cdots & -\left[\begin{array}{l}2(1+C)I_{1n} \\ + CI^{(3)}_{1n} - 4CI^{(2)}_{1n}\end{array}\right] \\
 & \ddots & & \vdots & & \vdots \\
0 & & \Pi^4 N_n^4 \frac{P i_\alpha M}{U_D^2} & -\left[\begin{array}{l}2(1+C)I_{n1} \\ + CI^{(3)}_{n1} - 4CI^{(2)}_{n1}\end{array}\right] & \cdots & -\left[\begin{array}{l}2(1+C)I_{nn} \\ + CI^{(3)}_{nn} - 4CI^{(2)}_{nn}\end{array}\right] \\
\hdashline
- CI^{(1)}_{11} & \cdots & - CI^{(1)}_{1n} & \frac{\Pi^2}{8} \frac{i_\alpha M}{U_D^2} - A & & 0 \\
\vdots & & \vdots & & \ddots & \\
- CI^{(1)}_{n1} & \cdots & - CI^{(1)}_{nn} & 0 & & \frac{\Pi^2}{2}(n-\tfrac{1}{2})^2 \frac{i_\alpha M}{U_D^2} - A
\end{array}\right| = 0$$

Solution of this determinant for its largest eigenvalue gives the divergence speed U_D . This is of interest in the ensuing work, particularly for studying dynamic stability of wings having steady-state lifting deflections in the presence of drag, which can reduce divergence speed considerably.

For zero steady drag (C=0) the classical divergence speed comes trivially from (2-29), which degenerates for $C = 0$. The classical divergence mode shape is just the first assumed torsion half-sine mode, and the first torsion modal equation uncouples to give the divergence speed,

$$U_D = \Pi\sqrt{\frac{i_\alpha M}{8A}} \tag{2-30}$$

When A is decreased to zero this classical divergence speed becomes infinite; yet when $C \neq 0$ (2-29) will still yield finite solutions with $A = 0$.

A direct comparison of solutions of (2-29) with Ref. 1 results for the effect of drag on divergence is presented in Table 2.4. Modal convergence is satisfactory, but the modal approach appears to differ more significantly from the Ref. 1 analysis for divergence calculations than for flutter results.

Case	n	U_F	Ω_F	% Difference of U_F from n=5
(a)				
$M = 10.0$	1	2.7175179	1.3105289	0.239%
$P = 0.4$	2	2.7239548	1.3114559	0.00239%
$i_\alpha = 0.25$	3	2.7240004	1.3114641	0.00072%
$S = 0.1$	4	2.7240178	1.3114673	0.000077%
$A = 0.1$	5	2.7240199	1.3114675	--
$C = 0.0$				
	(Ref. 1)	2.699	1.309	0.918%
(b)				
	1	4.2621908	0.842707	4.296%
$M = 10.0$	2	4.0842768	0.8849367	0.0576%
$P = 0.004$	3	4.0864182	0.8850560	0.0052%
$i_\alpha = 0.25$	4	4.0866066	0.8850659	0.000597%
$S = 0.1$	5	4.0866310	0.8850660	--
$A = 0.1$				
$C = 0.0$	(Ref. 1)	4.032	0.886	1.337%
(c)				
$M = 40.$	2	4.260823	1.294037	0.00155%
$P = 0.4$	3	4.260879	1.2940232	0.000235%
$i_\alpha = 0.25$	4	4.260882	1.2940250	0.00016%
$S = 0.1$	5	4.260889	1.2940236	--
$A = 0.1$				
$C = 0.04$	(Ref. 1)	4.199	1.293	1.4525%

TABLE 2.1 Comparison of Assumed Mode and Collacation Methods for Predicting Flutter Speeds and Frequencies for Three Configurations

Case	C	U_F			Ω_F		
		n = 5	Ref. 1	% Difference	n = 5	Ref. 1	% Difference
$P = 0.4$ $M = 10.0$ $i_\alpha = 0.25$ $S = 0.1$ $A = 0.1$	0.0	2.7240	2.699	0.93%	1.3115	1.309	0.19%
	0.02	2.7830	2.753	1.08%	1.3071	1.305	0.16%
	0.04	2.8623	2.823	1.37%	1.3024	1.300	0.18%
$P = 0.004$ $M = 40.0$ $i_\alpha = 0.24$ $S = 0.1$ $A = 0.1$	0.0	7.1778	7.127	0.71%	0.8651	0.875	1.14%
	0.02	6.8588	6.797	0.90%	0.9074	0.919	1.28%
	0.04	6.7704	6.715	0.82%	0.9223	0.934	1.27%

TABLE 2.2 Effect of Drag on Agreement of Modal Analysis with Ref. 1

Generalized Displacement	P = 0.4		P = 0.004	
	Amplitude	Phase	Amplitude	Phase
q_{w_1}	0.71276	219.62°	1.4515	195.46°
q_{w_2}	0.00132	21.95°	0.6288	217.24°
q_{w_3}	0.0000271	150.13°	0.00449	203.35°
q_{w_4}	0.00000408	147.28°	0.000674	-10.94°
q_{w_5}	0.00000213	163.47°	0.000189	157.41°
q_{ϕ_1}	1.0	0°	1.0	0°
q_{ϕ_2}	0.01503	222.02°	0.01454	147.11°
q_{ϕ_3}	0.000808	215.78°	0.01786	210.39°
q_{ϕ_4}	0.000773	221.31°	0.00930	210.13°
q_{ϕ_5}	0.000186	217.90°	0.00462	211.73°

TABLE 2.3 Flutter Mode Shapes for Low- and High-Aspect-Ratio Examples. ($M = 40$, $i_\alpha = 0.25$, $A = 0.1$, $S = 0.1$, $C = 0.04$)

	C = 0.02		C = 0.04	
n	U_D	% Difference From n = 5	U_D	% Difference From n = 5
1	4.58288	2.044%	3.90105	1.999%
2	4.48660	-0.0999%	3.81863	-0.156%
3	4.49174	0.0144%	3.82465	0.0017%
4	4.49067	-0.0094%	3.82403	-0.0144%
5	4.49109	--	2.82458	--
(Ref. 1)	4.66	3.63%	3.96	3.42%

TABLE 2.4 Comparison of Ref. 1 Results With (2-29) Solutions for Divergence Speeds in the Presence of Drag. ($P = 0.004$, $M = 40.$, $i_\alpha = 0.25$, $A = 0.1$). (For $C = 0$, $U_D = 11.1072$)

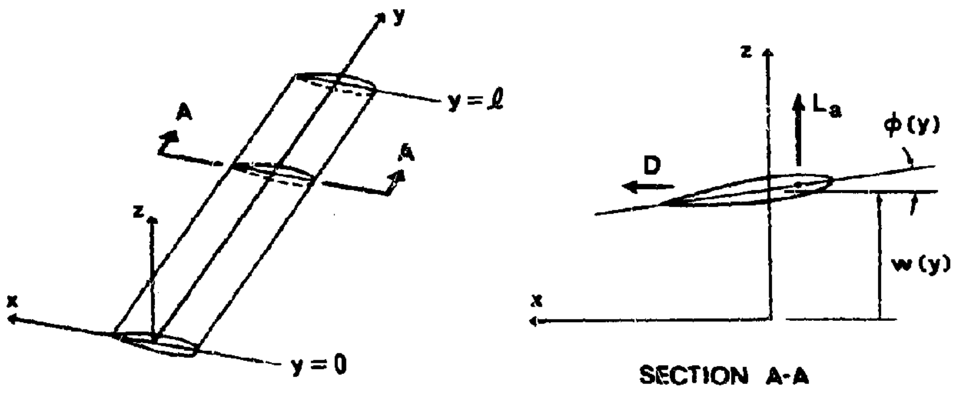

FIGURE 2-1 Physical Origin of Drag Coupling in Eq. (2-1a)

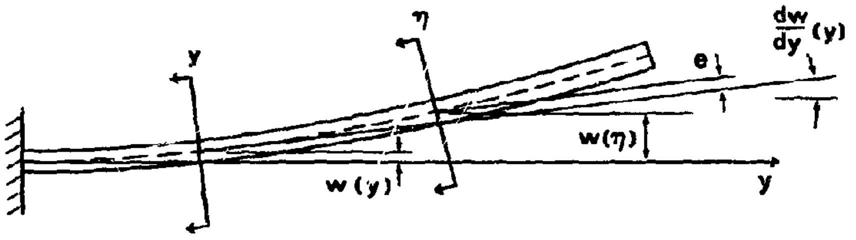

FIGURE 2-2 Physical Origin of Drag Coupling in Eq. (2-1b)

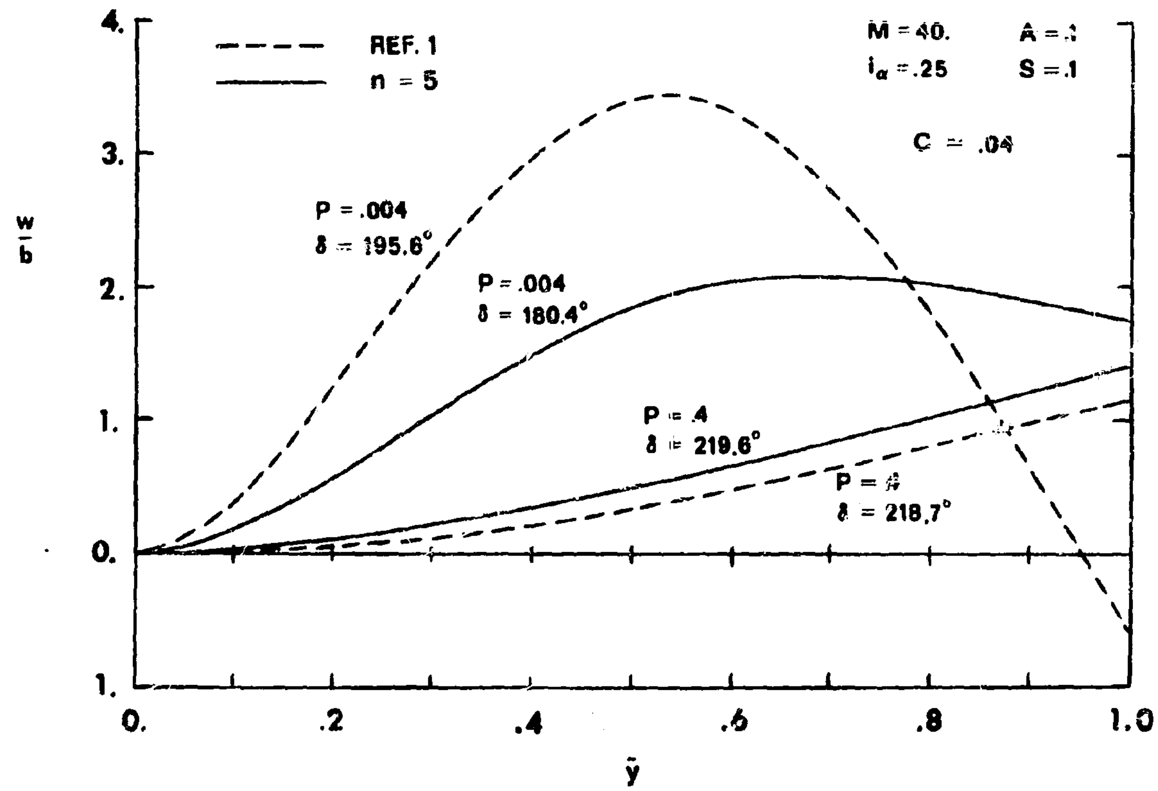

FIGURE 2-3 Comparison of Flutter Bending-Mode Shapes From Ref. 1 With Assumed Mode Results for Small- and Large-Aspect-Ratio Examples

Chapter III

DEVELOPMENT OF A GENERAL SYSTEM OF EQUATIONS FOR VERTICAL BENDING/CHORDWISE BENDING/TORSION (VCT)

A. Introduction

Chapter II includes drag loads in transverse bending and torsion but allows no chordwise deflections. In other words, it assumes infinitely large bending rigidity in the fore-and-aft direction. In this chapter we consider chordwise bending, which is a more complete model of the true physical situation.

A review of the literature for work concerning VCT motion of slender cantilever beams led to the field of hingeless helicopter rotor stability analysis. The structural modeling of a hingeless rotor is essentially the same as desired here, except that the wing has no rotational velocity. Accordingly, if an adequate model for a hingeless rotor can be found, it can be adapted for the cantilever wing by removing the inertial and centrifugal tension effects arising from rotation.

Much of the work pursued in the hingeless rotor field includes simplifications which either eliminate or restrict one of the three types of deformation, often torsion, in an effort to reduce complexity. This leaves a relatively small body of work that treats the full elastic problem. A well-known system of linear partial differential equations for coupled elastic torsion and bending of twisted nonuniform rotor blades is that developed by Houbolt and Brooks (Ref. 6); the initial effort to develop a VCT system for the cantilever wing centered on adapting this formulation. In the course of this work, however, the elastic coupling terms were found to be insufficient to account for the drag loads in transverse bending and torsion embodied by the terms containing M_z in (2-1). It then became apparent that this drag coupling is actually a nonlinear structural bending-torsion effect and that the new system of equations to be developed should, of necessity, retain all nonlinear elastic coupling terms having the same order of importance as these drag coupling terms.

Further search led to the system of nonlinear equations for twisted nonuniform rotor blades derived by Hodges and Dowell (Ref. 7). This work involves development of a more complete strain-displacement relation than that of Ref. 6, which is necessary to obtain the elastic bending-torsion coupling terms that produce the desired drag coupling effect. The equations in Ref. 7 are valid for straight, slender, homogeneous, isotropic beams undergoing moderate displacements, accurate to second order in the sense of a restriction that squares of bending slopes, twist, and airfoil chord and thickness divided by wing semispan are small with respect to unity.

Although the final form of the equations presented in Ref. 7 might appear to be immediately adaptable to the present case by setting the rotor rotation frequency to zero and removing the effects of pretwist, this is not entirely true. One important assumption by Hodges and Dowell required that the ratio between the transverse and chordwise beam bending stiffnesses be a quantity of order one. Whereas this is a standard feature of helicopter blade construction, it usually does not hold for conventional aircraft wings of any aspect ratio. As a result, the Ref. 7 derivation has been carefully retraced for the specific case of a nonrotating cantilever wing having arbitrary bending stiffness ratio. The development is outlined in the following section.

B. Development of the Nonlinear Equations of Motion

Derivation of the VCT model for the uniform cantilever wing is presented here in abbreviated form. Important modifications of the Ref. 7 derivation are emphasized, but duplicate manipulations are only briefly described. The notation and coordinate system for the cantilever wing is used exclusively.

The basic ordering scheme presented in equation (4) of Ref. 7 is retained. One exception is that spanwise warping of the cross section due to twisting, represented by a warp displacement function which is a solution of the Laplace equation over the cross section, is entirely neglected here. This assumption is made on the premise that a typical aircraft wing airfoil section would have a sufficiently small thickness that warping effects would be negligible within the second-order framework. The ordering scheme is applied to the energy expressions encountered in the variational derivation of the equations, to determine which terms should be retained and which discarded.

The nonlinear strain displacement relations developed in Ref. 7 have been carefully examined in the context of the present problem, and they are found to apply without modifications. These relations are derived from an exact transformation between the deformed and undeformed coordinate sytems and originate from the classical definition of strain of Novozhilov (Ref. 19) which is based upon increments in the deformed coordinates. After approximation to second order consistent with all assumptions, the final form in terms of engineering strain and in the present notation is

$$(3\text{-}1)\quad \begin{cases} \varepsilon_{yy} = u_y' + \dfrac{u_x'^2}{2} + \dfrac{u_z'^2}{2} - u_x''\,[\xi\cos\phi + \eta\sin\phi] \\ \qquad\qquad - u_z''[-\,\xi\sin\phi + \eta\cos\phi] \\ \varepsilon_{y\xi} = \eta\phi' \\ \varepsilon_{y\eta} = -\,\xi\phi' \end{cases}$$

These can be recognized as identical to equations (24), (25), (26), and (27) of Ref. 7 after the warp function and pretwist angle have been eliminated. The displacements u_x, u_y, u_z of the elastic axis and the principal coordinates ξ , η of the cross section are illustrated in Figure 3.1.

Development of the equations using the indirect method of the calculus of variations is based upon Hamilton's principle, which may be stated in the form

$$(3\text{-}2)\qquad \int_{t_1}^{t_2} [\delta(\mathcal{U}-\mathcal{T}) - \delta\mathcal{W}]dt = 0$$

The equations are obtained by combining expressions for the first variation of strain energy $\delta\mathcal{U}$, kinetic energy $\delta\mathcal{T}$, and virtual work of external forces $\delta\mathcal{W}$.

The first variation of strain energy in appropriate form for the standard Euler-Bernoulli beam uniaxial stress-strain relationship is

$$(3\text{-}3)\qquad \delta\mathcal{U} = \int_0^{\ell} \iint_{\text{area}} (\sigma_{yy}\,\delta\varepsilon_{yy} + \sigma_{y\xi}\,\delta\varepsilon_{y\xi} + \sigma_{y\eta}\,\delta\varepsilon_{y\eta})d\xi\,d\eta\,dy$$

The first variation of the engineering strains, expressed in terms of displacements, is

$$
(3\text{-}4)\quad \left\{
\begin{aligned}
\delta\varepsilon_{yy} &= \delta u'_y + u'_x\,\delta u'_x + u'_z\,\delta u'_z \\
&\qquad - [\xi\cos\phi + \eta\sin\phi](\delta u''_x - u''_z\,\delta\phi) \\
&\qquad - [\xi\sin\phi + \eta\cos\phi](\delta u''_z + u''_x\,\delta\phi) \\
\delta\varepsilon_{y\xi} &= \eta\ \delta\ \phi' \\
\delta\varepsilon_{y\eta} &= -\xi\ \delta\ \phi'
\end{aligned}
\right.
$$

The stresses are simply

$$
(3\text{-}5)\quad \left\{
\begin{aligned}
\sigma_{yy} &= E\varepsilon_{yy} \\
\sigma_{y\xi} &= G\varepsilon_{y\xi} \\
\sigma_{y\eta} &+ G\varepsilon_{y\eta}
\end{aligned}
\right.
$$

Substituting (3-1), (3-4), (3-5) into (3-3) yields

$$
(3\text{-}6)\quad \left\{
\begin{aligned}
\delta U = \int_0^{\ell} \iint_{\text{area}} \Big\{ & E\Big[u'_y + \frac{u'^2_x}{2} + \frac{u'^2_z}{2} - u''_x(\xi\cos\phi + \eta\sin\phi) \\
& - u''_z(-\xi\sin\phi + \eta\cos\phi)\Big]\Big[\delta u'_y + u'_x\delta u'_x + u'_z\ \delta u'_z \\
& - (\xi\cos\phi + \eta\sin\phi)(\delta u''_x - u''_z\ \delta\phi) \\
& - (-\xi\sin\phi + \eta\cos\phi)(\delta u''_z + u''_x\ \delta\phi)\Big] \\
& + G[\eta^2\ \phi'\ \delta\phi' + \xi^2\ \phi'\ \delta\phi']\Big\} d\eta\ d\xi\ dy
\end{aligned}
\right.
$$

Rearrangement of (3-6) by grouping of terms having the same virtual displacements leads to

$$\delta U = \int_0^{\ell} \{V_y(\delta u'_y + u'_x\ \delta u_x + u'_z\ \delta u'_z) + S_y\ \delta\phi'$$

(3-7)
$$+ [-M_z \cos\phi + M_x \sin\phi](\delta u''_x - u''_z\ \delta\phi)$$

$$+ [M_z \sin\phi + M_x \cos\phi](\delta u''_z + u''_x\ \delta\phi)\}dy$$

The stress resultants and moments formed in (3-7), which act on the deformed wing as illustrated in Fig. 3.2, are defined as follows

(3-8)
$$V_y \equiv \iint_{\text{area}} \sigma_{yy}\ d\xi\ d\eta$$

$$= EA_w\{u'_y + \frac{u'^2_x}{2} + \frac{u'^2_z}{2} - e_A(u''_x \cos\phi - u''_z \sin\phi)\}$$

where $A_w e_A \equiv \iint_{\text{area}} \xi\ d\xi\ d\eta$

and $\iint_{\text{area}} \eta\ d\xi\ d\eta = 0$, by definition

(3-9)
$$M_z \equiv \iint_{\text{area}} \xi\ \sigma_{yy}\ d\xi\ d\eta$$

$$= EI_z(-u''_x \cos\ + u''_z \sin\ ) + EA_w e_A(u'_y + \frac{u'^2_x}{2} + \frac{u'^2_z}{2})$$

where $I_z \equiv \iint_{\text{area}} \xi^2\ d\xi\ d\eta$

and $\iint_{\text{area}} \xi\ \eta\ d\xi\ d\eta = 0$

$$M_x \equiv - \iint_{\text{area}} \eta\ \sigma_{yy}\ d\xi\ d\eta$$

(3-10)
$$= EI_x(u''_x \sin\phi + u''_z \cos\phi)$$

where $I_x \equiv \iint_{\text{area}} \eta^2\ d\xi\ d\eta$

$$
\begin{aligned}
Sy &\equiv \iint_{\text{area}} (-\xi\,\sigma_{y\eta} + \eta\,\sigma_{x\xi})\,d\xi\,d\eta \\
&= GI_d\,\phi'
\end{aligned}
\qquad (3\text{-}11)
$$

where $I_d \equiv \iint_{\text{area}} (\xi^2 + \eta^2)\,d\xi\,d\eta$

At this point in the development the moments of inertia I_x, I_z are first introduced. Hereafter, it must be recognized that I_z may assume values much larger than I_x. The terms containing the quantity e_A, which measures the offset of the tensile axis (area centroid) from the elastic axis, will be dropped. The basis for this simplification is that, in the final modal formulation of the equations, the retention of e_A terms ultimately leads to a dimensionless parameter, $\frac{EA_w e_A^2}{EI_x}$, which appears only as a small quantity added or subtracted with unity. Since it will not significantly influence dynamic stability, hereafter $e_A = 0$ will be assumed.

After appropriate integrations by parts within equation (3-7), the final form for the first variation of strain energy, including boundary terms, is

$$
\begin{aligned}
\delta U = \int_0^{\ell} \{ &[-(V_y u_x')' + (-M_z\cos\phi + M_x\sin\phi)'']\delta u_x \\
&- (V_y)'\delta u_y + [-(V_y u_z')' + (M_z\sin\phi + M_x\cos\phi)'']\delta u_z \\
&+ [-(S_y)' - u_z''(-M_z\cos\phi + M_x\sin\phi) + u_x''(M_z\sin\phi + M_x\cos\phi)]\delta\phi\}dy \\
&+ V_y\,\delta u_y\Big|_0^{\ell} + u_x'\,V_y\,\delta u_x\Big|_0^{\ell} + u_z'\,V_y\,\delta u_z\Big|_0^{\ell} + S_y\,\delta\phi\Big|_0^{\ell} \\
&+ [-M_z\cos\phi + M_x\sin\phi]\delta u_x'\Big|_0^{\ell} - [-M_z\cos\phi + M_x\sin\phi]'\delta u_x\Big|_0^{\ell} \\
&+ [M_z\sin\phi + M_x\cos\phi]\delta u_z'\Big|_0^{\ell} - [M_z\sin\phi + M_x\cos\phi]'\delta u_z\Big|_0^{\ell}
\end{aligned}
\qquad (3\text{-}12)
$$

Formulation of the first variation of the kinetic energy is greatly simplified relative to the Ref. 7 derivation because there are no inertial effects introduced by rotation of the helicopter blade. Since the procedure is straightforward and well described in Ref. 7, the details of forming the kinetic energy in terms of displacement velocities, taking the first variation, integrating by parts over time, and expressing the resulting form of δT in terms of time derivatives of u_x, u_y, u_z, and ϕ are omitted here. After the ordering scheme has been applied, the form of the first variation of kinetic energy, with terms retained to second order and corresponding to equation (52) of Ref. 7, is

$$\begin{aligned} \delta T \cong \int_0^{\ell} \iint_{\text{area}} \rho_s \{ & - [\ddot{u}_x + \ddot{\phi}(-\xi\sin\phi + \eta\cos\phi)]\delta u_x \\ & - [\ddot{u}_z - \ddot{\phi}(\xi\cos\phi + \eta\sin\phi)]\delta u_z \\ & - [\ddot{u}_x(-\xi\sin\phi + \zeta\cos\phi) - \ddot{u}_z(\xi\cos\phi + \eta\sin\phi)]\delta\phi \\ & - \ddot{\phi}[(-\xi\sin\phi + \eta\cos\phi)^2 + (\xi\cos\phi + \eta\sin\phi)^2]\delta\phi\} d\eta \, d\xi \, dy \end{aligned} \tag{3-13}$$

As noted in Ref. 7, the last term in this expression is by definition a third order term, but it is retained in order to include torsional inertia in the torsion equation.

The final form of the first variation of kinetic energy is obtained by integration over the sectional area, which leads to the following definitions:

$$(3\text{-}14)\quad \left\{ \begin{aligned} m &\equiv \iint_{\text{area}} \rho_s \, d\xi \, d\eta \\ s_e &\equiv \iint_{\text{area}} \rho_s \, \xi \, d\xi \, d\eta \\ J &\equiv \iint_{\text{area}} \rho_s (\xi^2 + \eta^2) d\xi \, d\eta \end{aligned} \right.$$

$$\text{with} \quad \iint_{\text{area}} \rho_s \, \eta \, d\xi \, d\eta = 0$$

The final form is

$$(3\text{-}15)\quad \begin{aligned} \delta T \approx \int_0^{\ell} \{ &(-mu_x + s_e \phi \sin\phi) \delta u_x + (-m\ddot{u}_z + s_e \ddot{\phi} \cos\phi) \delta u_z \\ &+ [s_e \, \ddot{u}_x \, \sin\phi + s_e \, \ddot{u}_z \, \cos\phi - J\ddot{\phi}] \delta\phi \} dy \end{aligned}$$

The virtual work of the applied loads is

$$(3\text{-}16)\qquad \delta \mathcal{W} = \int_0^{\ell} (F_x \, \delta u_x + F_z \, \delta u_z + m_y \, \delta\phi) dy$$

Clearly the drag loads will now enter the equations of motion in the same manner as the lifting airloads, in contrast with (2-1), since F_x and F_z will consist of lift and drag force components.

Application of Hamilton's principle using (3-12), (3-15), and (3-16), together with (3-8), (3-9), (3-10), and (3-11), results in the following quantities being required to vanish:

<u>δu_y terms</u>

$$(3\text{-}17a)\qquad - [EA_w (u_y' + \frac{u_x'^2}{2} + \frac{u_x'^2}{2})]' \equiv T' = 0$$

$\underline{\delta u_x \text{ terms}}$

$$\begin{aligned}
&\{-EI_z(-u''_x\cos\phi + u''_z\sin\phi)\cos\phi \\
&+ EI_x(u''_x\sin\phi + u''_z\cos\phi)\sin\phi\}'' + m\ddot{u}_x \\
&- s_e\phi \sin\phi = 0
\end{aligned} \tag{3-17b}$$

$\underline{\delta u_z \text{ terms}}$

$$\begin{aligned}
&\{EI_z(-u''_x \cos\phi + u''_z \sin\phi)\sin\phi \\
&+ EI_x(u''_x \sin\phi + u''_z \cos\phi)\cos\phi\}'' + m\ddot{u}_z \\
&- s_e\ddot{\phi} \cos\phi - F_z = 0
\end{aligned} \tag{3-17c}$$

$\underline{\delta\phi \text{ terms}}$

$$\begin{aligned}
&-(GI_d\ \phi')' - u''_z[-EI_z(-u''_x \cos\phi + u''_z \sin\phi)\cos\phi \\
&+ EI_x(u''_x \sin\phi + u''_z \operatorname{coz}\phi)\sin\phi] \\
&+ u''_x[EI_z(-u''_x \cos\phi + u''_z \sin\phi)\sin\phi + EI_x(u''_x \sin\phi + u''_z \cos\phi)\cos\phi] \\
&- s_e\ \ddot{u}_x \sin\phi - s_e\ \ddot{u}_z \cos\phi + J\phi - M_y = 0
\end{aligned} \tag{3-17d}$$

In (3-17a), since it is known that for the nonrotating contilever wing the spanwise tension T will be zero everywhere, the expression can be integrated leaving

$$u'_y + \frac{u'^2_x}{2} + \frac{u'^2_z}{2} = 0 \tag{3-18}$$

(true only with $e_A = 0$) . This constraint indicates that the only manner by which axial deflections u_y enter the problem is by the purely geometric dependence on u_x and u_z due to shortening induced by the lateral deflections.

In replacing $\sin\phi$ and $\cos\phi$ by small angle approximations, it would be consistent with the ordering scheme to approximate the cosine by unity. Due to the possibility of a large ratio of bending stiffnesses, which can result in u_z being large compared with u_x , it was found necessary to keep the second-order approximation of the cosine at this step. This is done to derive properly certain elastic coupling terms involving u_z and u_x , while maintaining symmetry in the inertial and stiffness matrices of the final matrix equations.

Substitution of

$$\begin{aligned} \cos\phi &\approx 1 - \frac{\phi^2}{2} \\ \sin\phi &\approx \phi \end{aligned} \tag{3-19}$$

into (3-17) leads to

$$\begin{aligned} &[- EI_z(- u_x''(1-\phi^2) + u_z''\phi) + EI_x(u_x''\phi^2 + u''\phi)]'' \\ &\qquad + m\ddot{u}_x - s_e\ddot{\phi}\phi = F_x \end{aligned} \tag{3-20a}$$

$$\begin{aligned} &[EI_z(- u_x'' + u_z''\phi)\phi + EI_x(u_x''\phi + u_z''(1-\phi^2))]'' \\ &\qquad + m\ddot{u}_z' - s_e\ddot{\phi} = F_z \end{aligned} \tag{3-20b}$$

$$
\begin{aligned}
&- (GI_d\phi')' - u_z''[- EI_z(-u_x''(1-\phi^2) + u_z''\phi) + EI_x(u_x''\phi^2 + u_z''\phi)] \\
\text{(3-20c)}\qquad &+ u_x''[EI_z(-u_x''\phi + u_z''\phi^2) + EI_x(u_x''\phi + u_z''(1-\phi^2))] \\
&- s_e u_x \phi - s_e \ddot{u}_z + J\ddot{\phi} = m_y
\end{aligned}
$$

Reorganization of terms and introduction of the displacements w and v for u_z and u_x, respectively, gives

$$
\begin{aligned}
&\{[EI_z\phi^2 + EI_x(1-\phi^2)]w'' - (EI_z - EI_x)v''\phi\}'' \\
\text{(3-21a)}\qquad &\qquad + m\,\ddot{w} - s_e\ddot{\phi} = F_z
\end{aligned}
$$

$$
\begin{aligned}
&\{- (EI_z - EI_x)w''\phi + [EI_z(1-\phi^2) + \phi^2 EI_x]v''\}'' \\
\text{(3-21b)}\qquad &\qquad\qquad + m\,\ddot{v} - \underline{s_e\ddot{\phi}}\phi = F_x
\end{aligned}
$$

$$
\begin{aligned}
&GI_d\phi'' - (EI_z - EI_x)[(w''^2 - v''^2)\phi - v''w''(1-\underline{2\phi^2})] \\
\text{(3-21c)}\qquad &\quad + \underline{s_e\ddot{v}\phi} + s_e\ddot{w} - J\ddot{\phi} + m_y = 0
\end{aligned}
$$

The underlined terms are reasoned to represent higher-order effects and are dropped. In the case of the inertial terms coupling chordwise bending and torsion through the offset s_e, this is a third-order effect relative to terms like $m\ddot{v}$. The final form of the three-DOF system of equations, with some regrouping, is

$$
\begin{aligned}
&\{EI_x w'' - (EI_z - EI_x)(v''\phi - \underline{w''\phi^2})\}'' \\
\text{(3-22a)}\qquad &\qquad + m\ddot{w} - s_e\ddot{\phi} = F_z
\end{aligned}
$$

$$(3\text{-}22b) \qquad \{EI_z v'' - (EI_z - EI_x)(w''\phi + \underline{\underline{v''\phi^2}})\}'' + m\ddot{v} = F_x$$

$$(3\text{-}22c) \qquad GI_d\phi'' - (EI_z - EI_x)[(\underline{w''^2} - \underline{\underline{v''^2}})\phi - v''w'']$$

$$+ s_e\ddot{w} = J\ddot{\phi} + m_y = 0$$

This system is elastically and inertially self adjoint, which assures that the stiffness and inertia matrices eventually assembled during modal analysis will be symmetric. The terms containing $(EI_z - EI_x)$ represent the nonlinear coupling between the torsion and bending degrees of freedom; all remaining stiffness, inertial, and applied-load terms represent the same familiar forms encountered in linear beam theory. Terms in (3-22) which are underlined do not appear in the Ref. 7 equations and are retained here as a result of the absence of a restriction on the bending stiffness ratio EI_z/EI_x. Strictly speaking, when this ratio is large compared with unity, the single underlined terms will increase in relative importance while the double underlined terms are negligible in magnitude.

The nonlinear equations of motion (3-22) are next adapted to permit analysis of stability about a steady-state deflected position due to an equilibrium lifting flight condition, which could be level flight or a steady pullout at a high load factor. Small time-dependent perturbations about the equilibrium operating condition are introduced by expressing the deflections w, v, and ϕ in terms of steady-state equilibrium deflections w_o, v_o, and ϕ_o and small unsteady perturbation quantities w_1, v_1, and ϕ_1:

$$(3\text{-}23)\qquad \begin{cases} w(t) = w_o + w_1(t) \\ v(t) = v_o + v_1(t) \\ \phi(t) = \phi_o + \phi_1(t) \end{cases}$$

First, the steady equilibrium deflections only are substituted into (3-22) to obtain a nonlinear system of equations for the equilibrium solution. The resulting nonlinear steady system is

$$(3\text{-}24a)\qquad \{EI_x w''_o - (EI_z - EI_x)(v''_o\phi_o - w''_o\phi_o^2)\}'' = F_{z_o}$$

$$(3\text{-}24b)\qquad \{EI_z v''_o - (EI_z - EI_x)(w''_o\phi_o + v''_o\phi_o^2)\}'' = F_{x_o}$$

$$(3\text{-}24c)\qquad GI_d\phi''_o - (EI_z - EI_x)[(w''^2_o - v''^2_o)\phi_o - v''_o w''_o] + m_{y_o} = 0$$

Appropriate steady lifting aerodynamic loads are inserted for L_{w_o} and M_{ϕ_o}, and the assumed steady drag, which entered equations (2-1) in an entirely different manner, is introduced through L_{v_o}.

Next a linearized system of equations in the time dependent small perturbation deflections is obtained by substituting (3-23) into (3-22), subtracting the nonlinear equilibrium equations, and discarding products of the perturbation quantities. The linearized unsteady equations of motion are

$$(3\text{-}25a)\qquad \{EI_x w''_1 - (EI_z - EI_x)[\phi_o v''_1 + \phi_1 v''_o - \phi_o^2 w''_1 - 2\phi_o w''_o\phi_1]\}''$$
$$+ m\ddot{w}_1 - s_e\ddot{\phi}_1 - F_{z_1} = 0$$

$$\{EI_z v_1'' - (EI_z - EI_x)[\phi_o w_1'' + w_o''\phi + \phi_o^2 v_1 + 2\phi_o v_o''\phi_1]\}'' \tag{3-25b}$$

$$+ m\ddot{v}_1 - F_{x_1} = 0$$

$$GI_d\phi_1'' - (EI_z - EI_x)\{[2w_o''w_1'' - 2v_o''v_1'']\phi_o + [w_o''^2 - v_o''^2]\phi_1 \tag{3-25c}$$

$$- w_o''v_1'' - v_o''w_1''\} + s_e\ddot{w}_1 - J\ddot{\phi}_1 + m_{y_1} = 0$$

Analysis of stability with this system can be done with the standard techniques for linear systems, but first the coefficients must be found for a given equilibrium flight condition by solving (3-24). The loads appearing in this equation, including the chordwise forces, must be expressed as linear functions of perturbation displacements w_1 and ϕ_1. No dependence of aerodynamic loads on the fore-and-aft motion v_1 will be considered in this analysis.

C. Comparison of the VT and VCT Models

The VCT model (3-24) and (3-25), although different in appearance from the VT model (2-1), in fact reduces to the same form when $\tau \to \infty$ and the steady lift is zero. To illustrate this, first imagine that the steady loads applied to (3-24) are

$$\left\{ \begin{array}{l} F_{z_o} = 0 \\ m_{y_o} = 0 \\ F_{x_0} = D \end{array} \right. \tag{3-26}$$

where D is the same assumed drag force, constant in magnitude and direction along the span, as is considered in (2-2). The solution to (3-24) immediately gives $w_o = \phi_o = 0$, leaving just the chordwise bending equation as

$$EI_z v_o'''' = D \tag{3-27}$$

Substitution of τEI_x for EI_z in (3-25) together with $w_o = \phi_o = 0$ gives

$$EI_x w_1'''' - (\tau-1)EI_x(\phi_1 v_o'')'' + m\ddot{w}_1 - s_e\ddot{\phi}_1 - F_{z_1} = 0 \tag{3-28a}$$

$$\tau EI_x v_1'''' + m\ddot{v}_1 - F_{x_1} = 0 \tag{3-28b}$$

$$GI_d\phi_1'' - (\tau-1)EI_x[-v_o''^2\phi_1 - v_o''w_1''] + s_e\ddot{w}_1 - J\ddot{\phi}_1 + m_{y_1} = 0 \tag{3-28c}$$

The equation for v_1 uncouples and can be disregarded. Integration of (3-27) twice, using the zero shear and moment boundary conditions at the free end, gives

$$\begin{aligned} \tau EI_x v_o'' &= D\,\tfrac{1}{2}(\ell-y)^2 \\ &= -M_z \end{aligned} \tag{3-29}$$

where (2-2) has been used. Substitution of (3-29) into equations (3-28a, c) yields

$$EI_x w_1'''' + \frac{\tau-1}{\tau}(M_z\phi_1)'' + m\ddot{w}_1 - s_e\ddot{\phi}_1 - F_{z_1} = 0 \tag{3-30a}$$

$$(3\text{-}30b) \qquad GI_d\phi_1'' - \frac{\tau-1}{\tau} M_z(w_1'' + v_o''\phi_1) + s_e\ddot{w}_1 - J\ddot{\phi}_1 + m_{y_1} + 0$$

Finally, requiring that $\tau \to \infty$, with the consequent vanishing of v_o, causes (3-30) to reduce exactly to (2-1).

For the more general case of a steady lifting condition characterized by $w_o \neq 0$ and $\phi_o \neq 0$, (3-24) and (3-25) can still be cast into a form similar to (2-1), in which the v_1 displacements become dependent upon w_1 and ϕ_1 since $\tau \to \infty$. First, the nonlinear steady equations (3-24) are rewritten with τEI_x replacing EI_z together with some rearrangement of terms to give

$$(3\text{-}31a) \qquad EI_x w_o'''' - \tau EI_x \frac{\tau-1}{\tau} [v_o'' - w_o''\phi_o)\phi_o]'' = F_{z_o}$$

$$(3\text{-}31b) \qquad \tau EI_x[v_o'' - \frac{\tau-1}{\tau} (w_o''\phi_o + v_o''\phi_o^2)]'' = F_{x_o}$$

$$(3\text{-}31c) \qquad GI_d\phi_o'' - \frac{\tau-1}{\tau} \tau EI_x[(w_o''\phi_o - v_o'')w_o'' - v_o''^2\phi_o] + m_{y_o} = 0$$

Again, as $\tau \to \infty$ the elastic bending curvature about the η principal axis (Fig. 3.1) of the airfoil section should go to zero. But now, the section is displaced to a position fixed by the deflections w_o, v_o, and ϕ_o of its elastic axis, and the true elastic curvature about the η axis is now recognized as $v_o'' - w_o''\phi_o$.

In equation (3-31b), which is the fore-and-aft equilibrium equation, as τ becomes large and v_o becomes small, the term $v_o''\phi_o^2$ is of higher order and can be neglected relative to v_o''. Removing this term and letting $\frac{\tau-1}{\tau} \to 1$ leaves

$$\tau EI_x[v''_o - w''_o\phi_o]'' = F_{x_o} \tag{3-32}$$

Integrating this equation twice, using the shear and moment boundary conditions on v_o and w_o at the free end, leads to

$$\tau EI_x[v''_o - w''_o\phi_o] = F_{x_o}\,\tfrac{1}{2}(\ell - y)^2 \equiv -M_{z_o} \tag{3-33}$$

Here it is assumed for convenience that F_{x_o} is constant along the span; of course the integrations could as well be performed for any known spanwise variation of F_{x_o}. M_{z_o} is similar to M_z of (3-29), except that it represents the bending-torsion coupling effect upon the moment-curvature relation. As $\tau \to \infty$ the quantity $(v''_o - w''_o\phi_o)$ must go to zero according to (3-33). In the limit the v_o deflection becomes dependent upon w_o and ϕ_o as a result of bending-torsion coupling.

The two remaining independent equations in (3-31) are already arranged so that the coupled curvature quantity in (3-33) can be recognized. Substitution for this quantity leads to

$$\begin{aligned} &EIw''''_o + \frac{\tau-1}{\tau}\,[M_{z_o}\phi_o]'' = F_{z_o} \\ &GI_d\phi''_o - \frac{\tau-1}{\tau}\,[M_{z_o}w''_o - v''^2_o\phi_o] + m_{y_o} = 0 \end{aligned} \tag{3-34}$$

As $\tau \to \infty$, with $v''_o\phi_o$ recognized as a higher-order term, the nonlinear steady equilibrium equations finally become

$$EIw''''_o + [M_{z_o}\phi_o]'' - F_{z_o} = 0 \tag{3-35a}$$

$$GI_d\phi_o'' - M_{z_o}w_o'' + m_{y_o} = 0 \qquad (3\text{-}35b)$$

These resemble (2-1) with dynamic terms removed.

A final exercise is to demonstrate that the linearized unsteady perturbation equations (3-25) also reduce in a systematic fashion to a VT system when $\tau \to \infty$. When (3-25) are rearranged with τEI_x replacing EI_z and the combination of steady deflections in (3-33) replaced by M_{z_o}, the linearized system becomes

$$EI_x w_1'''' + [M_{z_o}\phi_1]'' - \tau EI_x \frac{\tau-1}{\tau}[v_1'' - \phi_o w_1'' - w_o''\phi_1)\phi_o]'' \qquad (3\text{-}36a)$$

$$+ m\ddot{w}_1 - s_e\ddot{\phi}_1 - F_{z_1} = 0$$

$$\tau EI_x[v_1'' - \frac{\tau-1}{\tau}(\phi_o w_1'' + w_o''\phi_1 + \underline{\phi_o^2 v_1''} + \underline{2\phi_o v_o''\phi_1})]'' \qquad (3\text{-}36b)$$

$$+ m\ddot{v}_1 - F_{x_1} = 0$$

$$GI_d\phi_1'' + \tau EI_x \frac{\tau-1}{\tau}[(v_1'' - \phi_1 w_1'' - w_o''\phi_1)w_o'' + \underline{2v_o''\phi_o v_1''} + \underline{v_o''^2\phi_1}] \qquad (3\text{-}36c)$$

$$- M_{z_o}w_1'' + s_e\ddot{w}_1 - J\ddot{\phi}_1 + m_{y_1} = 0$$

The underlined terms are of higher order for $\tau > 1$ and are discarded. When τ is sufficiently large that $\frac{\tau-1}{\tau} \simeq 1$, equation (3-36b) becomes

$$\tau EI_x[v_1'' - \phi_o w_1'' - w_o''\phi_1]'' = F_{x_1} - m\ddot{v}_1 \qquad (3\text{-}37)$$

The quantity β , defined as

(3-38) $$\beta = v''_1 - \phi_o w''_1 - w''_o \phi_1 ,$$

is recognized as the time-dependent curvature, in the linearized perturbation deflections, about the η axis of the steady-state deformed cross section. Thus it is expected that as $\tau \to \infty$ the curvature β must approach zero.

The dynamic linear moment M_{z_1} is defined as

(3-39) $$M_{z_1} \equiv - \tau E I_x \beta$$

Equations (3-37) and (3-36a, c) can be restated, after use of (3-38) and (3-39) together with $\tau \to \infty$, as

(3-40a) $$EI_x w''''_1 + [M_{z_o} \phi_1]'' + [M_{z_1} \phi_o]'' + m\ddot{w}_1 - s_e \ddot{\phi}_1 - F_{z_1} = 0$$

(3-40b) $$M''_{z_1} = F_{x_1} - m\ddot{v}_1$$

(3-40c) $$GI_d \phi''_1 - M_{z_o} w''_1 - M_{z_1} w''_o + s_e \ddot{w}_1 - J\ddot{\phi}_1 + m_{y_1} = 0$$

Since $\beta \to 0$, the acceleration term in the second equation could be expressed entirely in terms of w and ϕ accelerations by working from integration of

(3-41) $$\ddot{v}''_1 = \phi_o \ddot{w}''_1 - w''_o \ddot{\phi}_1$$

In this linearized unsteady system, $M_{z_1}(y,t)$ represents the moment at station y due to the instantaneous chordwise inertial loads and applied linearized unsteady drag forces acting outboard of the station. Because of the dependence of M_{z_1} upon w_1 and ϕ_1 , equation (3-40b) cannot be uncoupled to allow for a separate calculation of M''_{z_1} . Thus, even though v_1 can be eliminated, (3-40) still involves three unknowns w_1 , ϕ_1 , and M_{z_1} .

The purpose of this section has been to demonstrate analytically the connection between VCT representation of the cantilever wing, given by (3-24) and (3-25), and the VT system given in (2-1) and used in Ref. 1. It can be concluded that the VCT model remains valid for arbitrarily large bending stiffness ratio τ , and that the drag coupling effect has been satisfactorally accounted for by the nonlinear elastic bending-torsion coupling terms. Since the forms obtained in (3-35) and (3-40) are but special cases of (3-24) and (3-25), actual solutions will be found, using the latter system only, for practical values of τ .

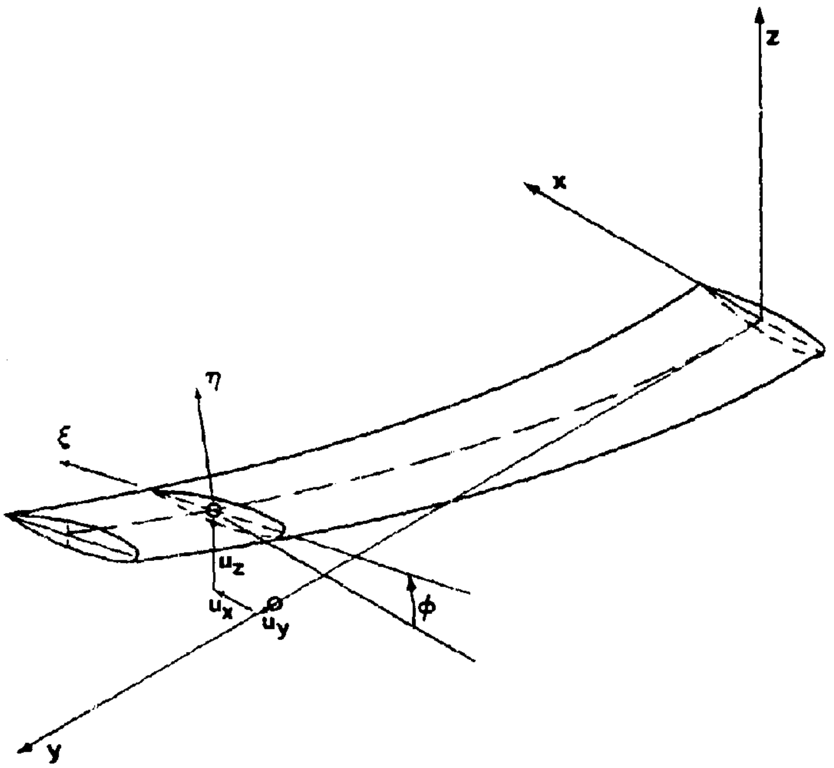

FIGURE 3-1 Coordinate System and Displacements

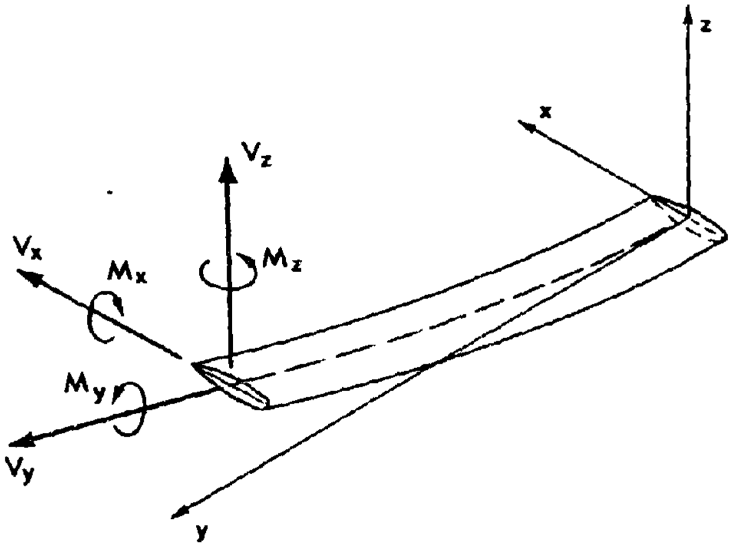

FIGURE 3-2 Stress Resultants and Moments

Chapter IV

FLUTTER VELOCITY CONSIDERING VERTICAL BENDING/CHORDWISE BENDING/TORSION (VCT)

A. Modal Equations for Small Oscillatory Motions About a Steady-State Deformation

The model for torsion, transverse bending, and chordwise bending of the uniform cantilever wing developed in the previous chapter is used to determine flutter velocity with of the same set of assumed modes used in (2-1). Use of n assumed modes in torsion, n in transverse bending, and n in chordwise bending results in a set of $3n$ modal equations in terms of modal generalized displacements. Since the assumed modes satisfy the natural as well as geometrical boundary conditions, which were obtained during the application of Hamilton's principle, Galerkin's method can be employed to transform the equations into algebraic relations in the generalized displacements. The nonlinear steady-state equilibrium equations (3-24) become nonlinear algebraic equations in the steady-state generalized displacements, which are solved iteratively. These displacements determine the coefficients of the linearized unsteady model by applying Galerkin's method to (3-25). Then the velocity is determined for which simple harmonic motion of this system is possible (neutral dynamic stability).

The steady aerodynamic loads for the equilibrium equations (3-24) are specified in terms of incompressible strip theory. A typical airfoil section (Fig. 4-1) has its zero-lift line inclined to the free-stream velocity V by the angle $\alpha + \phi_o(y)$. The resultant steady lift L_{a_o} (acting in a direction perpendicular to V) and the moment m_o are given by

$$(4\text{-}1)\quad \begin{cases} L_{a_o} = 2\Pi\rho V^2 b(\alpha + \phi_o) \\ m_{a_o} = 2\Pi\rho V^2 b^2 (\tfrac{1}{2}+a)(\alpha + \phi_o) \end{cases}$$

A drag force D is also present. These forces must be resolved into the axis system x , y, z fixed with respect to the wing root. The required transformation is

$$(4\text{-}2)\quad \begin{cases} F_{z_o} = L_{a_o}\cos\alpha + D\sin\alpha \\ F_{x_o} = D\cos\alpha - L_{a_o}\sin\alpha \end{cases}$$

Assuming $\sin\alpha \simeq \alpha$ and $\cos\alpha \simeq 1$ and neglecting the z component of drag shows that the steady aerodynamic forces to be used with (3-23) are

$$(4\text{-}3)\quad \begin{cases} F_{z_o} = 2\Pi\rho V^2 b(\alpha + \phi_o) \\ F_{x_o} = 2\Pi\rho V^2 b(C - \alpha^2 - \alpha\phi_o) \\ m_{y_o} = 2\Pi\rho V^2 b^2 A(\alpha + \phi_o) \end{cases}$$

The drag force represented by C is constant spanwise, and the definitions in (2-22) have been adapted.

The steady-state deflections are now expressed in terms of the assumed modes (cf. Appendix A for definitions)

$$
(4\text{-}4)\quad \left\{ \begin{aligned} w_o &= \sum_{i=1}^{n} f_{w_i}\, q^\circ_{w_i} \\ v_o &= \sum_{i=1}^{n} f_{v_i}\, q^\circ_{v_i} \\ \phi_o &= \sum_{i=1}^{n} f_{\phi_i}\, q^\circ_{\phi_i} \end{aligned} \right.
$$

Bending mode shape functions f_{w_i} and f_{v_i} are identical. Substituting (4-4) into (3-24) and (4-3) and applying Galerkin's procedure leads to

$$
(4\text{-}5a)\quad \left\{ \begin{aligned} & EI_x \int_0^\ell \Big(\sum_{i=1}^{n} f''''_{w_i} q^\circ_{w_i}\Big) f_{w_j}\, dy - (EI_z - EI_x)\Big\{\int_0^\ell \Big[\Big(\sum_{\mu=1}^{n} f''_{v_\mu} q^\circ_{v_\mu}\Big)\Big(\sum_{\nu=1}^{n} f_{\phi_\nu} q^\circ_{\phi_\nu}\Big)\Big]'' f_{w_j}\, dy \\ & - \int_0^\ell \Big[\Big(\sum_{i=1}^{n} f''_{w_i} q^\circ_{w_i}\Big)\Big(\sum_{\nu=1}^{n} f_{\phi_\nu} q^\circ_{\phi_\nu}\Big)\Big(\sum_{\mu=1}^{n} f_{\phi_\mu} q^\circ_{\phi_\mu}\Big)\Big]'' f_{w_j}\, dy\Big\} \\ & \quad = 2\Pi\rho V^2 b\Big\{\alpha \int_0^\ell f_{w_j}\, dy + \int_0^\ell \Big(\sum_{i=1}^{n} f_{\phi_i}\, q^\circ_{\phi_i}\Big) f_{w_j}\, dy\Big] \end{aligned} \right.
$$

$$
(4\text{-}5b)\quad \left\{ \begin{aligned} & EI_z \int_0^\ell \Big(\sum_{i=1}^{n} f''''_{v_i} q^\circ_{v_i}\Big) f_{v_j}\, dy - (EI_z - EI_x)\Big\{\int_0^\ell \Big[\Big(\sum_{i=1}^{n} f_{w_i} q^\circ_{w_i}\Big)\Big(\sum_{\nu=1}^{n} f_{\phi_\nu} q^\circ_{\phi_\nu}\Big)\Big]'' f_{v_j}\, dy \\ & + \int_0^\ell \Big[\Big(\sum_{i=1}^{n} f''_{v_i} q^\circ_{v_i}\Big)\Big(\sum_{\nu=1}^{n} f_{\phi_\nu} q^\circ_{\phi_\nu}\Big)\Big(\sum_{\mu=1}^{n} f_{\phi_\mu} q^\circ_{\phi_\mu}\Big)\Big]'' f_{v_j}\, dy\Big\} \\ & \quad = 2\Pi\rho V^2 b\Big[(C - \alpha^2)\int_0^\ell f_{v_j}\, dy - \alpha \int_0^\ell \Big(\sum_{i=1}^{n} f_{\phi_i} q^\circ_{\phi_i}\Big) f_{v_j}\, dy\Big] \end{aligned} \right.
$$

$(1 \le j \le n)$

$$
(4\text{-}5c)\quad \left\{ \begin{aligned} & GI_d \int_0^\ell \Big(\sum_{i=1}^{n} f''_{\phi_i}\, q^\circ_{\phi_i}\Big) f_{\phi_j}\, dy \\ & - (EI_z - EI_x)\Big\{\int_0^\ell \Big(\sum_{i=1}^{n} f''_{w_i} q^\circ_{w_i}\Big)\Big(\sum_{\nu=1}^{n} f''_{w_\nu} q^\circ_{w_\nu}\Big)\Big(\sum_{\mu=1}^{n} f_{\phi_\mu} q^\circ_{\phi_\mu}\Big) f_{\phi_j}\, dy \\ & - \int_0^\ell \Big(\sum_{i=1}^{n} f''_{v_i} q^\circ_{v_i}\Big)\Big(\sum_{\nu=1}^{n} f''_{v_\nu} q^\circ_{v_\nu}\Big)\Big(\sum_{\mu=1}^{n} f_{\phi_\mu} q^\circ_{\phi_\mu}\Big) f_{\phi_j}\, dy \\ & - \int_0^\ell \Big(\sum_{i=1}^{n} f''_{v_i} q^\circ_{v_i}\Big)\Big(\sum_{\nu=1}^{n} f''_{w_\nu} q^\circ_{w_\nu}\Big) f_{\phi_j}\, dy \\ & \quad = -\, 2\Pi\rho V^2 b^2 A\Big[\alpha \int_0^\ell f_{\phi_j}\, dy + \int_0^\ell \Big(\sum_{i=1}^{n} f_{\phi_i} q^\circ_{\phi_i}\Big) f_{\phi_j}\, dy\Big] \end{aligned} \right.
$$

The indicated differentiations in the first two equations are carried out, and appropriate integrations by parts of the resulting modal integrals is performed. The first terms of each equation are then expressed in terms of modal natural frequencies as in (2-10) and (2-11) which leads to the form

$$(4\text{-}6a)\quad \left\{ \begin{aligned} & m\omega_{w_j}^2 \ell q_{w_j}^\circ - \frac{EI_x}{\ell^3}(\tau-1)\sum_{\mu=1}^{n}\sum_{\nu=1}^{n} H_{\nu j\mu}\, q_{\phi_\nu}^\circ\, q_{v_\mu}^\circ \\ & \qquad + \frac{EI_x}{\ell^3}(\tau-1)\sum_{\mu=1}^{n}\sum_{\nu=1}^{n}\sum_{i=1}^{n} R_{ij\nu\mu}\, q_{\phi_\nu}^\circ q_{\phi_\mu}^\circ\, q_{w_i}^\circ \\ & \qquad - 2\Pi\rho V^2 b\ell \sum_{\nu=1}^{n} I_{j\nu}\, q_{\phi_\nu}^\circ = 2\Pi\rho V^2 b\ell\left[-\frac{2B_j\alpha}{N_j\Pi}\right] \end{aligned} \right.$$

$$(4\text{-}6b)\quad \left\{ \begin{aligned} & \tau m\, \omega_{w_j}^2\, \ell\, q_{v_j}^\circ - \frac{EI_x}{\ell^3}(\tau-1)\sum_{\nu=1}^{n}\sum_{\mu=1}^{n} H_{\nu\mu j}\, q_{\phi_\nu}^\circ q_{w_\mu}^\circ \\ & - \frac{EI_x}{\ell^3}(\tau-1)\sum_{\nu=1}^{n}\sum_{\mu=1}^{n}\sum_{i=1}^{n} R_{ij\mu\nu}\, q_{\phi_\nu}^\circ\, q_{\phi_\mu}^\circ\, q_{v_i}^\circ \\ & + 2\Pi\rho V^2 b\ell\alpha \sum_{\nu=1} I_{j\nu}\, q_{\phi_\nu}^\circ = 2\Pi\rho V^2 b\ell\left[-\frac{2B_j}{N_j\Pi}(C-\alpha^2)\right] \end{aligned} \right.$$

$(1 \leq j \leq n)$

$$(4\text{-}6c)\quad \left\{ \begin{aligned} & J\, \omega_{\phi_j}^2 \frac{\ell}{2} q_{\phi_j}^\circ + \frac{EI_x}{\ell^3}(\tau-1)\sum_{\nu=1}^{n}\sum_{\mu=1}^{n}\sum_{i=1}^{n} R_{\mu\nu ji}\, q_{w_\nu}^\circ\, q_{w_\mu}^\circ\, q_{\phi_i}^\circ \\ & - \frac{EI_x}{\ell^3}(\tau-1)\sum_{\nu=1}^{n}\sum_{\mu=1}^{n}\sum_{i=1}^{n} R_{\mu\nu ji}\, q_{v_\mu}^\circ\, q_{v_\nu}^\circ\, q_{\phi_i}^\circ \\ & = 2\Pi\rho V^2 b^2 \ell A \frac{1}{\Pi(j-\frac{1}{2})}\alpha \end{aligned} \right.$$

B_j and N_j are properties of the assumed bending modes described in Appendix A, and I_{ij} represent the modal integrals previously encountered and defined in (2-13). The nonlinear bending-torsion coupling terms give rise to two new forms of modal integrals,

$$(4\text{-}7)\qquad H_{j\mu\nu} = \int_0^1 f_{\phi_j}(\tilde{y})\, f''_{w_\mu}(\tilde{y})\, f''_{w_\nu}(\tilde{y})\, d\tilde{y}$$

$$(4\text{-}8)\qquad R_{ij\mu\nu} = \int_0^1 f''_{w_i}(\tilde{y})\, f''_{w_j}(\tilde{y})\, f_{\phi_\mu}(\tilde{y})\, f_{\phi_\nu}(\tilde{y})\, d\tilde{y}$$

Equations (4-6) can be arranged in the final format used for computations by dividing the torsion equation by $\Pi\rho V^2 \ell b^2$ and the two bending equations by $\Pi\rho V^2 \ell b$, using modal natural frequency relations in (2-14) and (2-15), and nondimensionalizing with the parameters given in (2-16) and (2-26).

$$(4\text{-}9a)\quad \left\{ \begin{aligned} &\Pi^4 N_j^4 \frac{MPi_\alpha}{U^2} \frac{q^\circ_{w_j}}{b} - \frac{(\tau-1)MPi_\alpha}{U^2} \left[\sum_{\mu=1}^{n} \sum_{\nu=i}^{n} H_{\nu j \mu}\, q^\circ_{\phi_\nu} \frac{q^\circ_{v_\mu}}{b} \right. \\ &\left. - \sum_{\mu=1}^{n} \sum_{\nu=1}^{n} \sum_{i=1}^{n} R_{ij\mu\nu} q^\circ_{\phi_\mu}\, q^\circ_{\phi_\nu} \frac{q^\circ_{w_i}}{b} \right] - 2 \sum_{\nu=1}^{n} I_{j\nu}\, q^\circ_{\phi_\nu} = - \frac{4B_j}{\Pi N_j} \end{aligned} \right.$$

$$(4\text{-}9b)\quad \left\{ \begin{aligned} &\Pi^4 N_j^4 \frac{\tau MPi_\alpha}{U^2} \frac{q^\circ_{v_j}}{b} - (\tau-1) \frac{MPi_\alpha}{U^2} \left[\sum_{\nu=1}^{n} \sum_{\mu=1}^{n} H_{\nu\mu j} q^\circ_{v_\nu} \frac{q^\circ_{w_\mu}}{b} \right. \\ &\left. + \sum_{\nu=1}^{n} \sum_{\mu=1}^{n} \sum_{i=1}^{n} R_{ij\mu\nu}\, q^\circ_{\phi_\nu}\, q^\circ_{\phi_\mu} \frac{q^\circ_{v_i}}{b} \right] + 2\alpha \sum_{\nu=1}^{n} I_{j\nu} q^\circ_{\phi_\nu} = \frac{4B_j}{N_j \Pi} (C-\alpha^2) \end{aligned} \right.$$

$(i \leq j \leq n)$

$$(4\text{-}9c)\quad \left\{ \begin{aligned} &[\tfrac{1}{2}\Pi^2 (j-\tfrac{1}{2})^2 \frac{Mi_\alpha}{U^2} - A] q^\circ_{\phi_j} \\ &+ (\tau-1) \frac{MPi_\alpha}{U^2} \left[\sum_{\nu=1}^{n} \sum_{\mu=1}^{n} \sum_{i=1}^{n} R_{\mu\nu j i} \frac{q^\circ_{w_\nu}}{b} \frac{q^\circ_{w_\mu}}{b} q^\circ_{\phi_i} \right. \\ &\left. - \sum_{\nu=1}^{n} \sum_{\mu=1}^{n} \sum_{i=1}^{n} R_{\mu\nu j i} \frac{q^\circ_{v_\mu}}{b} \frac{q^\circ_{v_\nu}}{b} q^\circ_{\phi_i} - \sum_{\mu=1}^{n} \sum_{\nu=1}^{n} H_{j\nu\mu} \frac{q^\circ_{v_\nu}}{b} \frac{q^\circ_{w_\mu}}{b} \right] \\ &= 2A\, \alpha \frac{1}{\Pi(j-\tfrac{1}{2})} \end{aligned} \right.$$

A solution to (4-9) can be found for a given wing configuration once drag C, root angle of attack α, and dimensionless speed U have been specified. The solution procedure involves Newton's method and is described in Appendix C.

When simple harmonic motion is assumed, the linearized perturbation equations of motion (3-25) are converted into linear algebraic equations via the same steps described in Chapter II in deriving modal equations (2-18) from (2-1). The perturbation displacements are expanded in terms of n assumed modes and generalized displacements,

$$\begin{aligned} w_1(y,t) &= \sum_{i=1}^{n} f_{w_i}(y) q_{w_i}\, e^{i\omega t} \\ v_1(y,t) &= \sum_{i=1}^{n} f_{w_i}(y) q_{v_i}\, e^{i\omega t} \qquad (4\text{-}10) \\ \phi_1(y,t) &= \sum_{i=1}^{n} f_{\phi_i}(y) q_{\phi_i}\, e^{i\omega t} \end{aligned}$$

where q_{w_i} and q_{v_i} have dimensions of length, whereas q_{ϕ_i} are dimensionless. Anticipating solution for flutter boundaries using the V-g method, structural damping g is included by introducing a complex elastic modulus, and the simple harmonic airloads are assumed to have been expressed in terms of unit generalized forces as in (2-9). With the addition of the fore-and-aft bending degree of freedom, the generalized forces now appear as

$$(4\text{-}11a) \qquad \int_0^{\ell} F_{z_1}(\phi_1, w_1; t) f_{w_j}\, dy$$

$$(1 \le j \le n) \qquad = \pi\rho\omega^2 b^3 \ell \Big[\sum_{i=1}^{n} Q_{j,i} \frac{q_{w_i}}{b} + \sum_{i=1}^{n} Q_{j,i+2n}\, q_{\phi_i} \Big] e^{i\omega t}$$

$$(4\text{-}11b)\qquad \int_0^\ell F_{x_1}(\phi_1, w_1; t) f_{v_j}\, dy = \Pi\rho\omega^2 b^3 \ell \Big[\sum_{i=1}^{n} Q_{j+n,i} \frac{q_{w_i}}{b} + \sum_{i=1}^{n} Q_{j+n,i+2n}\, q_{\phi_i} \Big] e^{i\omega t}$$

$(1 \leq j \leq n)$

$$(4\text{-}11c)\qquad \int_0^\ell m_{y_1}(\phi_1, w_1; t) f_{\phi_j}\, dy = \Pi\rho\omega^2 b^4 \ell \Big[\sum_{i=1}^{n} Q_{j+2n,i} \frac{q_{w_i}}{b} + \sum_{i=1}^{n} Q_{j+2n,i+2n}\, q_{\phi_i} \Big] e^{i\omega t}$$

The omission of columns in the array $Q_{j,i}$ having $n+1 \leq i \leq 2n$ reflects the assumption that there is no dependence of unsteady airloads upon fore-and-aft motions v_i.

After Galerkin's method has been implemented for equations (3-25) by the same manipulations required to develop (2-17), the system of $3n$ modal equations which determine linear stability about the ~~steady~~ equilibrium deflections appear in the form

$$(4\text{-}12a)\quad \left\{ \begin{aligned} & \{M - \Pi^4 X_j^4\, MPi_\alpha Z\}\frac{q_{w_j}}{b} \\ & + \sum_{i=1}^{n} \{Q_{j,i} - (\tau-1) MPi_\alpha Z \sum_{\mu=1}^{n}\sum_{\nu=1}^{n} R_{ij\mu\nu}\, q^*_{\phi_\mu} q^*_{\phi_\nu}\} \frac{q_{w_i}}{b} \\ & + \sum_{i=1}^{n} \{(\tau-1) MPi_\alpha Z \sum_{\mu=1}^{n} H_{\mu ij}\, q^*_{\phi_\mu}\} \frac{q_{v_i}}{b} \\ & + \sum_{i=1}^{n} \{(\tau-1) MPi_\alpha Z \Big[\sum_{\mu=1}^{n} H_{i\mu j} \frac{q^*_{v_\mu}}{b} - 2 \sum_{\mu=1}^{n}\sum_{\nu=1}^{n} R_{\nu j\mu i}\, q^*_{\phi_\mu} \frac{q^*_{w_\nu}}{b}\Big] \\ & - S M I_{ji} + Q_{j,i+2n}\} q_{\phi_i} = 0 \end{aligned} \right.$$

$$
(4\text{-}12b)\quad \left\{
\begin{aligned}
&\sum_{i=1}^{n}\{Q_{j+n,i} + (\tau-1)MPi_{\alpha}\, Z \sum_{\mu=1}^{n} H_{\mu ij}\, q^{\circ}_{\phi_{\mu}}\}\frac{q_{v_i}}{b}\\
&+ \{M - \tau\Pi^4 N_j^4 MPi_{\alpha} Z\}\,\frac{q_{v_j}}{b}\\
&+ \sum_{i=1}^{n}\{(\tau-1)MPi_{\alpha}\, Z \sum_{\mu=1}^{n}\sum_{\nu=1}^{n} R_{ij\mu\nu}\, q^{\circ}_{\phi_{\mu}}\, q^{\circ}_{\phi_{\nu}}\}\frac{q_{v_i}}{b}\\
&+ \sum_{i=1}^{n}\{(\tau-1)MPi_{\alpha}\, Z[\sum_{\mu=1}^{n} H_{i\mu j}\frac{q^{\circ}_{w_{\mu}}}{b} + 2\sum_{\mu=1}^{n}\sum_{\nu=1}^{n} R_{\nu j\mu i}\, q^{\circ}_{\phi_{\mu}}\,\frac{q^{\circ}_{v_{\nu}}}{b}]\\
&+ Q_{j+n,i+2n}\}q_{\phi_i} = 0
\end{aligned}\right.
$$

$(1 \leq j \leq n)$

$$
(4\text{-}12c)\quad \left\{
\begin{aligned}
&\sum_{i=1}^{n}\{(\tau-1)MPi_{\alpha}\, Z[\sum_{\mu=1}^{n} H_{\mu ij}\,\frac{q^{\circ}_{v_{\mu}}}{b} - 2\sum_{\mu=1}^{n}\sum_{\nu=1}^{n} R_{\mu i\nu j}\, q^{\circ}_{\phi_{\nu}}\,\frac{q^{\circ}_{w_{\mu}}}{b}]\\
&- S\, M\, I_{ij} + Q_{j+2n,i}\}\,\frac{q_{w_i}}{b}\\
&+ \sum_{i=1}^{n}\{(\tau-1)MPi_{\alpha} Z[\sum_{\mu=1}^{n} H_{\mu ij}\,\frac{q^{\circ}_{w_{\mu}}}{b} + 2\sum_{\mu=1}^{n}\sum_{\nu=1}^{n} R_{\mu i\nu j} q^{\circ}_{\phi_{\nu}}\frac{q^{\circ}_{v_{\mu}}}{b}]\}\frac{q_{v_i}}{b}\\
&+ \sum_{i=1}^{n}\{(\tau-1)MPi_{\alpha} Z[\sum_{\mu=1}^{n}\sum_{\nu=1}^{n} R_{\mu\nu ij}\frac{q^{\circ}_{v_{\mu}}}{b}\,\frac{q^{\circ}_{v_{\nu}}}{b} - \sum_{\mu=1}^{n}\sum_{\nu=1}^{n} R_{\mu\nu ij}\,\frac{q^{\circ}_{w_{\mu}}}{b}\,\frac{q^{\circ}_{w_{\nu}}}{b}]\\
&+ Q_{j+2n,i+2n}\}q_{\phi_i} + \{\tfrac{1}{2}MI_{\alpha}[1 - \Pi^2(j-\tfrac{1}{2})^2 Z]\}q_{\phi_j} = 0
\end{aligned}\right.
$$

Here $H_{j\mu\nu}$ and $R_{ij\mu\nu}$ are the modal integrals defined in (4-7) and (4-8), which appear in this system multiplied by steady-state generated displacements. The cofficients of terms which couple the steady deflections into this system must first be constructed by the indicated summations before the eigenvalues can be determined.

The unit generalized forces required in (4-12) will now be expressed in terms of the two-dimensional incompressible unsteady aerodynamics adopted for (2-2) and (2-3). It will be necessary, as it was for the steady aerodynamics, to transfer the airloads from wind oriented axes to the coordinate system fixed at the wing root. For the present case, the circulatory part of the unsteady lift will be assumed perpendicular to the direction of the freestream velocity, whereas the noncirculatory portion will be assumed to act normal to the chord of the airfoil section in its steady-state deflected position. The inclusion of unsteady leading-edge suction effects will be considered in the next chapter.

To separate the circulatory and noncirculatory contributions to the lift, L_a in (2-2) and (2-3) can be rewritten in the form (cf. Eq. (4-126) of Ref. 5)

$$\text{(4-13)} \qquad La(w_1,\phi_1;t) = \Pi\rho b^3\omega^2\left[\frac{\tilde{w}_1}{b} + \frac{i\tilde{\phi}_1}{k} + a\tilde{\phi}_1\right]e^{i\omega t}$$

$$+ \Pi\rho b^3\omega^2 C(k)\left[-\frac{2i}{k}\frac{\tilde{w}_1}{b} + \frac{2\tilde{\phi}_1}{k^2} + \frac{2i}{k}(\tfrac{1}{2}-a)\tilde{\phi}_1\right]e^{i\omega t}$$

Here the first term on the right represents noncirculatory lift $L_{a_{NC}}$ and the second term the circulatory portion L_{a_C}. Referring to Fig. 4-2, these terms can be expressed as resultant forces in the xz frame by

$$\text{(4-14)} \qquad \begin{cases} F_{z_1} = L_{a_C}\cos\alpha + L_{a_{NC}}\cos\phi_o \\ \\ F_{x_1} = -L_{a_C}\sin\alpha + L_{a_{NC}}\sin\phi_o \end{cases}$$

Making the assumptions $\cos\alpha \approx 1$ and $\cos\phi_o \approx 1$ yields the identity

$$F_{z_1} \approx L_a(w_1, \phi_1; t) \tag{4-15}$$

When it is assumed that $\sin\alpha \approx \alpha$ and $\sin\phi_o \approx \phi_o$, the chordwise force components become

$$F_{x_1} = \Pi\rho b^3\omega^2\alpha\ C(k)\left[\frac{2i}{k}\frac{\tilde{w}_1}{b} - \frac{2\tilde{\phi}_1}{k^2} - \frac{2i}{k}(\tfrac{1}{2}-a)\tilde{\phi}_1\right]e^{i\omega t} + \Pi\rho b^3\omega^2\phi_o\left[\frac{\tilde{w}_1}{b} + \frac{i\tilde{\phi}_1}{k} + a\tilde{\phi}_1\right]e^{i\omega t} \tag{4-16}$$

Preparatory to steps that lie ahead, it can be seen that when the unit generalized forces are determined from (4-11) with the modal series for ϕ_o, w_1, and ϕ_1 inserted, modal integrals of the forms

$$\int_0^1 f_{w_i}(\tilde{y})f_{v_j}(\tilde{y})f_{\phi_\nu}(\tilde{y})d\tilde{y}$$

$$\int_0^1 f_{v_i}(\tilde{y})f_{\phi_j}(\tilde{y})f_{\phi_\nu}(\tilde{y})d\tilde{y}$$

will be encountered as a consequence of the noncirculatory contribution to (4-16). Since these integrals do not occur elsewhere and the effect they introduce is expected to be minor, the noncirculatory contribution to F_{x_1} is neglected altogether. This simplification has the result that the unsteady noncirculatory force illustrated in Fig. 4-2 acts in the z direction at all spanwise stations.

The remaining circulatory contribution to F_{x_1} can be expressed, using the notation in (2-3) and after some manipulation, as

$$(4\text{-}17) \qquad F_{x_1} = \Pi\rho b^3\omega^2\alpha\{(1-L_w)\frac{\tilde{w}_1}{b} + [L_\phi - \tfrac{1}{2} + \frac{i}{k} + A(1-L_w)]\tilde{\phi}_1 \, e^{i\omega t}$$

With the aerodynamic loads given in (4-17), (4-15), and (2-2), where $m_{y_1}(\phi_1,w_1;t) = m_a(w_1,\phi_1;t)$, the unit generalized forces can be developed, starting from (4-11), by means of the same steps followed in assembling (2-22). The final result is

$$\begin{array}{l} (4\text{-}18) \\ (1\le j\le n) \\ (1\le i\le n) \end{array} \left\{ \begin{array}{lcl} Q_{j,i} & = & \begin{cases} L_w & (i=j) \\ 0 & (i\neq j) \end{cases} \\ Q_{j,i+2n} & = & -(L\phi - AL_w)I_{ji} \\ Q_{j+n,i} & = & \begin{cases} (1-L_w)\alpha & (i=j) \\ 0 & (i\neq j) \end{cases} \\ Q_{j+n,i+2n} & = & [L_\phi - \tfrac{1}{2} + \frac{i}{k} + A(1-L_w)]I_{ij} \\ Q_{j+2n,i} & = & -(M_w - AL_w)I_{ij} \\ Q_{j+2n,i+2n} & = & \begin{cases} \tfrac{1}{2}[M_\phi - A(L_\phi + M_w) + A^2L_w] & (i=j) \\ 0 & (i\neq j) \end{cases} \\ Q_{\nu,i+n} & = & 0 \qquad \text{for } 1 \le \nu \le 3n \end{array} \right.$$

B. Solution Procedure for Flutter Velocity of a Lifting Wing

The 3n modal equations (4-12), with (4-18) inserted, can be expressed in matrix form

$$(4\text{-}19) \qquad ([M_s] + [Q])\{q\} - Z[k_s]\{q\} = 0$$

The mass and stiffness matrices M_s and K_s are real and symmetric and are written out in Fig. 4-3. The terms in K_s include sums of products of modal integrals and the steady equilibrium generalized displacements found as solutions of (4-9). The aerodynamic matrix Q, whose elements appear in (4-18), is complex and nonsymmetric. Equation (4-19), therefore, represents a complex eigenvalue problem for the complex frequency parameter Z. Its solution yields damping, speed, and frequency as in the case of (2-25) and (2-27).

The logic used to compute neutral stability conditions from (4-19) is diagrammed in Fig. 4-4. The primary difficulty encountered when steady deflections are introduced is that a preliminary estimate of speed U_e must be made before the eigenvalue problem can be solved. Steady deflections for U_e are used to generate coefficients in K_s, and unsteady aerodynamic loads are then computed for large enough reduced frequency that the eigenvalue corresponding to the aeroelastic mode which flutters has negative (stable) damping g. Successively smaller values of k are then substituted and aerodynamic terms recomputed. The eigenvalues are recalculated until positive damping occurs for the flutter mode. From this point a zero-locating subroutine determines the reduced frequency for which damping g is zero, whereupon one can calculate flutter speed U_F. The entire procedure is repeated with a new estimate U_e until the speeds U_e and U_F are adequately matched. The flutter speed determined for zero lift serves as a good first estimate for U_e. With care, close agreement of the two speeds can be achieved in three or four iterations.

Three assumed modes in each degree of freedom, corresponding to a system order of 9, are found to give adequate convergence for all cases. The model integrals were computed to allow $n \leq 4$, a task which required numerical integration of 100 quantities of type $R_{ij\mu\nu}$ and 40 of type $H_{i\mu\nu}$.

C. The Nonlinear Elastic Coupling Terms

The need to retain all terms in (3-22), including third degree nonlinear, in order to model adequately the nonlinear elastic bending-torsion coupling mechanism is now demonstrated by means of typical applications. Of course, neglecting higher-order nonlinear effects would have the appeal of reducing complexity. For example, removal of all third-degree nonlinear terms would result in the elimination of all terms containing quadruple modal integrals $R_{ij\nu\mu}$ from both the nonlinear steady equilibrium system and the linearized dynamic stability analysis. In order to examine the effects of such approximations, numerical experiments were conducted wherein higher degree terms in both the steady and unsteady modal equations were neglected.

First, static deflections are considered. Clearly, if the equations do not adequately represent the steady-state deflections of the wing over a realistic range of lifting conditions, then any linearized unsteady perturbation analysis based on the same level of approximation cannot be expected to succeed. The nonlinear steady equations (3-23) will be solved at three levels of approximation:

(1) Linear terms only retained.

(2) Second degree monlinear terms included.

(3) All nonlinear terms included.

The linear set of modal equations is just (4-9) with the nonlinear terms removed:

$$\Pi^4 N_j^4 \frac{MPi_\alpha}{U^2} \frac{q^\circ_{w_j}}{b} - 2 \sum_{\nu=1}^{n} I_{j\nu}\, q^\circ_{\phi_\nu} = - \frac{4B_j}{\Pi N_j}$$

$$\Pi^4 N_j^4\, \tau \frac{MPi_\alpha}{U^2} \frac{q^\circ_{v_j}}{b} + 2\alpha \sum_{\nu=1}^{n} I_{j\nu}\, q^\circ_{\phi_\nu} = - \frac{4B_j}{\Pi N_j} (C - \alpha^2) \qquad (4\text{-}20)$$

$$[\tfrac{1}{2}\Pi^2 (j-\tfrac{1}{2})^2 \frac{Mi_\alpha}{U^2} - A] q^\circ_{\phi_j} = \frac{2A\alpha}{\Pi(j-\frac{1}{2})}$$

The torsion equations are now seen to be n uncoupled and immediately-solveable relations for the n generalized displacements $q^\circ_{\phi_j}$. The results permit solution for the bending displacements, thus eliminating the need for matrix operations. Since all elastic coupling terms are absent, deflections w_o and ϕ_o are independent of the stiffness ratio τ and the steady drag parameter C . A very important consequence is that the mechanism by which drag influences divergence is missing. One concludes that (4-20) is a particularly poor representation for steady deflections in the presence of steady drag.

Retention of the second-degree nonlinear effects from (4-9) involves adding to (4-20) all terms containing the triple modal integrals $H_{i\nu\mu}$. The system becomes fully coupled, and solutions are found by the same iterative scheme described in Appendix C for solving the full nonlinear system.

The behavior of the second degree nonlinear solution is compared with the linear deflection from (4-20) in Figs. 4-5 and 4-6 . Here it is shown how the deflection in the first vertical bending mode and the first torsion mode vary with increasing speed for a fixed angle of attack $\alpha = 0.01$ radians of the wing root. The parameters M , P , i_α , A , and τ for these examples correspond to the idealization of a sailplane wing discussed in Chapter VI, and sufficient modal convergence is assured by using $n=3$. Numbers on the ordinate of Fig. 4-5 show the actual twist in radians of the wingtip due to the first torsion mode; the vertical deflection in semichords of the wingtip due to $q^{o}_{w_1}$ is just twice the value read from the ordinate of Fig. 4-6.

The important influence of drag on the steady deflections is evident. But there is poor correspondence between the second degree nonlinear deflections and the divergence speeds indicated in Fig. 4-5 , which are solutions of the linear static stability determinant (2-28). This discrepancy is most pronounced when $C=0$, and the rapid divergence of the second-degree nonlinear deflections for all values of drag suggests trouble with the second-degree approximation.

Figures 4-7 through 4-10 show solutions of the complete nonlinear system (4-9) for the same wing configuration, together with the linear results. Correlation with the divergence predictions appears to be excellent, and the sudden blowing up of deflections characteristic of the second-degree nonlinear solutions is not encountered. Since the iterative procedure used to solve for nonlinear deflections commences with the linear solution as an initial estimate, nonlinear solutions which do exist for C=0 above the classical divergence speed cannot be obtained.

The full nonlinear solutions conform with nonlinear behavior expected by intuition. For zero drag, the vertical bending and torsion deflections should fall below the linear solution owing to the effective increase in stiffness "seen" by each degree of freedom due to deformation in the other. This effect is observed. The slight rearward chordwise displacement (Fig. 4-9) for C=0 when w_o and ϕ_o are large comes from bending-torsion coupling, and the negative contribution of the second torsion mode (Fig. 4-10) reflects a redistribution of elastic twist toward the wingtip where the curvature due to w_o is less. Drag alters the deformed state radically and causes large displacements at much lower speeds.

A clue to the reason why the second-degree terms alone are inadequate is found by looking at the sensitivity of solutions to changes in the bending stiffness ratio τ. The second degree nonlinear solution for bending deflections, given in Fig. 4-11, reveals increasingly poor behavior as τ is increased. Conversely, the complete nonlinear solution behaves as intuition would anticipate, becoming insensitive to changing τ as this parameter grows toward ∞ (Fig. 4-12).

In Chapter III the behavior for $\tau \to \infty$ of the steady nonlinear equilibrium equations was analytically investigated. In the discussion following equation (3-33) it was pointed out that the quantity $v''_o - \phi_o w''_o$ represents the actual curvature about the principal axis of chordwise bending for the deflected airfoil section, and that this quantity should vanish as $\tau \to \infty$. In this limit any chordwise deflection is a geometric consequence of elastic coupling between ϕ_o and w_o ; terms which contain the product $\tau(v''_o - \phi_o w''_o)$ approach a finite value. Now, referring to equations (3-24), it can be seen that in the second degree approximation this product is retained in the second equation but not in the vertical bending equation (where $w''_o\phi^2_o$ is dropped but $v''_o\phi_o$ retained). Likewise in the torsion equation, $w''^2_o\phi_o$ is dropped but $v''_o w''_o$ is kept. The result is that terms containing $\tau v''_o$ remain and blow up in the limit $\tau \to \infty$. Accordingly, the conclusion is reached that, for structures representative of aircraft wings for which τ is reasonably large, the third-degree terms containing the product $w''_o\phi_o$ must be retained. It may be added that, although this elastic coupling effect was neglected in the helicopter blade equations developed in Ref. 7, in that case the ordering scheme required τ to be on the order of unity. Another point is that the remaining third-degree terms in (3-24), which contain the product $v''_o\phi_o$, actually can be neglected when τ is large.

Since it has been determined that third degree terms cannot be excluded from the steady nonlinear equilibrium analysis, it follows that they must also be kept in the linearized unsteady perturbation equations (3-25). The original dynamic stability equations used early in this investigation, on the other hand, consisted of a linearized unsteady perturbation system based on the second-degree nonlinear approximation. That is, they are the result of removing all terms containing the modal integrals $R_{ij\mu\nu}$ from (4-12). Irregular behavior of the flutter speed with increasing angle of attack α was discovered, as was an extreme sensitivity to large τ which could not be justified physically. Furthermore, linear steady-state deflections were used-- a particularly unsuitable approximation for inclusion of steady drag.

Examples of these original flutter calculations appear in Figs. 4-13 and 4-14. The former gives a comparison of the early results with the full analysis by (4-12) for the sailplane example, showing how the simpler approximation differs significantly in flutter speed even in the presence of moderate steady deflections. Figure 4-14, based on a different wing configuration, gives an idea of the difficulty encountered for large τ when using the simpler analysis. (Note that the steady deflections are quite small in view of the fact that this example is a large-aspect-ratio wing). All of these stability boundaries abruptly terminate, at which point the eigenvalue solutions began to behave erratically. In contrast, flutter solutions of (4-19) can be obtained for arbitrarily large steady deformations-- indeed for tip deflections well beyond practical limits of material linearity.

D. Comparison of VT and VCT Calculations

The flutter velocities found using the VCT model can be checked directly against velocity computed from the VT model developed in Chapter II. Although such a comparison restricts the former method to the special nonlifting case $w_o = \phi_c = 0$, its basic approach of linearized perturbation motions about a steady-state deflection solution can nevertheless be tested by inclusion of steady drag. This is because the drag effect enters the stability determinant through coefficients depending on v_o. The chordwise bending equation of motion is uncoupled when $w_0 = v_0 = 0$, and flutter modes involve just vertical bending and torsion.

The VCT stability equations were analytically reduced to the VT form (2-1) in the last chapter by specifying $\alpha = 0$ and $\tau \to \infty$. This agreement is reflected in numerical results, as evidenced by Fig. 4-15. For an exceptionally large magnitude of drag, $C = 0.04$, chosen to magnify the importance of drag coupling and hence the steady deflections in the stability analysis, the two methods are used to compute flutter speeds for the same nonlifting configuration. The VCT analyses were made for τ ranging from 1 to 10,000.

As is always true for $EI_z = EI_x$, the drag coupling effect vanishes at $\tau = 1$ with flutter speed unaffected by drag. At the other extreme, for $\tau = 10{,}000$ the computed flutter speeds for $C = 0.04$ differ by a mere 0.052%. The Ref. 1 flutter speeds calculated for this same configuration are also shown and agree quite well.

When one examines the VCT dependence of flutter speed on τ (Fig. 4-15), the effect of drag is apparently insensitive to τ over the range of this parameter representative of practical aircraft applications. Hence the VT system (2-1) does not suffer by its inherent assumption that $\tau \to \infty$.

Table 4.1 presents a further comparison of results from the two approaches for a different configuration, in which modal convergence is emphasized. Of course, since $\tau = 50$ exact agreement cannot be expected.

Convergence of flutter speeds and frequencies and also mode shapes for the VCT solutions is documented in Table 4.2 for zero steady lift and in Table 4.3 for a lifting condition specified by $\alpha = .01$ rad. In the latter case, the apparent slower convergence is related to the steady lifting deflections (also tabulated), which also vary with n .

n	U_F, VT	U_F, VCT
2	4.260823	4.258457
3	4.260879	4.258351
4	4.260882	4.258335
5	4.260889	4.258336

TABLE 4.1 Comparison of Modal Flutter Speeds Computed with the VT and VCT Systems. (M = 40., P = 0.4, i_α = 0.25, A = 0.1, S = 0.1, τ = 50, C = 0.04)

	n = 1 U_F = 4.15027 Ω_F = 0.85254		n = 2 U_F = 4.183899 Ω_F = 0.088768		n = 3 U_F = 4.183883 Ω_F = 0.88757		n = 4 U_F = 4.183916 Ω_F = 0.88758	
	AMPL.	PHASE	AMPL.	PHASE	AMPL.	PHASE	AMPL.	PHASE
q_{w_1}	2.1800	224.54°	2.0650	223.87°	2.0659	223.87°	2.0659	223.87°
q_{w_2}	-		0.6345	-46.85°	0.6309	-46.84°	0.6308	-46.85°
q_{w_3}	-		-		0.0107	- 4.46°	0.0107	- 4.26°
q_{w_4}	-		-		-		0.0022	1.89°
q_{ϕ_1}	1.0	0°	1.0	0°	1.0	0°	1.0	0°
q_{ϕ_2}	-		0.03067	199.53°	0.03075	199.70°	0.03075	199.70°
q_{ϕ_3}	-		-		0.00340	- 5.55°	0.00339	- 5.67°
q_{ϕ_4}	-		-		-		0.0059	220.49°

TABLE 4.2 Modal Convergence for Flutter at Zero Steady Lift. (M = 9.4, P = 0.01, i_α = 0.25, A = 0.1, S = 0.1, τ = 25., C = 0)

	n = 2 U_F = 3.5495 Ω_F = 0.68200		n = 3 U_F = 3.5329 Ω_F = 0.67468		n = 4 U_F = 3.5315 Ω_F = 0.67276	
$q^{\circ}_{w_1}$	1.19055		1.18142		1.18074	
$q^{\circ}_{w_2}$	0.01336		0.01333		0.01333	
$q^{\circ}_{w_3}$	-		0.000817		0.000818	
$q^{\circ}_{w_4}$	-		-		0.000151	
$q^{\circ}_{v_1}$	0.002270		0.002296		0.002305	
$q^{\circ}_{v_2}$	-0.000279		-0.000284		-0.000284	
$q^{\circ}_{v_3}$	-		-0.000033		-0.000033	
$q^{\circ}_{v_4}$	-		-		-0.000005	
$q^{\circ}_{\phi_1}$	0.0087100		0.0087591		0.0087656	
$q^{\circ}_{\phi_2}$	0.0000373		0.0000915		0.0000983	
$q^{\circ}_{\phi_3}$	-		0.0000017		0.0000090	
$q^{\circ}_{\phi_4}$	-		-		0.0000013	
	AMPL.	PHASE°	AMPL.	PHASE°	AMPL.	PHASE°
q_{w_1}	2.4492	227.45	2.4765	227.68	2.4860	227.76
q_{w_2}	0.52487	-26.65	0.50948	-26.27	0.51068	-26.23
q_{w_3}	-		0.01637	- 6.54	0.01612	- 6.57
q_{w_4}	-		-		0.00250	- 1.47
q_{v_1}	0.84595	- 4.77	0.85914	- 4.89	0.86569	- 4.98
q_{v_2}	0.03071	179.03	0.02979	180.02	0.02916	180.20
q_{v_3}	-		0.00923	172.67	0.00532	172.76
q_{v_4}	-		-		0.00122	172.56
q_{ϕ_1}	1.0	0	1.0	0	1.0	0
q_{ϕ_2}	0.07178	-21.65	0.07798	-20.83	0.07947	-20.73
q_{ϕ_3}	-		0.02793	- 4.83	0.02925	- 5.06
q_{ϕ_4}	-		-		0.00998	- 8.60

TABLE 4.3 Modal Convergence for Flutter at Steady Lift for α = 0.01 rad. (M = 9.4, P = 0.01, i_α = 0.25, A = 0.1, S = 0.1, τ = 25, C = 0)

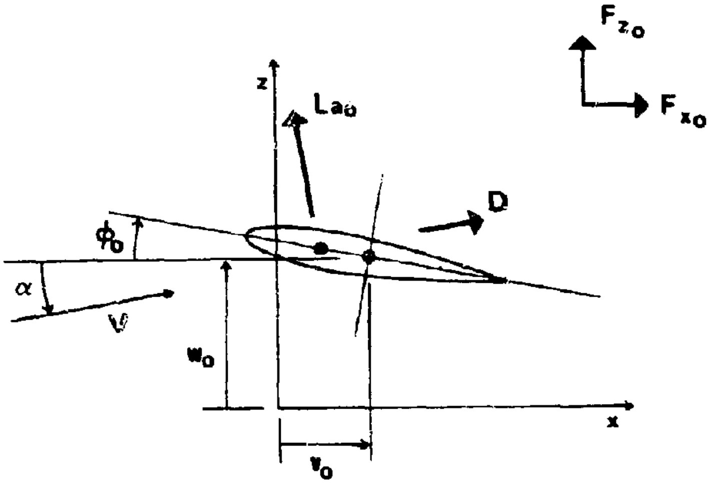

FIGURE 4-1 Resolution of Applied Steady Loads into Components F_{x_o} , F_{z_o}

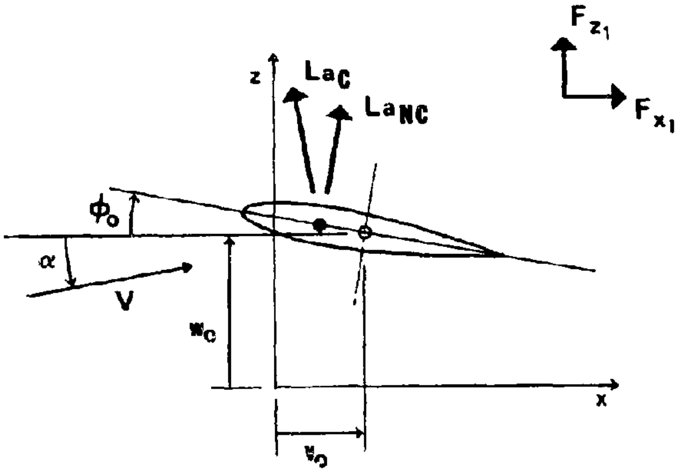

FIGURE 4-2 Resolution of Unsteady Airloads into Components F_{x_1} , F_{z_1}

$$[M_s] = M \left[\begin{array}{c|c|c} \lceil I \rfloor & 0 & \begin{matrix} -S\ell_{11} & \cdots & -S\ell_{n1} \\ \vdots & & \vdots \\ -S\ell_{1n} & \cdots & -S\ell_{nn} \end{matrix} \\ \hline 0 & \lceil I \rfloor & 0 \\ \hline \begin{matrix} -S\ell_{11} & \cdots & -S\ell_{1n} \\ \vdots & & \vdots \\ -S\ell_{n1} & \cdots & -S\ell_{nn} \end{matrix} & 0 & \frac{1}{2} i_\alpha \lceil I \rfloor \end{array} \right]$$

ABBREVIATIONS OF SUMMATIONS APPEARING IN $[K_s]$:

$$R_{ij\phi\phi} = \sum_{\mu=1}^{n} \sum_{\nu=1}^{n} R_{ij\mu\nu} \, q^{o}_{\phi\mu} \, q^{o}_{\phi\nu}$$

$$R_{wi\phi j} = \sum_{\mu=1}^{n} \sum_{\nu=1}^{n} R_{\nu i\mu j} \, q^{o}_{\phi\mu} \, \frac{q^{o}_{w\nu}}{b}$$

$$H_{\phi ij} = \sum_{\nu=1}^{n} H_{\nu ij} \, q^{o}_{\phi\nu}$$

$$H_{iwj} = \sum_{\nu=1}^{n} H_{i\nu j} \, \frac{q^{o}_{w\nu}}{b}$$

etc.

FIGURE 4-3(a) Mass and Stiffness Matrices Appearing in Equation (4-19)

$$[K_s] = Pi_{\alpha}M \left[\begin{array}{ccc|ccc|ccc}
(\pi N_1)^4 + (\tau-1)R_{11\phi\phi} & \cdots & (\tau-1)R_{1n\phi\phi} & -(\tau-1)H_{\phi 11} & \cdots & -(\tau-1)H_{\phi 1n} & (\tau-1)[-H_{1v1} + 2R_{w1\phi 1}] & \cdots & (\tau-1)[-H_{nv1} + 2R_{w1\phi n}] \\
\vdots & \ddots & \vdots & \vdots & & \vdots & \vdots & & \vdots \\
(\tau-1)R_{n1\phi\phi} & \cdots & (\pi N_n)^4 + (\tau-1)R_{nn\phi\phi} & -(\tau-1)H_{\phi n1} & \cdots & -(\tau-1)H_{\phi nn} & (\tau-1)[-H_{1vn} + 2R_{wn\phi 1}] & \cdots & (\tau-1)[-H_{nvn} + 2R_{wn\phi n}] \\
\hline
-(\tau-1)H_{\phi 11} & \cdots & -(\tau-1)H_{\phi 1n} & \tau(\pi N_1)^4 - (\tau-1)R_{11\phi\phi} & \cdots & -(\tau-1)R_{1n\phi\phi} & -(\tau-1)[H_{1w1} + 2R_{v1\phi 1}] & \cdots & -(\tau-1)[H_{nw1} + 2R_{v1\phi n}] \\
\vdots & & \vdots & \vdots & \ddots & \vdots & \vdots & & \vdots \\
-(\tau-1)H_{\phi n1} & \cdots & -(\tau-1)H_{\phi nn} & -(\tau-1)R_{n1\phi\phi} & \cdots & \tau(\pi N_n)^4 - (\tau-1)R_{nn\phi\phi} & -(\tau-1)[H_{1wn} + 2R_{vn\phi 1}] & \cdots & -(\tau-1)[H_{nwn} + 2R_{vn\phi n}] \\
\hline
(\tau-1)[-H_{1v1} + 2R_{w1\phi 1}] & \cdots & (\tau-1)[-H_{1vn} + 2R_{wn\phi 1}] & -(\tau-1)[H_{1w1} + 2R_{v1\phi 1}] & \cdots & -(\tau-1)[H_{1wn} + 2R_{vn\phi 1}] & \frac{\pi^2}{8P} + (\tau-1)[R_{ww11} - R_{vv11}] & \cdots & (\tau-1)[R_{ww1n} - R_{vv1n}] \\
\vdots & & \vdots & \vdots & & \vdots & \vdots & \ddots & \vdots \\
(\tau-1)[-H_{nv1} + 2R_{w1\phi n}] & \cdots & (\tau-1)[-H_{nvn} + 2R_{wn\phi n}] & -(\tau-1)[H_{nw1} + 2R_{v1\phi n}] & \cdots & -(\tau-1)[H_{nwn} + 2R_{vn\phi n}] & (\tau-1)[R_{wwn1} - R_{vvn1}] & \cdots & \frac{(n-\frac{1}{2})^2\pi^2}{2P} + (\tau-1) \cdot [R_{wwnn} - R_{vvnn}]
\end{array}\right]$$

FIGURE 4-3(b)

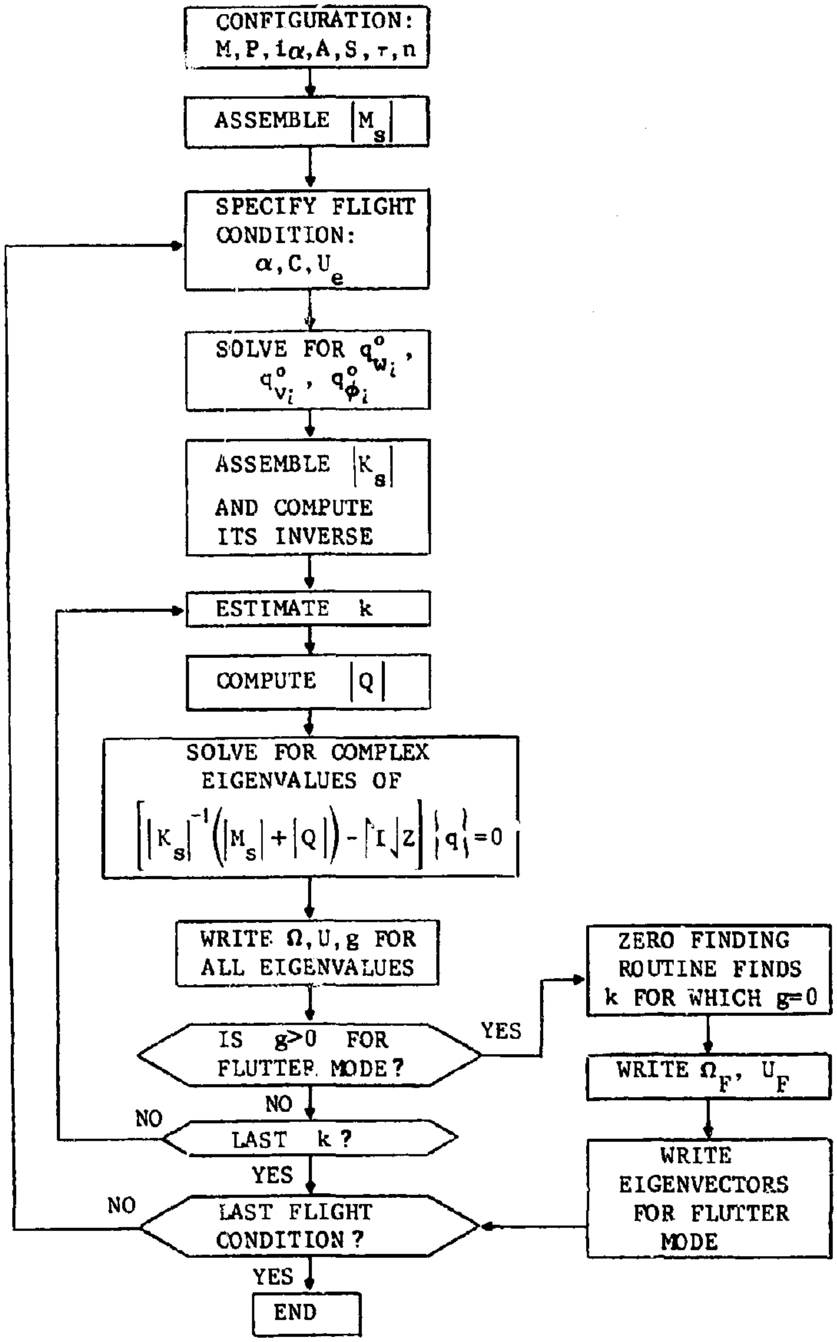

FIGURE 4-4 Flow Chart for Solution Procedure Using V-g Method

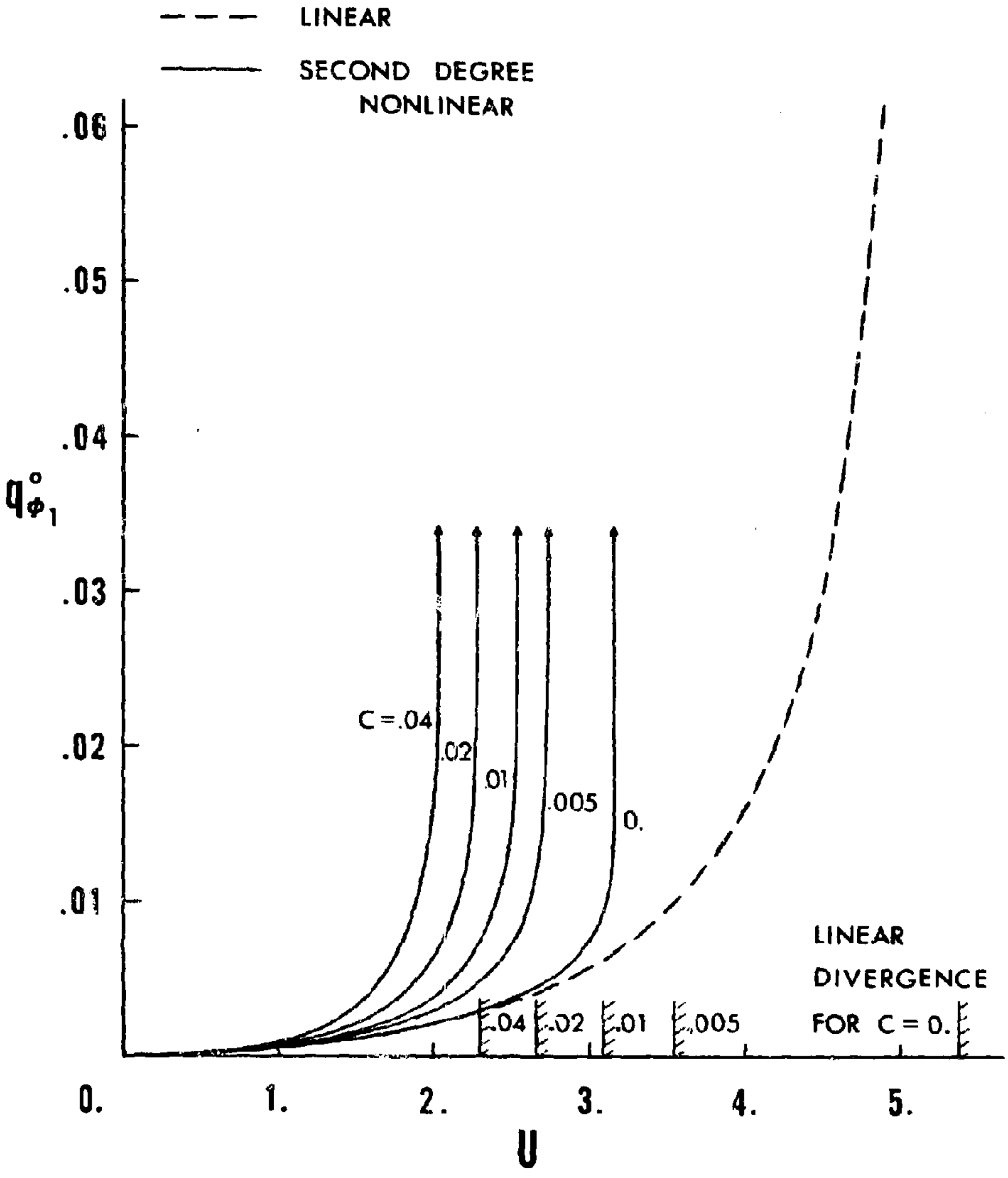

FIGURE 4-5 Deflection of the First Torsion Assumed Mode for $\alpha = .01$ and Increasing Speed, Comparing Linear and Second-Degree Nonlinear Solutions. ($M = 9.4$, $F = 0.01$, $i_\alpha = 0.25$, $A = 0.1$, $S = 0.1$, $\tau = 25$, and $n = 3$)

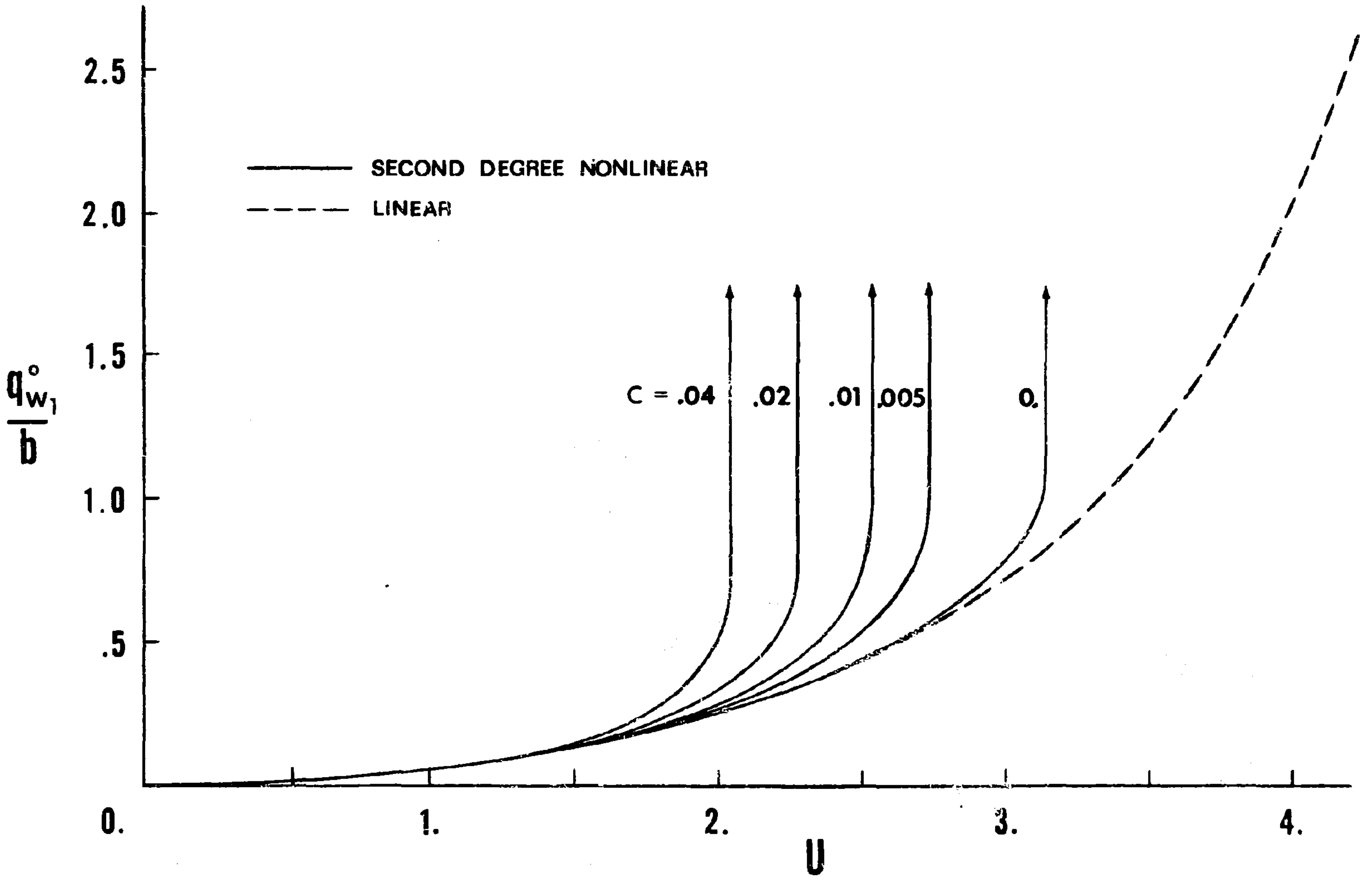

FIGURE 4-6 Amplitude of the First Vertical Bending Mode. (Same Conditions as in Figure 4-5)

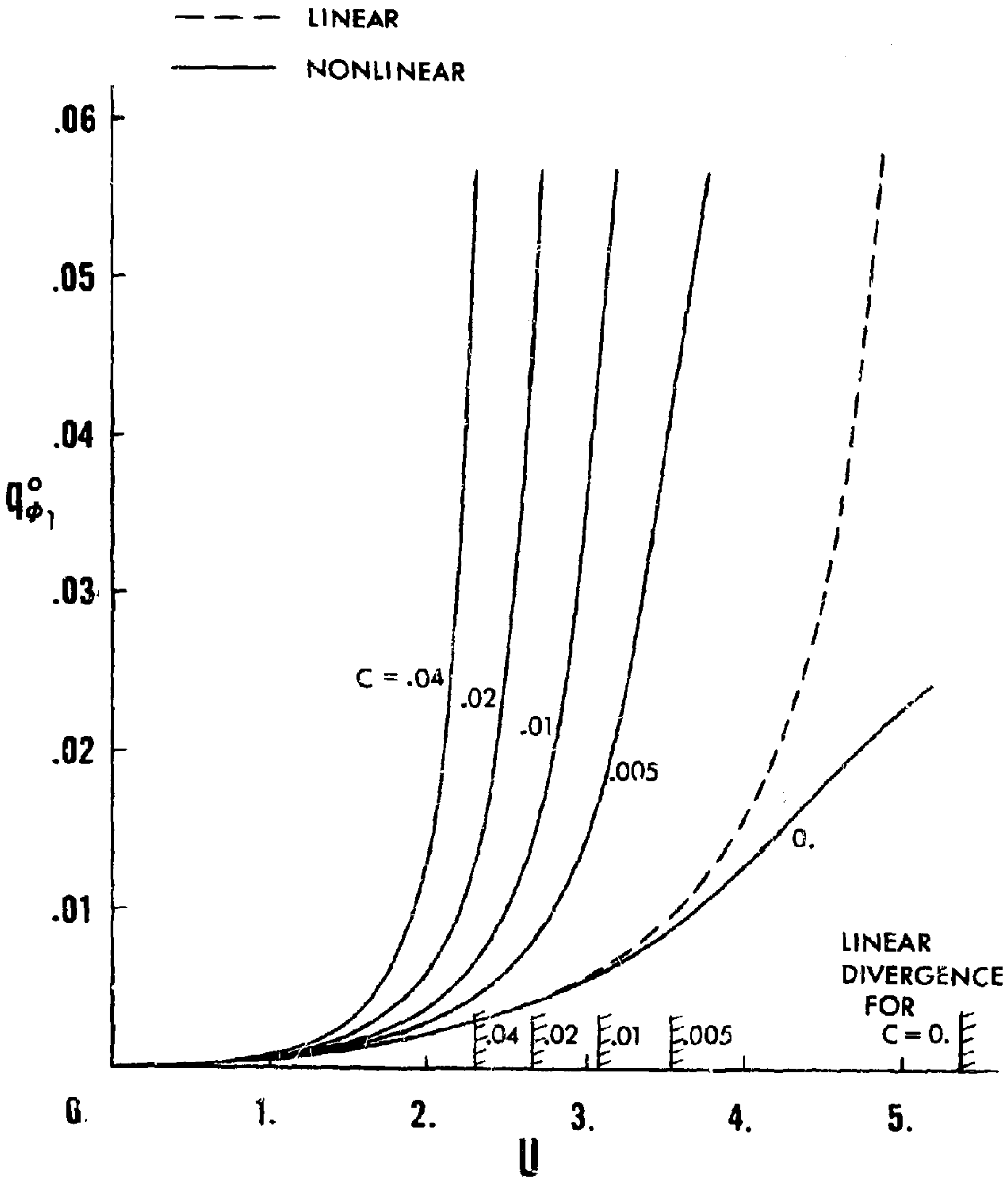

FIGURE 4-7 Amplitude of the First Torsion Mode for $\alpha = 0.01$ and Increasing Speed, Comparing Linear and Full Nonlinear Solutions. ($M = 9.4$, $P = 0.01$, $i_\alpha = 0.25$, $A = 0.1$, $S = 0.1$, $\tau = 25$, and $n = 3$)

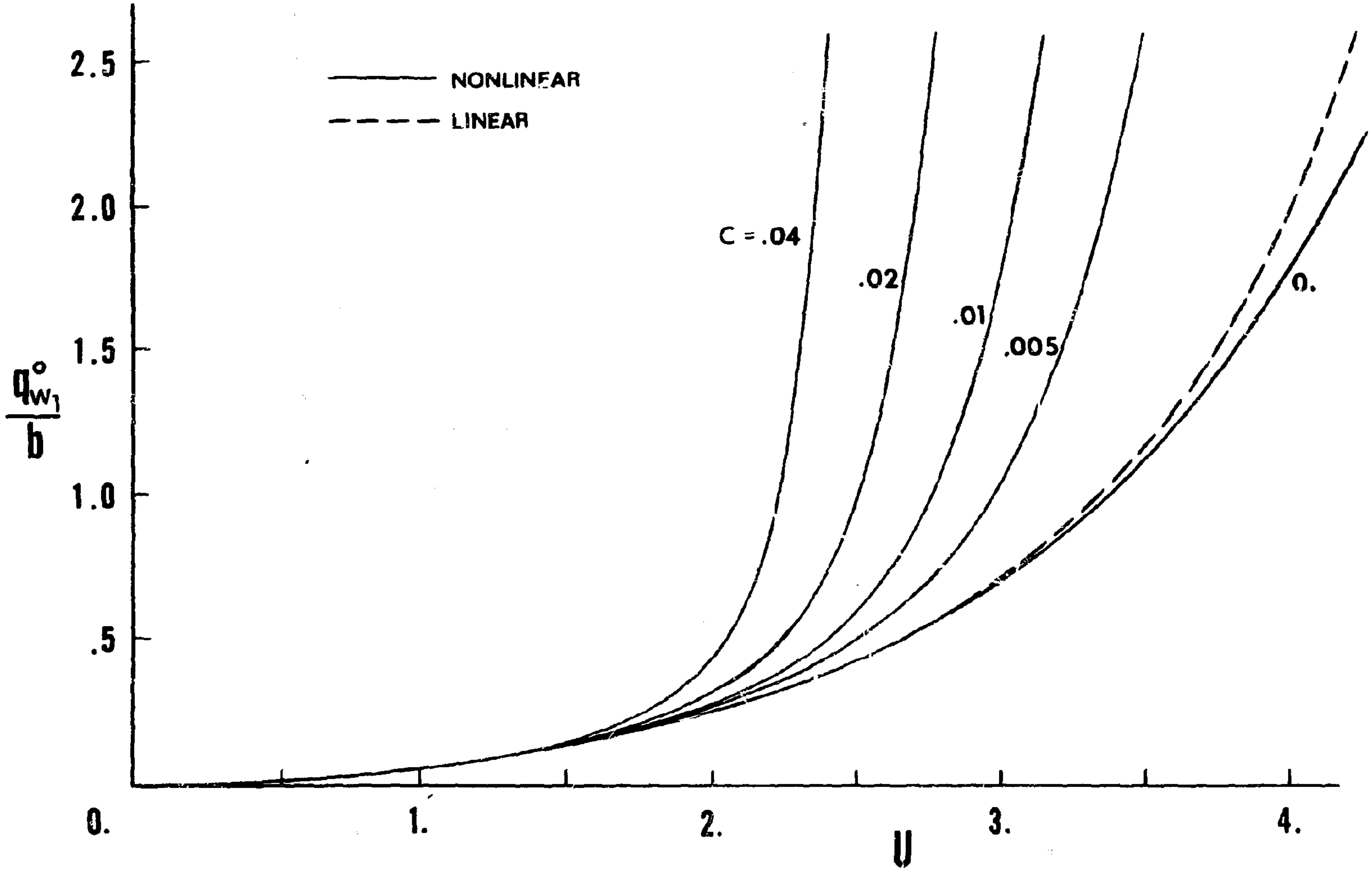

FIGURE 4-8 Amplitude of the First Vertical Bending Mode. (Same Conditions as in Fig. 4-7)

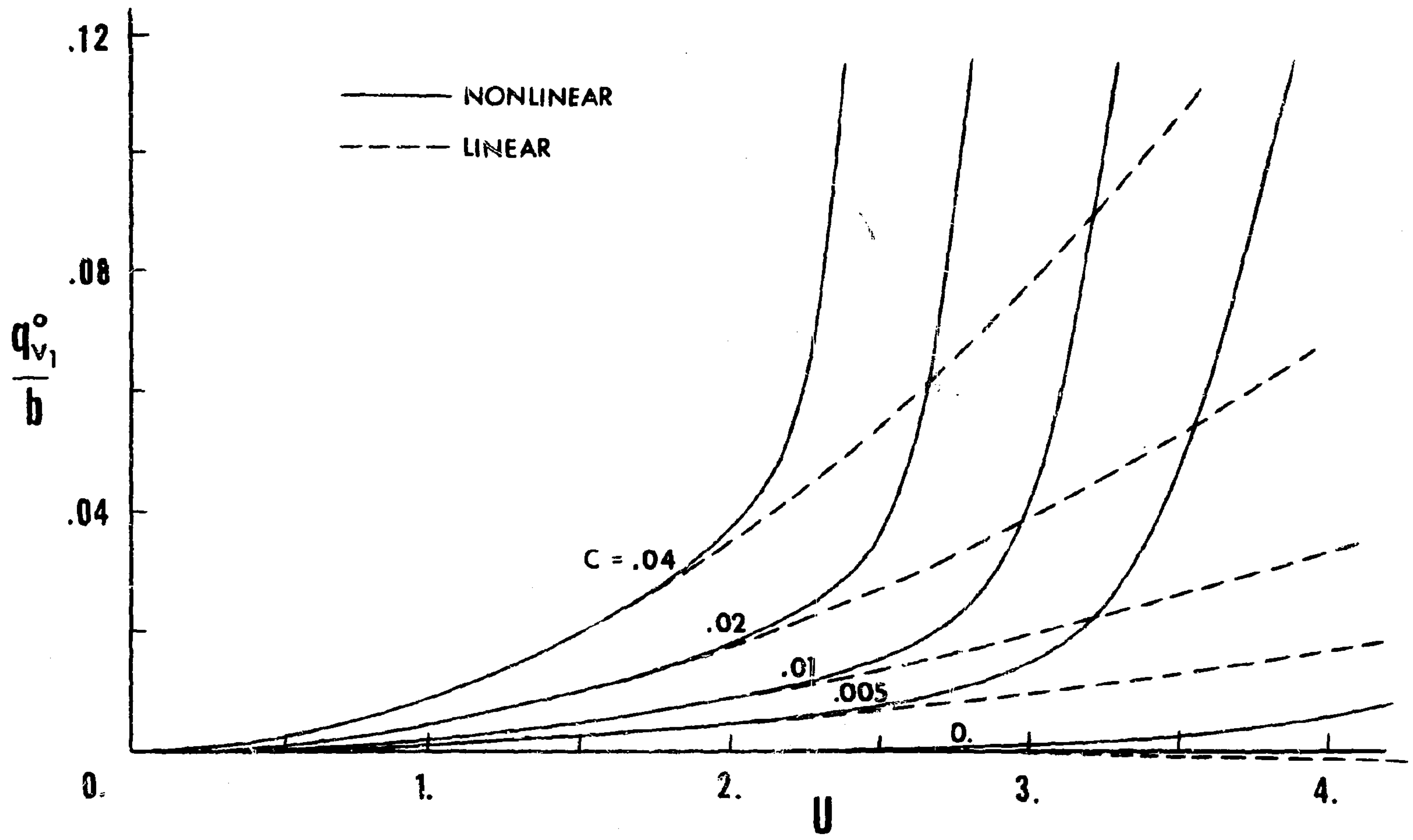

FIGURE 4-9 Amplitude of the First Chordwise Bending Mode. (Same Conditions as in Fig. 4-7)

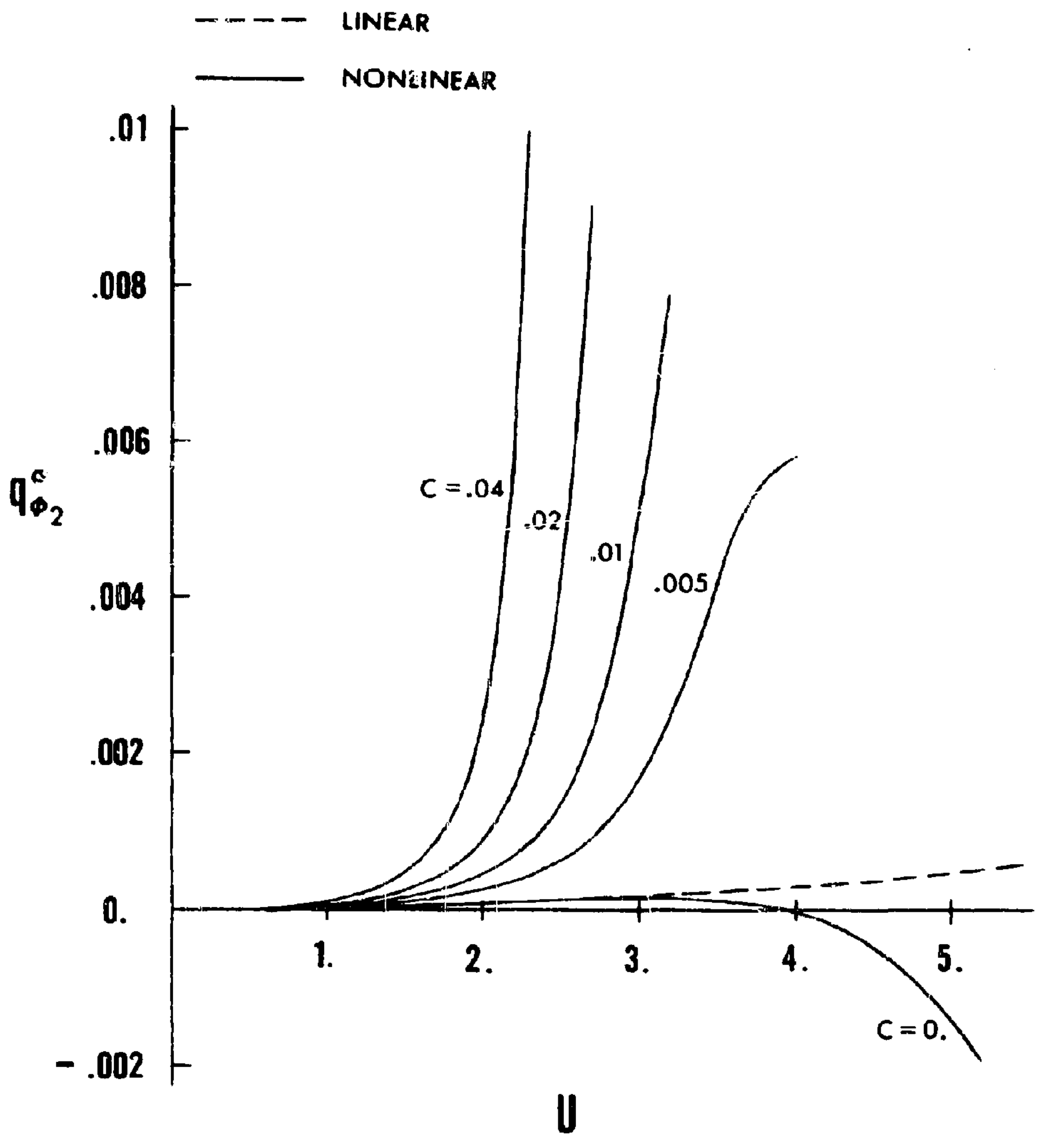

Figure 4-10 Amplitude of the Second Torsion Mode. (Same conditions as in Fig. 4-7)

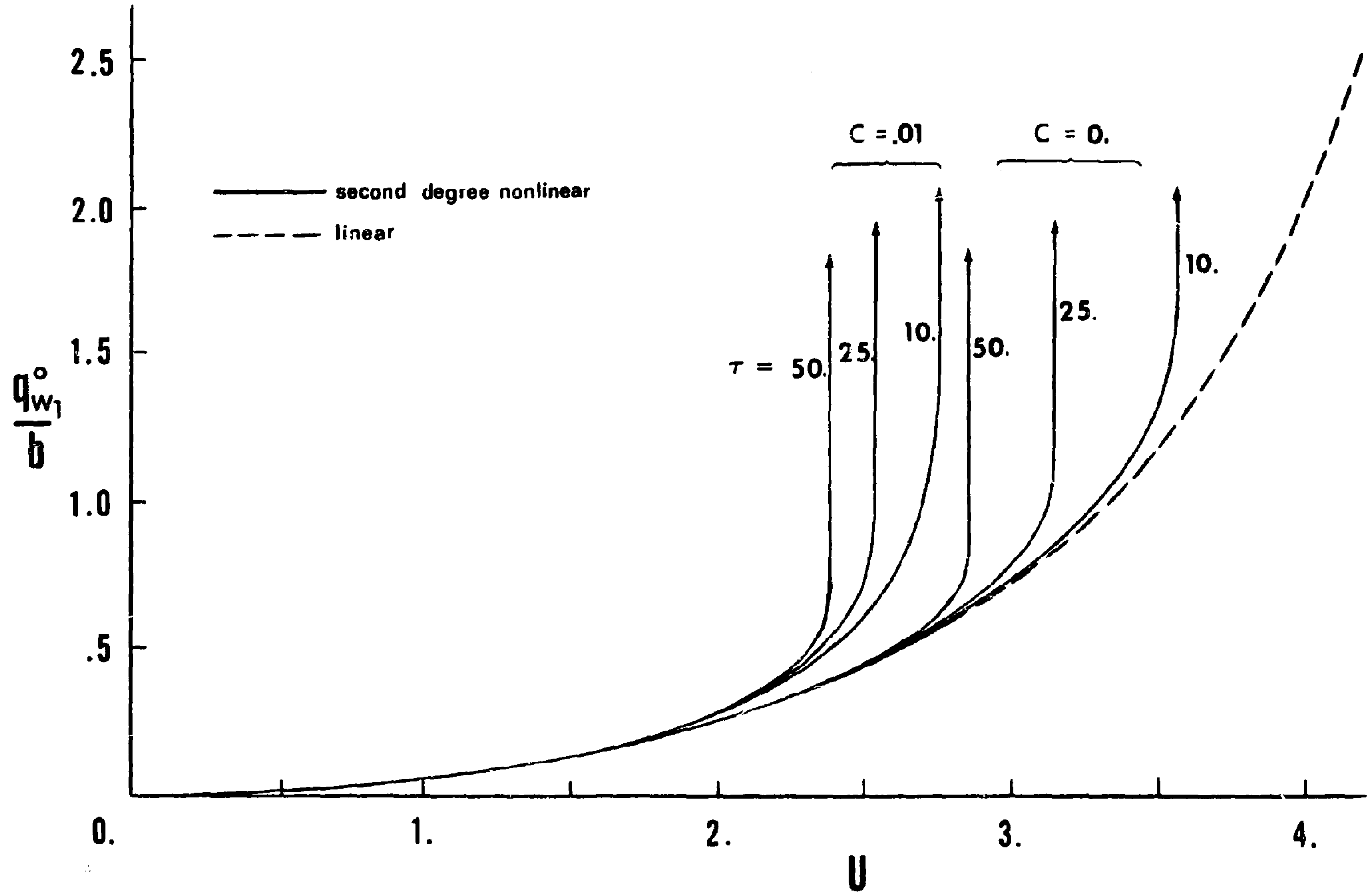

FIGURE 4-11 Amplitude of the First Vertical Bending Mode vs. τ, Using Second-Degree Nonlinear and Linear Approximations. (Remaining Parameters Same as in Fig. 4-5)

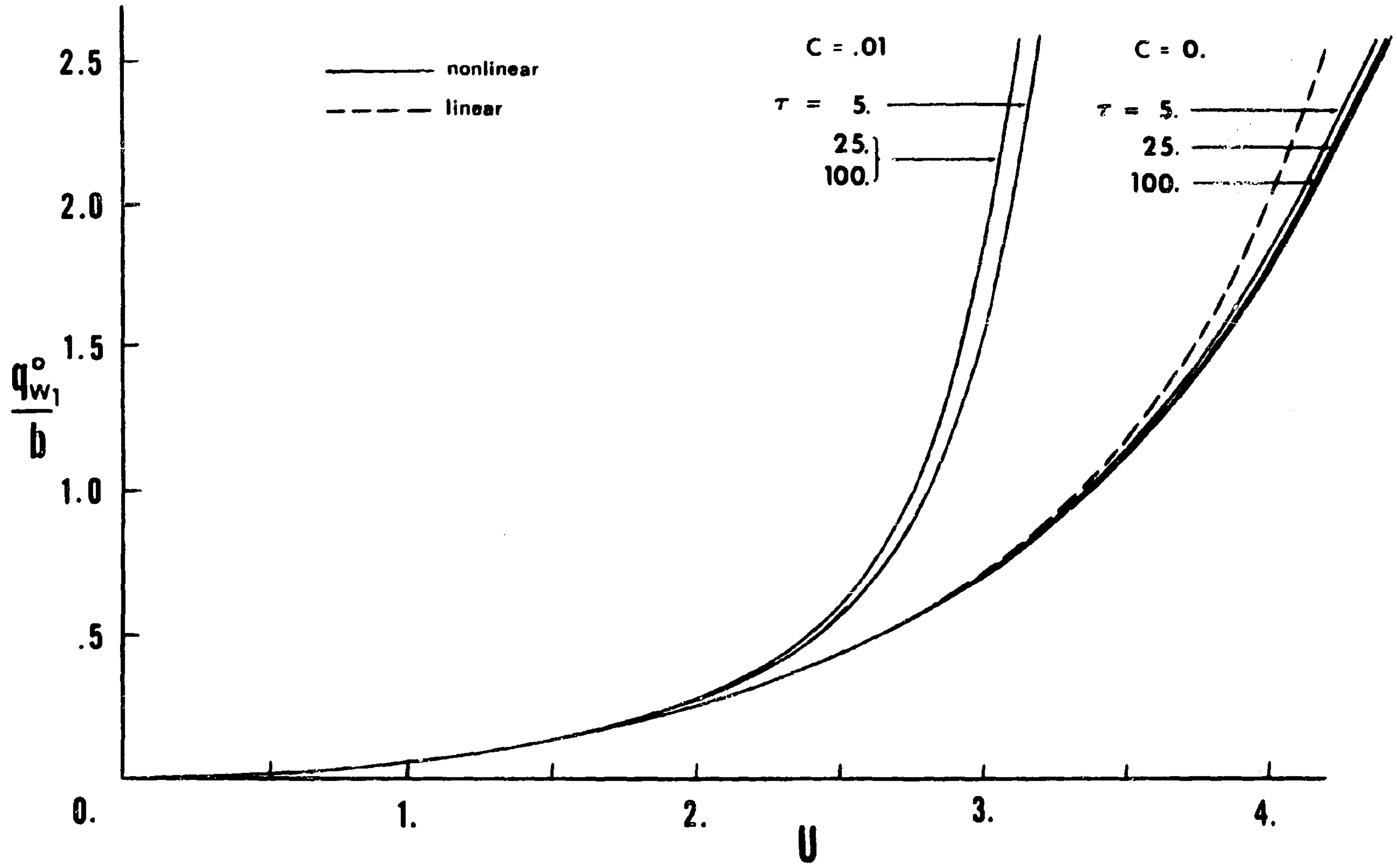

FIGURE 4-12 Amplitude of the First Vertical Bending Mode vs. τ, Using Full Nonlinear and Linear Approximations. (Remaining Parameters Same as in Fig. 4-7)

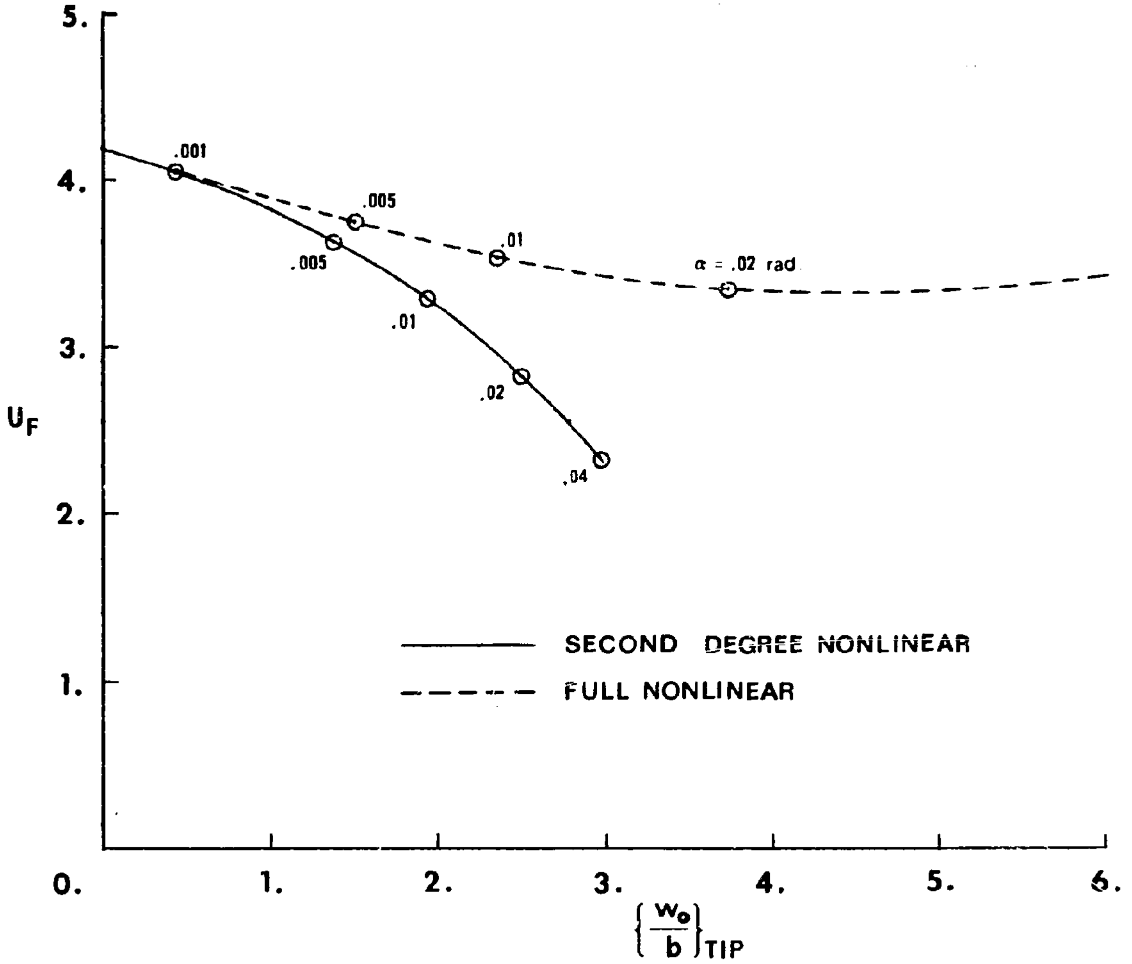

FIGURE 4-13 Flutter Speed as a Function of Steady Wing-Tip Displacement for Two Different Approximations in the Analysis. ($M = 9.4$, $P = 0.01$, $i_{\alpha} = 0.25$, $A = 0.1$, $S = 0.1$, $\tau = 25$, $C = 0$, and $n = 3$)

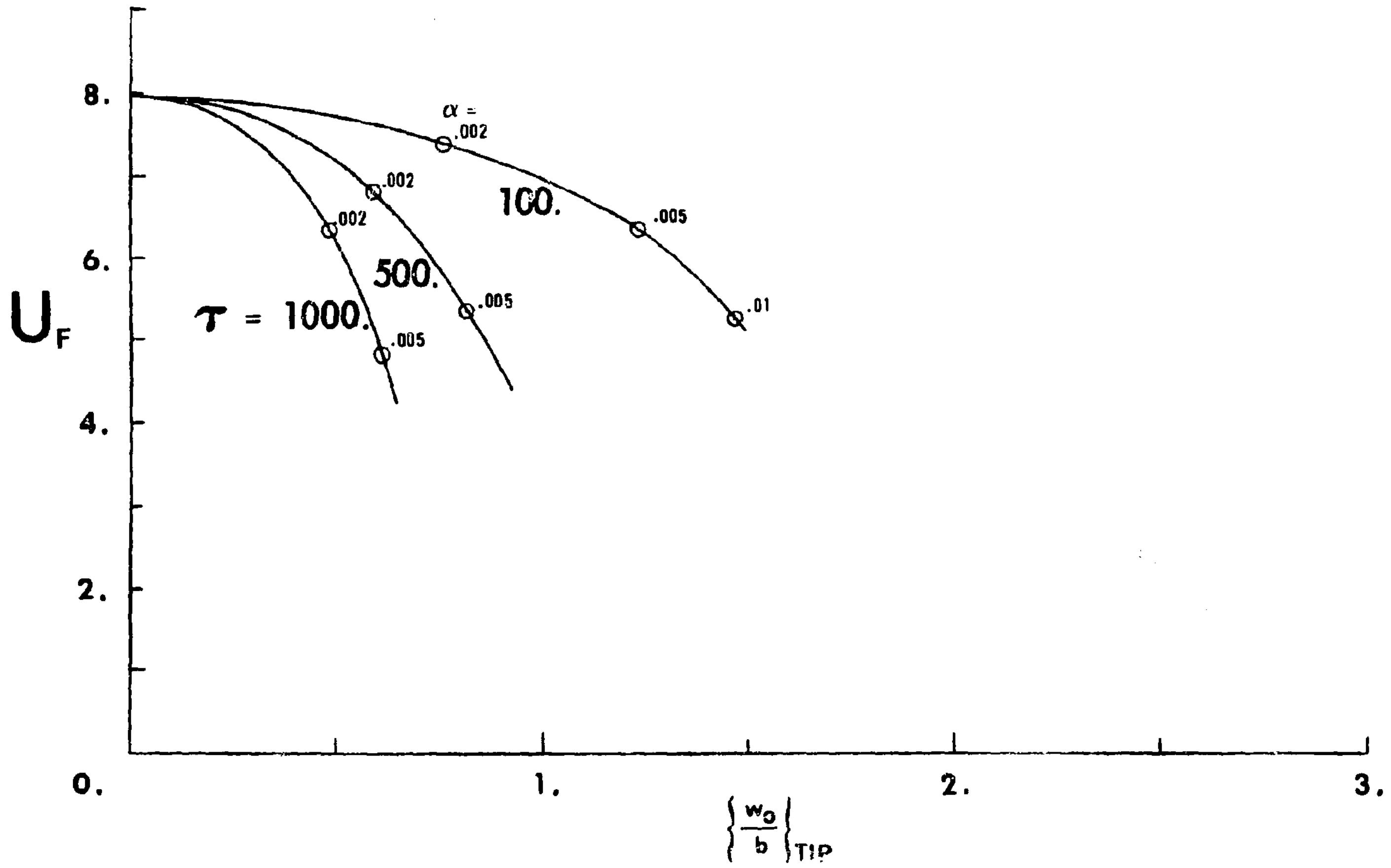

FIGURE 4-14 Flutter Speed as a Function of Steady Wing-Tip Displacement and Chordwise Bending Stiffness. M = 40, P = 0.004, r_α = 0.35, A = 0.1, S = 0.1, C = 0, and n = 3)

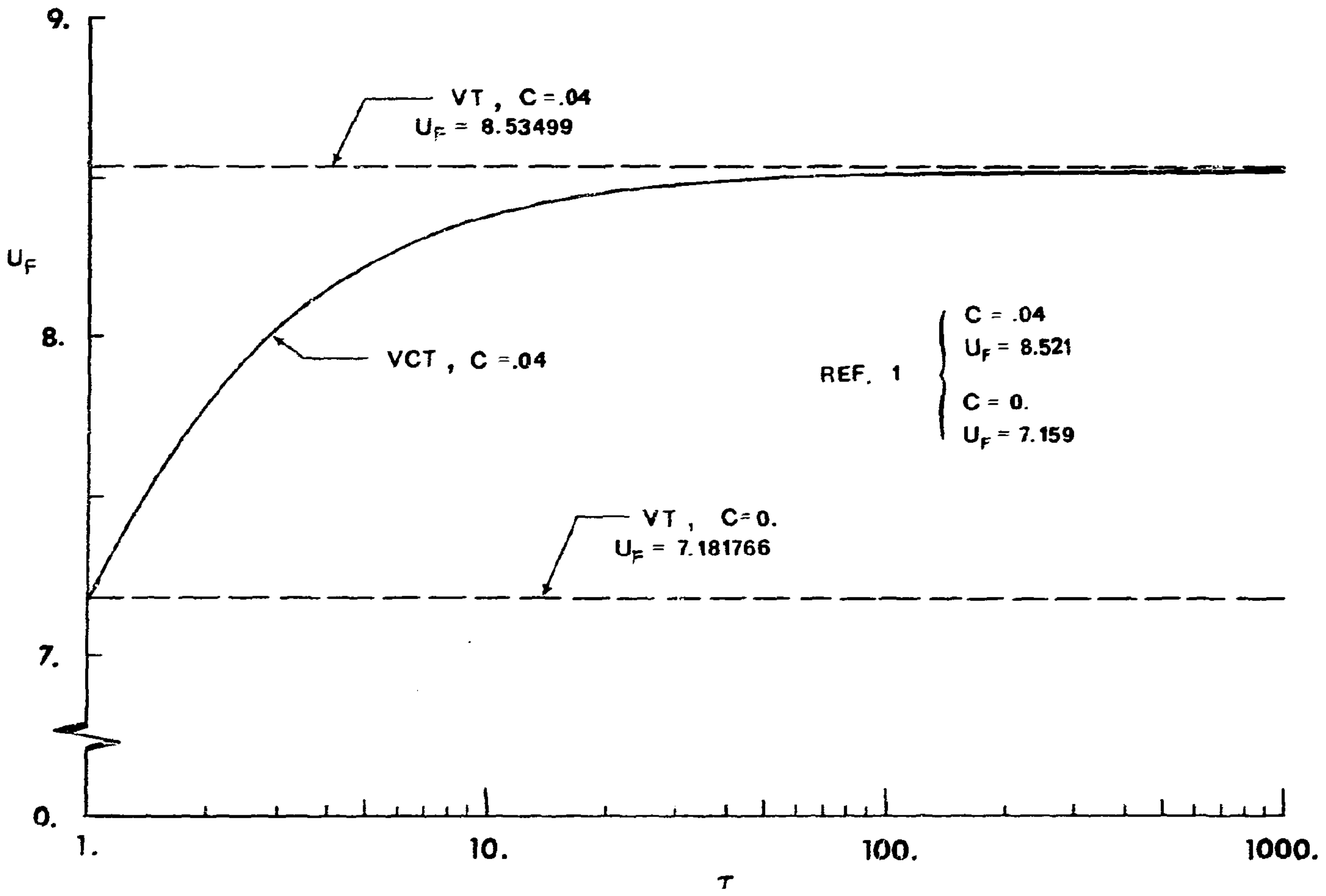

FIGURE 4-15 Comparison of Zero-Lift Flutter Speeds Found Using the VT and VCT Models. ($M = 40$, $P = 0.04$, $i_\alpha = 0.25$, $A = 0.1$, $S = 0.1$, $n = 3$)

Chapter V

THE DETERMINATION OF AEROELASTIC MODES FOR ARBITRARY VELOCITY

A. Incompressible Strip Theory Airloads for Arbitrary Motion

The procedure for determining flutter velocity developed in Chapter IV has several drawbacks. It requires a matched point analysis in which an estimated velocity U_e used to calculate steady deflections has to be iteratively matched to the lowest calculated flutter speed U_F for the proper structural damping. Consequently the solution for a stability boundary over a range of lifting conditions can be lengthy. Furthermore, intermediate computations have no physical significance and are of limited qualitative value. The behavior and degree of stability of individual aeroelastic modes, which becomes more interesting with the addition of the fore-and-aft bending degree of freedom, has proven to be difficult to deduce from the V-g solutions. The only quantitative information available pertains to the neutral stability conditions found for the mode which experiences flutter.

We would like to have physically meaningful information regarding dynamics of the system at any desired speed. That is, we would like to know the complex eigenvalues of the aeroelastic modes at subcritical and supercritical velocities. Obviously a major drawback of the V-g method is its dependence upon simple harmonic air loads.

Several solution procedures were studied, which replace the Fourier transformation with respect to t by Laplace transformation with respect to t and obtain at least an approximation to the modal stability below and above the flutter velocity. The p-k method, a

British flutter analysis technique (Ref. 8), uses the same simple harmonic airloads but assumes that these loads are approximately complex eigenvalues $s = \sigma + i\omega$, where ω is the frequency used in calculating the airloads and $|\sigma| << |\omega|$.

Another approach, commonly applied in helicopter blade stability analysis, involves use of quasisteady aerodynamic theory by assuming k is small enough to permit $C(k) \simeq 1$. Laplace transformation of the system then yields only linear and quadratic terms in s. Linear matrix techniques can then be used in determining the roots. This level of approximation neglects entirely the effect of the unsteady wake upon the circulatory airloads and is not appropriate for the magnitudes of reduced frequencies observed in many flutter calculations by the V-g method.

A third possible course is to apply an augmented-state method, which approximates the actual unsteady aerodynamic loads for arbitrary motion with a transfer function relating airfoil displacements to loads having a rational Laplace transform, resulting in a linear matrix eigenvalue problem for the aeroelastic modes. Goland and Luke (Ref. 9) used this route to study wing bending-torsion flutter. They adopted the R.T. Jones (Ref. 10) approximation to the Wagner indicial lift function to express unsteady airloads in rational form, taking the Laplace transform in time. In addition to their accurate description of the basic bending-torsion aeroelastic behavior at all flight speeds, Goland and Luke demonstrated that the severity of flutter cannot be reliably inferred from solutions by the V-g method.

Each of the techniques mentioned above attempts to gain information about aeroelastic modes whose eigenvalues have nonzero real parts. The true effect of the unsteady wake on the aerodynamic loads for arbitrary motions is approximated to varying degrees. This is done quite well for most motions in the case of augmented-state methods, marginally in the p-k method, and not at all in the quasisteady case.

For present purposes all of these schemes were rejected in favor of the more exact approach developed by Edwards (Ref. 11*). An important contribution of Ref. 11 (adapted from Sears, Ref. 21) is the definition of a generalized Theodorsen function to represent the exact circulatory two-dimensional incompressible unsteady airloads in the Laplace domain for arbitrary motions. The generalized Theodorsen function is expressible in terms of the modified Bessel functions of complex argument K_o and K_1 as

$$C(\bar{s}) \equiv \frac{K_1(\bar{s})}{K_o(\bar{s}) + K_1(\bar{s})} \tag{5-1}$$

where

$$\bar{s} = \frac{sb}{V}$$

Although previous investigators had recognized that this form was convergent for the right half plane, representing divergent oscillatory motions with $\text{Re}(s) > 0$, the restriction on the integral definitions of the modified Bessel functions caused some investigators to believe that convergent oscillatory motions (s in the left half plane) could

---

*See also Milne (Ref. 22).

not be so represented. Edwards observed that $K_o(\bar{s})$ and $K_1(\bar{s})$ are defined and analytic throughout the s-plane except for a branch point at the origin. When one places a branch cut along the negative real axis, $C(\bar{s})$ can be shown by analytic continuation to relate circulatory loads and displacements throughout the s-plane except along this cut. It is, in effect, an "aerodynamic transfer function" in the Laplace domain.

With substitution of $\bar{s} = ik$ in (5-1), the familiar Theodorsen function of reduced frequency for simple harmonic motion is recovered. Although arbitrary motion is now being considered rather than simple harmonic motion, the two approaches yield similar forms when the initial conditions arising in the transforms are neglected. In fact, the simple harmonic airloads (4-18) and (2-3) can be used for arbitrary unsteady motion simply substituting $C(\bar{s})$ for $C(k)$ and s for $i\omega$.

The modified Bessel functions are computed from their ascending power series expansions, as mentioned in Ref. 11 and described in Appendix B. Since the transforms of aerodynamic loads will be multiple-valued functions because of the branch point of $C(\bar{s})$ at the origin, the convention

$$-\Pi < \mathrm{Arg}(s) \leq \Pi$$

is used for the cut on the negative real axis. The generalized Theodorsen function is computed by Edwards in the form $C(\bar{r}e^{i\theta})$ for representative values $0 \leq \theta \leq \Pi$. It is shown to approach 1 as $\bar{r} \to 0$ and ½ as $\bar{r} \to \infty$ for all θ.

With the ability to compute unsteady two-dimensional incompressible airloads for arbitrary motions in hand, the simple harmonic stability analysis developed in Chapter IV can be generalized for this case. All of the true aeroelastic eigenvalues and eigenfunctions can be obtained for any prescribed speed U_e . Stability can be displayed with root locus diagrams. The solution technique is developed in the following section.

B. Solution for the Aeroelastic Roots by Means of Assumed Modes

Formally, the procedure for developing the modal equations needed for the true aeroelastic modes throughout the complex plane begins with Laplace transformation of the linearized equations of motion (3-25). The transformed perturbation displacements are then expressed as series expansions in the assumed modes as

$$\bar{w}_1(y;s) = \sum_{i=1}^{n} f_{w_i}(y)\bar{q}_{w_i}(s)$$

$$\bar{v}_1(y;s) = \sum_{i=1}^{n} f_{v_i}(y)\bar{q}_{v_i}(s) \tag{5-2}$$

$$\bar{\phi}_1(y;s) = \sum_{i=1}^{n} f_{\phi_i}(y)q_{\phi_i}(s)$$

A system of homogeneous, linear, algebraic equations in the generalized displacements $\bar{q}_{w_i}$, $\bar{q}_{v_i}$, $\bar{q}_{\phi_i}$ can then be derived by Galerkin's method, as before. Nontrivial solutions are given by the zeros of the determinant in s . Since the coefficients in this determinant which arise from the aerodynamic loads will contain the nonrational function $C(\bar{s})$, this will not be a polynomial eigenvalue problem. Roots $s = \sigma + i\omega$ will thus have to be obtained by iteration.

Since full development of the modal equations is analogous to that for the simple harmonic case, the stability determinant in s will simply be constructed directly from the modal equations for simple harmonic motion defined by (4-12), (4-18), and (2-3). One replaces $i\omega$ by s, ik by $\bar{s}$, and eliminates g. The elements of the aerodynamic matrix given in (4-18) for simple harmonic loads become, for arbitrary motion,

$$
\begin{array}{l}
(5\text{-}3) \\
(1 \le i \le n) \\
(1 \le j \le n)
\end{array}
\left\{
\begin{array}{ll}
\bar{Q}_{j,i} & = \begin{cases} \bar{L}_w & (i=j) \\ 0 & (i \ne j) \end{cases} \\
\bar{Q}_{j,i+2n} & = -(\bar{L}_\phi - A\bar{L}_w) I_{ji} \\
\bar{Q}_{j+n,i} & = \begin{cases} (1 - \bar{L}_w)\alpha & (i=j) \\ 0 & (i \ne j) \end{cases} \\
\bar{Q}_{j+n,i+2n} & = [\bar{L}_\phi - \tfrac{1}{2} - \frac{1}{\bar{s}} + A(1-\bar{L}_w)] I_{ji}\alpha \\
\bar{Q}_{j+2n,i} & = -(\bar{M}_w - A\bar{L}_w) I_{ij} \\
\bar{Q}_{j+2n,i+2n} & = \begin{cases} \tfrac{1}{2}[\bar{M}_\phi - A(\bar{L}_\phi + \bar{M}_w) + A^2 \bar{L}_w] & (i=j) \\ 0 & (i \ne j) \end{cases} \\
\bar{Q}_{\nu,i+n} & = 0 \quad \text{for} \quad 1 \le \nu \le 3n
\end{array}
\right.
$$

in which

$$
(5\text{-}4) \left\{
\begin{array}{l}
\bar{L}_w = 1 + 2\,\dfrac{C(\bar{s})}{\bar{s}} \\
\bar{L}_\phi = \tfrac{1}{2} + \dfrac{1}{\bar{s}}\,[1 + 2C(\bar{s})] + 2\,\dfrac{C(\bar{s})}{\bar{s}^2} \\
\bar{M}_w = \tfrac{1}{2} \\
\bar{M}_\phi = \dfrac{3}{8} + \dfrac{1}{\bar{s}}
\end{array}
\right.
$$

These aerodynamic loads are based on the assumptions discussed prior to Eq. (4-13).

With the same mass and stiffness matrices M_s and K_s illustrated in Fig. 4-3, and the aerodynamic matrix $\bar{Q}$ whose elements are defined by (5-3), the matrix form of the modal equations in s becomes

$$\{([M_s] + [\bar{Q}]) + \frac{GI_d}{J\ell^2 s^2} [K_s]\}\{\bar{q}(s)\} = 0 \tag{5-5}$$

(5-5) may be compared with the simple harmonic form (4-19). It is convenient to define a dimensionless Laplace transform variable

$$p \equiv s\ell\sqrt{\frac{J}{GI_d}} \tag{5-6}$$

which is related to the reduced Laplace transform variable through the dimensionless velocity by

$$\bar{s} = \frac{sb}{V} = \frac{p}{U} \tag{5-7}$$

The stability determinant thus takes the form

$$|p^2([M_s] + [\bar{Q}]) + [K_s]| = 0 \tag{5-8}$$

Zeros of this determinant will yield 3n exact roots for the aeroelastic modes in terms of the 3n assumed modes. These roots describe modal frequencies and stability at the speed U_e used to calculate the steady-state deflections which enter as coefficients in the stiffness matrix.

A computer program was developed to locate numerically the zeros of the determinant (5-8); the logic is outlined in Fig. 5-1. This format proved to be quite convenient for constructing root locus diagrams having either the speed U, the root angle of attack α, or the drag parameter C as the changing parameter. Any of the important aeroelastic modes, at any degree of stability, could be traced through the complex plane as long as the initial guess of $\bar{s}$ was sufficiently close to its particular root locus.

Since the determinant order is $3n$ and $n \geq 2$ is desirable to model adequately the physical system, numerical expansion of the determinant was not practical. A library subroutine, employed to calculate the complex determinant, proved to be the source of numerical difficulties. It was found that for $1 \leq n \leq 4$ and $\alpha = 0$ the Fig. (5-1) program gave accurate results when compared to parallel V-g method neutral stability computations, agreeing to at least seven digits in flutter speeds. For $n = 2$ and $\alpha \neq 0$, which gives rise to steady deflections due to lift, similar good agreement was encountered. But for $n \geq 3$ and $\alpha \neq 0$, the program converged on zeros which did not match the neutrally stable V-g predictions and were obviously incorrect from a physical standpoint. Subsequent investigation revealed that the numerical difficulties originated in the library subroutine.

When $\alpha = 0$ the fore-and-aft bending degree of freedom is dynamically uncoupled, and the order of the determinant which was actually computed by the library subroutine was reduced to $2n$. Thus, for $n = 3$ and $\alpha = 0$, the actual computed determinant was of order 6, whereas for $n = 3$ and $\alpha \neq 0$ the order was 9. For the latter case the actual magnitude of computed determinants was often $O(10^{16})$, while for $\alpha = 0$ the $n = 3$ determinants $O(10^{10})$. For $n = 2$

and $\alpha = 0$ determinants again were $O(10^{10})$. The magnitude of the computed determinant thus appears to be related to the numerical difficulties. Since $n = 2$ results are judged to model the problem adequately and never encountered numerical problems, correction of the above difficulties was not pursued.

As a result, all root loci shown herein for steady lifting conditions involve $n = 2$. As will be discussed, however, this restriction does not compromise the modeling of the physical system nor prevent qualitative understanding of its behavior. Furthermore, numerical results always agree reasonably well when compared with V-g computations for $n = 3$, $\alpha \neq 0$.

The algorithm used to estimate the zeros of the determinant in the $\bar{s}$ plane, using an initial guess $\bar{s}_o$, is illustrated graphically in Fig. 5-2. The complex determinant is first calculated at $\bar{s}_o$ and at the two related points $\bar{s}_o + .001$ and $\bar{s}_o + i.001$. Points A and C are then determined, at which linear extrapolation in the two orthogonal directions predicts that the real part of the determinant will vanish. Similarly points B and D are predicted, for which the imaginary part vanishes by extrapolation. A new guess for the root $\bar{s}_1$ is then determined as the intersection point of dashed lines in the figure. The process is repeated until satisfactory convergence is realized. This simple scheme worked quite well and never failed to converge on a root, usually within four or five iterations. The convergence criterion used was generally $||\bar{s}_1| - |\bar{s}_o|| \leq 10^{-5}$. Typical performance of the algorithm is documented in Table 5.1.

C. Mode Shapes for Aeroelastic Modes

The mode shapes associated with roots determined for arbitrary motion by the determinant iteration method were conveniently calculated with the same linear eigenvalue routine applied in solving the simple harmonic stability problem. For a root computed by iteration, the nonrational aerodynamic terms containing $C(\bar{s})$ in the matrix $\bar{Q}$ can be immediately evaluated. Thus one is led to a conventional matrix eigenvalue problem, which obtains the same root as one of its eigenvalues and also provides its eigenvector. This approach worked well and, as a bonus, verified the accuracy of the roots computed by the determinant iteration scheme.

Since numerical difficulties were encountered with the determinant evaluation routine for $n = 3$ and $\alpha \neq 0$, this eigenvalue approach of rechecking its results for $n = 2$, $\alpha \neq 0$ (and for all n with $\alpha = 0$) is valuable. It offers the only means of verifying computed roots lying off of the $i\omega$ axis. Correlation to at least six significant digits was always observed. Moreover, the accuracy of the $n = 2$, $\alpha \neq 0$ determinant iteration solutions has been checked for a few representative cases by letting $n = 3$ in the eigenvalue routine, with the known $n = 2$ root as a first guess to evaluate the aerodynamic loads, and iterating until the true $n = 3$ root is obtained. Two cases for which this was done, together with their eigenvectors, are shown in Table 5.1, where $n = 4$ roots are also given. The $n = 2$ results obtainable by the determinant iteration routine are thus seen to be acceptably accurate even for the higher frequency mode.

D. Inclusion of Unsteady Chordwise Loads Due to Leading Edge Suction

Since motion of the wing in fore-and-aft bending is permitted, unsteady chordwise loads can participate in the dynamic stability problem. Unsteady two-dimensional incompressible airloads given in Eqs. (4-18) and in (5-3) are strictly based upon the assumption that the instantaneous resultant unsteady lift on any airfoil section along the span is always perpendicular to the direction of the free stream velocity. Two-dimensional incompressible potential flow theory, however, does predict an unsteady leading edge suction force which arises from the inverse square root singularity of the vorticity distribution along the airfoil chord at its leading edge. This effect will be included into the analysis within the framework of the linearized unsteady perturbation theory used to determine stability. The effect of the unsteady propulsive force on stability can then easily be isolated by comparison of roots computed for the (4-18) airloads directly with roots determined with the airloads derived in this section.

The existence of a leading-edge suction force due to the leading-edge singularity was determined by Von Karman and Sears (Ref. 12). Greenberg (Ref. 13) in developing the propulsive force on an airfoil in an oscillating stream, states that a propulsive force acting on the airfoil in the upstream direction,

$$(5\text{-}9) \qquad F_S = \Pi \rho C_F^2$$

arises from the unsteady vorticity distribution which behaves at the leading edge as

$$(5\text{-}10) \qquad \gamma\Big|_{\tilde{x} \to -1} = \frac{2C_F}{\sqrt{b}\ \sqrt{\tilde{x}+1}}\Bigg|_{\tilde{x} \to -1}$$

In this application the coefficient C_F will contain contributions from the superposed vorticity distributions due to the steady and the unsteady lifting flow fields. Therefore C_F will be a sum of steady and unsteady parts, and C_F^2 will involve a steady portion, a linear unsteady cross multiplication part, and a nonlinear quadratic unsteady term. In the context of the linearized unsteady perturbation approach to stability analysis, only the cross multiplication term will enter the dynamic equations. To include consistently the nonlinear unsteady propulsive force effect on stability, the nonlinear structural coupling terms discarded during linearization would have to be reintroduced.

As a consequence of linearization, the unsteady propulsive force can be included only when both steady and unsteady vorticity distributions are present. Thus the case of zero steady lift will have no contribution due to this effect to the state of stability. The effect will become increasingly pronounced as the steady lift is increased.

The vorticity singularity strength C_F in (5-9) was given by Garrick (Ref. 14) for an airfoil oscillating in a uniform stream as

$$C_F = \sqrt{2b}\ \{[\dot{h} + V\alpha + b\dot{\alpha}(\tfrac{1}{2}-a)]C(k) - \tfrac{1}{2}b\dot{\alpha}\} \tag{5-11}$$

with h positive downward. Converting to present notation, introducing the generalized Theodorsen function, and introducing superposition of steady and unsteady deflections gives

$$\alpha \rightarrow \alpha + \phi_o + \phi_1$$

$$h \rightarrow - w_o - w_1$$

$$C_F = \sqrt{2b}\ \{(\alpha+\phi_o)V + [-\dot{w}_1 + \phi_1 V + b(\tfrac{1}{2}-a)\dot{\phi}_1]C(\bar{s}) - \tfrac{1}{2}b\dot{\phi}_1\} \tag{5-12}$$

The propulsive force F_s , using (5-9), is

$$\begin{aligned} F_s = 2\Pi\rho b\{(\alpha+\phi_o)^2\ V^2 &+ 2V(\alpha+\phi_o)[(-\dot{w}_1 + \phi_1 V \\ &+ b(\tfrac{1}{2}-a)\dot{\phi}_1)C(\bar{s}) - \tfrac{1}{2}b\dot{\phi}_1] + [(-\dot{w}_1 - \phi_1 V + b(\tfrac{1}{2}-a)\dot{\phi}_1)C(\bar{s}) \\ &- \tfrac{1}{2}b\dot{\phi}_1]^2 \end{aligned} \tag{5-13}$$

The last squared term is the nonlinear time-dependent contribution and is neglected hereafter. The first squared term is the propulsive force on a flat-plate airfoil at incidence in steady flow. The resultant steady aerodynamic force should act at right angles to the free stream velocity in potential flow, and this steady propulsive force can be interpreted physically as the component which tilts the resultant lift vector, obtained by summing the pressure distribution at right angles to the chord, forward to become normal to the airstream.

The propulsive force can thus be seen to correct for the chordwise component of the lift which is computed normal to the airfoil chord. The assumption incorporated into (4-18) that the unsteady circulatory lift acts at right angles to the airstream must be discarded and the force assumed rather to be normal to the chord of the airfoil in its steady-state orientation. The assumed direction of forces is shown in Fig. 5-3.

In the structure axis system, the loads are

$$(5\text{-}14)\qquad \begin{aligned} F_{x_1} &= - F_s \cos\phi_o + L_a \sin\phi_o \\ F_{z_1} &= L_a \cos\phi_o + F_s \sin\phi_o \end{aligned}$$

The following assumptions are made

$$\cos\phi_o \approx 1$$

$$\sin\phi_o \approx \phi_o$$

$$F_s \sin\phi_o << L_a$$

so that

$$F_{z_1} \cong L_a$$

$$F_{x_1} \cong - F_s + L_a \phi_o$$

The lift for arbitrary motion in time is given by Ref. (5) as

$$(5\text{-}16)\qquad L_a = 2\Pi\rho bV[- \dot{w}_1 \, C(\bar{s}) + \phi_1 \, V \, C(\bar{s}) + b(\tfrac{1}{2}-a)\phi_1 \, C(\bar{s})] + \Pi\rho b^2[-\ddot{w}_1 + V\dot{\phi}_1 - ba\ddot{\phi}_1]$$

Combining (5-16) and the linear unsteady part of (5-13) into the second of (5-15) yields

$$(5\text{-}17)\qquad F_{x_1} = -4\Pi\rho Vb(\alpha + \tfrac{1}{2}\phi_o)[- \dot{w}_1 \, C(\bar{s}) + \phi_1 \, V \, C(\bar{s}) + ((\tfrac{1}{2}-a)C(\bar{s}) - \tfrac{1}{2})b\dot{\phi}_1] + \Pi\rho b^2 V\phi_o\dot{\phi}_1 + \Pi\rho b^2\phi_o[-\ddot{w}_1 + V\dot{\phi}_1 - ba\ddot{\phi}_1]$$

The loads can now be arranged into the unit generalized force format of (5-3) by Laplace transformation in time, substitution of the assumed modes as in (5-2), and formation of the generalized forces from relations such as (4-11). After this work, which is straightforward, the elements of the aerodynamic matrix which incorporate the linearized unsteady propulsive force are

$$(5\text{-}18)\qquad \begin{aligned} \bar{Q}_{j+n,i} &= 2(1-\bar{L}_w)\alpha\,\delta_{ij} \\ &\quad + (2-\bar{L}_w)\sum_{\nu=m+1}^{n} H_{\nu ij}\, q^{\circ}_{\phi_\nu} \qquad\qquad (1 \le i \le n) \\ &\qquad\qquad\qquad\qquad\qquad\qquad\qquad\quad (1 \le j \le n) \\ \bar{Q}_{j+n,i+2n} &= 2[\bar{L}_\phi - \tfrac{1}{2} - \frac{2}{\bar{s}} + A(1-\bar{L}_w)]I_{ji}\,\alpha \\ &\quad + [\bar{L}_\phi - 1 - \frac{4}{\bar{s}} + (2-\bar{L}_w)A] \sum_{\nu=m+1}^{n} Y_{j\nu i}\, q^{\circ}_{\phi_\nu} \end{aligned}$$

where the new modal integrals appear,

$$(5\text{-}19)\qquad Y_{i\nu j} = \int_0^1 f_{w_1}\, f_{\phi_\nu}\, f_{\phi_j}\, d\tilde{y}$$

The remainder of the terms of the aerodynamic matrix remain the same as in (5-3).

Prior to actual calculations a further approximation is made. The terms in (5-18) which depend on sums of $q^{\circ}_{\phi_\nu}$ are neglected, eliminating the need to compute the $Y_{i\nu j}$. This is equivalent to assuming that the lift L_a in Fig. 5-3 is aligned with the z-axis and that ϕ_o is neglected relative to α in the linear term of (5-13). Strictly, this simplification will alter the results somewhat, but it is not expected to change the overall effect of the propulsive force on stability and does simplify computations. The first order trend of the effect of 100% leading edge suction on stability is the main point of interest and should not be affected.

The changes made to the aerodynamic matrix are therefore substitution of the terms

$$(5\text{-}20) \qquad \bar{\ddot{Q}}_{j+n,i} = \begin{cases} 2(1-\bar{L}_w)\alpha & (i=j) \\ 0 & (i\neq j) \end{cases} \qquad (1 \leq j \leq n)$$

$$\bar{Q}_{j+n,i+2n} = 2[\bar{L}_\phi - \tfrac{1}{2} - \frac{2}{s} + A(1-\bar{L}_w)]I_{ji}\,\alpha \qquad (1 \leq i \leq n)$$

for their counterparts in (5-3).

The program described in Section B includes the option of using either of these unsteady aerodynamic force systems, and a comparison of their relative effect on stability is made in the next chapter. Except for the $-\frac{2}{s}$ term in the second of (5-20), incidentally, the newer system simply involves doubling the magnitude of the terms in (5-3) that are replaced.

$M = 40$, $P = 0.005$, $i_{\alpha} = 0.25$, $A = 0.1$, $S = 0.1$, $\tau = 25$, $\alpha = 0$, $n = 3$,
$C = 0$, $U = 6.5$

ITERATION	$\bar{s}$	DETERMINANT AT $\bar{s}$
0	$-0.072968 + i0.0582071$	$0.326\text{x}10^{9} + i0.1266\text{x}10^{10}$
1	$-0.078290 + i0.067052$	$-0.259\text{x}10^{9} + i0.504\text{x}10^{8}$
2	$-0.079541 + i0.065839$	$0.106\text{x}10^{8} + i0.504\text{x}10^{7}$
3	$-0.079527 + i0.065910$	$0.106\text{x}10^{6} - i0.178\text{x}10^{6}$
4	$-0.079526 + i0.065910$	$-0.281\text{x}10^{4} + i0.499\text{x}10^{4}$

$M = 40$, $P = 0.02$, $i_{\alpha} = 0.25$, $A = 0.1$, $S = 0.1$, $\tau = 25$, $\alpha = 0.02$, $n = 2$,
$C = 0$, $U = 7$

ITERATION	$\bar{s}$	DETERMINANT AT $\bar{s}$
0	$-0.0055179 + i0.119612$	$0.261\text{x}10^{11} - i0.253\text{x}10^{10}$
1	$-0.0014167 + i0.1074866$	$0.125\text{x}10^{10} + i0.428\text{x}10^{10}$
2	$0.0005501 + i0.1085285$	$-0.459\text{x}10^{7} + i0.135\text{x}10^{9}$
3	$0.0005027 + i0.1084861$	$-0.129\text{x}10^{6} + i0.178\text{x}10^{6}$
4	$0.0005026 + i0.1084861$	

TABLE 5.1 Performance of the Determinant Iteration Algorithm for Two Cases, One Nonlifting With $n = 3$ and One at Steady Lift With $\alpha = 0.02$, $n = 2$

STEADY-STATE DEFLECTIONS:

	n = 2	n = 3	n = 4
$q^\circ_{w_1}/b$	1.97768	2.01496	2.019088
$q^\circ_{w_2}/b$	0.022566	0.023221	0.023274
$q^\circ_{w_3}/b$	-	0.001453	0.001464
$q^\circ_{w_4}/b$	-	-	0.000271
$q^\circ_{v_1}/b$	0.003170	0.003534	0.003594
$q^\circ_{v_2}/b$	-0.00363	-0.000403	-0.000407
$q^\circ_{v_3}/b$	-	-0.000044	-0.000046
$q^\circ_{v_4}/b$	-	-	-0.000007
$q^\circ_{\phi_1}$	0.0068192	0.0072034	0.0072456
$q^\circ_{\phi_2}$	-0.0001112	0.0000129	0.0000303
$q^\circ_{\phi_3}$	-	-0.0000322	-0.0000130
$q^\circ_{\phi_4}$	-	-	-0.0000103

$M = 40$
$P = 0.005$
$i_\alpha = 0.25$
$A = 0.1$
$S = 0.1$
$\tau = 60$

$\alpha = 0.01$ RAD.
$C = 0$
$U = 7$

ROOT FOUND BY DETERMINANT
ITERATION WITH $n = 2$: $p = 0.03579 + i0.55875$

RESULTS OF LINEAR EIGENVALUE ANALYSIS FOR $n = 2, 3, 4$:

	n = 2: p = .035795 + i.55875		n = 3: p = .036828 + i.52903		n = 4: p = .036486 + i.52309	
	AMPLITUDE	PHASE	AMPLITUDE	PHASE	AMPLITUDE	PHASE
$\bar{q}_{w_1}/b$	4.2245	215.40°	4.6573	217.75°	4.7497	218.17°
$\bar{q}_{w_2}/b$	1.2064	-40.51°	1.1808	-37.53°	1.1815	-37.07°
$\bar{q}_{w_3}/b$	-		0.03432	-18.25°	0.03544	-17.97°
$\bar{q}_{w_4}/b$	-		-		0.00530	-12.46°
$\bar{q}_{v_1}/b$	0.083839	- 7.71°	0.87304	- 8.79°	0.88887	- 9.12°
$\bar{q}_{v_2}/b$	0.05128	181.23°	0.05146	181.49°	0.050487	181.93°
$\bar{q}_{v_3}/b$	-		0.009128	169.96	0.009314	169.12°
$\bar{q}_{v_4}/b$	-		-		0.002135	165.92°
$\bar{q}_{\phi_1}$	1.0	0.0°	1.0	0.0°	1.0	0.0°
$\bar{q}_{\phi_2}$	0.05780	-33.85°	0.07738	-30.30°	0.08213	-29.93°
$\bar{q}_{\phi_3}$	-		0.02511	-19.79°	0.02969	-18.96°
$\bar{q}_{\phi_4}$	-		-		0.00912	-22.80°

TABLE 5.2 Modal Convergence for Convergent and Divergent Oscillatory Aeroelastic Modes (see Fig. 6-24(a))

ROOT FOUND BY DETERMINANT
ITERATION WITH $n = 2$: $p = -0.216505 + i1.632293$

RESULTS OF LINEAR EIGENVALUE ANALYSIS FOR $n = 2, 3, 4$

	$n = 2$: $p = -.2165053 + i1.6322931$		$n = 3$: $p = -.21485 + i1.59221$		$n = 4$: $p = -.21564 + i1.57794$	
	AMPLITUDE	PHASE	AMPLITUDE	PHASE	AMPLITUDE	PHASE
$\bar{q}_{w_1}/b$	0.02478	175.84°	0.02627	175.18°	0.025894	174.95°
$\bar{q}_{w_2}/b$	0.05039	181.31°	0.07554	178.03°	0.07883	177.63°
$\bar{q}_{w_3}/b$	-		0.02535	181.07°	0.02054	178.99°
$\bar{q}_{w_4}/b$	-		-		0.00047	159.19°
$\bar{q}_{v_1}/b$	0.14780	160.48°	0.14548	160.42°	0.14364	160.30°
$\bar{q}_{v_2}/b$	0.04973	181.88°	0.05680	181.47°	0.05937	181.34°
$\bar{q}_{v_3}/b$	-		0.000618	122.60°	0.000565	242.35°
$\bar{q}_{v_4}/b$	-		-		0.000081	- 6.87°
$\bar{q}_{\phi_1}$	1.0	0.0°	1.0	0.0°	1.0	0.0°
$\bar{q}_{\phi_2}$	0.20484	175.75°	0.18586	175.28°	0.18223	175.24°
$\bar{q}_{\phi_3}$	-		0.05215	176.65°	0.05252	176.50°
$\bar{q}_{\phi_4}$	-		-		0.01955	177.66°

TABLE 5.2 CONCLUDED

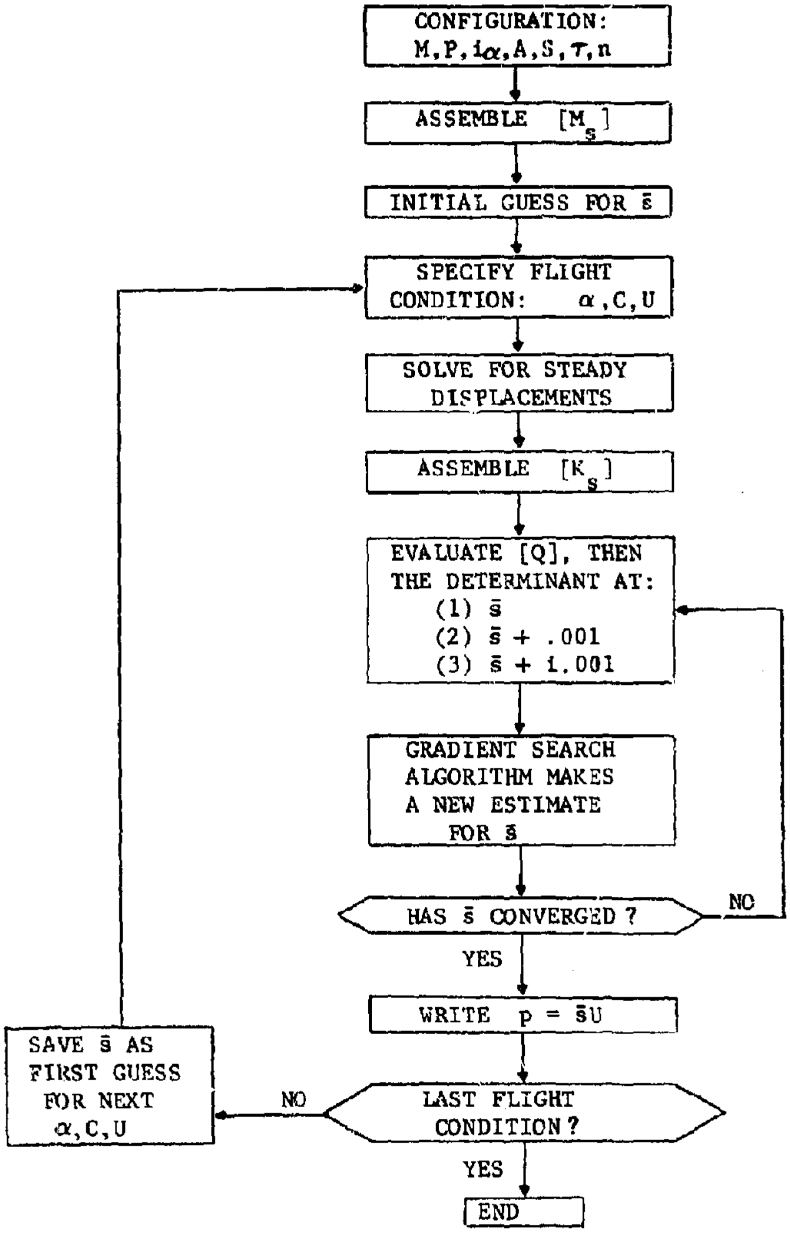

FIGURE 5-1 Flow Chart for Locating Zeros of (5-8)

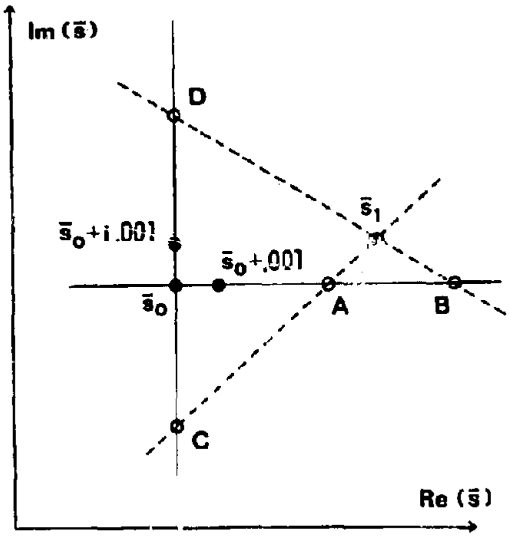

FIGURE 5-2 Gradient Search Algorithm

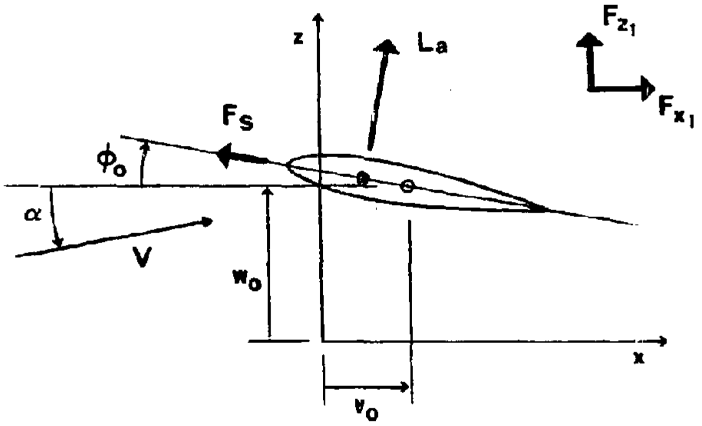

FIGURE 5-3 Resolution of Unsteady Airloads Including Leading Edge Suction into Components F_{x_1} , F_{z_1}

Chapter VI

AEROELASTIC MODES USING AIRLOADS FROM INCOMPRESSIBLE STRIP THEORY

A. The Effect of Steady Drag on Flutter of a Nonlifting Wing

Before considering steady-state deflections due to lift, a thorough understanding of the stability behavior of the cantilever wing at zero steady lift is needed. With w_o and ϕ_o at zero, the fore-and-aft bending degree of freedom is dynamically uncoupled from vertical bending and torsion motions, and the system analyzed in Ref. 1 results. In the zero lift case, then, solutions for stability involve $2n$ aeroelastic modes consisting of coupled motions in w_1 and ϕ_1 ; the remaining n modes represent uncoupled free vibration in each of the assumed modes in v_1 . As demonstrated in previous chapters, the flutter conditions obtained by this assumed mode analysis compare favorably with Ref. 1 results over all practical combinations of the parameters M , P , i_α , A , S , and C . Owing to this good agreement, the results and conclusions of Ref. 1 apply here as well, yet the assumed mode solution method still is useful in providing additional insight into the flutter behavior of the nonlifting wing.

The parameters M , i_α , A , and S offer no suprising effect, and most importantly here, the nature of their influence is not altered by the inclusion of drag. The Ref. 1 results indicate that an increase in the elastic axis - A.C. offset given by A is destablizing, an increase in the sectional C.G - elastic axis offset given by S is destabilizing, an increase in the radius of gyration parameter i_α is stabilizing, and that the flutter speed is approximately proportional to the square root of the mass ratio parameter M . Since Ref. 1

establishes that the influence of drag is not sensitive to these four parameters, more detailed study in this area is not considered here.

The most curious finding of Ref. 1 involves the effect of C in conjunction with the aspect-ratio parameter P , which is the product of the vertical bending-to-torsion stiffness ratio with the inverse square of the geometric aspect ratio. The effect of steady drag on flutter speed is stabilizing for smaller aspect ratios (larger P) but destabilizing for larger aspect ratio wings. The reversal of the effect of drag on flutter occurs near $P = 0.01$, and the behavior in this neighborhood, including flutter mode shapes, appears to be quite interesting. No conclusions regarding physical causes of this phenomenon were made in Ref. 1, however.

Figure 6-1 is a reproduction from Ref. 1, showing the effect of drag on flutter speed as a function of P for intermediate values of M , i_α , A , and S . Numbers in parentheses on the abscissa give the true aspect ratio for a typical value of the ratio $EI_x/GI_d = 1.6$. Clearly wings of practical interest include the region within which the effect of drag on flutter appears to be most interesting.

To help gain a better physical understanding of the behavior near $P = 0.01$, flutter solutions for this same example have been found via the simple harmonic method of Chapter IV, over the range $0.002 \leq P \leq 0.02$. Results appear in Fig. 6-2 that show flutter speeds and flutter mode shape amplitudes and phase relations as functions of P . Since a finite chordwise to vertical bending stiffness ratio τ must be specified, and the effect of drag on flutter depends on τ as in Fig. 4-15 the value $\tau = 50$ was used to allow adequately for the

$\tau \to \infty$ behavior inherent in the Ref. 1 formulation. Three assumed modes in each degree of freedom are used.

The flutter speeds in Fig. 6-2a closely match the Fig. 6-1 results. The flutter mode shapes include participation by the three generalized displacements q_{ϕ_1} , q_{w_1} , and q_{w_2} , with the remaining assumed modes contributing negligibly to the motions. In Fig. 6-2b the amplitude and phase of the two assumed bending modes at flutter are shown for unit magnitude and zero phase angle of the first assumed torsion mode.

It can be seen that for any C the sharp drop in flutter speed that comes with decreasing P is accompanied by a sudden change in the flutter mode shape. The amplitudes of the two bending modes merge, and the second bending mode undergoes a large phase shift. Further decrease in P gives a gradual separation of the assumed bending mode amplitudes with the fundamental mode again becoming dominant.

To help visualize the physical appearance of these flutter mode shapes, phasor diagrams of the spanwise distribution of bending displacements, for $C = 0.02$, are given in Fig. 6-3 for five values of P . Arrows depict the modal generalized displacements from Fig. 6-2, and the curves give the relative displacements along the span and their phase referenced to q_{ϕ_1} . For both $P = 0.02$ and $P = 0.002$ all stations are nearly in phase and the mode shape is dominated by the first assumed bending mode. But for the intermediate values of P , where the transition in phase of the second bending mode takes place, the displacements at different locations along the span can be over 90° out of phase.

The behavior of flutter modes in this range of P offers the greatest discrepancy found between the results reported in Ref. 1 and the assumed mode solution, suggested by Fig. 2-1. For $P < 0.04$ in Ref. 1, collocation at only five spanwise stations was used, and the mode shapes in bending and torsion were permitted to have spanwise phase differences. It was found, however, that these phase differences never exceeded a few degrees, in contrast to the results presented here. Possibly the use of only five spanwise collocation points did not allow enough freedom to represent the flutter mode shape transition found using assumed modes. In any case good agreement between flutter speeds and frequencies is still observed for the two methods.

Figure 6-2 seems to indicate that the second assumed bending mode plays a significant role in the reversal of the effect of drag on flutter near $p = .01$, which coincides with the natural frequency of this mode crossing the flutter frequency. Interaction of actual aeroelastic modes is masked by the limitations of the solution method, however, which only gives neutrally stable solutions. In order to better understand these results, the Laplace transform approach of Chapter V is used to allow tracing all of the aeroelastic modes in the complex plane for speeds from zero into the supercritical range.

Figures 6-4(a) - 6-4(h) give root locus diagrams for increasing speed at eight representative values of aspect-ratio parameter P. Each locus originates for $U = 0$ at one of the normal modes of free vibration of the structure, which are easily calculated in terms of the uncoupled assumed bending and torsion modes. Zero drag branches are shown in all of the figures, with loci corresponding to $C \neq 0$ added where their behavior differs significantly from that for zero drag.

The first two figures represent stubby low-aspect-ratio wings, for which the strip-theory aerodynamic assumption is certainly inadequate. Due to the manner in which the Laplace variable p is nondimensionalized, the predominantly first torsion normal mode of free vibration remains essentially fixed on the $i\omega$ axis near 1.6 on all of these diagrams. The predominantly bending normal modes move down the $i\omega$ axis as P decreases, since their natural frequencies decrease relative to the torsion frequencies. In Fig. 6-4(a) the bending branch of the aeroelastic modes leads to flutter, whereas in Fig. 6-4(b) the torsion branch eventually becomes unstable. The normal mode having the third lowest natural frequency, predominantly the second bending assumed mode, occurs well up the $i\omega$ axis and off these two diagrams and has negligible influence on flutter. These low-aspect-ratio cases show entirely two-degree-of-freedom behavior and closely resemble the root locus given by Edwards (Ref. 11) for a typical section in plunge-and-pitch motion in incompressible flow.

Figures 6-4(c) and 6-4(d) represent values of P just above the condition where the effect of drag on flutter reverses. Although the flutter phenomenon is still similar to that for larger P, the third normal mode frequency has now decreased sufficiently to appear on the diagram, and it produces a branch which does not lead to flutter for all values of drag.

According to the flutter curve of Fig. 6-2, for $P = 0.01$ the cases $C = 0.02$ and $C = 0.04$ result in decrease of flutter speed from the zero-drag condition whereas for $C = 0.01$ it is still increased. Figure 6-4(e) gives the $P = 0.01$ root locus, which reveals that the aeroelastic mode emanating from the predominantly second bending normal mode now plays an important role. The next illustration, Fig. 6-4(f) with $P = 0.007$, gives this branch as becoming unstable for all C. In the final two of these illustrations, with $P = 0.005$ and 0.002, the flutter phenomenon appears to be returning to the type of behavior seen for small-aspect-ratio wings, with the second bending contribution assuming a lesser influence. In Fig. 6-4(h) a fourth normal mode, the third bending mode, has made its appearance but does not noticeably influence flutter.

The nature of the aeroelastic modes on the various branches of the root locus diagrams can be clarified by looking at their mode shapes. In Fig. 6-5, phasor diagrams are used to show $C = 0$ mode shapes for each branch of the .005 locus (Fig. 6-4(g)). At selected speeds both subcritical and supercritical, the generalized displacements are shown with the phase angle of q_{ϕ_1} taken as zero.

The dependence of drag's effect on flutter upon P is also given for a second configuration having a smaller mass ratio $M = 9.4$, more representative of light aircraft and sailplanes. Shown in Fig. 6-6, the basic behavior resembles the first configuration, with certain differences. For example, the reduction in flutter speed by drag for small P is moderate relative to that for the larger mass ratio; this is also seen in the tabulated Ref. 1 results. Also the transition as P reduces through the 0.01 region is much less severe. Again the reversal coincides with the crossing of the second assumed mode frequency below the flutter frequency.

In conclusion, assumed mode results attribute the reversal of the effect of drag on flutter speed to the interaction of the structure's second natural bending mode with the basic cantilever wing flutter mechanism involving the first bending and first torsion modes. The exact reason that drag increases the flutter speed for P above this apparent "resonance" condition and decreases it for smaller P is not evident in these results, and like many aeroelastic phenomena may not have a simple physical explanation. It does appear, however, that the drag force enhances the coupling of the second bending mode into the flutter behavior and thereby magnifies its already present effect on flutter speed.

Since the Ref. 1 tabulated results give a fairly complete picture of flutter of the nonlifting case in the presence of steady drag and are not disputed by current results, further work herein is directed towards the more general case involving steady deformations due to lift.

B. Effect of Steady Deformations Due to Lift

The good agreement in prediction of dynamic stability between the current analysis and the Ref. 1 collocation method for nonlifting wings with a steady drag force included furnishes confidence that the modal scheme will be successful for steady lifting conditions. The effect of steady deformations due to lift is incorporated into the dynamic stability analysis by the same means as the steady drag effect-- namely through coefficients of the stiffness matrix determined in a separate nonlinear solution for the steady-state deflections. Thus, the agreement indicates that the scheme allowing small time dependent perturbations about a static deflection is working properly. When steady lifting deflections are introduced through a nonzero root angle of attack α , the fore-and-aft bending is no longer dynamically uncoupled. Coupling in both elastic terms (the stiffness matrix coefficients containing w_o and ϕ_o) and aerodynamic coupling terms (arising from unsteady aerodynamic force components in the x-direction) now appears in the fore-and-aft bending dynamic equations. The 3n aeroelastic modes will consist of coupled motions in w_1, ϕ_1, and v_1.

Three basic wing configurations are selected to illustrate the effects introduced by steady-state lifting deformations. Parameters M, i_α, A, and S are taken the same as in Fig. 6-1, and aspect ratio parameter P is assigned three different values in order to consider wings of large, moderate, and low aspect ratio. For large aspect ratio, $P = 0.005$ is chosen to provide a case for which steady drag decreases the flutter speed (Fig. 6-1). A moderate aspect ratio example with $P = 0.02$ having an increase in flutter speed due to steady drag, and a low-aspect-ratio case, $P = 0.1$, are also included. For the typical bending-to-torsion stiffness ratio

$$\frac{EI_x}{GI_d} = 1.6$$

these examples correspond to actual retangular planforms having aspect ratios of 17.89, 8.94, and 4 respectively. The bending stiffness ratio τ now becomes important, and is given the nominal value 25. The essential features of the flutter behavior encountered when steady deformations enter can be illustrated by using these basic configurations as examples.

The flutter stability boundary for the moderate-aspect-ratio example is shown in Fig. 6-7 for $C = 0$ and $C = 0.01$; the steady bending displacement w_o of the wingtip is the measure of steady lift. An alternative would be to show flutter speeds as a function of α , but this is a poor means for comparing curves having different steady drag and gives no information about the elastic steady deformations. A better way to indicate the steady flight condition would be the total lift force on the deformed wing nondimensionalized, for example as $\frac{L\ell^2}{4EI_x b}$. As can be seen in Fig. 6-8 this dimensionless total lift parameter, which depends on the steady twist $\phi_o(y)$, varies for constant wingtip deflection as C changes for points along the stability boundary of Fig. 6-7. This is because the drag force alters the relative ϕ_o and w_o distributions for the same total steady lift. But since this effect is small, and w_o gives the best indication of the magnitude of the steady equilibrium deflections, this deflection is used to indicate the steady lift condition. In Fig. 6-7, the semispan of the wing is about 9 semichords, and steady deformations well exceeding the limits of the moderate displacement beam theory are therefore shown. This demonstrates that flutter solutions can be found for arbitrarily large steady displacements and that it is a matter of practical engineering judgment to recognize when the assumptions made in the derivation of the equations have been violated.

For $C = 0$ Fig. 6-7 indicates that the flutter speed reduces continuously with increasing steady lift until a maximum reduction of about 13% is achieved at an excessively large deflection of 4 semichords. The frequency at flutter reduces monotonically with w_o ; this effect is generally observed for all wing configurations.

With steady drag included, the situation for the deformed wing is not as simple as it is for the $\alpha = 0$ case. As exhibited by the nonlinear steady deformations shown in Chapter IV, drag can greatly alter the deformation state associated with a given speed and root angle of attack. Even more importantly, drag significantly reduces divergence speeds, possibly to less than the flutter speed. This is revealed in the stability analysis when the nonlinear steady solution blows up before dynamic instabilities appear.

In Fig. 6-7 divergence speeds found by the linear VT determinant (2-29) are also indicated for several values of C. Results of a dynamic stability analysis with $C = 0.01$ also appear. The flutter speed for $\alpha = 0$ and $C = 0.01$ is the single point on the ordinate and is greater than the divergence speed for the same drag. During the search for a neutrally stable oscillating condition for the very small angle of attack $\alpha = 0.001$ rad. and $C = 0.01$, the nonlinear steady displacement solution was sensitive to U in the neighborhood of flutter owing to the proximity of divergence. For specified larger angles of attack, the $C = 0.01$ flutter boundary is found without difficulty. The slight increase in flutter speed due to drag observed for $\alpha = 0$ appears to be preserved in the presence of steady deformations. For decreasing α, however, a point is reached as $\alpha \to 0$ at which the steady displacements are still nonzero at flutter. For smaller steady deflections divergence becomes the instability encountered for increasing speed. For $C = 0.02$, divergence was observed for all lifting conditions with no flutter points found.

As steady deformation increases from zero, the flutter mode shape undergoes a smooth transition, originating with the same zero lift mode shapes shown in Fig. 6-2 for $P = .02$. For zero drag, the amplitudes of modal generalized displacements which contribute significantly to the flutter mode are shown in Fig. 6-9, normalized to the first torsion mode amplitude. Their phase angles relative to zero phase for q_{ϕ_1} appear in Fig. 6-10. Participation by the first chordwise bending mode increases steadily with increasing w_o , reflecting the increased strength of the elastic bending-torsion coupling. Vertical bending motions are increasingly dominated by the first assumed bending mode, and the contribution of the second torsion assumed mode increases significantly.

The flutter mode shapes at one steady lifting condition are presented in Fig. 6-11 in a form giving a clearer physical description of the motion. Above the phasor diagram (which contains the information given in Fig. 6-9 and 6-10) is a sketch of the cyclic path traced in the x-z plane by wing sections at the wingtip and at midsemispan. Points where the first torsion assumed mode is at phase angles of 0° , 90° , 180° , and 270° are located. These diagrams emphasize the three-degree-of-freedom nature which flutter can have when steady deflections are present.

The low-aspect-ratio example ($P = 0.1$ and $\mathcal{R} \simeq 4$) shows only minor effects upon its flutter characteristics due to steady deformations, as might be anticipated. As given in Fig. 6-12, even for the extreme condition $\alpha = .12$ rad. yielding a 1.7 semichord tip deflection at flutter, there is only a 0.62% reduction in flutter speed due to lift. The flutter mode shapes (Fig. 6-12) undergo little change, with a slight contribution by q_{v_1} the only new feature. Owing to these unremarkable results, further work centers on the moderate-and-high-aspect-ratio examples, where the effects of steady deformations and chordwise forces are significant and interesting.

For the high-aspect-ratio example with $P = 0.005$, the flutter behavior is quite different when steady deformations enter. Figure 6-13 shows the dependence of flutter speed upon the steady wingtip bending deflection for two drag cases, $C = 0$ and 0.01. The minimum flutter speed in this case is over 20% below its undeflected counterpart, but quite interestingly as $w_o \to 0$ the stability boundaries do not converge continuously to their respective zero lift flutter speeds but approach lower points on the ordinate.

The flutter mode shapes, Figs. 6-14, 6-15, explain this new behavior. As the steady deflection becomes small, the flutter mode becomes dominated by the first chordwise bending mode, and as $\alpha \to 0$ this type of instability approaches simple free uncoupled vibration in this degree of freedom. For moderately large steady deflection the flutter mode shape closely resembles that for the medium-aspect-ratio wing, Figs. 6-9 and 6-10.

Flutter mode shapes for two steady-lift conditions are diagrammed in Fig. 6-16 using the same technique as in Fig. 6-11. Relative to the $P = 0.02$ example, this wing shows a greater amount of participation in fore-and-aft bending, and a greater contribution from the second vertical bending mode. This mode's contribution causes the noticeable difference in the eccentricities of the elliptical paths traced in the x-z plane by different wing stations. The phase relationship among q_{ϕ_1}, q_{w_1}, and q_{v_1} appears similar in this and other examples.

The most noticeable effect of steady drag again is its reduction of the divergence speed. Figure 6-17 gives divergence speeds found by the linear determinant (2-29) together with zero lift flutter speeds for increasing steady drag for the moderate- and high-aspect-ratio cases. Divergence is clearly more important relative to flutter for the larger aspect ratio.

The effect of steady drag on the dynamic behavior (Fig. 6-13) appears to cause only slight adjustments to the zero drag flutter results for any steady deflection. The flutter mode shape amplitudes and phase angles show but small changes for the rather large drag $C = 0.01$. The flutter speeds fall just below the $C = 0.01$ divergence speed.

The stability boundaries in Fig. 6-13 do not allow for structional damping and give no feel for the degree of stability at speeds near flutter. To gain a better understanding of the type of instability that has been found with steady deformations, and also define the overall aeroelastic behavior, the Laplace transform approach detailed in Chapter V is applied to the large- and moderate-aspect-ratio examples. The true aeroelastic modes are then conveniently traced in the complex plane at any flight conditions using root locus diagrams.

Before showing the root-locus results, it is interesting to see how stability is suggested by the simple harmonic method with nonzero structural damping assumed. The $C = 0$ stability boundary of Fig. 6-13 is reproduced in Fig. 6-18, to which stability boundaries for three values of structural damping are added. The sizeable increase in flutter speed with g hints that the instability is not of severe nature, and as w_0 becomes small the predominantly fore-and-aft bending motion is obviously very lightly damped. For small deflections with structural damping included, there is a change in the flutter mode back to the basic bending-torsion type encountered for zero steady lift. In spite of structural damping's stabilizing influence, there still exists the possibility of a reduction in flutter speed at high load factor flight conditions.

Root locus diagrams depicting the dynamic stability of the moderate- and large-aspect-ratio-wing examples with steady deflections appear in Figs. 6-19 and 6-20 respectively. Dashed lines in these figures show the zero steady lift loci of roots for increasing speed, which are the same as the zero drag diagrams of Figs. 6-4(c) and 6-4(g). Solid lines trace the elastic modes for selected constant speeds as the angle of attack α is varied, and originate for $\alpha = 0$ at nonlifting roots corresponding to these speeds.

In addition to the normal modes of free vibration involving vertical bending and torsion, previously seen on the $i\omega$ axis in Figs. 6-4, the first fore-and-aft bending mode natural frequency now also must be included. This normal mode remains an uncoupled, undamped aeroelastic mode at all speeds at $\alpha = 0$, but a family of constant speed branches emanates from this root with steady lift included. Since its natural frequency ω_{v_1} is a factor $\sqrt{\tau}$ larger than the first vertical bending assumed mode frequency ω_{w_1}, this new normal mode lies on the $i\omega$ axis approximately at a multiple $\sqrt{\tau}$ of the lowest normal mode frequency. This falls above the zero-lift flutter frequency for the moderate aspect ratio wing, but less than it in the high-aspect-ratio example.

A general feature of Fig. 6-19 and 6-20 is that as steady lift increases from zero, one group of constant-speed branches tends to stabilize and rapidly increase in frequency, whereas another lower frequency family of root paths reduces in stability and decreases in frequency. This latter group is responsible for the stability boundaries of Figs. 6-7 and 6-13. In the high-aspect-ratio example, they originate from the lowest chordwise bending normal mode, but for the moderate-aspect-ratio wing they originate on the zero-lift torsion branch of the root locus. The constant-speed branches which originate on the first and second vertical bending zero lift paths, for both examples, do not show much sensitivity to steady deflections.

To illustrate more clearly the role played by the chordwise bending upon stability, the large-aspect-ratio example is modified by increasing the bending-stiffness ratio τ from 25 to 60. This raises the dimensionless natural frequency of the first chordwise bending mode from 0.6216 to 0.9629, which is greater than the zero lift bending-torsion flutter frequency of 0.8921. The stability boundary calculated for this modified example appears in Fig. 6-21 and the associated flutter modes are presented in Figs. 6-22 and 6-23. The root locus obtained via the Laplace transform method appears in Fig. 6-24(a) and the true stability of constant-speed branches yielding instability is better depicted in 6-24(b) using the damping ratio ζ .

The discontinuity in the stability boundary is only a consequence of the solution procedure of Chapter IV and covers a region where solutions that do exist could not be determined. It is due to an interaction of the predominantly second bending, stable aeroelastic mode with the roots that yield instability. The simple harmonic solution method involves fixing the angle of attack α and searching for the neutrally stable lifting condition whose speed matches the calculated flutter speed. In Fig. 6-21, the gap in the curve falls between points found for $\alpha = .0095$ and $.01$ rad.

For all points on the left segment of the stability boundary, the simple harmonic solution yielded an additional highly damped eigenvalue whose frequency was slightly below the flutter frequency. On the right portion its frequency was above the flutter frequency. From the root-locus diagram (Fig. 6-24(a)) this highly damped eigenvalue can be identified as the predominantly second vertical bending aeroelastic mode, and the discontinuous behavior in Fig. 6-21 coincides with the crossing of frequencies as the downward moving constant speed loci associated with flutter pass the stable second bending aeroelastic mode frequency. By correlation with the section VI-A discussion of the effect of P and C on flutter, the general effect of the second bending mode appears to be destabilizing when its frequency is just below that of flutter, and stabilizing when its frequency is just above.

The flutter mode shapes (Fig. 6-22, 6-23) reflect an interesting transition as flutter frequency drops below the second bending aeroelastic mode frequency for increasing w_o . To the left of the discontinuity the mode shapes resemble the zero-lift large-aspect-ratio flutter behavior, to which they converge as $\alpha \to 0$. For larger w_o , though, the modes closely resemble flutter mode shapes for the $\tau = 25$ case (Figs. 6-14, 6-15) which in turn resemble mode shapes for the moderate-aspect-ratio example. This similarity is most evident in q_{w_2} and q_{ϕ_2} .

In Fig. 6-25 the flutter mode shapes are diagrammed for two lifting conditions to assist physical visualization of the motion. The larger steady deflection illustration is similar to those given in Fig. 6-16. But the smaller steady deformation mode shape, with its large contribution by the second assumed bending mode, has the wingtip rotating in a clockwise direction about its elliptical path for a counterclockwise motion at midsemispan. In spite of the relatively small steady deflection (a deflection of 1.226 semichords at the wingtip for a semispan of roughly 19 semichords) the motion is quite three-dimensional, indicating a significant inertial contribution to flutter in fore-and-aft bending.

The three root-locus diagrams (Figs. 6-19, 6-20, and 6-24) exhibit the basic effect which steady deflections have upon dynamic stability when incompressible strip-theory airloads are used. The basic zero-steady-lift bending-torsion flutter root together with the first fore-and-aft assumed mode produce a pair of constant-speed branches, one of which rapidly stabilizes and increases in frequency while the other decreases in frequency and becomes unstable for speeds below the $\alpha = 0$ flutter speed. These latter aeroelastic modes are lightly damped, and generally the onset of flutter at constant speed for increasing steady deflections would not be as severe as for that encountered with increasing speed. The reduction of flutter speed with steady deformations has been noted to be greatest when the first fore-and-aft natural frequency is near to the basic bending-torsion flutter frequency.

A better comprehension of the various aeroelastic modes comes from inspecting mode shapes at both subcritical and supercritical conditions. In Fig. 6-26, mode shapes for selected points along the $U = 6$ and 7 branches in Fig. 6-19, the moderate-aspect-ratio example, are shown in phasor form. Likewise for the high-aspect-ratio wing having $\tau = 60$. Fig. 6-27 presents mode shapes for certain steady deflections along the $U = 6$ and 7 paths from Fig. 6-24. These mode shapes disclose that the branches which stabilize and increase in frequency consist largely of motion in the first assumed torsion mode, having a small q_{v_1} contribution locked in a characteristic phase relationship with q_{ϕ_1} of near 180°. The branches producing instabilities, furthermore, have q_{v_1} nearly in phase with q_{ϕ_1} and give the previously shown flutter mode shapes as they cross the $i\omega$ axis. Mode shapes (Fig. 6-27) for the essentially second bending aeroelastic modes show the dominance of the second assumed vertical bending mode in this branch, which remain nearly fixed in the complex plane at a frequency close to the second assumed bending mode natural frequency.

The role of the bending-stiffness ratio τ in flutter of lifting wings is next examined. Figures 6-28 and 6-29 give flutter speeds and frequencies found for the same moderate-aspect-ratio example used earlier compared with solutions for different values of τ. For $\tau = 12$ the dimensionless natural frequency of the first chordwise bending mode is 0.86124, which is only slightly higher than the zero-lift flutter frequency of 0.8332, and its stability boundary shows the most marked decrease in flutter speed as w_o increases from zero. The other extreme, $\tau = 1000$, has a dimensionless natural frequency in chordwise bending of 7.862, yet some decrease in flutter speed still occurs. Elastic deformation in bending about the major principal axis of the airfoil cross section should be virtually suppressed and all fore-and-aft motion connected with vertical bending-torsion elastic coupling. Calculations are impractical for larger τ since numerical problems begin to appear, such as convergence difficulties with the nonlinear steady deflection iterative solution.

The uniform decrease in flutter frequencies as τ is decreased reflects the additional inertia from the larger fore-and-aft motions brought about by the reduced elastic stiffness in bending about the airfoil major principal axis. Decreasing flutter frequencies for increasing steady deformations likewise should be due in part to the increasing contribution of q_{v_1}, although the increase in the relative participation of q_{w_1} is also a factor.

In Fig. 6-30 the stability boundaries shown earlier for the large-aspect-ratio example with $\tau = 25$ and 60 are compared along with curves having $\tau = 10$, 40, and 200. The appearance is complicated by the interaction of the flutter modes with the predominantly second vertical bending aeroelastic mode as discussed earlier, and by fore-and-aft bending natural frequencies sufficiently low to cause convergence as $\alpha \to 0$ to speeds below the true nonlifting flutter speed.

For both $\tau = 200$ and 60 the flutter frequencies descend through the range of the second vertical bending mode frequency as w_0 is increased, causing the discontinuous stability boundaries. The flutter frequencies (Fig. 6-31) reflect the role of this second bending mode, whose dimensionless natural frequency is 0.77904 and (as already shown) a stable aeroelastic mode with approximately this frequency exists at flutter. As mentioned in discussing the $\tau = 60$ results, these curves are actually continuous, but the simple harmonic solution procedure could not produce results within the gaps.

For the $\tau = 40$, 25, and 10 cases, stability boundaries converge to free vibration in the first fore-and-aft mode as $\alpha \to 0$; their frequency curves converge to the respective natural frequencies of this mode. In the case $\tau = 40$, this frequency is 0.7862, quite close to the second vertical bending assumed mode natural frequency 0.77904. This near resonance caused difficulty in precisely locating the neutral stability curves for small w_o, as the damping became extremely small; of course this trouble is unimportant since even small structural damping would raise flutter speeds considerably here.

The stiffness in chordwise bending is thus a factor in the flutter of lifting cantilever wings. Although stability is most adversely affected for ω_{v_1} near the zero-lift flutter frequency, this effect appears over a wide range of τ. Higher-aspect-ratio-wings apparently experience a greater decrease in flutter speed with steady deformations, given that ω_{v_1} is sufficiently near the $\alpha = 0$ flutter frequency.

The mass ratio M is the only parameter which can change for a specific wing, as it depends upon altitude. In Fig. 6-32 the dependence of both flutter and divergence speeds on M for the moderate-aspect-ratio example appears for the complete range of mass ratios of practical interest. Divergence speeds for several values of steady drag together with zero-lift flutter speeds for $C = 0$ and 0.01 are compared. In addition zero drag flutter speeds for steady lift giving

$$\left(\frac{w_o}{b}\right)_{Tip} = 1 \text{ , } 3$$

are shown for $M = 10$, 40, and 100. This same information is depicted in Fig. 6-33 for the large-aspect-ratio example except wingtip deflections of 2 and 4 semichords are used.

Divergence speeds for all drag values vary exactly as $\sqrt{M}$, as can be seen from the divergence determinant (2-29), where M appears only as a product with the inverse square of divergence speed. The $C = 0$ divergence speeds for these two examples are identical, but U_D decreases more rapidly with C for the higher aspect ratio.

For mass ratios above about 5, nonlifting flutter speeds behave approximately as $\sqrt{M}$. A minimum in flutter speed is found near $M = 5$, whith a rapid asymptotic rise to infinity following a further decrease in M . This reflects well known results for incompressible flow (Ref. 5, page 247). A practical application for mass ratios sufficiently small to be theoretically free from flutter is the stability of hydrofoils used in high-speed marine transportation. Divergence would be the type of instability encountered. This conclusion emphasizes the importance of allowing for steady drag since its effect on divergence is proportionally the same for any mass ratio and the decrease of divergence speed with C can be considerable.

Divergence is more important relative to flutter for mass ratios around 10 than for higher mass ratios; this indicates a greater likelihood of light aircraft and sailplanes experiencing divergence. Calculation of divergence speeds for a high-performance sailplane appears as a likely application in which allowance for steady drag effects would be desireable.

The effect of steady deformation on flutter appears insensitive to M . For equal tip deflections, U_F reduces by about the same proportion at each of the three mass ratios in the two figures. For the high-aspect-ratio wing, these deflected flutter speeds correspond to the aeroelastic mode connected with chordwise bending, as discussed for $M = 40$.

The effect of changes in the remaining parameters A , S , and i_α has also been investigated for the steady deformed case, but no new interesting behavior was found. Their influence at zero lift, as tabulated in Ref. 1, is carried over into the deflected flutter behavior. Stability boundaries and flutter mode shapes for increasing steady lift show the same alterations of the basic flutter phenomenon as is demonstrated by the examples used here.

To clarify the strong influence which steady chordwise loads can have upon divergence, particularly for high aspect ratios, the dependence of U_D upon C as aspect ratio parameter P is varied appears in Fig. 6-34. The corresponding zero-lift flutter speeds for this configuration (Fig. 6-1) can be compared directly. Unquestionably, for higher aspect ratios ($P \lesssim 0.01$) drag forces typically encountered in flight (i.e., $C = 0.0025$) can cause divergence to become no less important for flight safety than primary bending-torsion flutter.

C. Effect of Unsteady Leading-Edge Suction Forces from Two Dimensional Incompressible Flow

Substituting the terms in (5-20) for their counterparts in the aerodynamic matrix (5-3) allows inclusion of the linearized unsteady chordwise forces arising from incompressible potential strip theory as described in Chapter V. This effect is present only for $\alpha \neq 0$ and will grow as angle of attack is increased. The initial trend of stability as α increases from zero should be unchanged from the results already discussed, but at higher steady lifting conditions leading edge suction should have a noticeable influence.

Figure 6-35 displays how allowance for the linearized unsteady propulsive force affects the destabilizing, constant speed, increasing steady lift branches of the root locus in Fig. 6-19, which is the moderate-aspect-ratio-wing example. For this case a tip deflection of just one semichord is a very large deformation assuming a conventional bending-to-torsion stiffness ratio EI_x/GI_d , since the semispan would be about 9 semichords. Thus larger deflections shown are only of academic interest, since they exceed in practice the limits imposed by several underlying assumptions.

Figure 6-36 recasts the Fig. 6-35 information into a better form for inferring stability; the damping ratio of the same root branches is plotted for wingtip deflection. Stability is slightly increased when leading-edge suction is added, but for practical deformations its effect is really not too significant. A stability characteristic of deformed wings, also evident in the format of Fig. 6-36, is the reduced severity of flutter onset with increasing speed at constant w_0 for higher load factors.

Figure 6-37 gives the manner in which the root locus for the high-aspect-ratio example (Figure 6-20) is altered by allowing for linearized unsteady suction forces. Shown is the destabilizing family of constant-speed branches associated with the first fore-and-aft bending normal mode. Again true stability with steady wingtip deflection is also shown (Fig. 6-38). Also added are the constant-speed branches which stabilize and increase in frequency as steady deformations increase.

Once again the unsteady suction force has a slightly stabilizing influence. Given the same ratio EI_x/GI_d , this example has twice the span in semichords of that for the moderate-aspect-ratio example, hence larger wingtip deflections in semichords can be tolerated. After allowing for this factor, the unsteady chordwise potential forces do not appear to have any greater influence on stability for the larger aspect ratio.

Figure 6-39 shows how stability of the modified high-aspect-ratio example (having $\tau = 60$, presented in Fig. 6-24) depends on steady deformations and on the linearized unsteady propulsive force. Comparison with Fig. 6-38 shows a similar effect due to leading-edge suction, but steady deformations definitely have a stronger and more immediate destabilizing effect for the stiffer chordwise bending case. This is due to the proximity of the fore-and-aft bending normal mode frequency to the zero-lift bending-torsion flutter frequency.

Inclusion of the linearized unsteady leading-edge suction terms derived in Section D of Chapter V is thus found to be stabilizing for deformed wings. Aeroelastic modes involving a primary contribution by the first chordwise bending mode appear to be most affected by these terms. With their inclusion, potential flow strip theory has been fully exploited for this problem, and further improvement in the aerodynamics involves the compressible three-dimensional loads of Chapter VII.

D. Two Practical Examples

The manner in which chordwise forces and steady deformations influence the aeroelastic stability of cantilever wings has thus far been illustrated by means of idealized examples. After one has identified the fundamental effects, it is instructive to apply the same solution techniques to typical designs. Sailplanes, having large aspect ratios, low mass ratio, and low operating speeds (which permit the use of incompressible aerodynamics), are a logical choice for practical examples. Accordingly, two existing sailplanes are modeled within the approximations imposed by the assumption of uniform spanwise mass and stiffness properties and strip theory airloads. Their stability is studied using the same techniques applied before.

The first example is modeled from information given about the Slingsby Dart 17R in Ref. 15, as summarized in Table 6.1. The approach taken in determining the wing stiffnesses, in lieu of looking at wing construction details, was to use photographs in Ref. 15, from which tip deflection and twist at a load factor of 4 could be measured. The stiffness EI_x so obtained is clearly larger than would be expected for the weight and type of construction; this inaccuracy is due to the uniform stiffness restriction, the rectangular planform, and strip theory steady airloads. The torsion stiffness GI_d is more reasonable. The ratio

$$\frac{EI_x}{GI_d} = 4.41$$

turns out impractically large. This number leads to a larger value of P than would be expected, which causes bending natural frequencies to be larger relative to torsion natural frequencies than would probably occur on the actual vehicle. It can be added that, had GI_d been increased to compensate for the seemingly excessive EI_x, then the flutter speeds would have been absurdly high. Since wing construction details were not available, typical values for the parameters A, S, i_α, and τ were simply assigned.

A different philosophy was applied when modelling the second vehicle, the Gemini two-place high performance sailplane detailed in Ref. 16. With construction details of the metal wing structure described in Ref. 16, it was possible to assign reasonably accurate values to all six of the dimensionless parameters from a diagram of the average wing cross section (Fig. 6-40). The pertinent details of modeling the Gemini are listed in Table 6-2.

One notable result is a much lower bending stiffness EI_x than for the Dart 17R. This result will compromise the static deflection-load factor relationship but should favor the dynamic modeling. The considerable difference in bending stiffnesses between the two examples is revealed in Fig. 6-41, which shows how the true load factor (found using the respective aircraft gross weights) varies with steady vertical tip deflection at speeds near the expected flutter speeds. The poor static modeling of the Gemini should not adversely affect its flutter results, however, tip deflection rather than load factor should be used to measure the amount of steady lift.

The mass per unit span of the Gemini wing was taken to be the average for the outer two-thirds of the semispan, so as better to model it dynamically. The mass ratio-- over twice that for the Dart 17R-- reflects the heavier construction needed for a two-place vehicle and the smaller average semichord. This design (Ref. 16) intentionally has a higher wing loading to optimze the glide slope, with thermalling performance improved using full-span flaps. The chordwise bending stiffness was conservatively estimated yet still yielded a quite low value of $\tau = 5$. The low EI_x/GI_d ratio, together with the very large aspect ratio, result in the extremely small $P = 0.00128$. This wing thus is an extreme case in the context of the examples studied earlier.

The effect of steady drag on divergence speeds and nonlifting flutter speeds is shown in Fig. 6-42 for the Dart 17R example and in Fig. 6-43 for the Gemini. For both, the divergence speed drops below the zero lift flutter speed at drag values which can be realistically expected in flight. The excessively large P of the Dart 17R model moderates the drop in its divergence speed due to drag. For flutter only a slight dependence of speed on C is found. On the Gemini, in fact, the $C = 0.02$ flutter speed is only 0.28% less that for $C = 0$. Its larger S tends to lower the flutter speed relative to divergence.

Figure 6-44 depicts the stability boundary as affected by steady wingtip deflection for the Dart 17R. The associated flutter mode shape amplitudes and phase relations appear in Figs. 6-45(a), (b). The coupling effect between the first fore-and-aft bending mode and the primary zero-lift bending-torsion flutter mechanism appears to be responsible for a decrease in flutter speed with lift, as in earlier examples. The corresponding root locus diagram (Fig. 6-46) reveals that the first chordwise bending natural frequency by coincidence happened to fall almost exactly on the zero lift flutter frequency. This phenomenon causes the pronounced drop in flutter speed for small deflections seen in Fig. 6-44. Inclusion of the unsteady propulsive force is slightly stabilizing at large deflections, as in previous cases.

A parallel analysis of the Gemini example, given by Figs. 6-47, 6-48, and 6-49, yields a very different response to steady deflections. Flutter speed decreases only slightly at representative tip displacements, and the mode shape contributions from q_{w_1} , q_{w_2} , and q_{ϕ_1} show almost no sensitivity to w_o . The chordwise bending contribution suggests the cause, made clear in the root locus diagram. The combination of a very small P and small τ produces a fundamental fore-and-aft bending natural frequency which is much smaller relative to the zero lift flutter frequency than in any example yet treated. Furthermore, the second chordwise frequency drops to near the flutter frequency. This second mode (rather than the fundamental) participates in flutter of the deformed wing, yet it is not as strongly coupled elastically with the first vertical bending and torsion modes. The aeroelastic-mode branches associated with the first chordwise bending mode no longer play an important role in stability with steady deformations. Indeed it has degenerated into a virtually uncoupled, neutrally damped fore-and-aft vibration. The linearized effect of unsteady leading-edge suction on this type of flutter is negligible.

Evidently, for extreme cases such as the Gemini model with a fore-and-aft bending frequency much lower than the zero-lift bending-torsion flutter frequency, the lowest chordwise mode will not participate strongly in flutter. The low-frequency root branches associated with it give no cause for concern. Before this calculation is accepted as a definitive flutter analysis of an existing sailplane, however, the cantilever root boundary conditions must especially be recalled. While these results do offer insight into symmetric flutter of the actual vehicle, the possibility of anti-symmetric motions involving fuselage roll and yaw is entirely suppressed. For the Gemini in particular, there remains the likelihood that anti-symmetric vertical and fore-and-aft bending modes may couple to produce a different type of flutter-- possibly one with a greater sensitivity to steady deformations. Although the results here are insensitive to both steady deflections and to chordwise forces, steady drag unquestionably plays a critical part in divergence.

DART 17R SPECIFICATIONS (REF. 15):

SPAN	55.8 ft.
AREA	149 ft^2
ASPECT RATIO	20.9
GROSS WEIGHT	800 lb.

ASSUMPTIONS:

WING WEIGHT	200 lb $\Rightarrow$ $m = 0.1242 \frac{\text{slug}}{\text{ft.}}$
AVG. SEMICHORD	1.33 ft.

FROM REF. 15 PHOTOGRAPHS:

$(w_o)_{TIP} = 3$ ft. at 4g $\Rightarrow EI_x \approx 1{,}500{,}000$ lb ft^2

$(\phi_o)_{TIP} = 1.5°$ at 4g $\Rightarrow GI_d \approx 340{,}000$ lb ft^2

FROM THIS INFORMATION ONE CAN SPECIFY

$P \approx 0.01$ $\quad$ $M \approx 9.4$ (sea level)

ASSUME THE REMAINING PARAMETERS

$i_\alpha = 0.25$ $\quad$ $S = 0.1$

$A = 0.1$ $\quad$ $\tau = 25.$

EXPRESS SPEED V IN FT./SEC. IN TERMS OF U :

$$U = \frac{\ell}{b}\sqrt{\frac{J}{GI_d}}\,V = 0.008432\,V$$

LOAD FACTOR AT SEA LEVEL:

$$N = \frac{4\Pi\rho V^2 b\ell}{W}\left(\alpha + \sum_{j=1}^{n} \frac{2}{\Pi}\frac{1}{(2j-1)} q^{\circ}_{\phi_j}\right)$$

TABLE 6.1 Modeling of the Dart 17R Wing

GEMINI SPECIFICATIONS (REF. 16)

SPAN	60.5 ft.
AREA	124 ft^2
ASPECT RATIO	29.4
GROSS WEIGHT	1065 lb.
TOTAL WING WEIGHT	400 lb.
WEIGHT OF OUTER 20 FT.	110 lb. => $m = 0.1708\ \frac{\text{slug}}{\text{ft.}}$

ASSUME $b = 1.00$ ft.

PROPERTIES ESTIMATED FROM THE TYPICAL SECTION (Fig. 6-40)

EI_x	444,900 lb-ft^2
GI_d	402,400 lb-ft^2
EI_z	2,179,000 lb-ft^2
J	0.04697 slug-ft.
a	-0.4
s_e/m	0.2322 ft.

RESULTING DIMENSIONLESS PARAMETERS

$M = 22.9$ $\quad$ $A = 0.1$

$P = 0.00128$ $\quad$ $S = 0.23$

$i_\alpha = 0.275$ $\quad$ $\tau = 5$

EXPRESS SPEED V IN FT./SEC. IN TERMS OF U

$$U = \frac{\ell}{b}\sqrt{\frac{J}{GI_d}}\ V = 0.010335\ V$$

TABLE 6.2 Modeling of the Gemini Wing

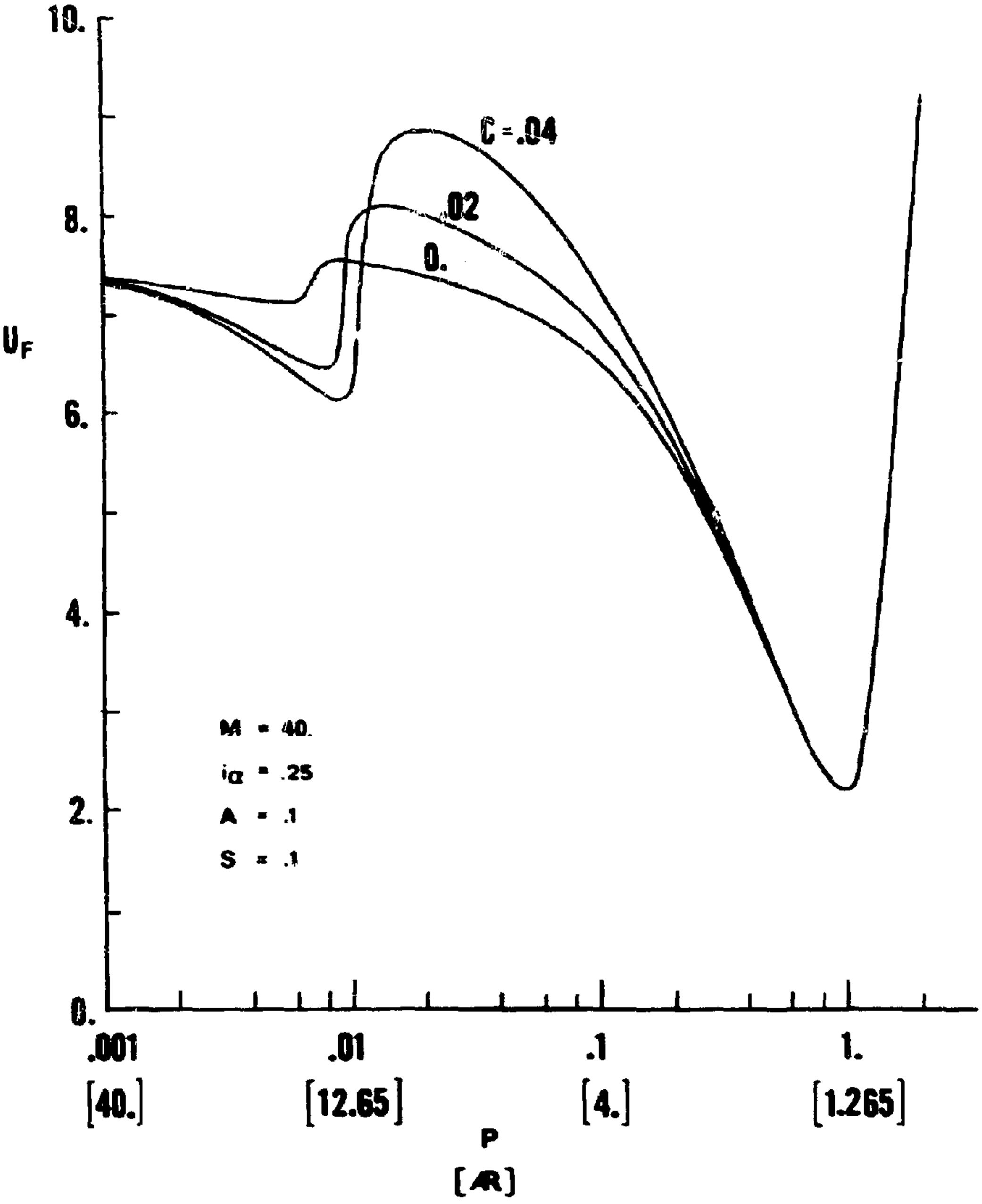

FIGURE 6-1 Dependence of Flutter Speed on C and P , Ref. 1 Solution

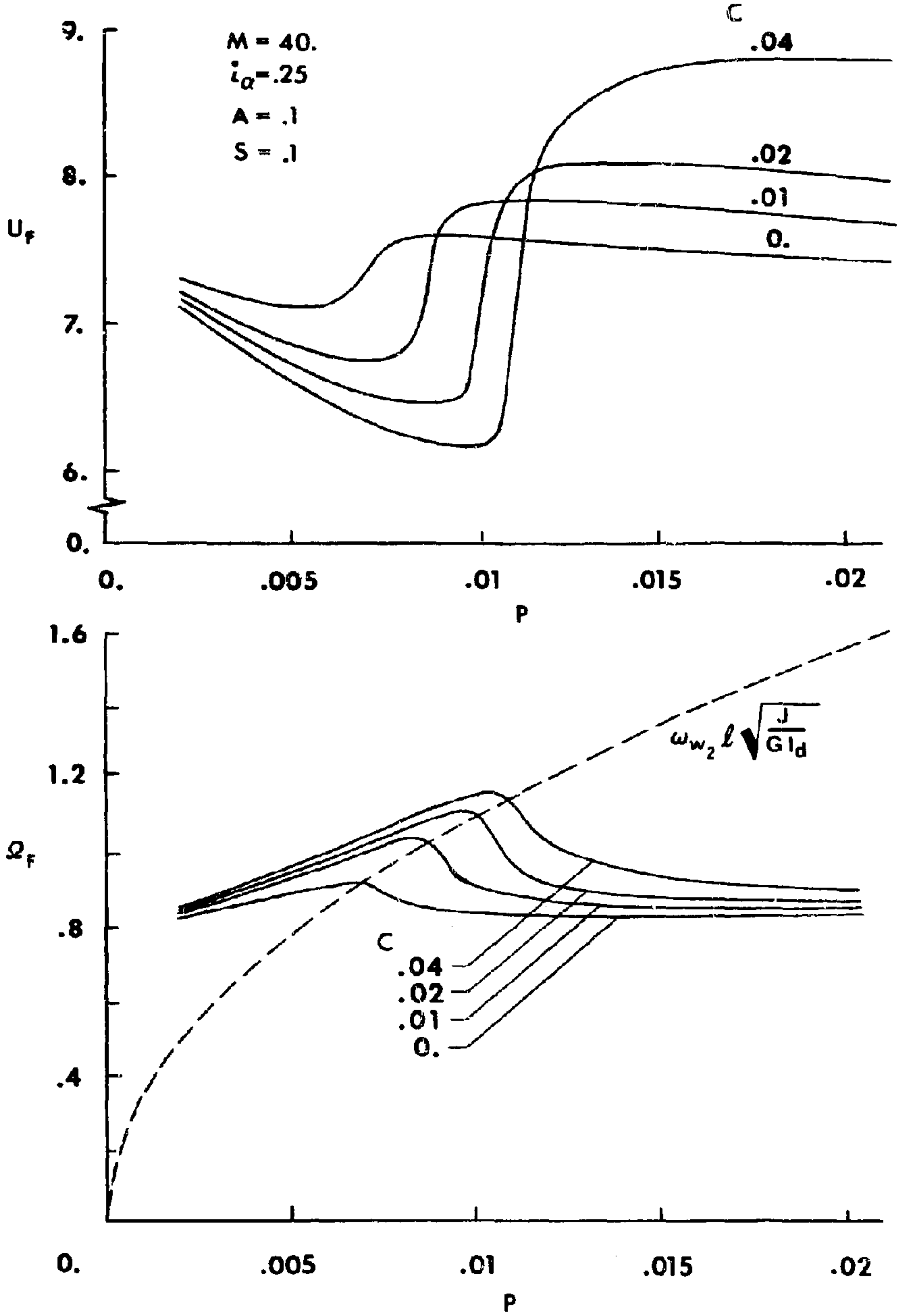

FIGURE 6-2(a) Flutter Speeds, Frequencies, and Mode Shapes for Different C as P Varies, Modal Solution of the Fig. 6-1 Configuration

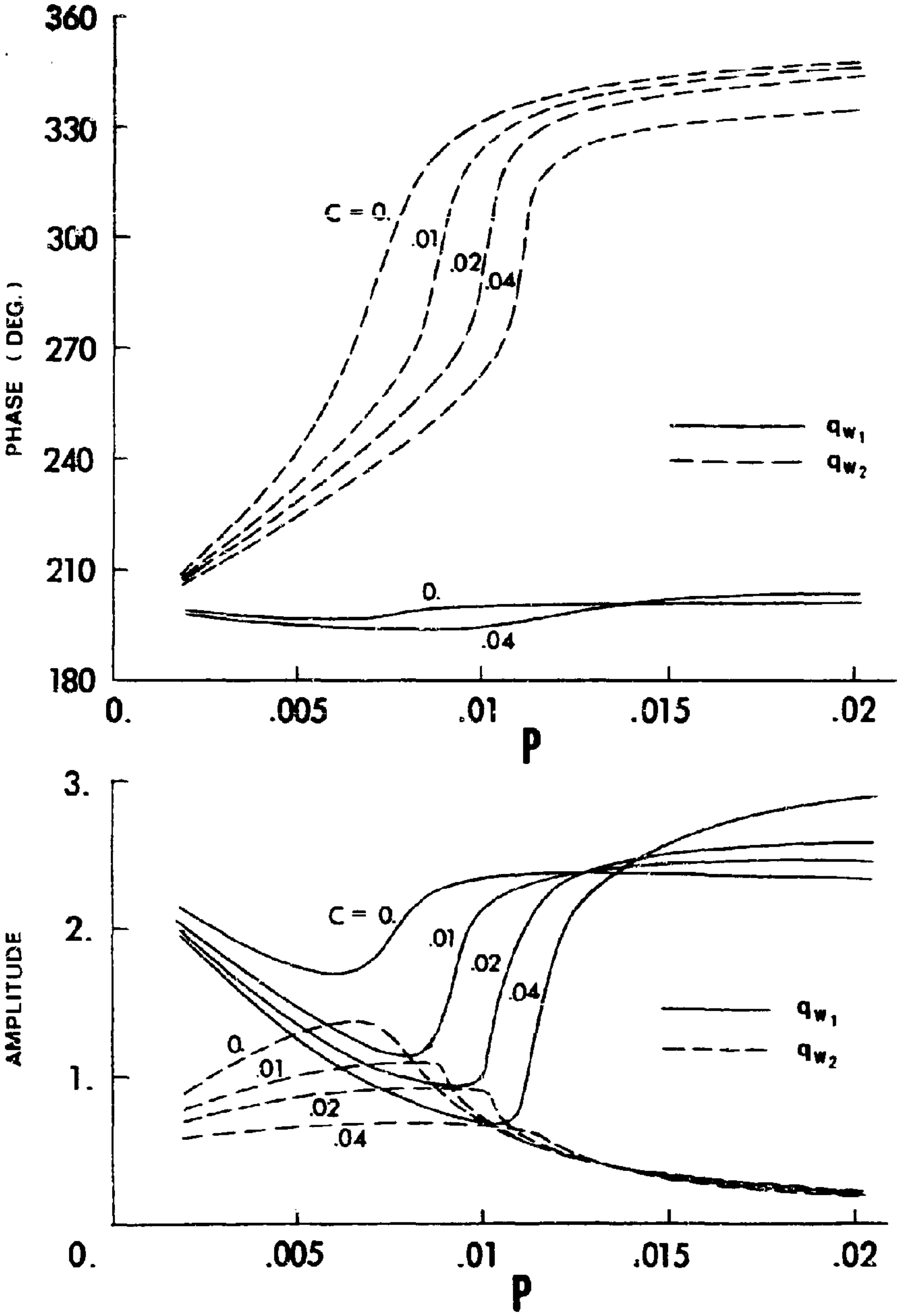
360
330
300
270
240
210
180
PHASE (DEG.)
C = 0.
.01
.02
.04
0.
.04
q_{w_1}
q_{w_2}
0.
.005
.01
.015
.02
P
3.
2.
1.
AMPLITUDE
C = 0.
.01
.02
.04
0.
.01
.02
.04
q_{w_1}
q_{w_2}
0.
.005
.01
.015
.02
P

FIGURE 6-2(b)

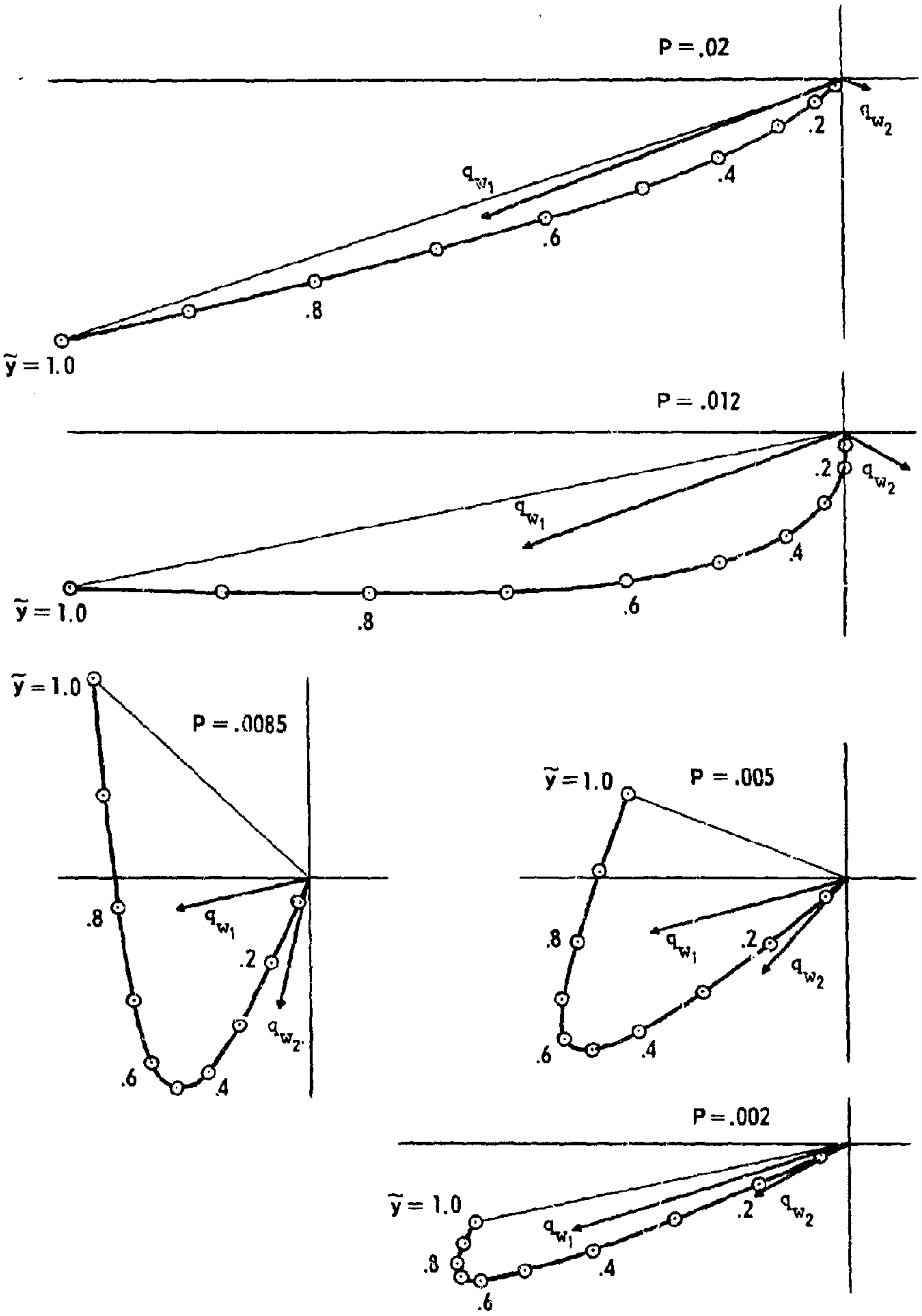

FIGURE 6-3 Phasor Representation of Flutter Mode Bending Displacements From Fig. 6-2 for C = 0.02 at Selected Values of P

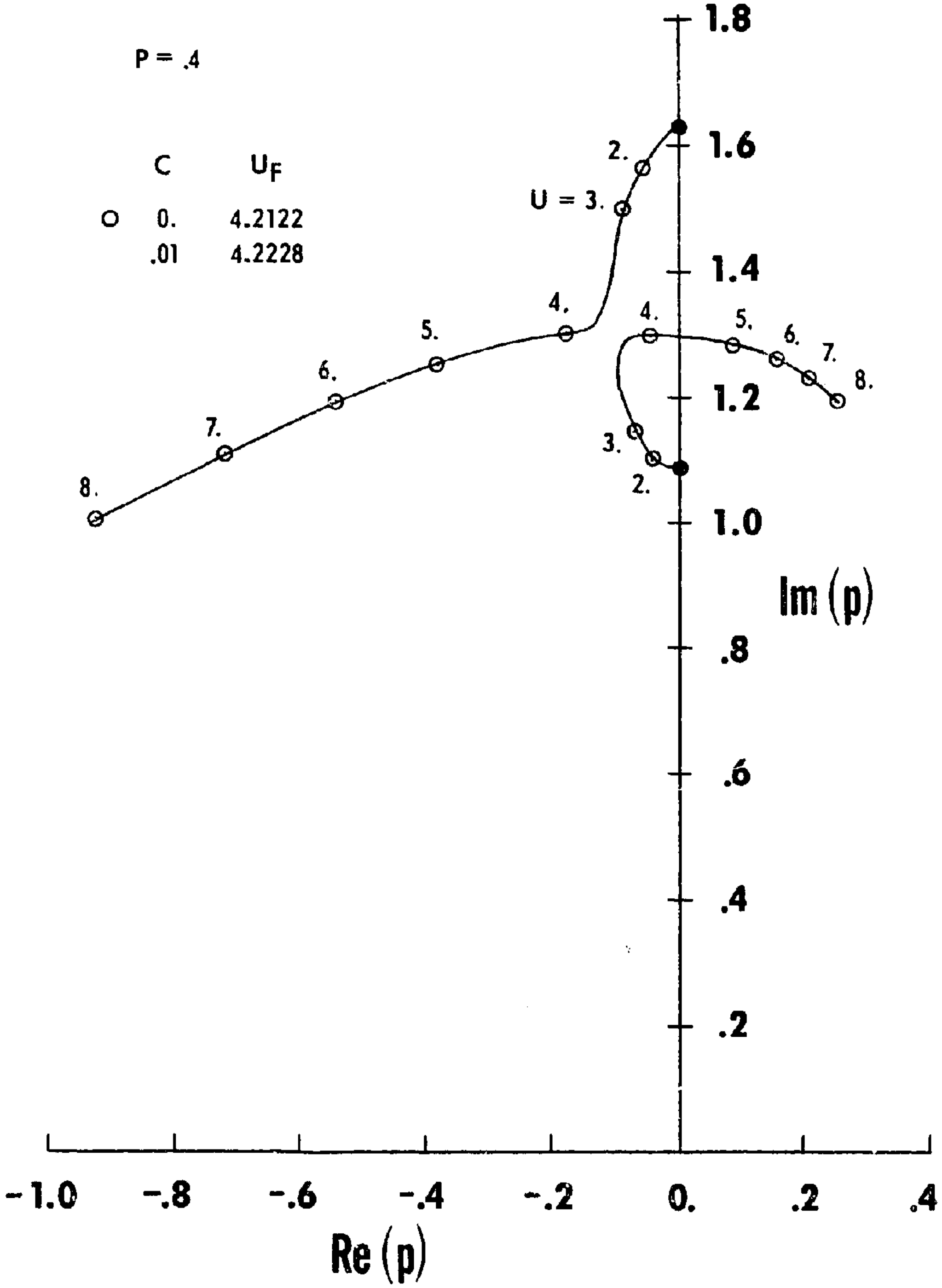

FIGURE 6-4(a) Locus of Roots as Speed Increases From Zero to Supercritical for Eight Values of P , With M = 40, i_α = 0.25, A = 0.1, S = 0.1, n = 3

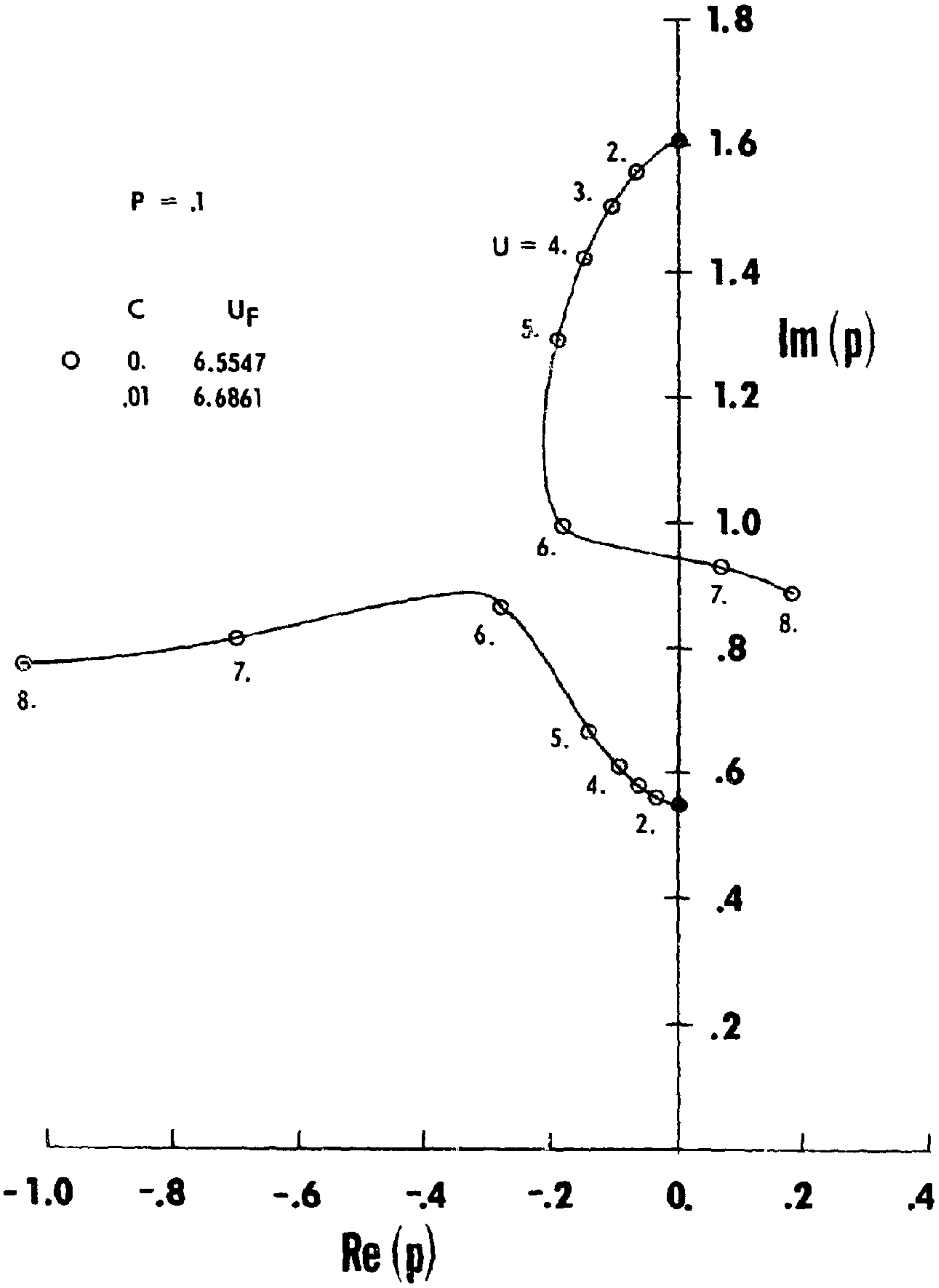
P = .1
C
U_F
○ 0. 6.5547
.01 6.6861
U = 4.
2.
3.
5.
6.
7.
8.
5.
4.
2.
6.
7.
8.
1.8
1.6
1.4
1.2
1.0
.8
.6
.4
.2
Im (p)
-1.0
-.8
-.6
-.4
-.2
0.
.2
.4
Re (p)

Figure 6-4(b)

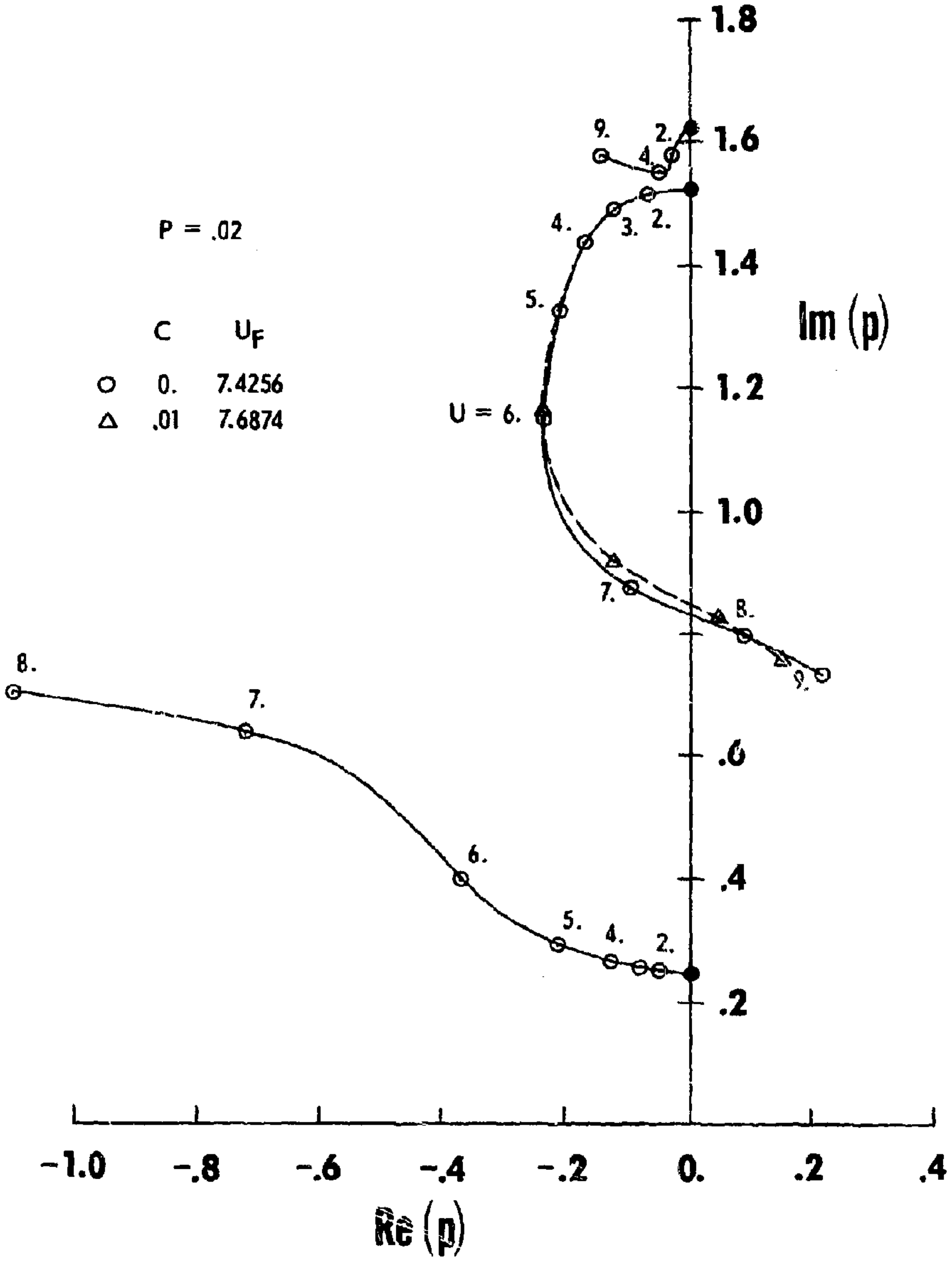
P = .02
C
U_F
○ 0. 7.4256
△ .01 7.6874
U = 6.
9.
2.
4.
3.
2.
4.
5.
7.
8.
9.
8.
7.
6.
5.
4.
2.
1.8
1.6
1.4
1.2
1.0
.6
.4
.2
Im (p)
-1.0
-.8
-.6
-.4
-.2
0.
.2
.4
Re (p)

FIGURE 6-4(c)

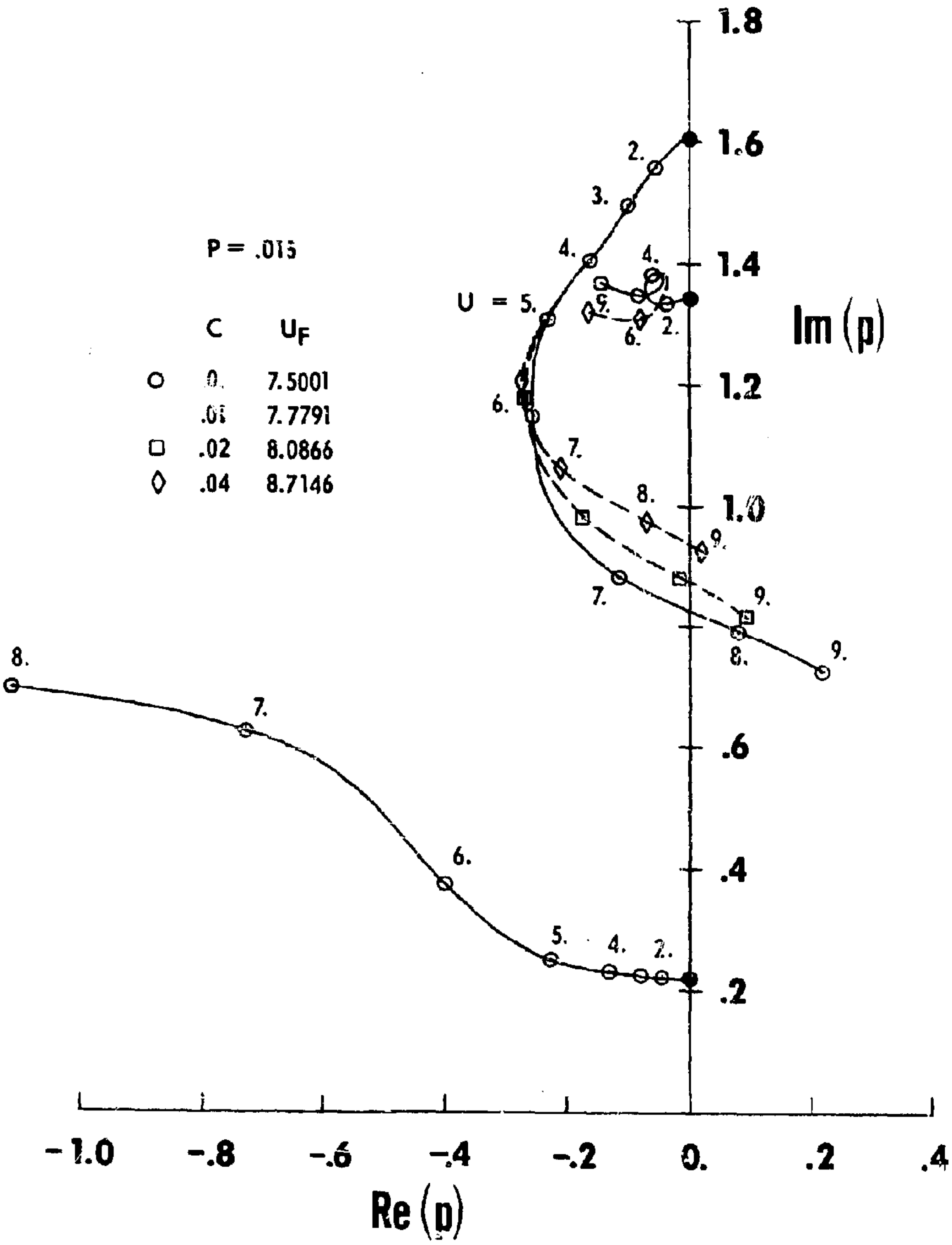
P = .015
C
U_F
○ 0. 7.5001
.01 7.7791
□ .02 8.0866
◇ .04 8.7146
U = 5.
2.
3.
4.
6.
7.
8.
9.
4.
2.
6.
9.
5.
4.
2.
6.
7.
8.
1.8
1.6
1.4
1.2
1.0
.6
.4
.2
Im (p)
-1.0
-.8
-.6
-.4
-.2
0.
.2
.4
Re (p)

FIGURE 6-4(d)

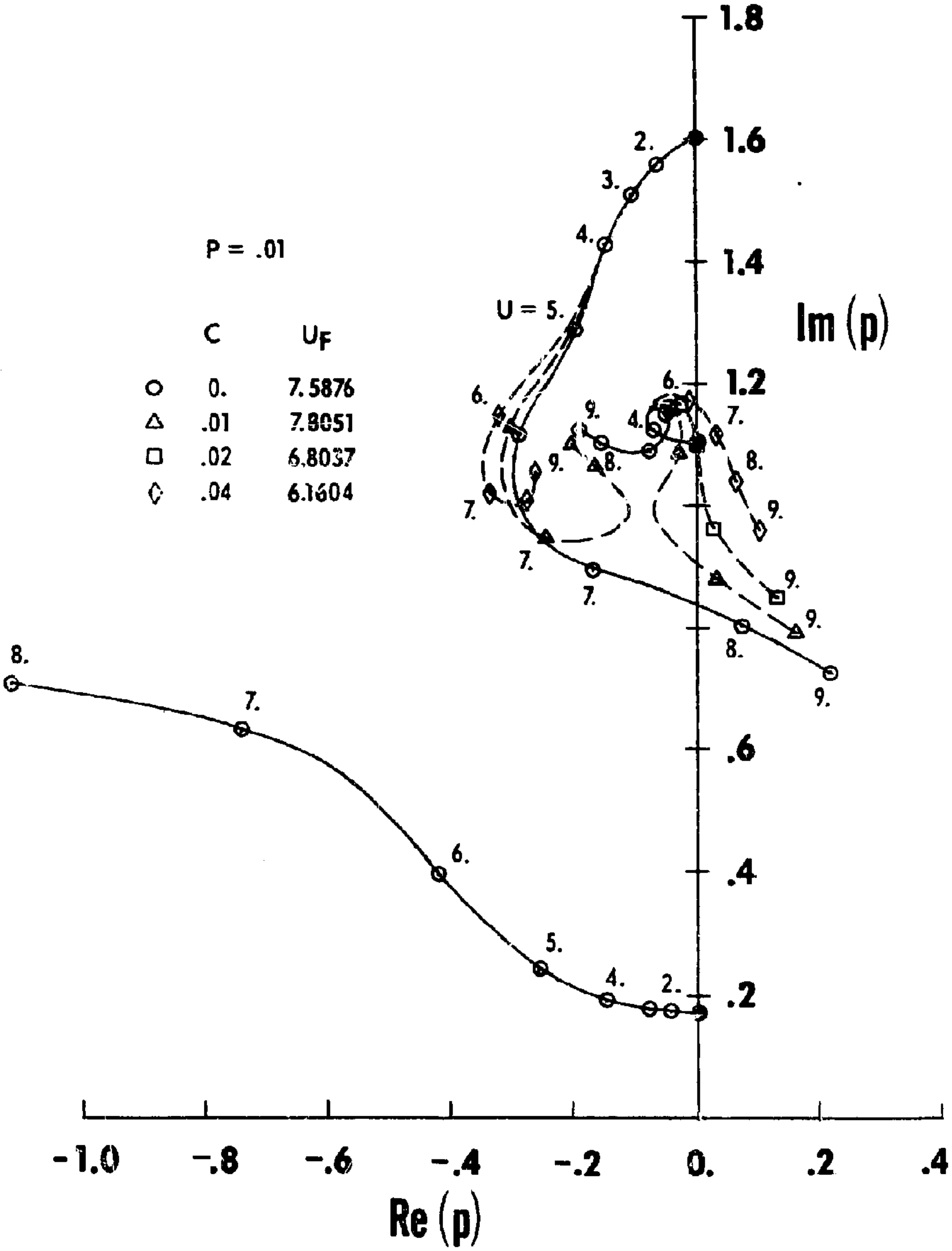
P = .01
C
U_F
○ 0. 7.5876
△ .01 7.8051
□ .02 6.8037
◇ .04 6.1604
U = 5.
2.
3.
4.
6.
7.
8.
9.
1.8
1.6
1.4
1.2
.6
.4
.2
Im (p)
-1.0
-.8
-.6
-.4
-.2
0.
.2
.4
Re (p)

FIGURE 6-4(e)

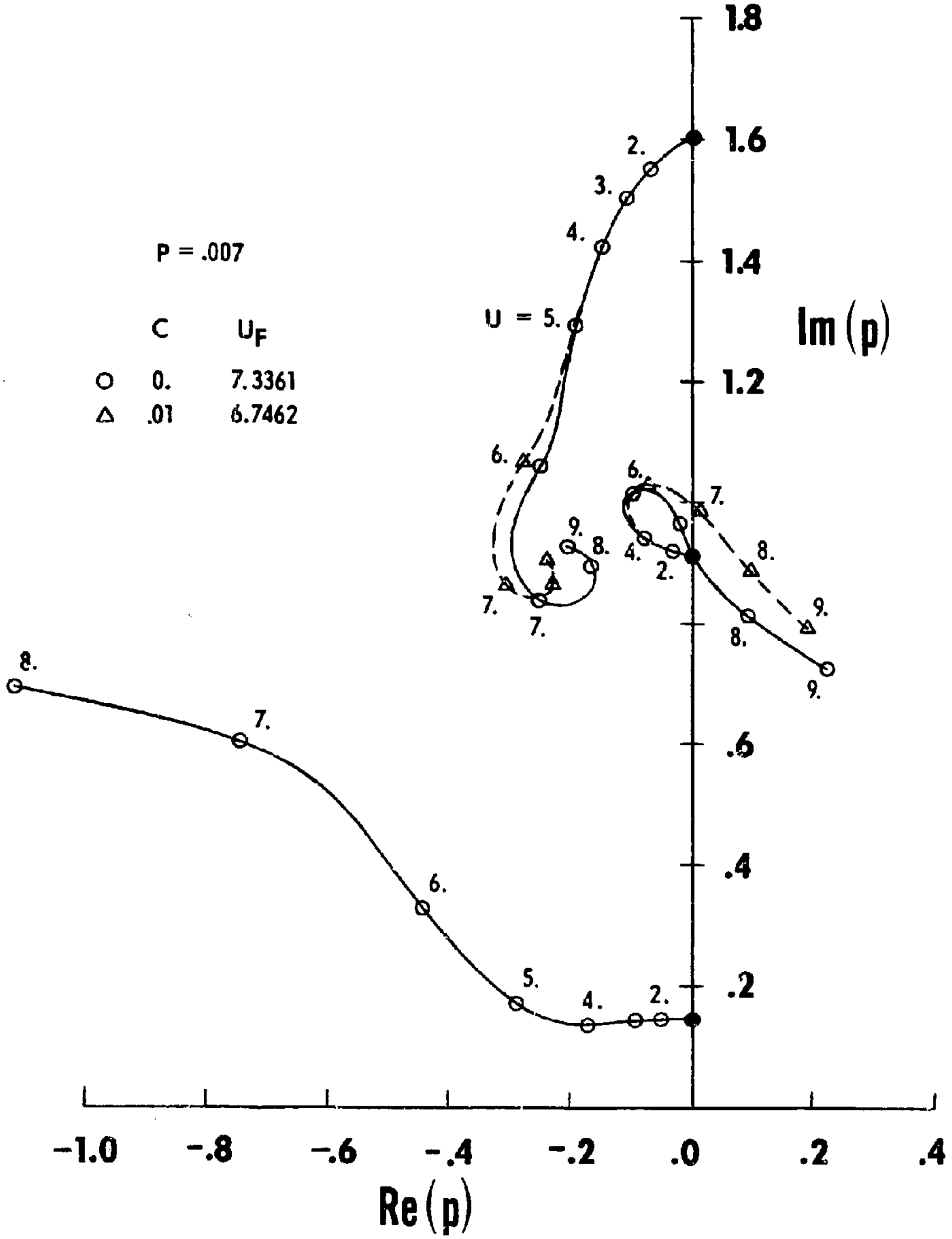
P = .007
C U_F
○ 0. 7.3361
△ .01 6.7462
U = 5.
2.
3.
4.
6.
7.
8.
9.
1.8
1.6
1.4
1.2
.6
.4
.2
Im(p)
-1.0
-.8
-.6
-.4
-.2
.0
.2
.4
Re(p)

FIGURE 6-4(f)

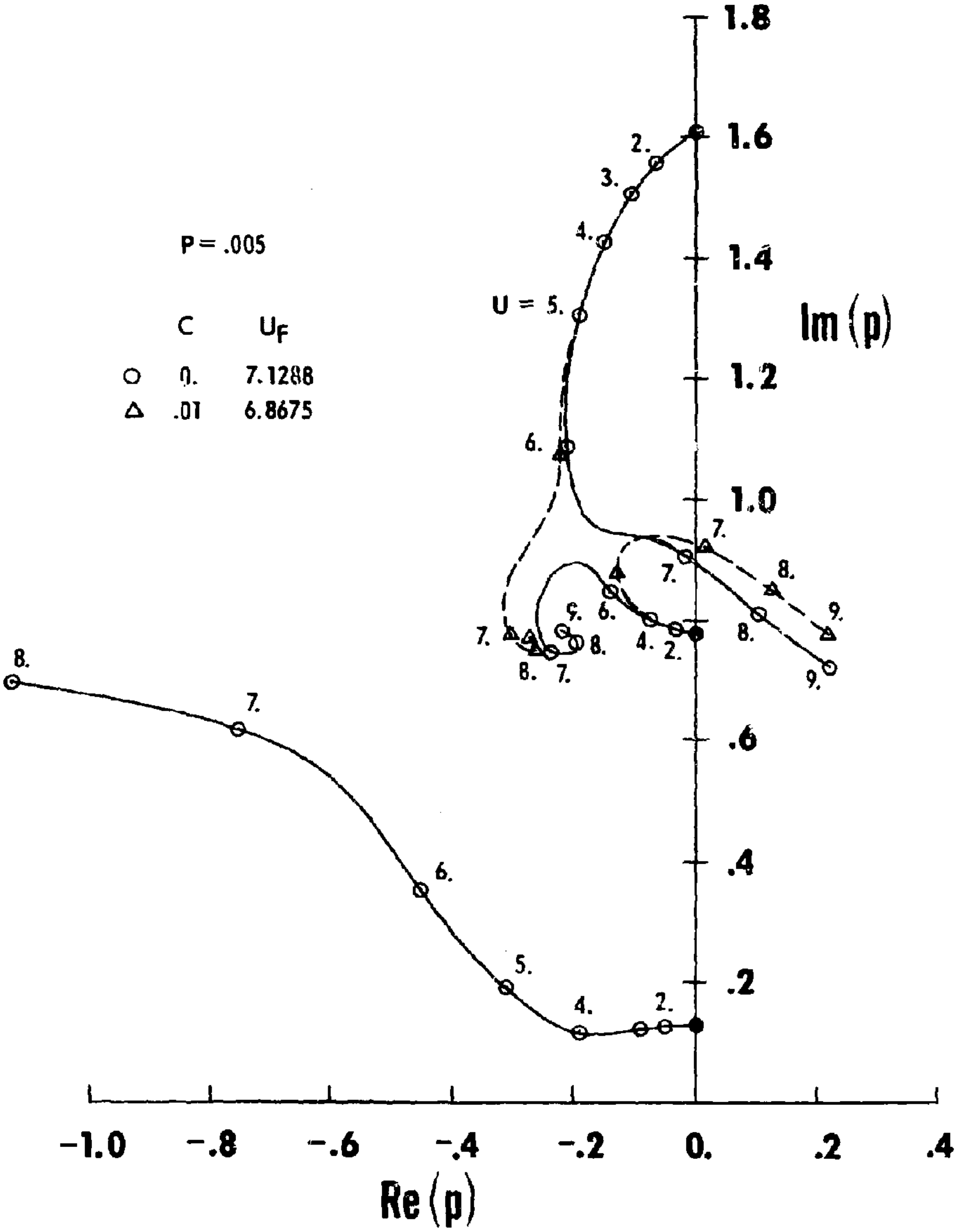
P = .005
C U_F
○ 0. 7.1288
△ .01 6.8675
U = 5.
2.
3.
4.
6.
7.
8.
9.
Im (p)
Re (p)
1.8
1.6
1.4
1.2
1.0
.6
.4
.2
−1.0
−.8
−.6
−.4
−.2
0.
.2
.4

FIGURE 6-4(g)

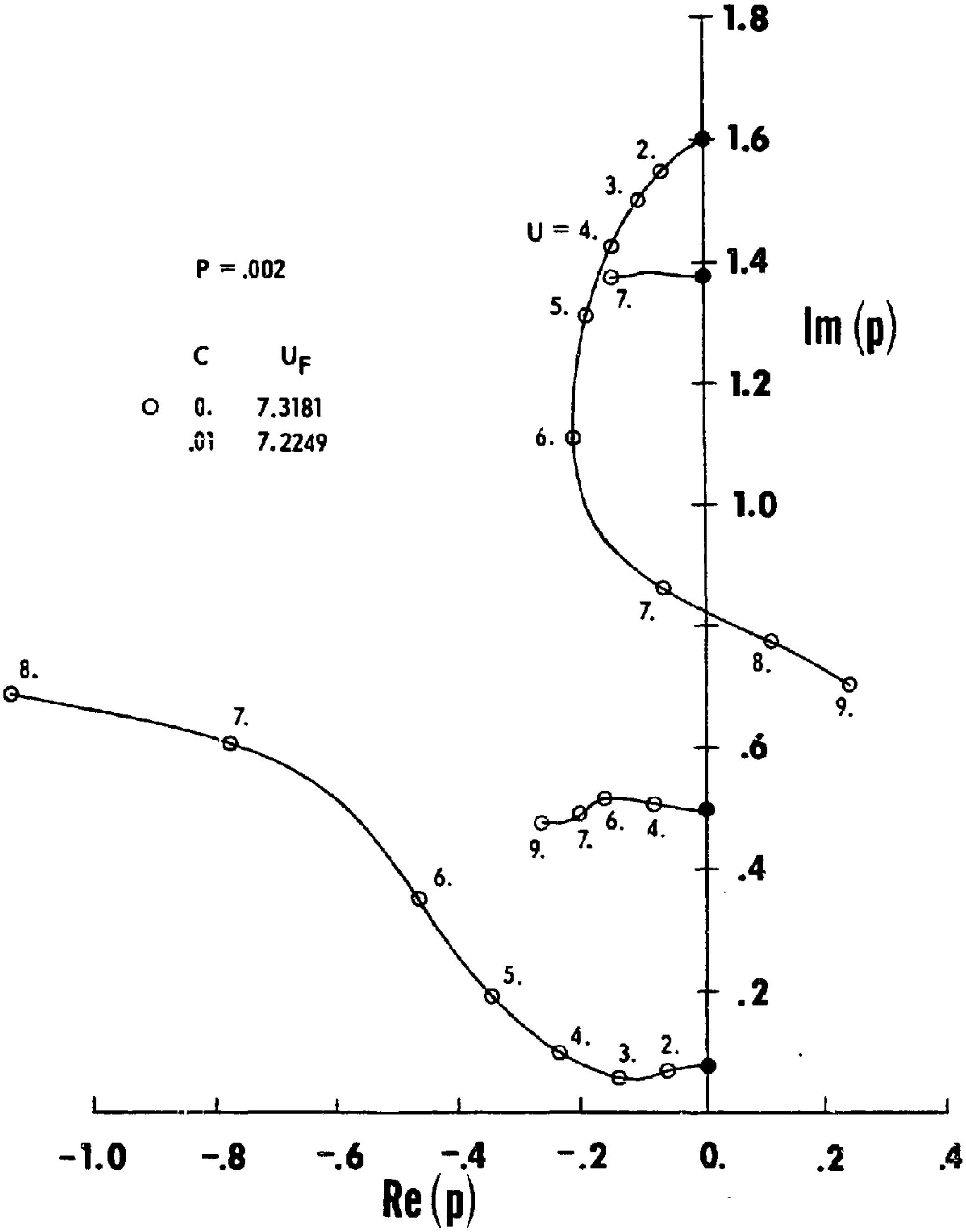

P = .002
C
U_F
○ 0. 7.3181
.01 7.2249
U = 4.
2.
3.
5.
6.
7.
8.
9.
4.
1.8
1.6
1.4
1.2
1.0
.6
.4
.2
Im (p)
-1.0
-.8
-.6
-.4
-.2
0.
.2
.4
Re (p)

FIGURE 6-4(h)

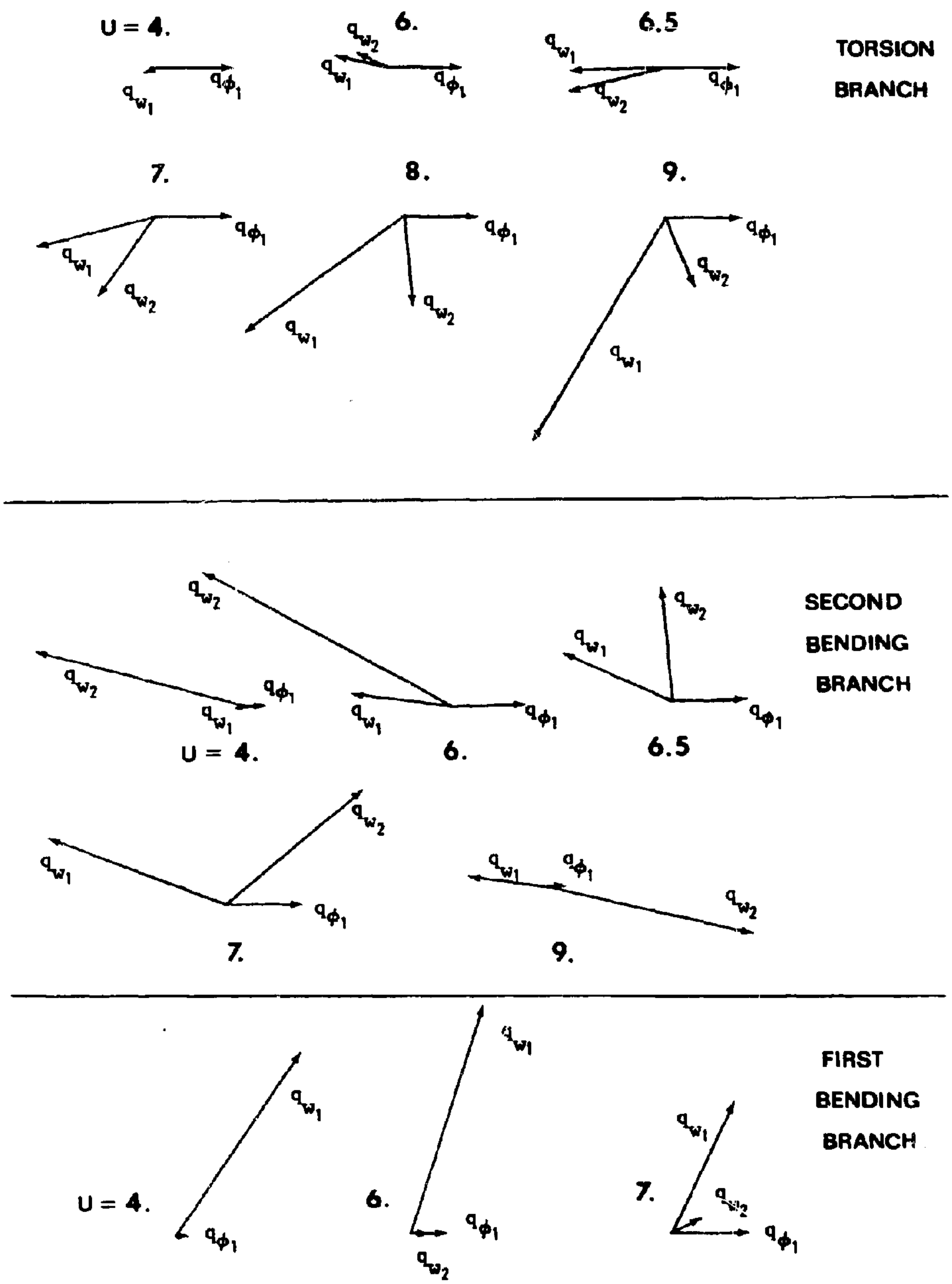

FIGURE 6-5 Mode Shapes for Selected Roots on Each Branch of Fig. 6-4(g) for C = 0

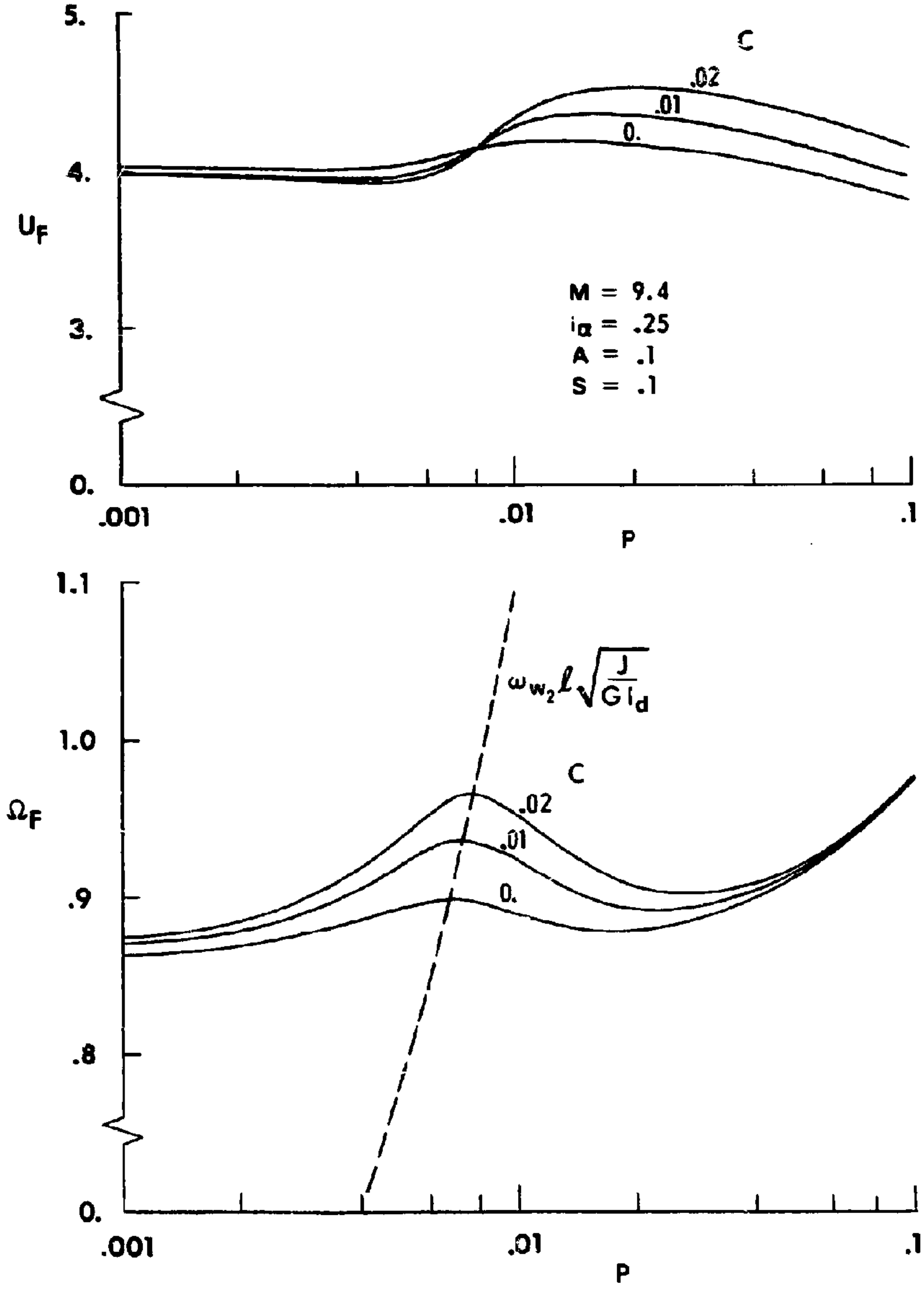

FIGURE 6-6(a) Flutter Speeds, Frequencies, and Mode Shapes for Different C as P Varies, Fig. 6-2 Configuration with Smaller Mass Ratio

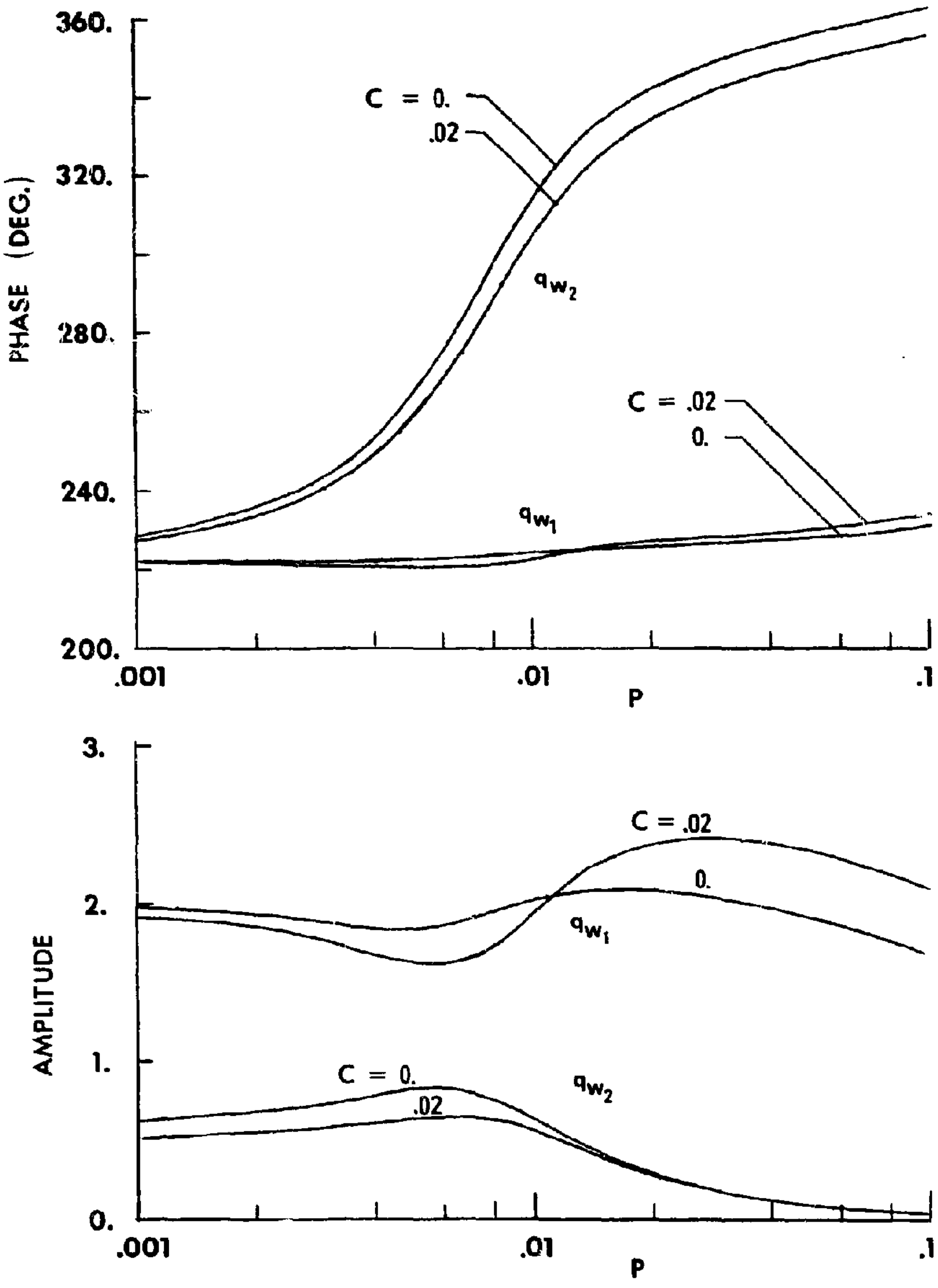
360.
320.
280.
240.
200.
PHASE (DEG.)
C = 0.
.02
q_{w_2}
C = .02
0.
q_{w_1}
.001
.01
.1
P
3.
2.
1.
0.
AMPLITUDE
C = .02
0.
q_{w_1}
C = 0.
.02
q_{w_2}
.001
.01
.1
P

FIGURE 6-6(b)

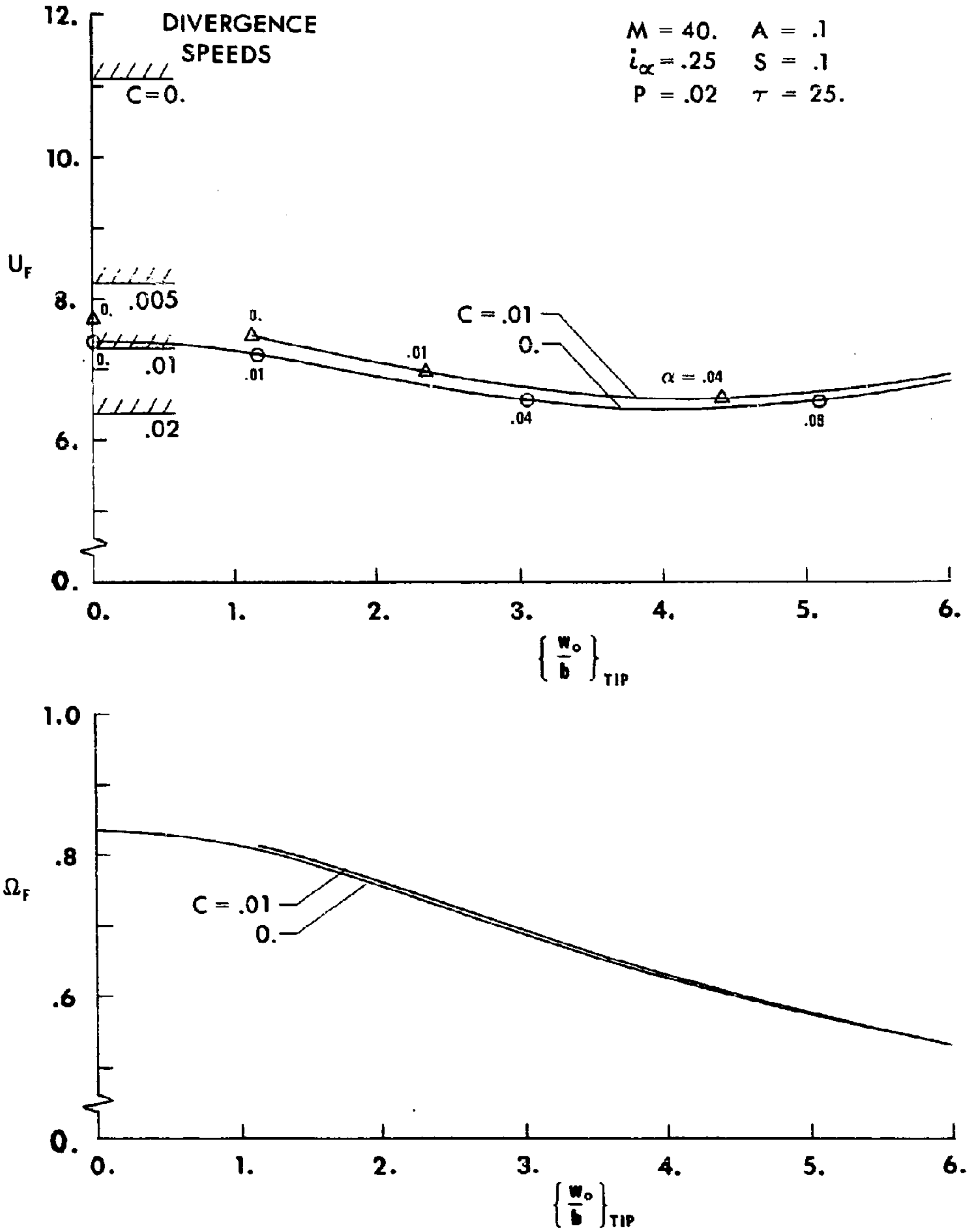

FIGURE 6-7 Flutter Speeds and Frequencies as Affected by Steady Deformations; Moderate-Aspect-Ratio Example

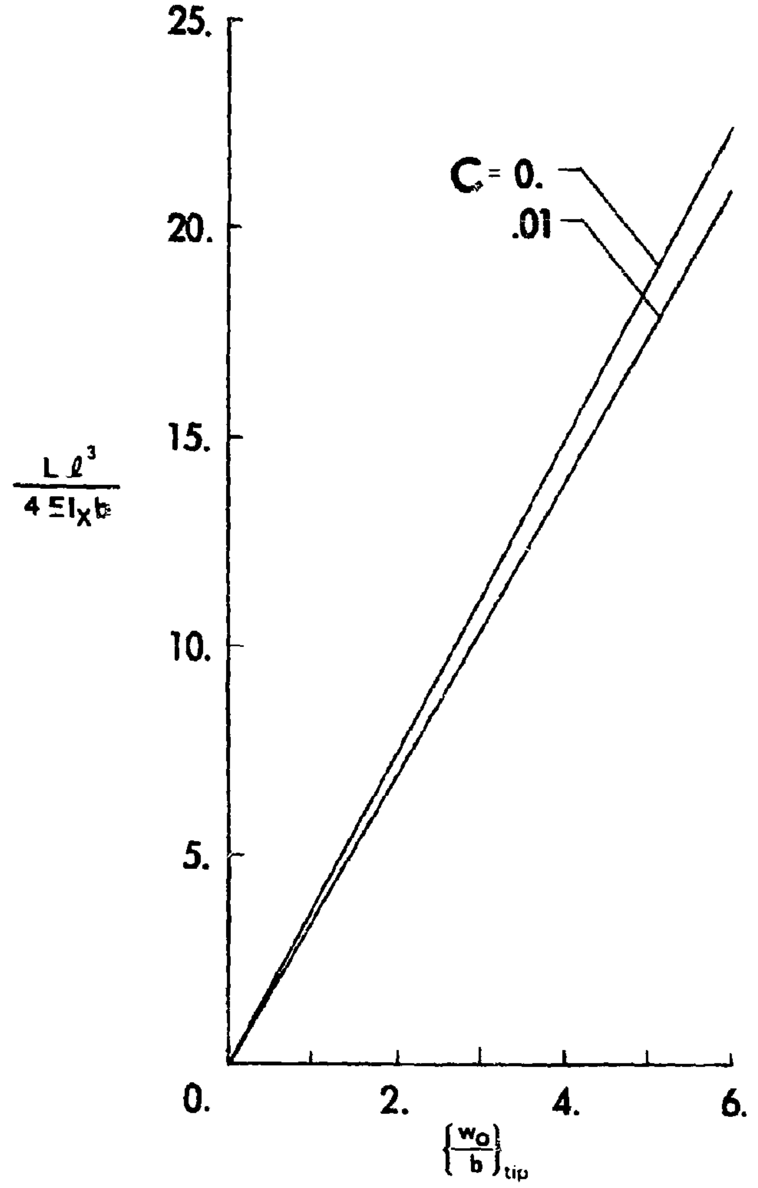

FIGURE 6-8 Effect of Drag on the Relation Between Steady Lift and Steady Bending Deflection, For the Fig. 6-7 Flutter Conditions

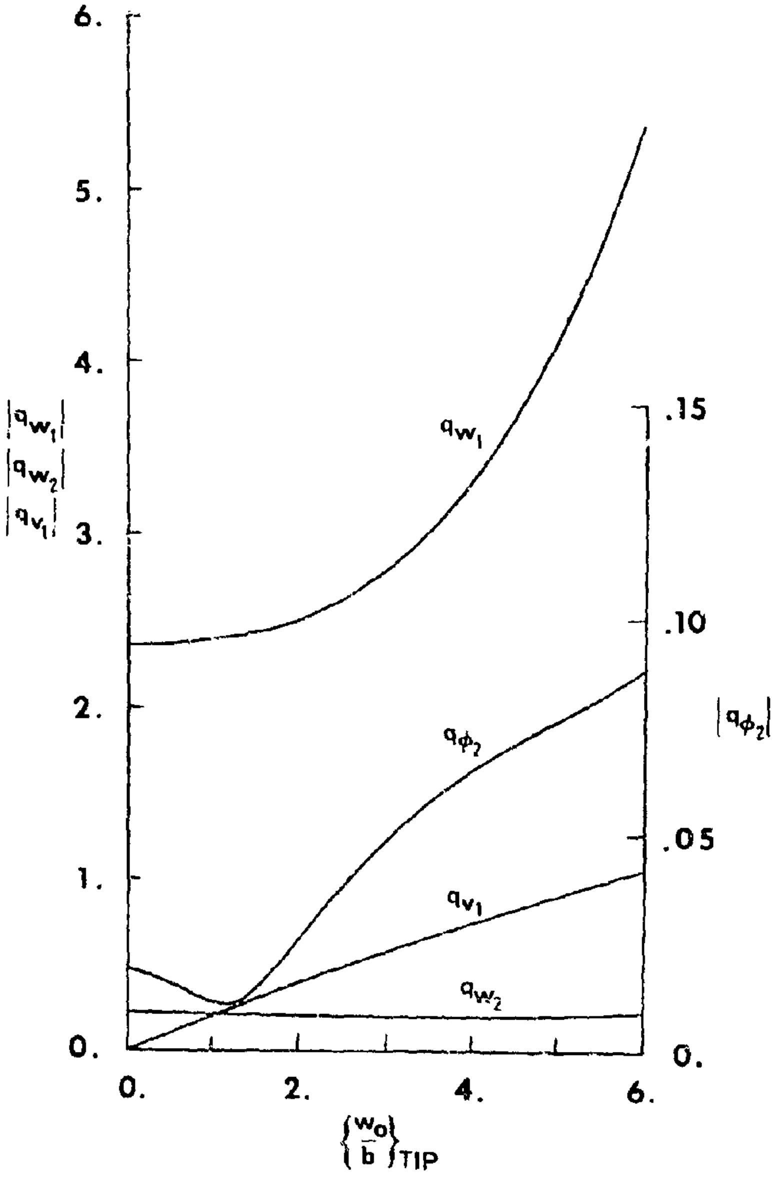

FIGURE 6-9 Flutter Mode Shape Amplitudes for Unit $|q_{\phi_2}|$, for the Fig. 6-7 Stability Boundary With $C = 0$

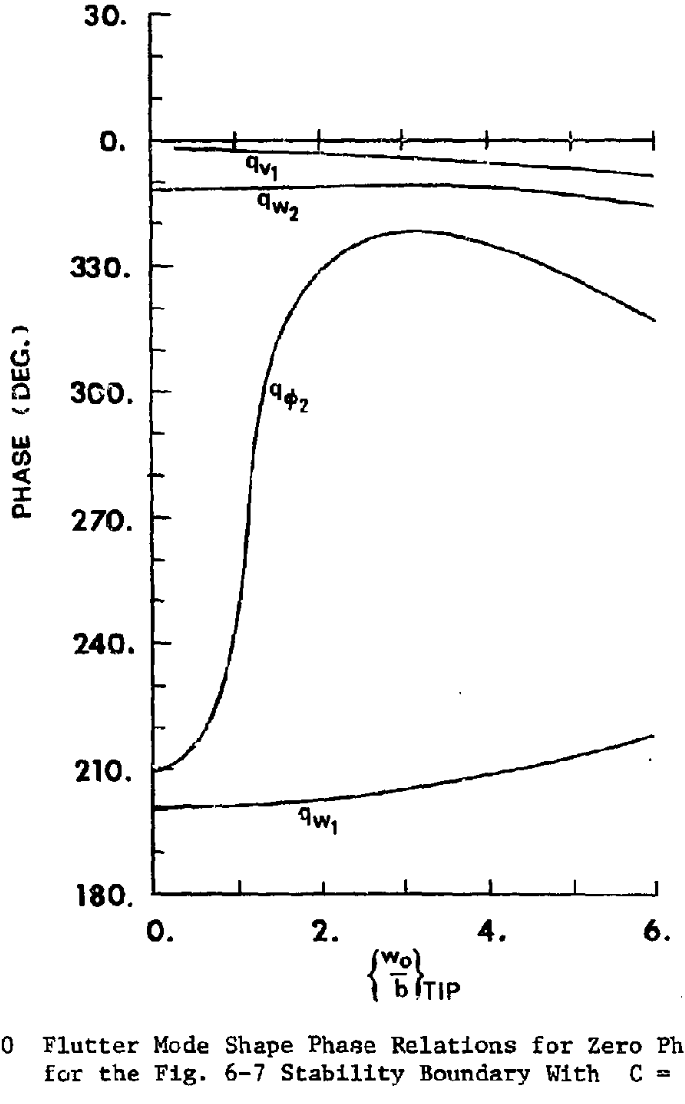

FIGURE 6-10 Flutter Mode Shape Phase Relations for Zero Phase of q_{ϕ_1}, for the Fig. 6-7 Stability Boundary With C = 0

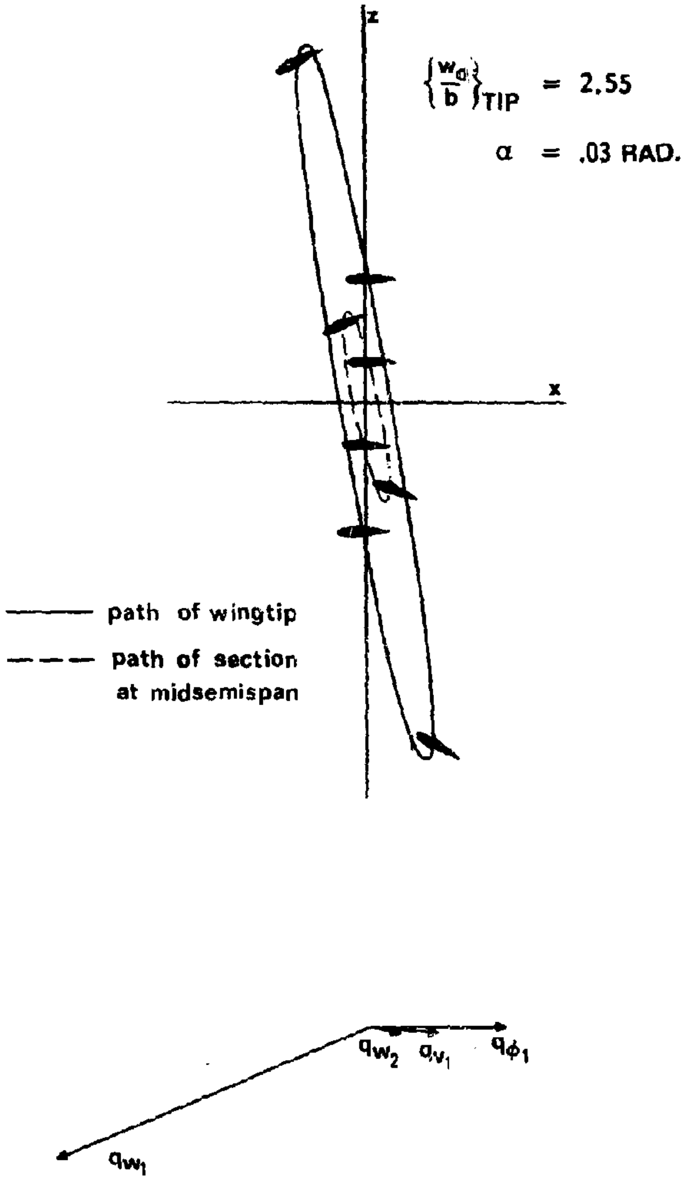

FIGURE 6-11 Physical Appearance of Flutter Mode of Deflected Wing; Fig. 6-7 Configuration With C = 0

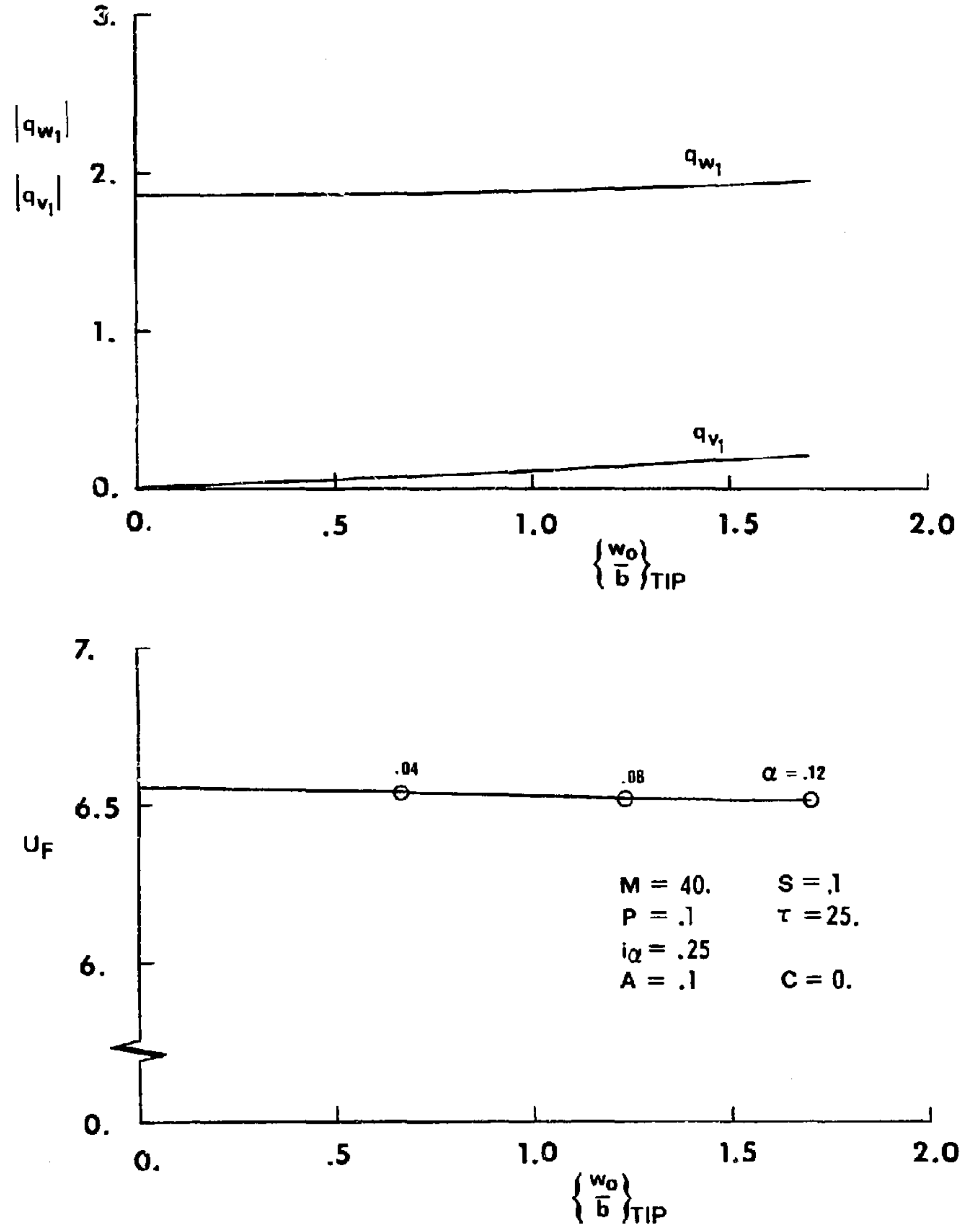

FIGURE 6-12 Flutter Speed and Mode Shape Amplitudes, for Unit $|q_{\phi_1}|$, As Affected By Steady Deflections; Low-Aspect-Ratio Example

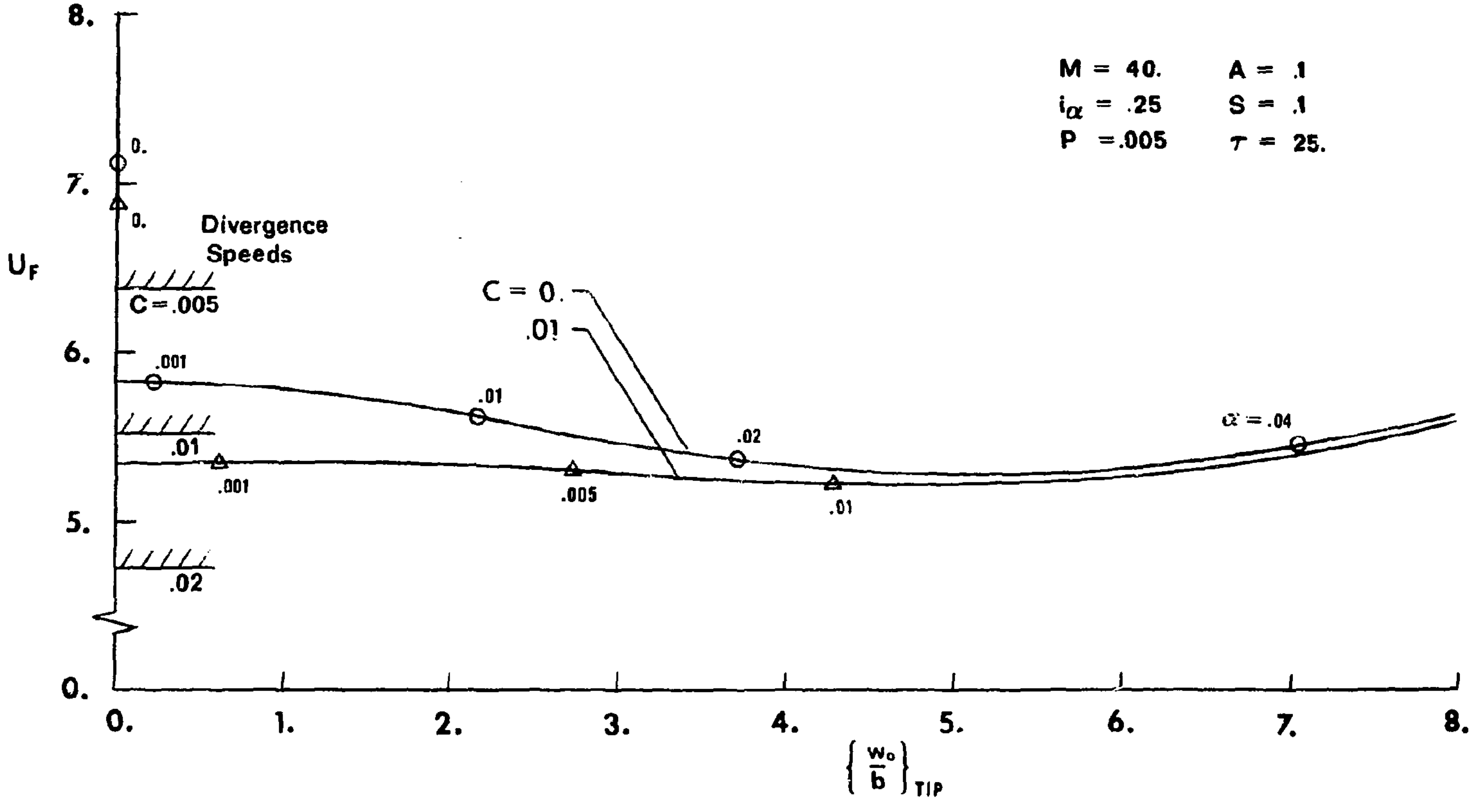

FIGURE 6-13 Flutter Speeds as Affected By Steady Deformations; Large-Aspect-Ratio Example

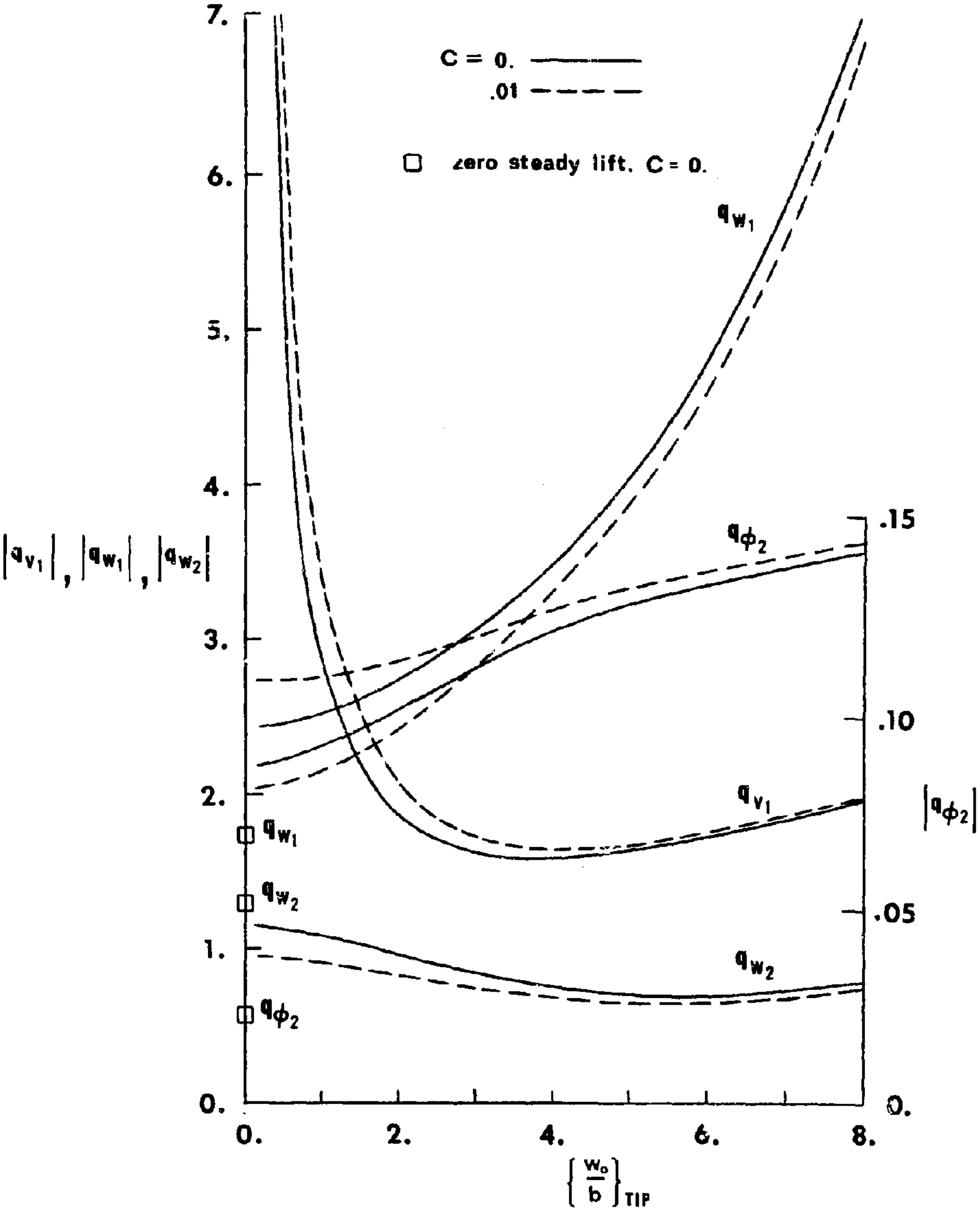

FIGURE 6-14 Flutter Mode Shape Amplitudes for Unit $|q_{\phi_1}|$ Corresponding to Fig. 6-13

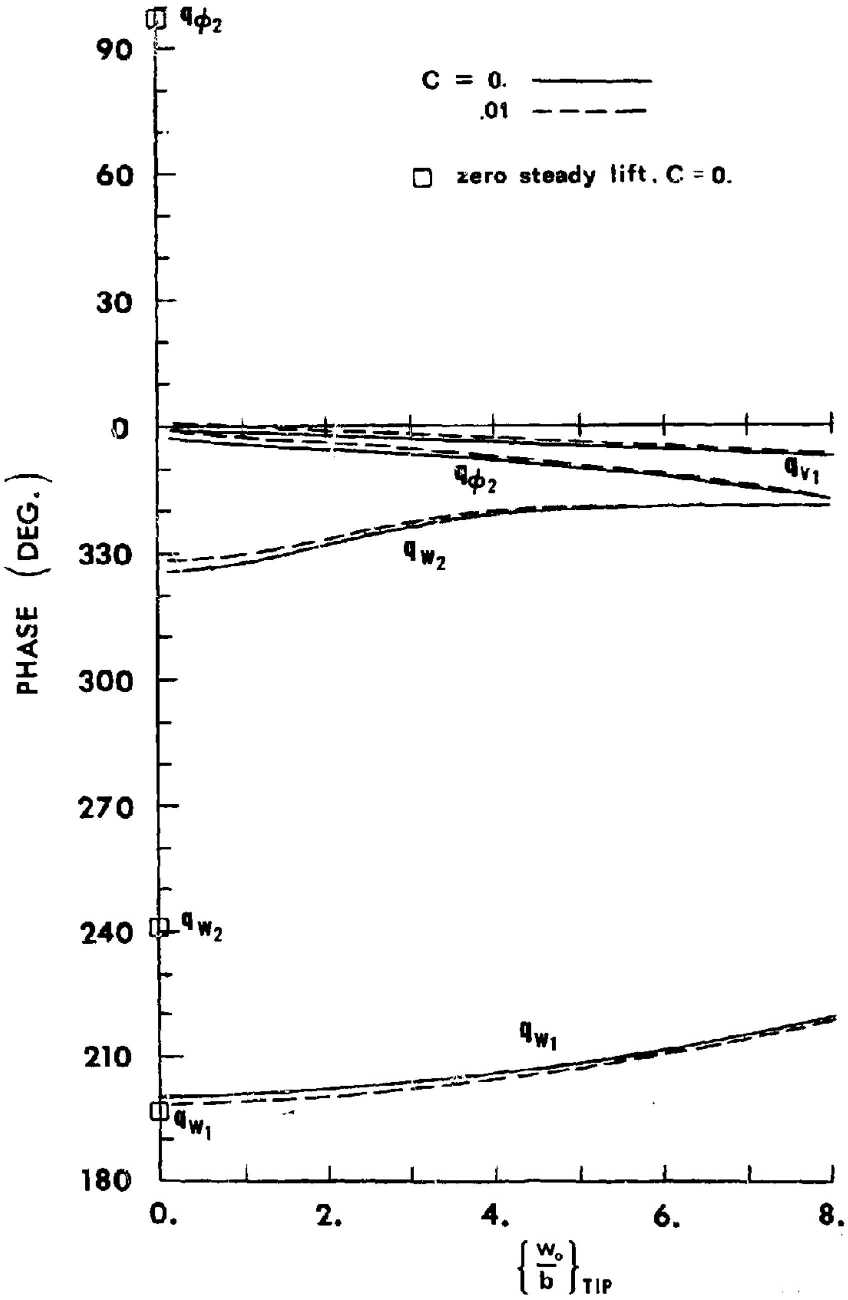

FIGURE 6-15 Flutter Mode Shape Phase Relations for Zero Phase of q_{ϕ_1} Corresponding to Fig. 6-13

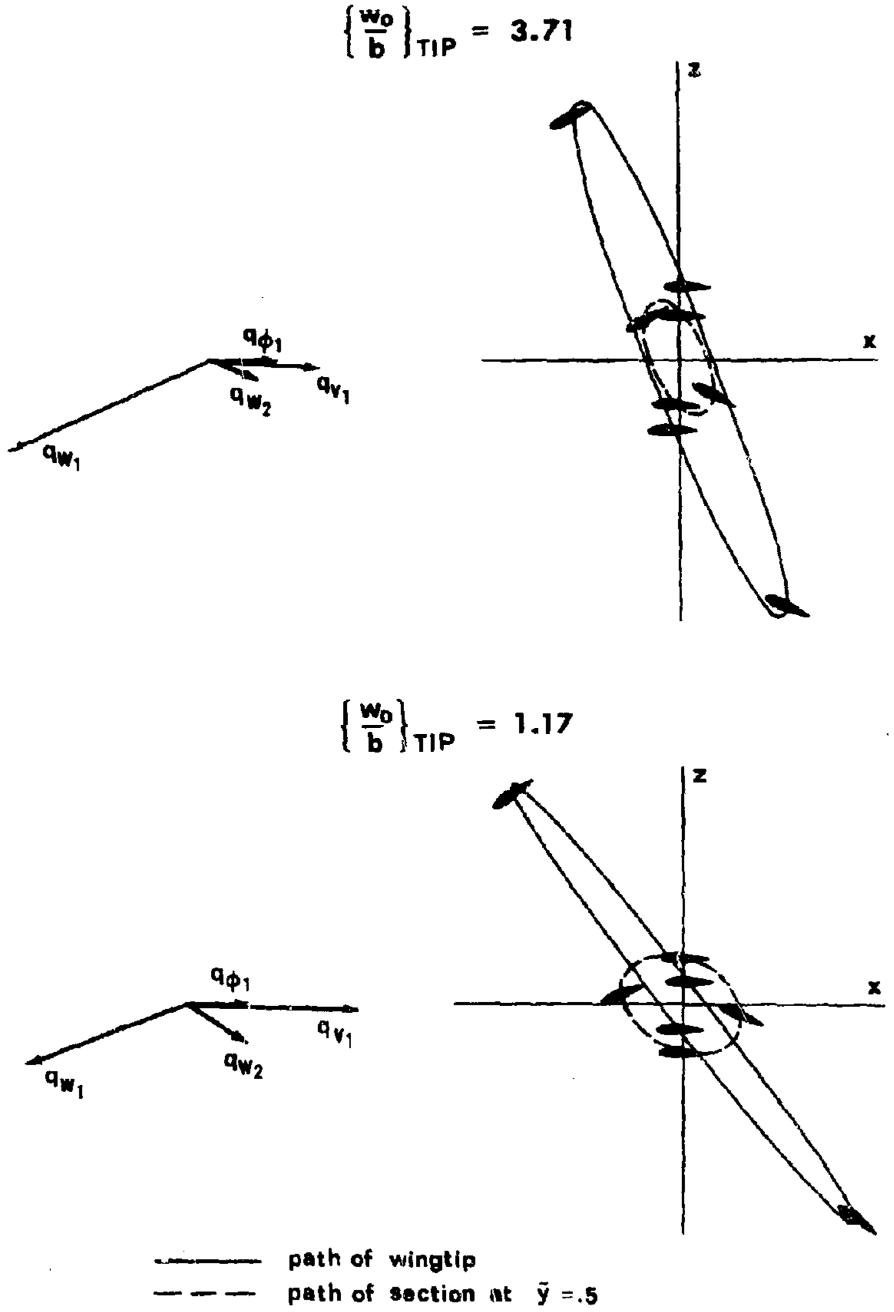

FIGURE 6-16 Physical Appearance of Flutter Mode of Deflected High Aspect Ratio Wing of Fig. 6-13

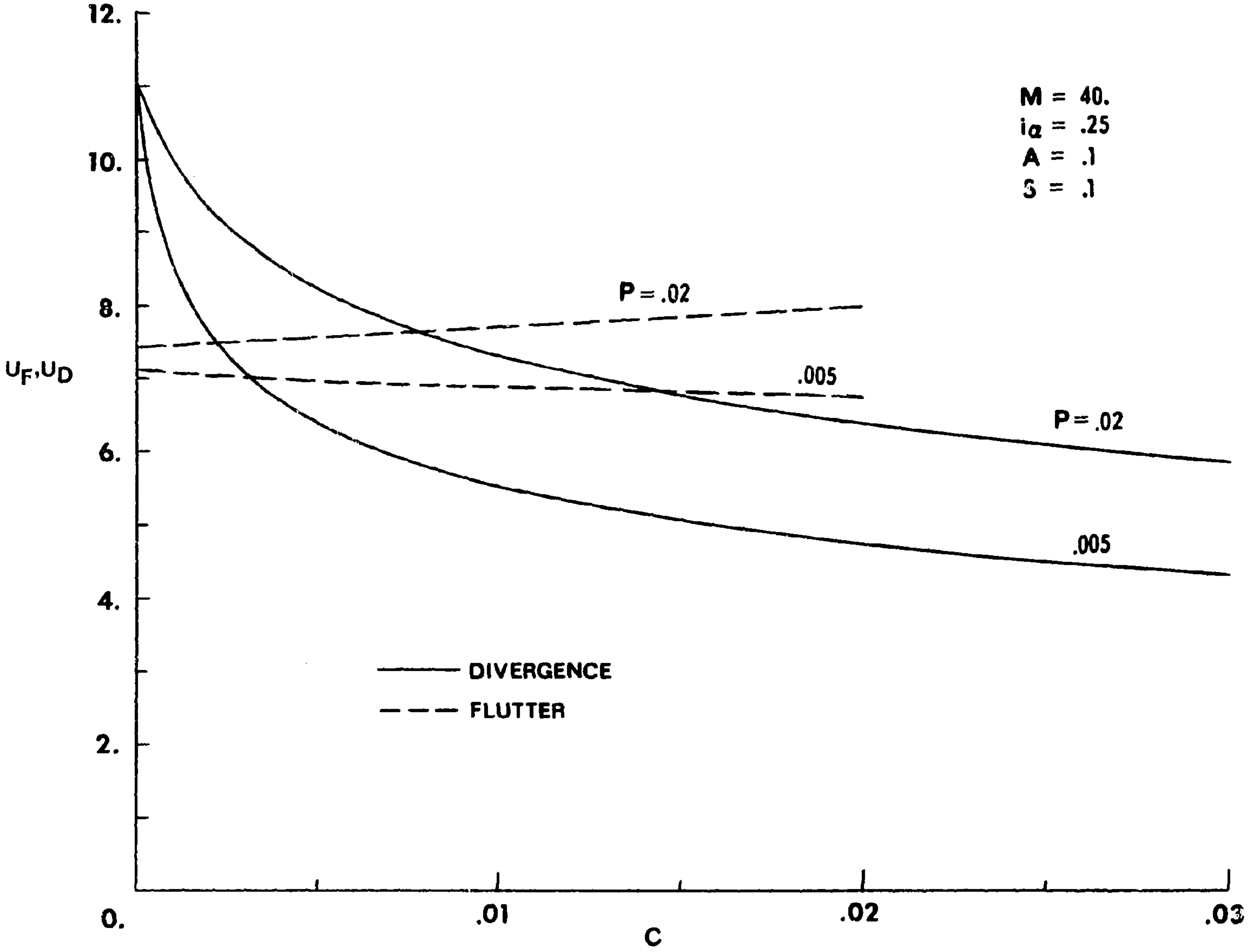

FIGURE 6-17 Comparison of Drag Effect Upon Divergence and Flutter At Zero Steady Lift for the Moderate- and High-Aspect-Ratio Examples

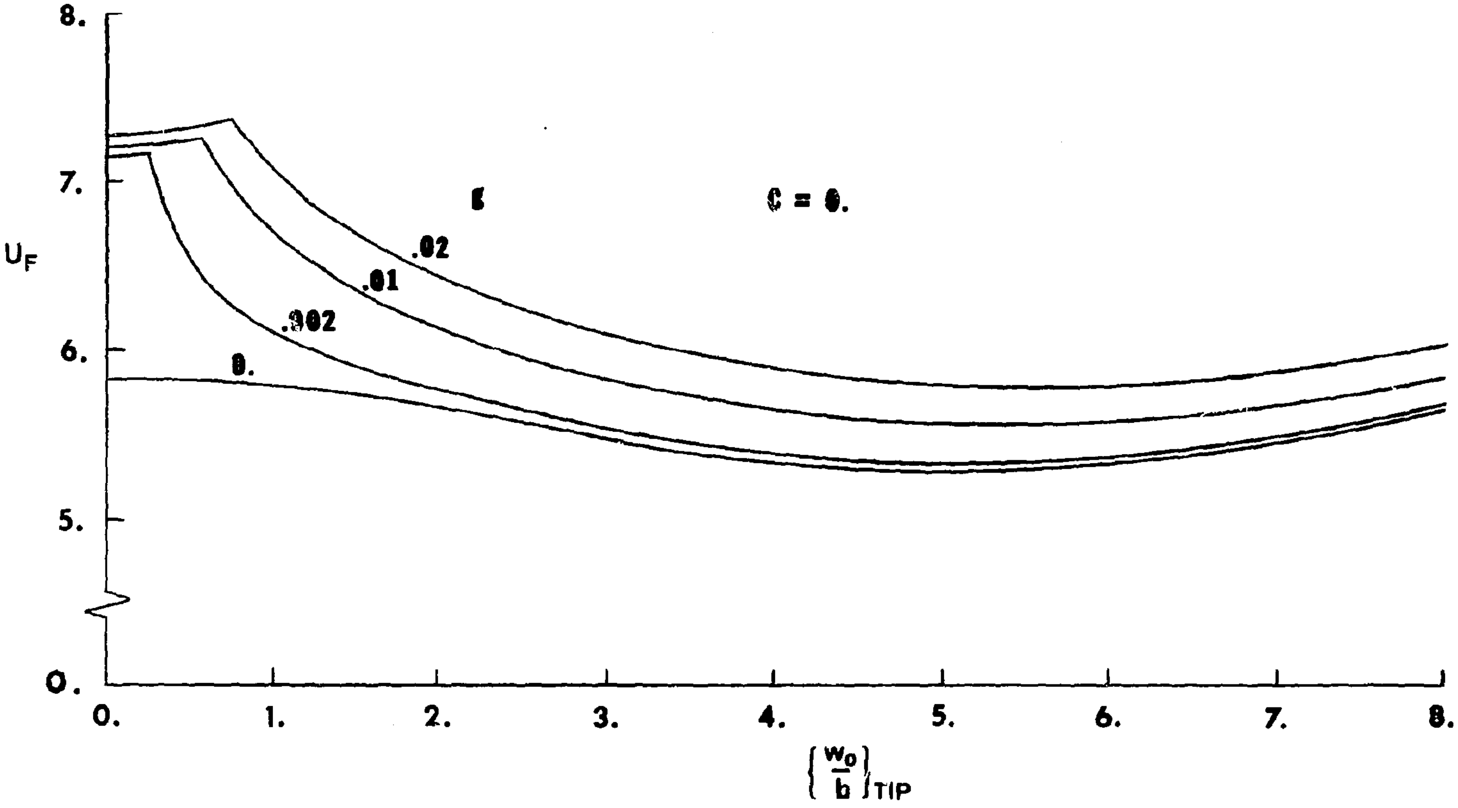

FIGURE 6-18 Effect of Structural Damping on the Fig. 6-13 Stability Boundary

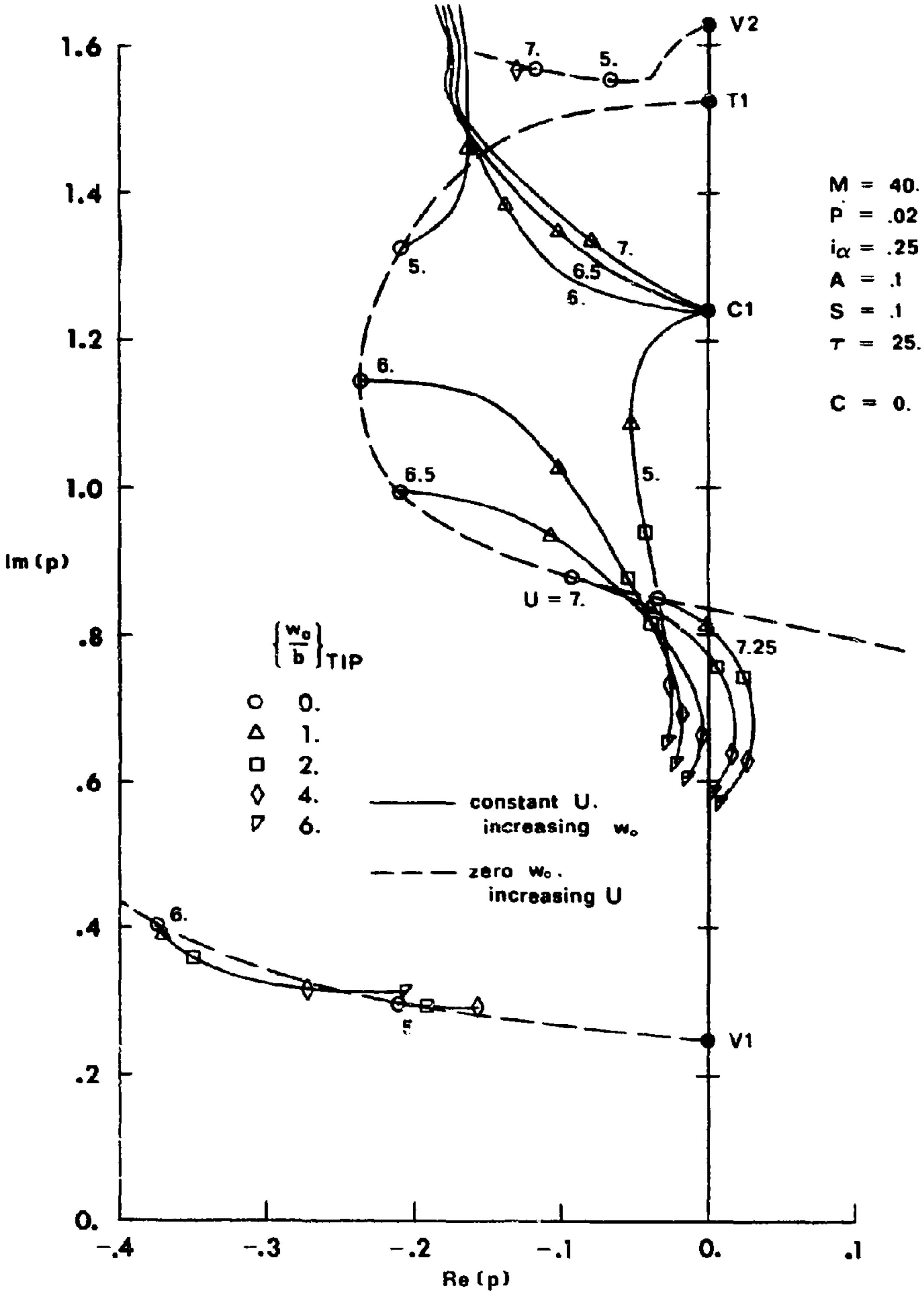

FIGURE 6-19 Locus of Roots for True Aeroelastic Modes, Moderate-Aspect-Ratio Example

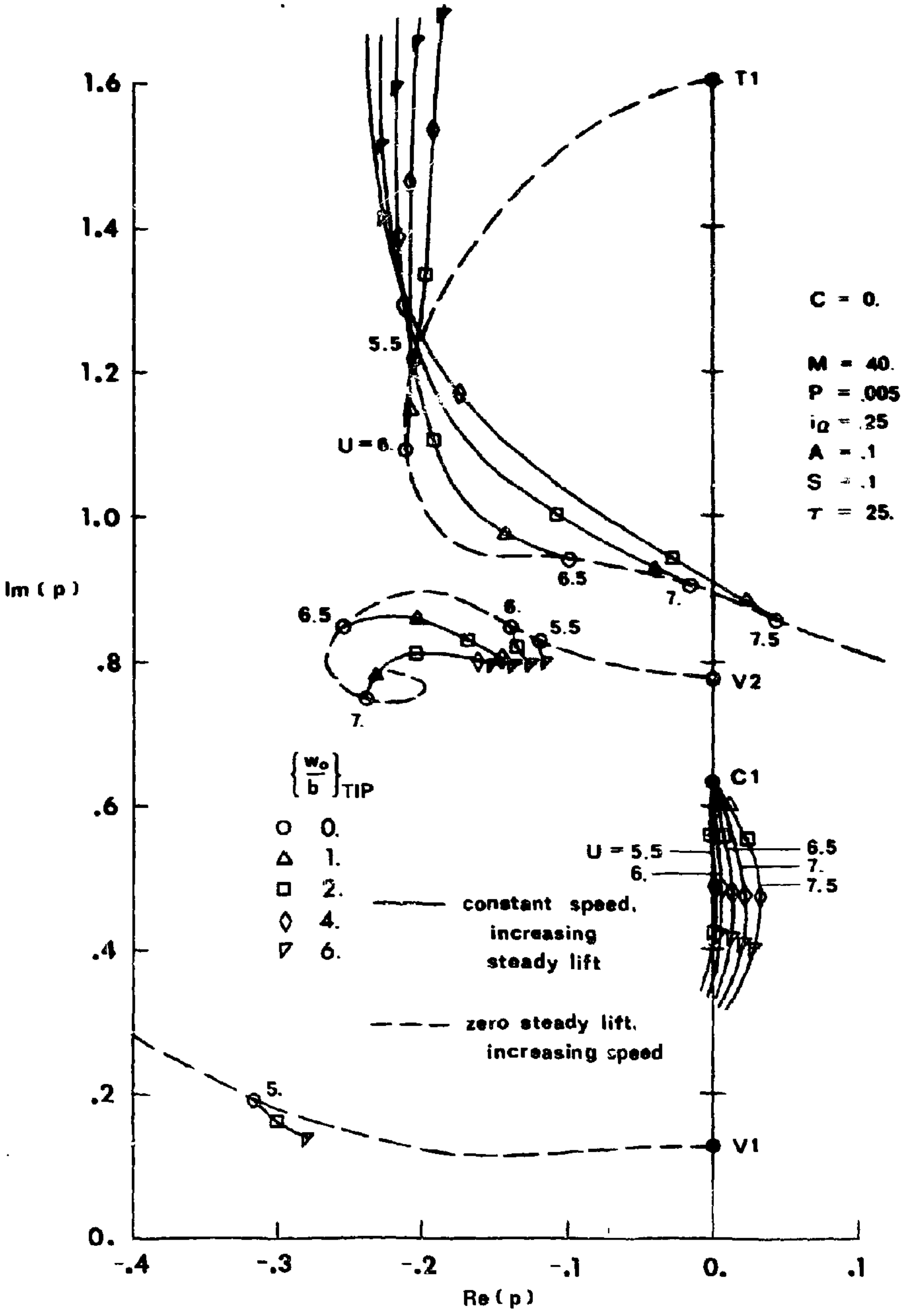

FIGURE 6-20 Locus of Roots for True Aeroelastic Modes, High-Aspect-Ratio Example

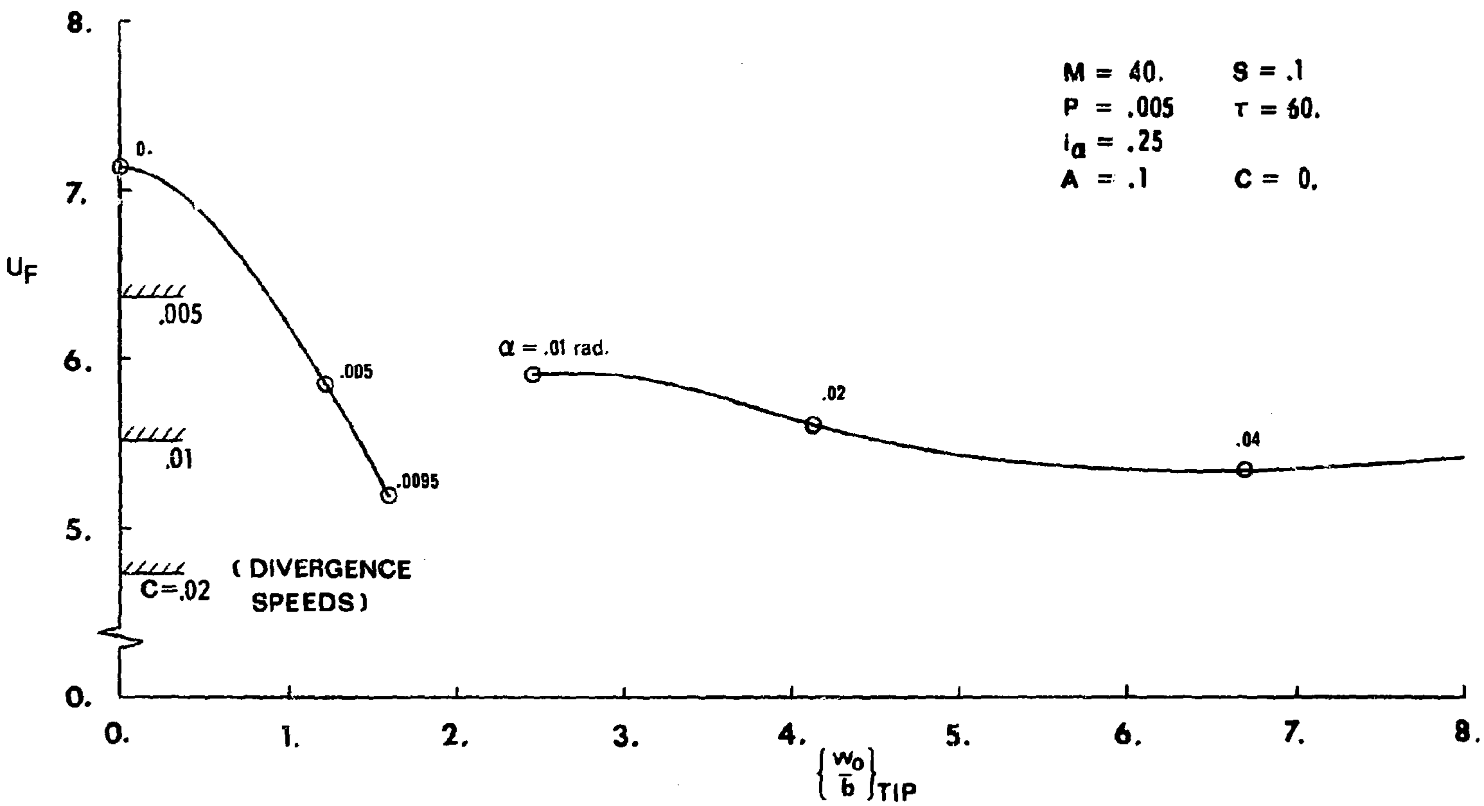

FIGURE 6-21 Flutter Speeds As Affected By Steady Deformation, Large-Aspect-Ratio Example with τ = 60

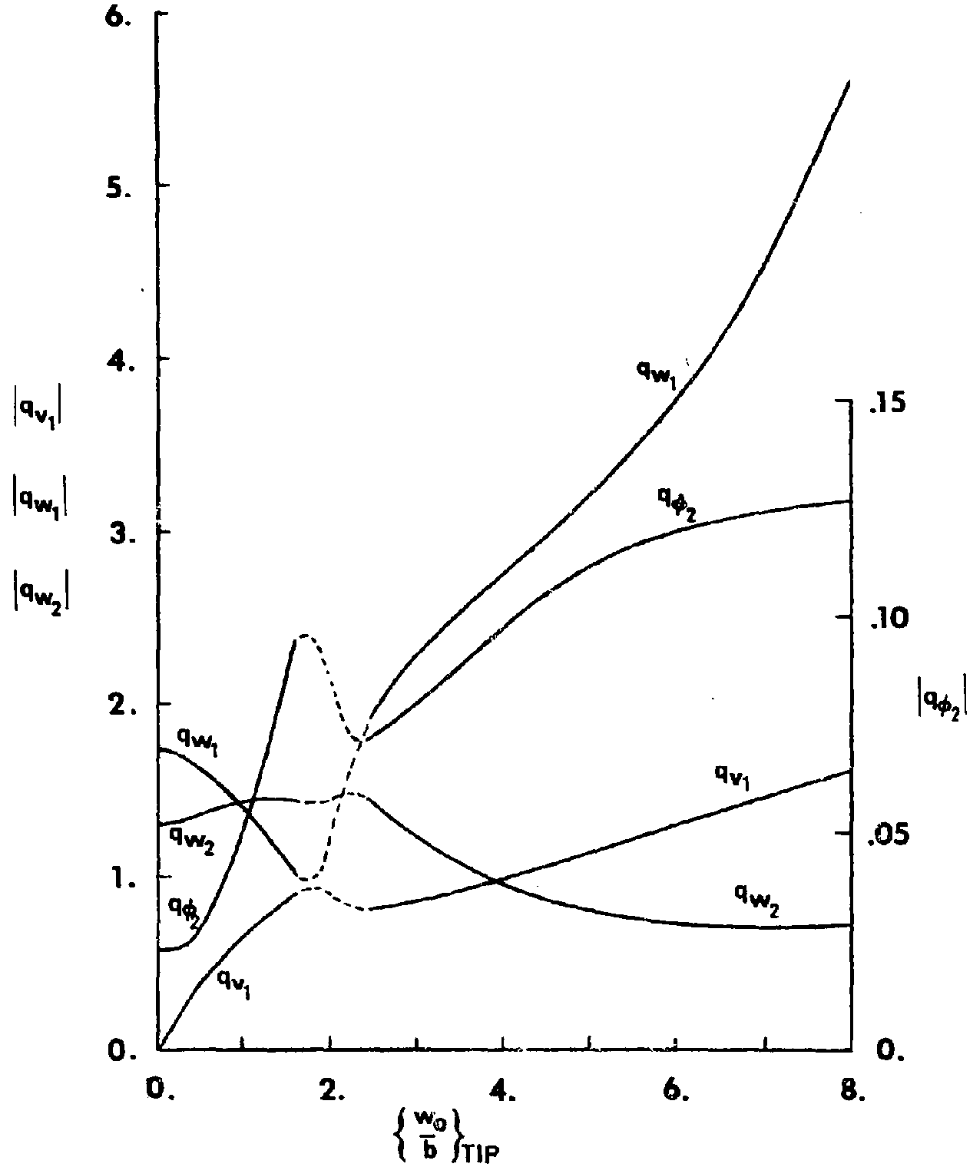

FIGURE 6-22 Flutter Mode Shape Amplitudes for Unit $|q_{\phi_1}|$ Corresponding to Fig. 6-21

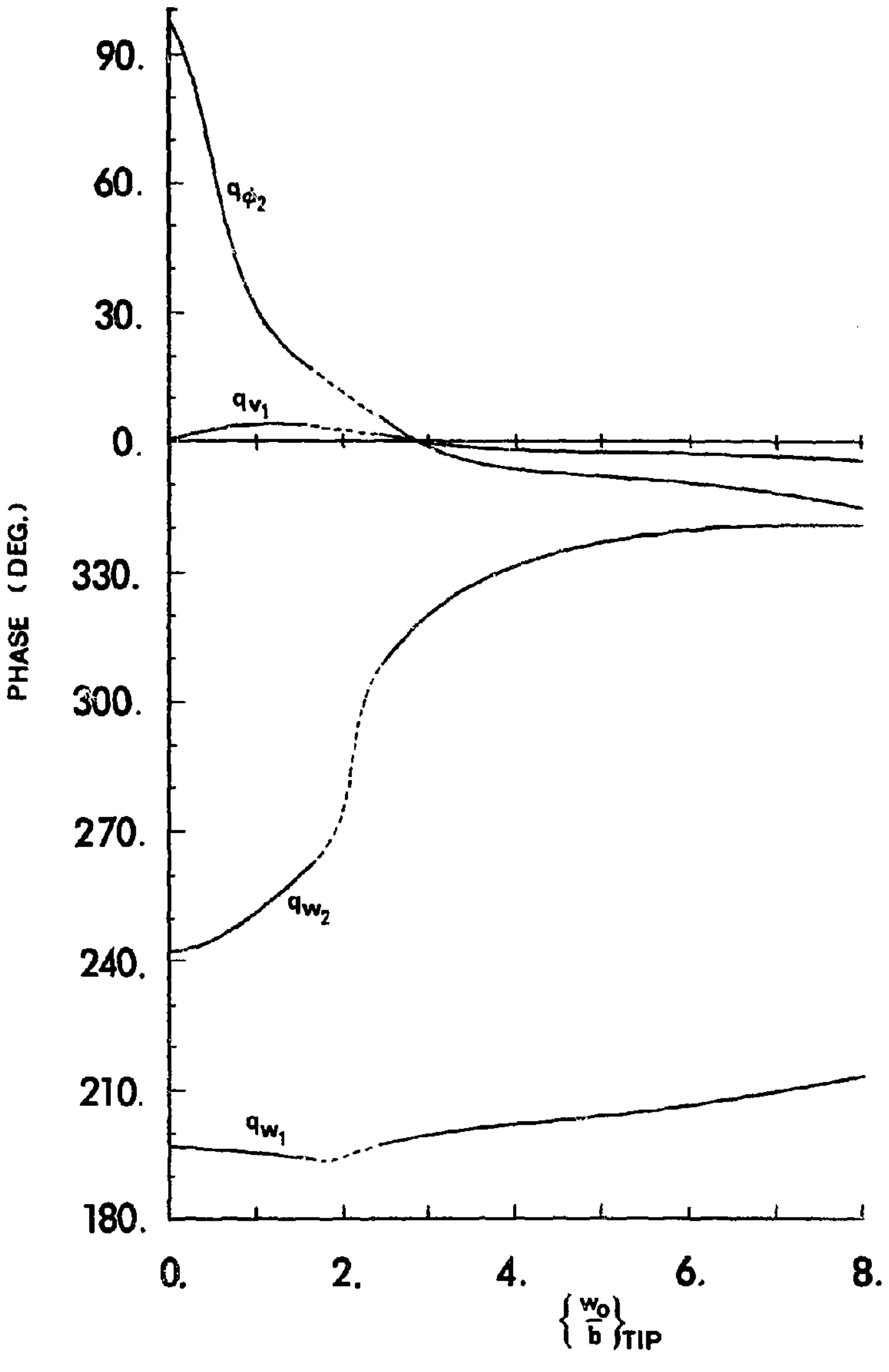

FIGURE 6-23 Flutter Mode Shape Phase Relations for Zero Phase of q_{ϕ_1}, Corresponding to Fig. 6-21

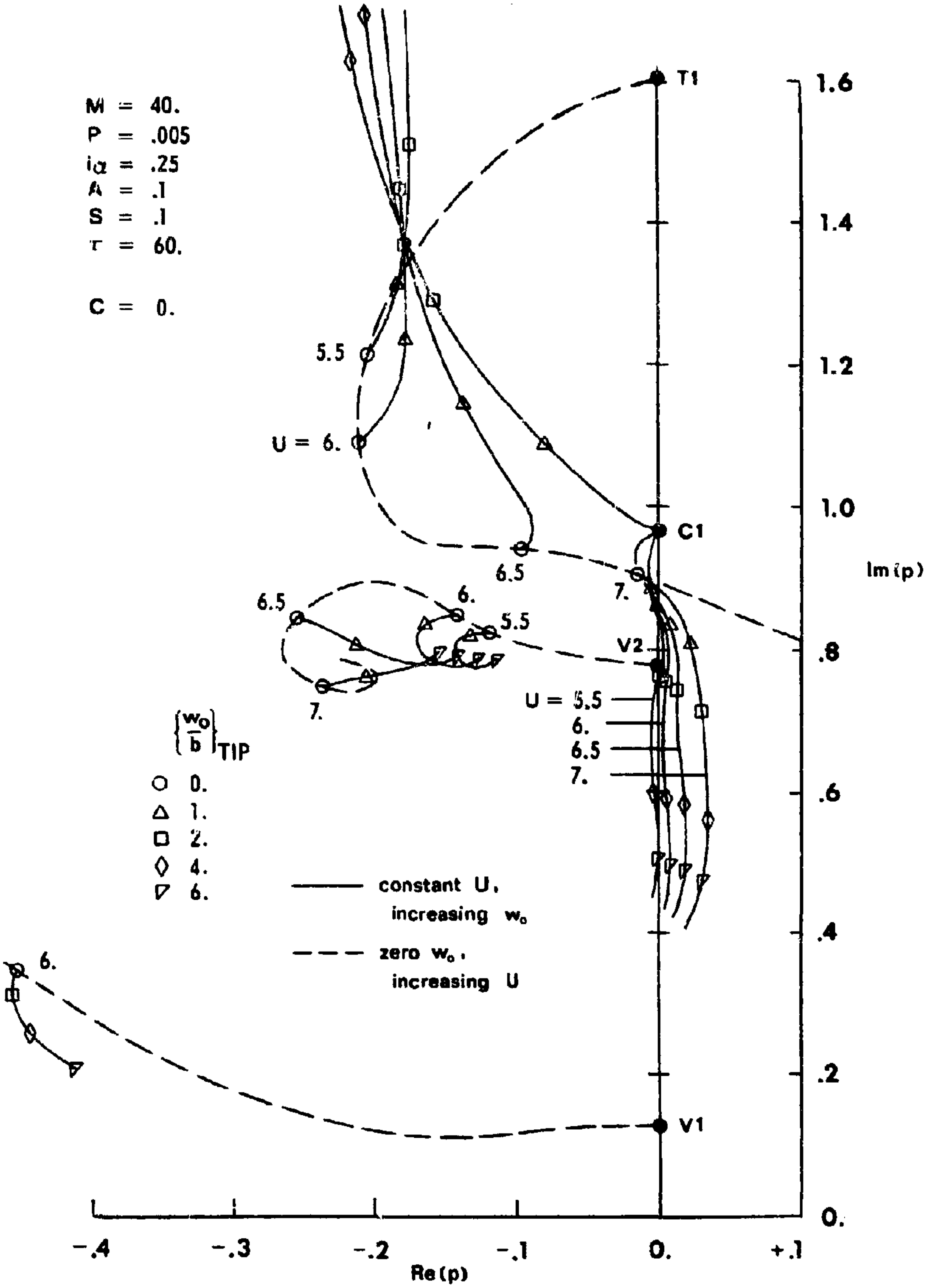

Figure 6-24(a) Locus of Roots for True Aeroelastic Modes, Large-Aspect-Ratio Example with $\tau = 60$

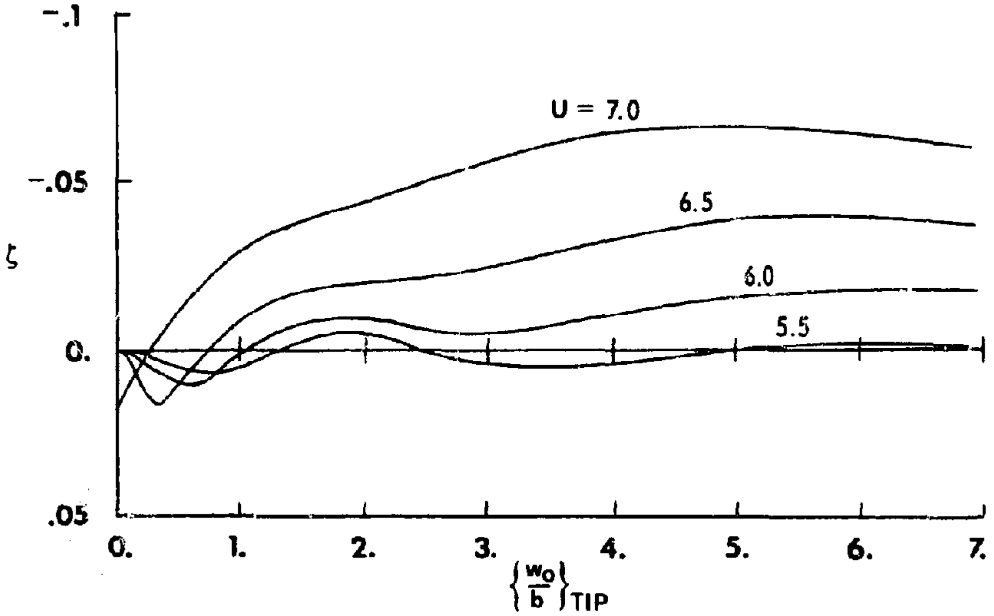

FIGURE 6-24(b) Damping Ratio of Flutter Mode Constant Speed Branches

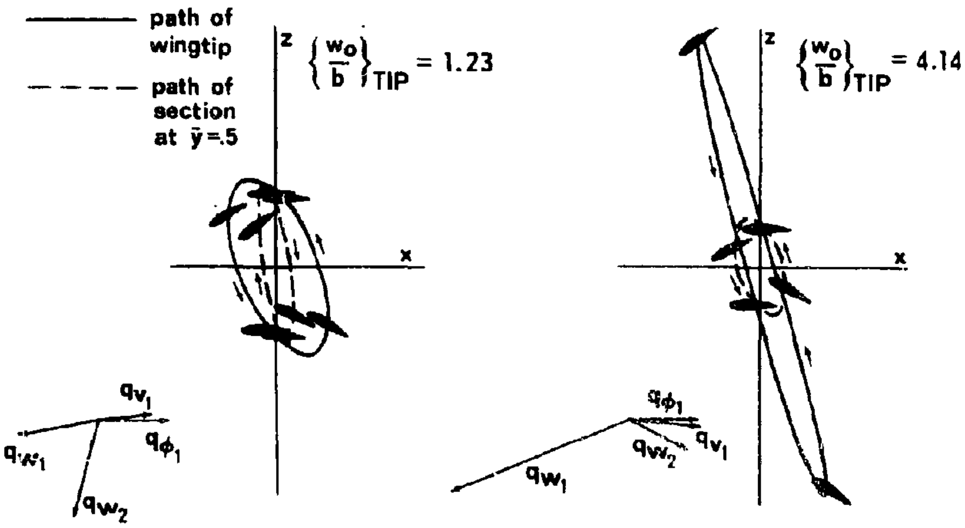

FIGURE 6-25 Physical Appearance of Flutter Modes Defined in Figs. 6-22, 6-23

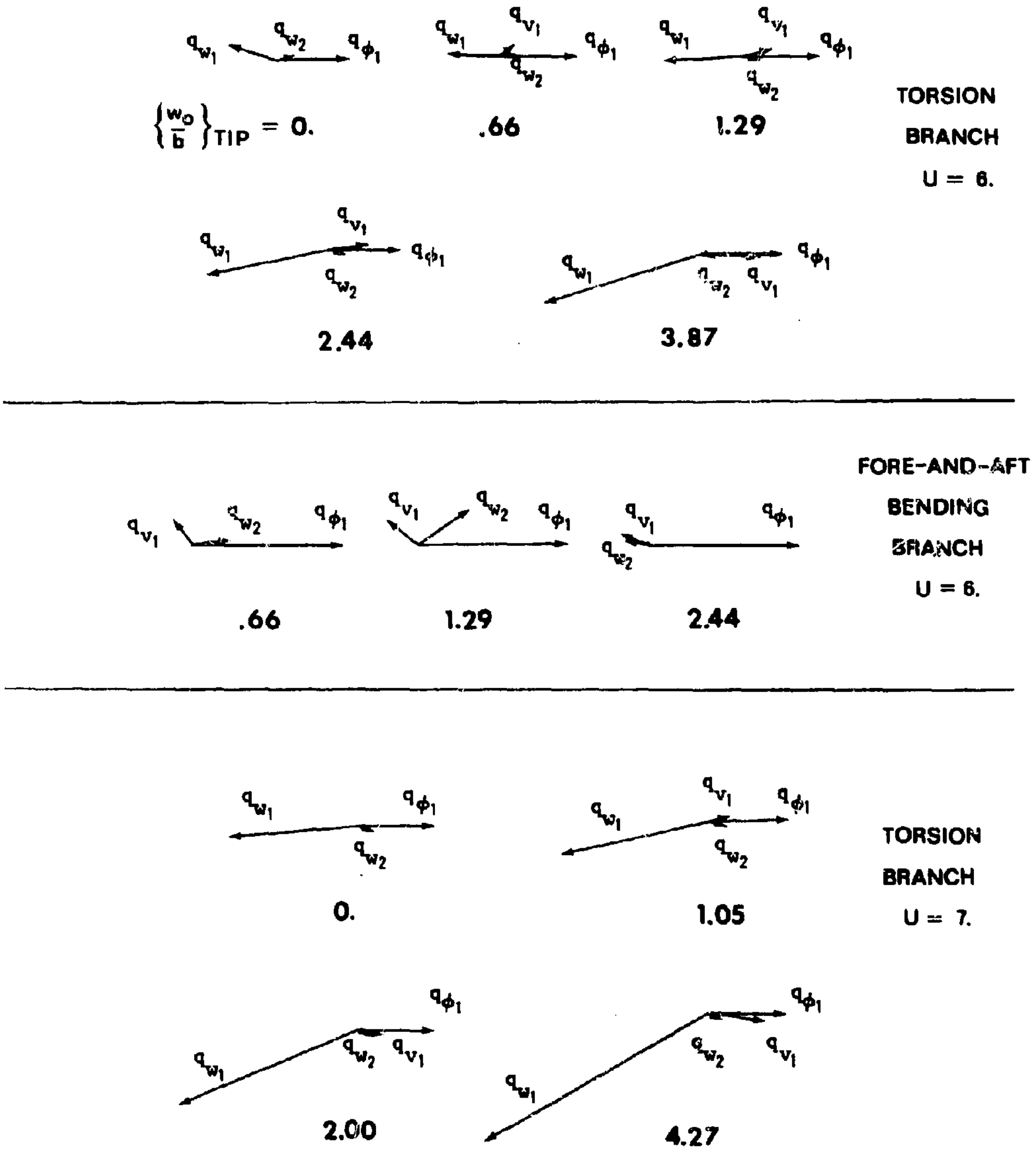

FIGURE 6-26 Mode Shapes for Selected Roots from Fig. 6-19

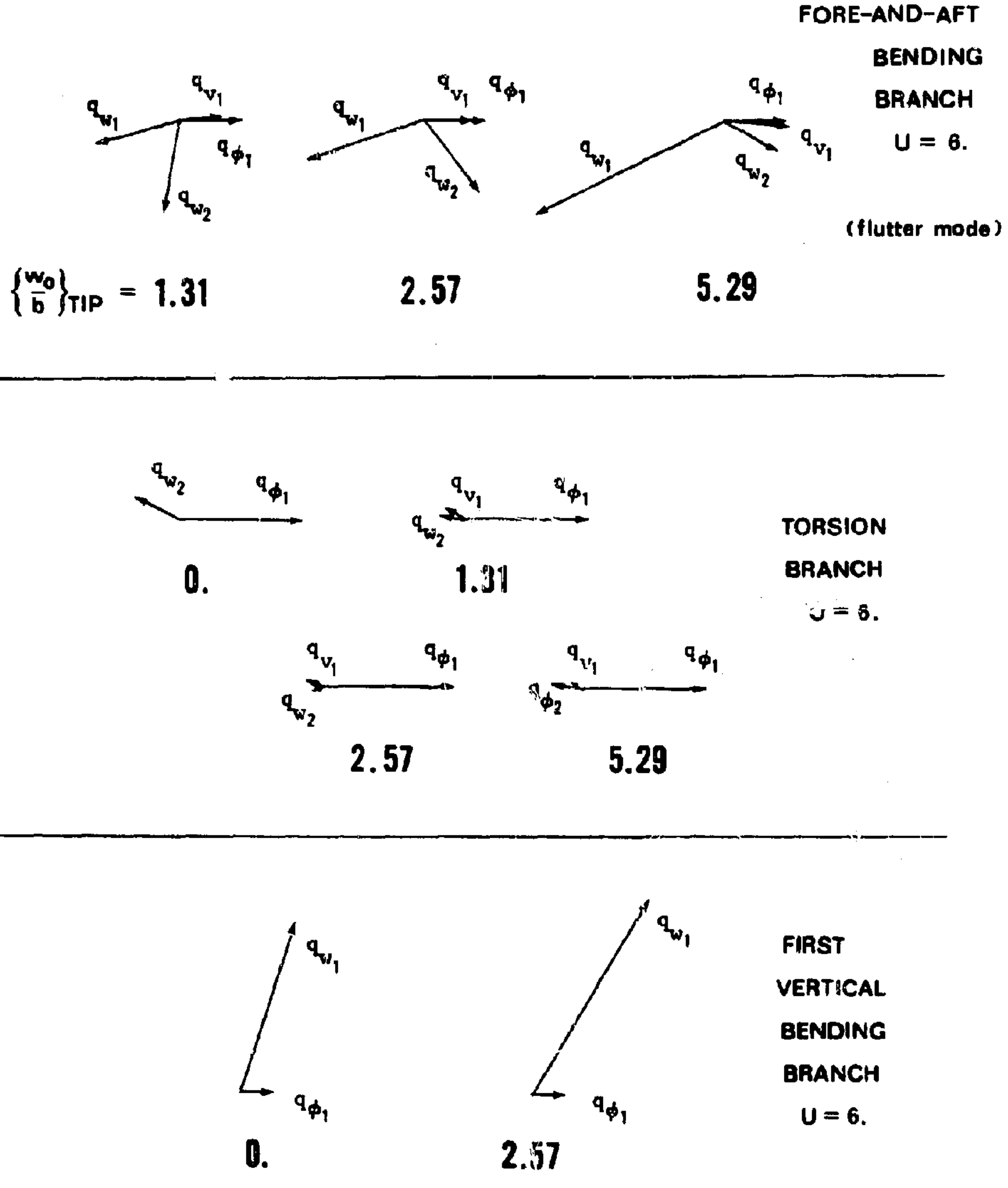

FIGURE 6-27(a) Mode Shapes for Selected Roots from Fig. 6-24

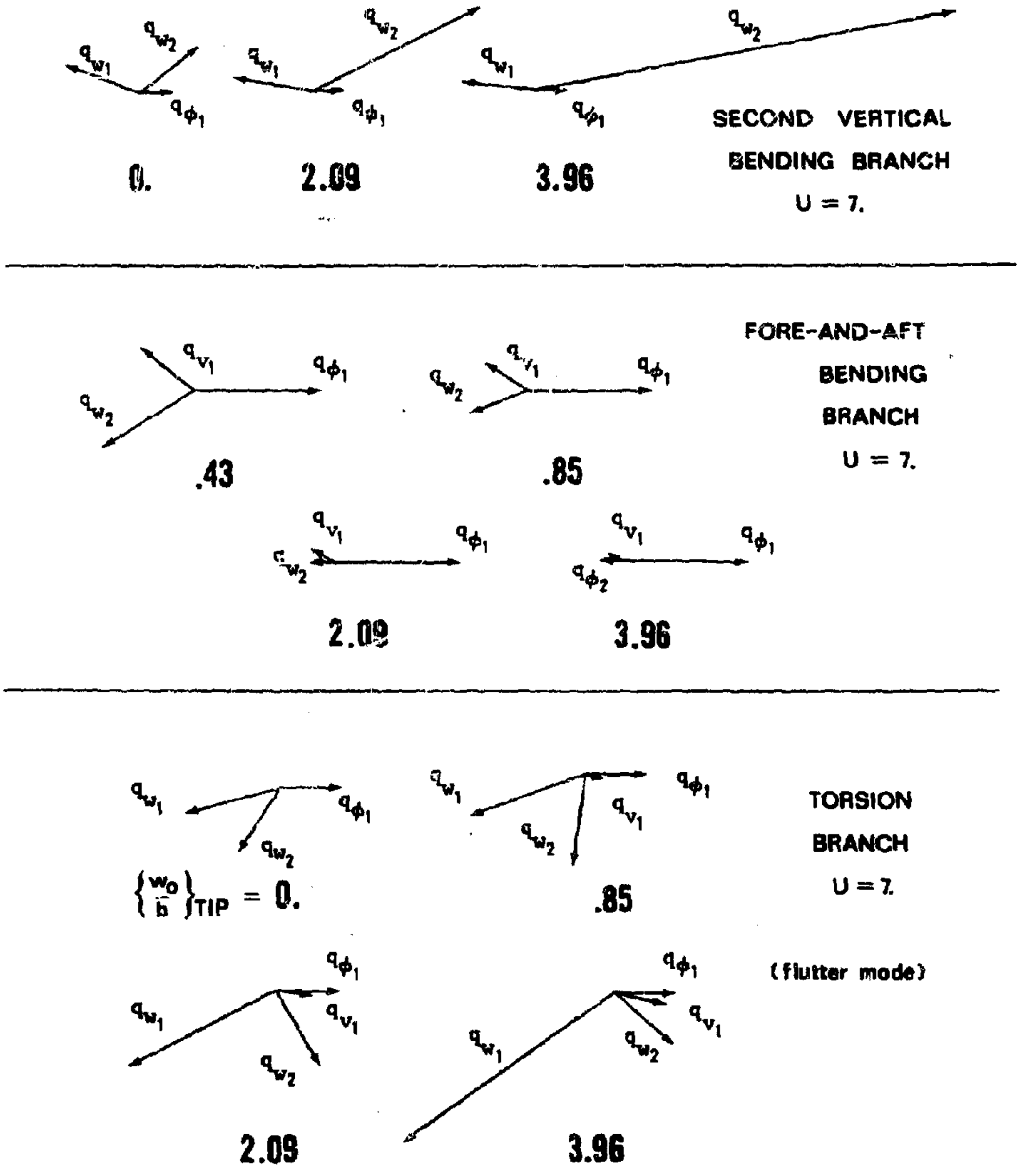
SECOND VERTICAL BENDING BRANCH
U = 7.

FORE-AND-AFT BENDING BRANCH
U = 7.

TORSION BRANCH
U = 7.
(flutter mode)

FIGURE 6-27(b)

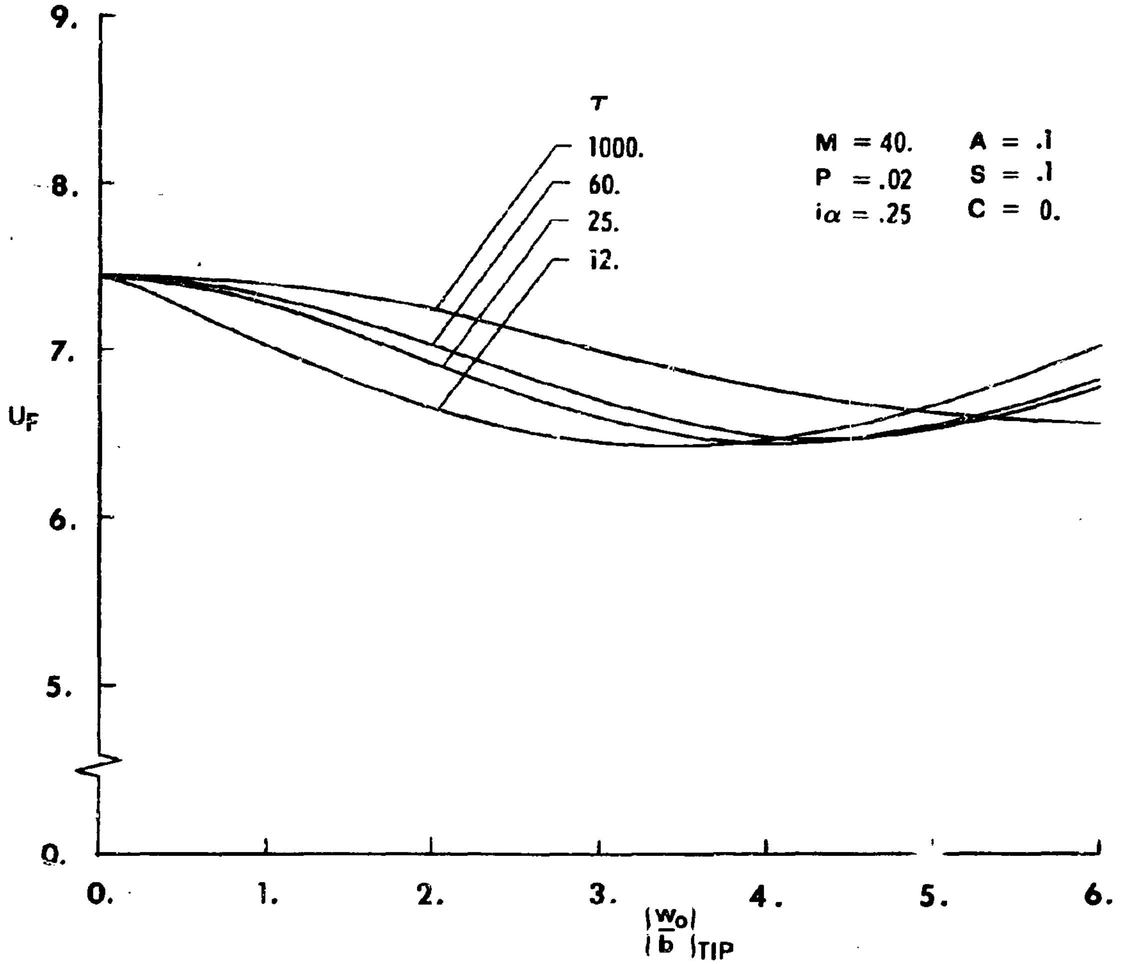

FIGURE 6-28 Effect of τ on Flutter Speeds, Moderate-Aspect-Ratio Example

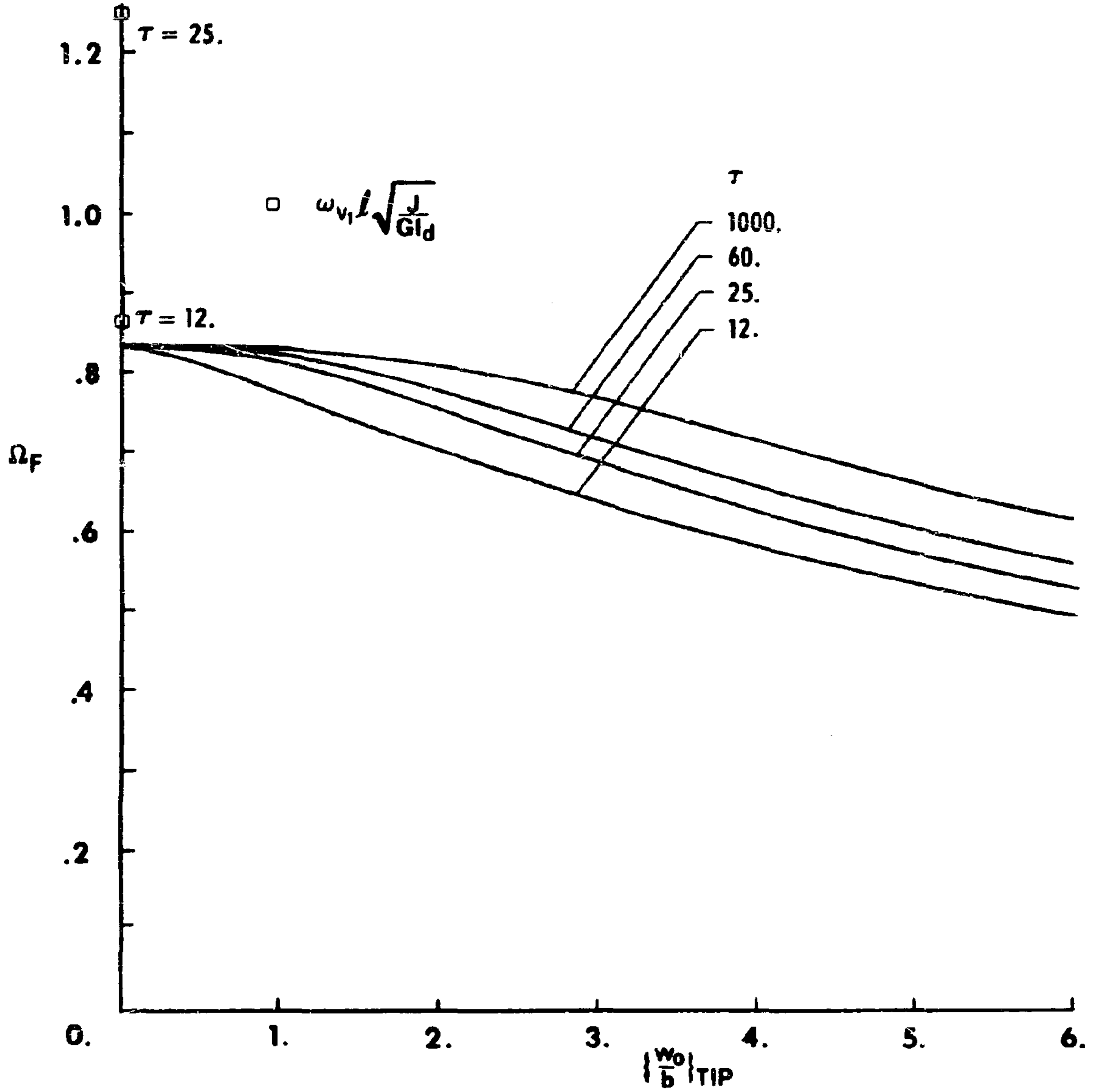

FIGURE 6-29 Effect of τ on Flutter Frequencies, Moderate-Aspect-Ratio Example

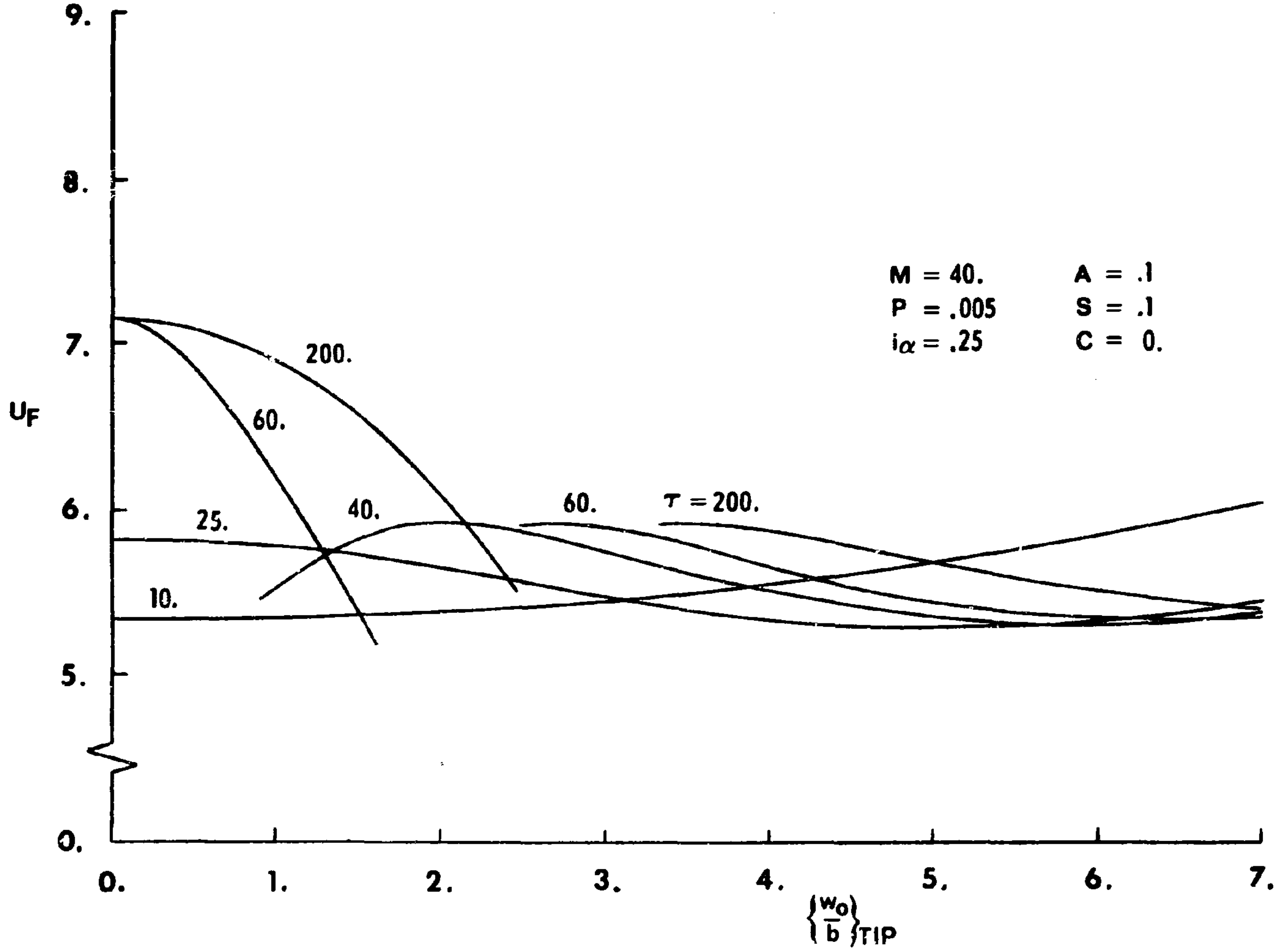

FIGURE 6-30 Effect of τ On Flutter Speeds, Large-Aspect-Ratio Example

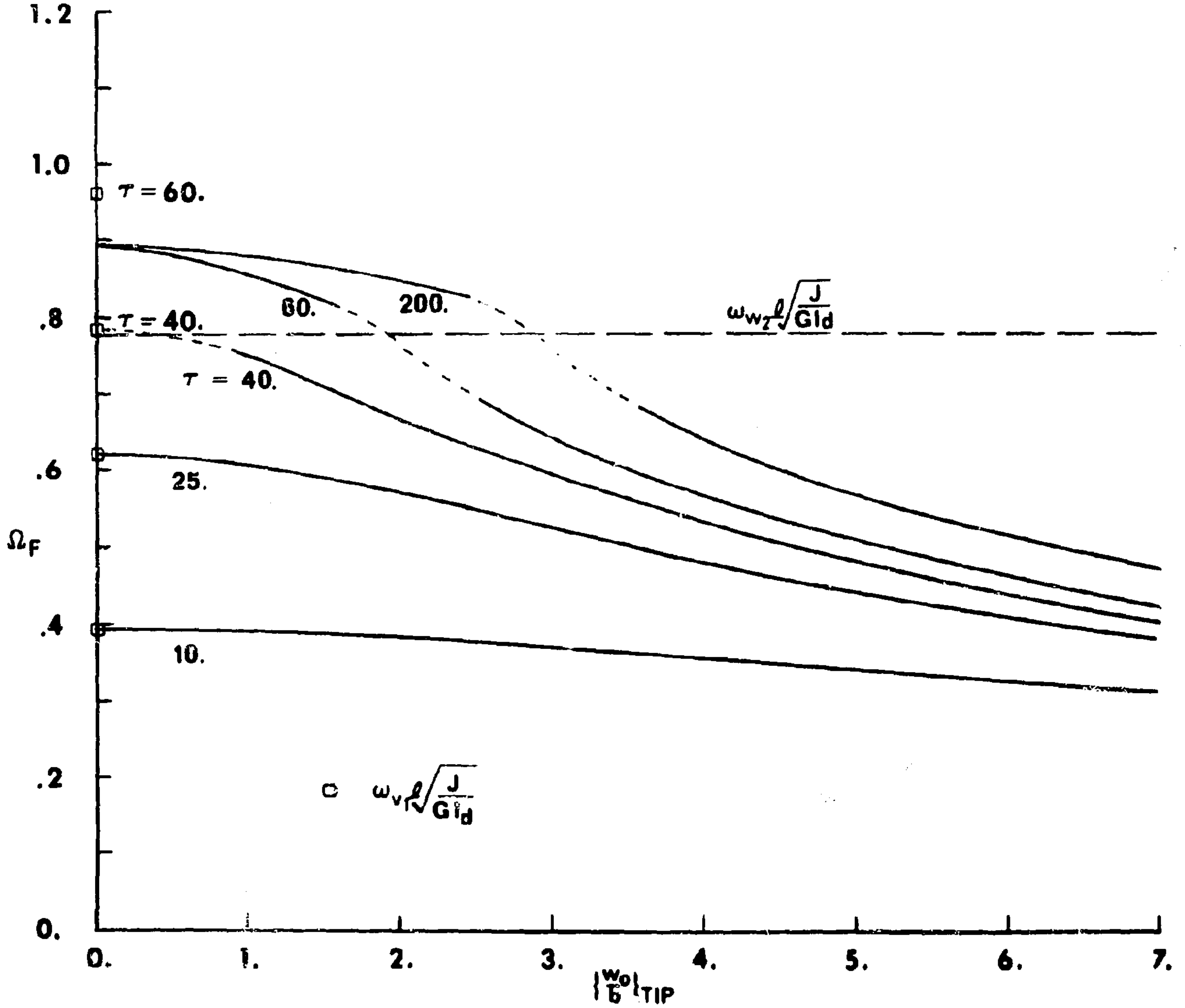

FIGURE 6-31 Effect of τ On Flutter Frequencies, Large-Aspect-Ratio Example

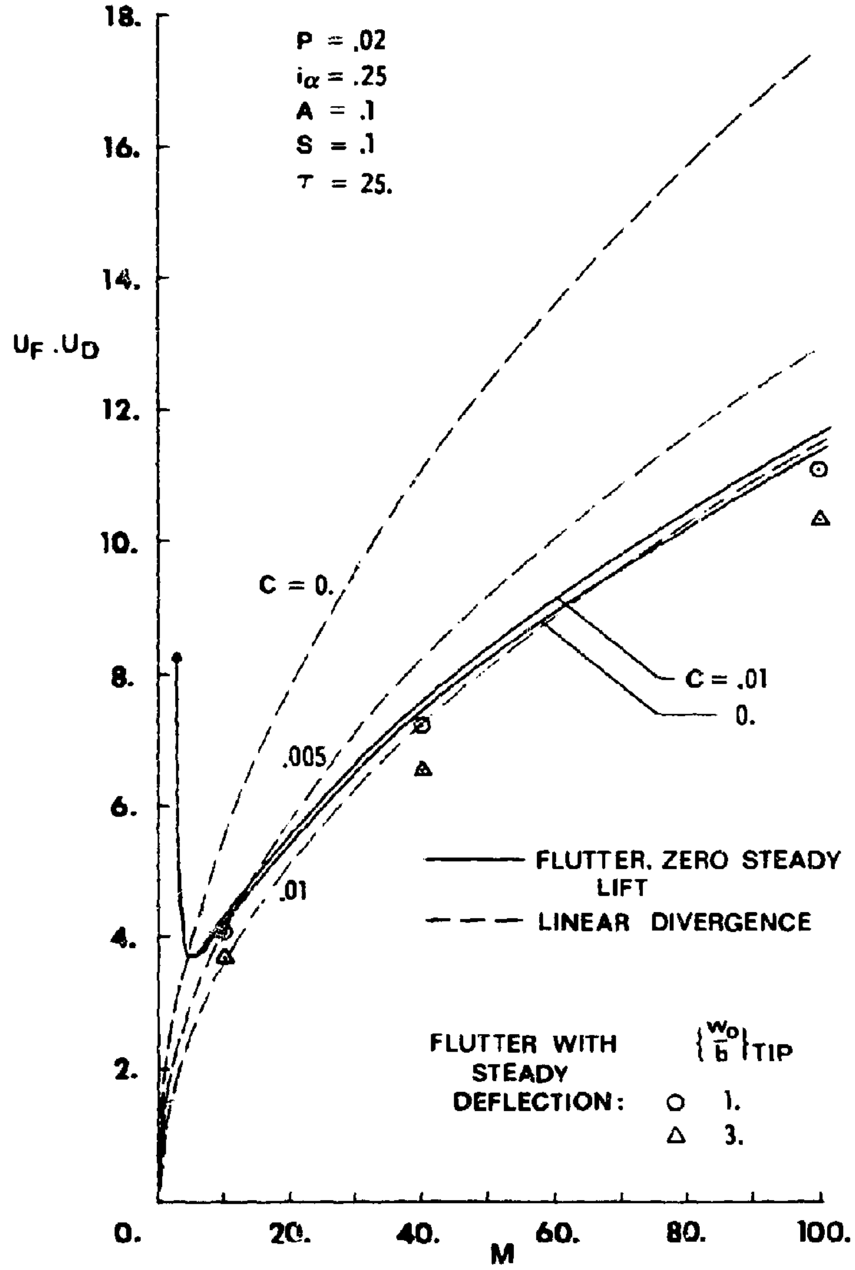

Figure 6-32 Effect of Mass Ratio on Divergence and Flutter, Moderate-Aspect-Ratio Example

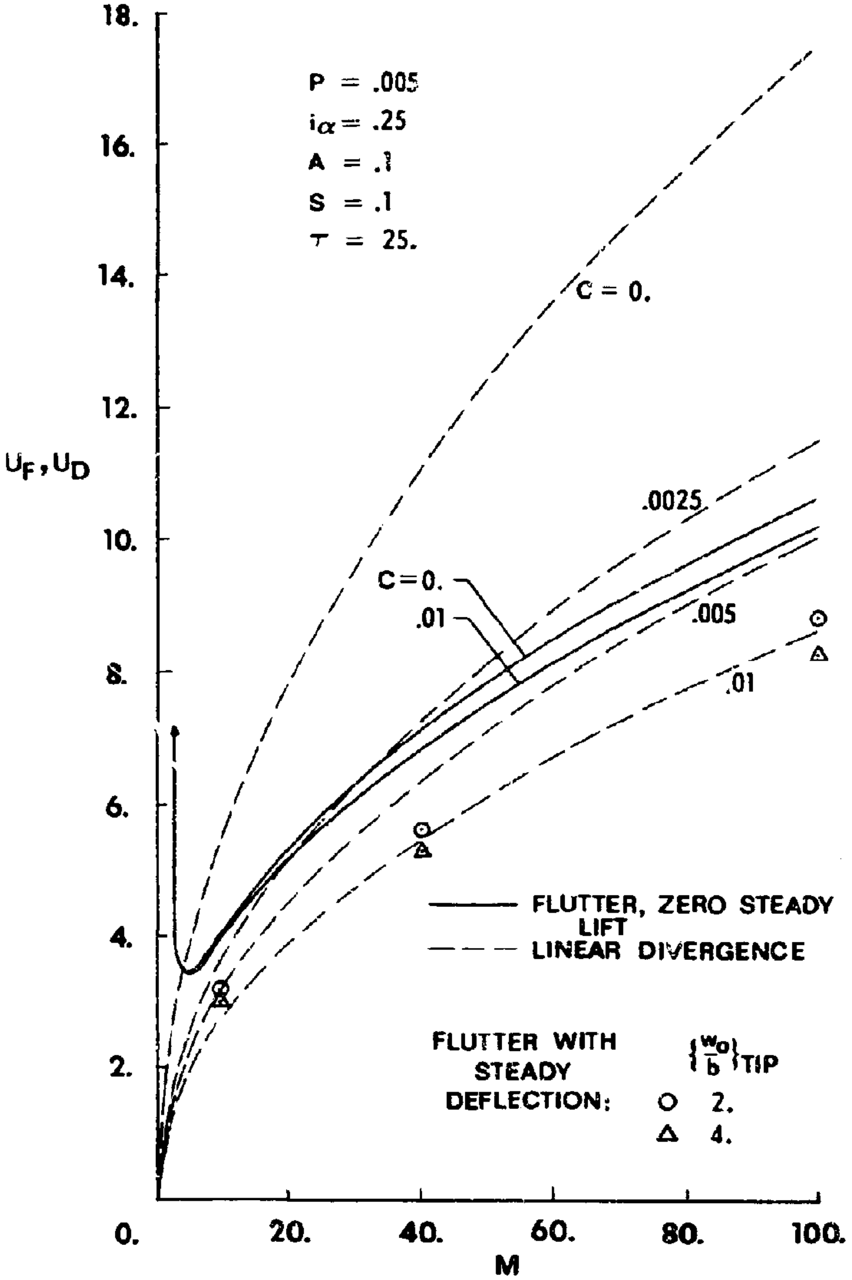

FIGURE 6-33 Effect of Mass Ratio on Divergence and Flutter, Large-Aspect-Ratio Example

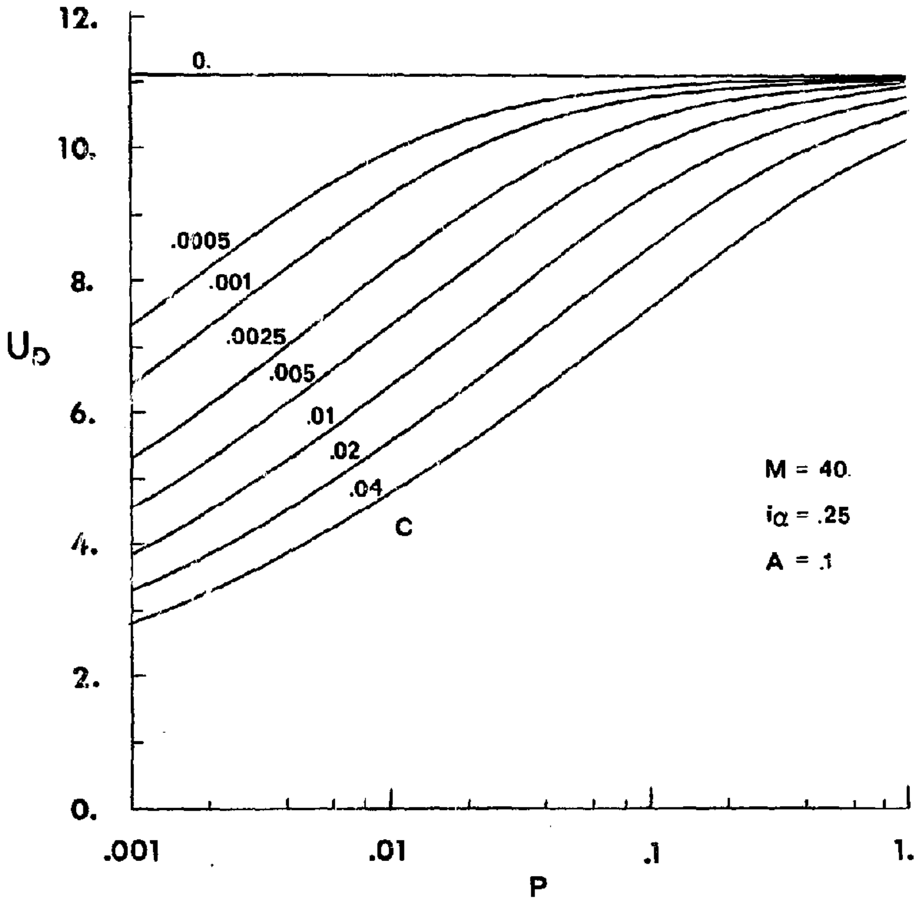

FIGURE 6-34 Divergence Speeds for Selected Values of Drag Parameter C as Aspect Ratio Parameter P Varies

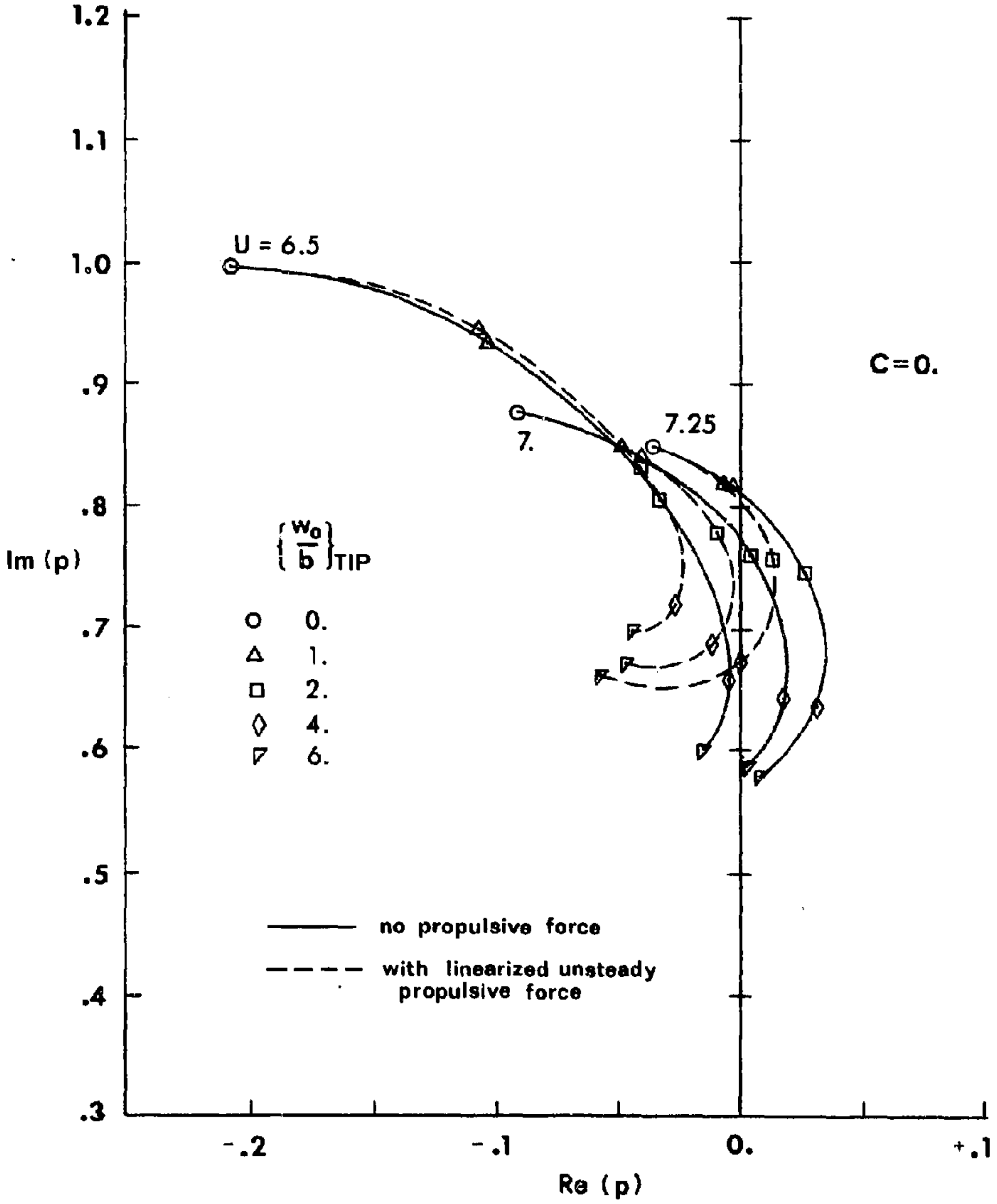

FIGURE 6-35 Effect of Including Unsteady Leading Edge Suction Forces Upon the Constant Speed Branches of Fig. 6-19

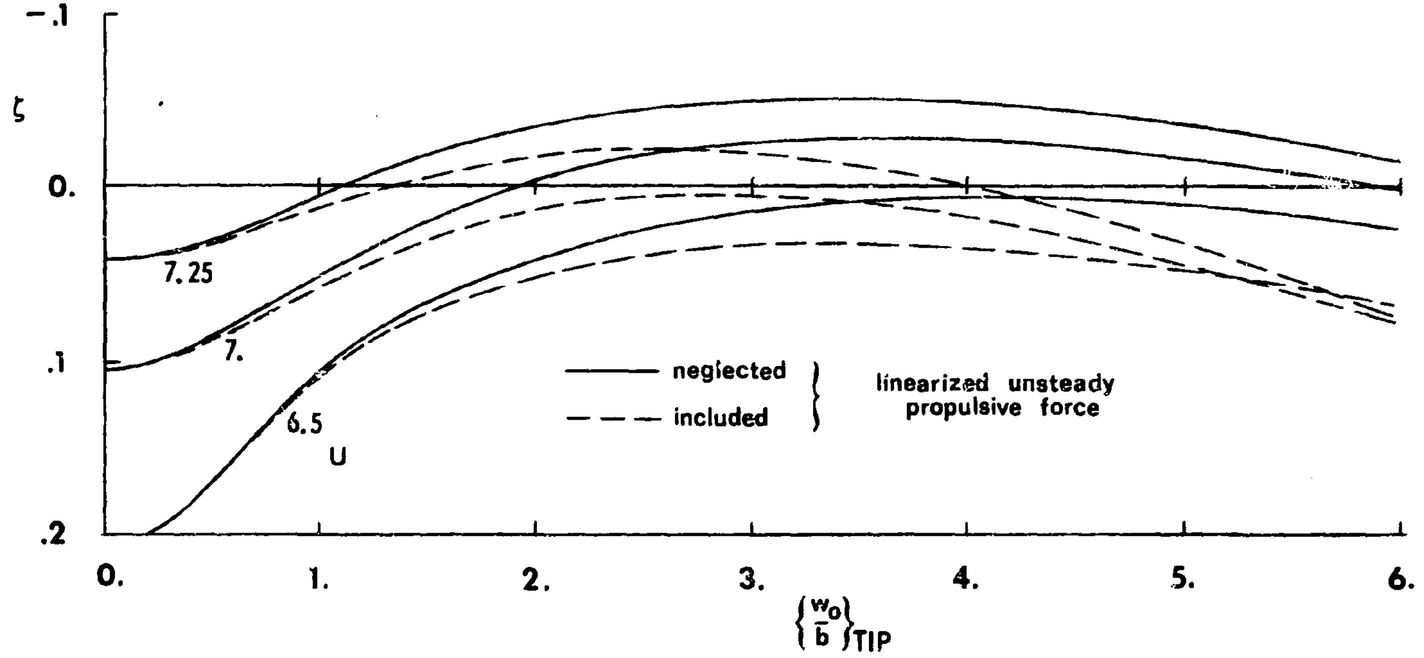

FIGURE 6-36 Damping Ratio of the Branches in Fig. 6-34

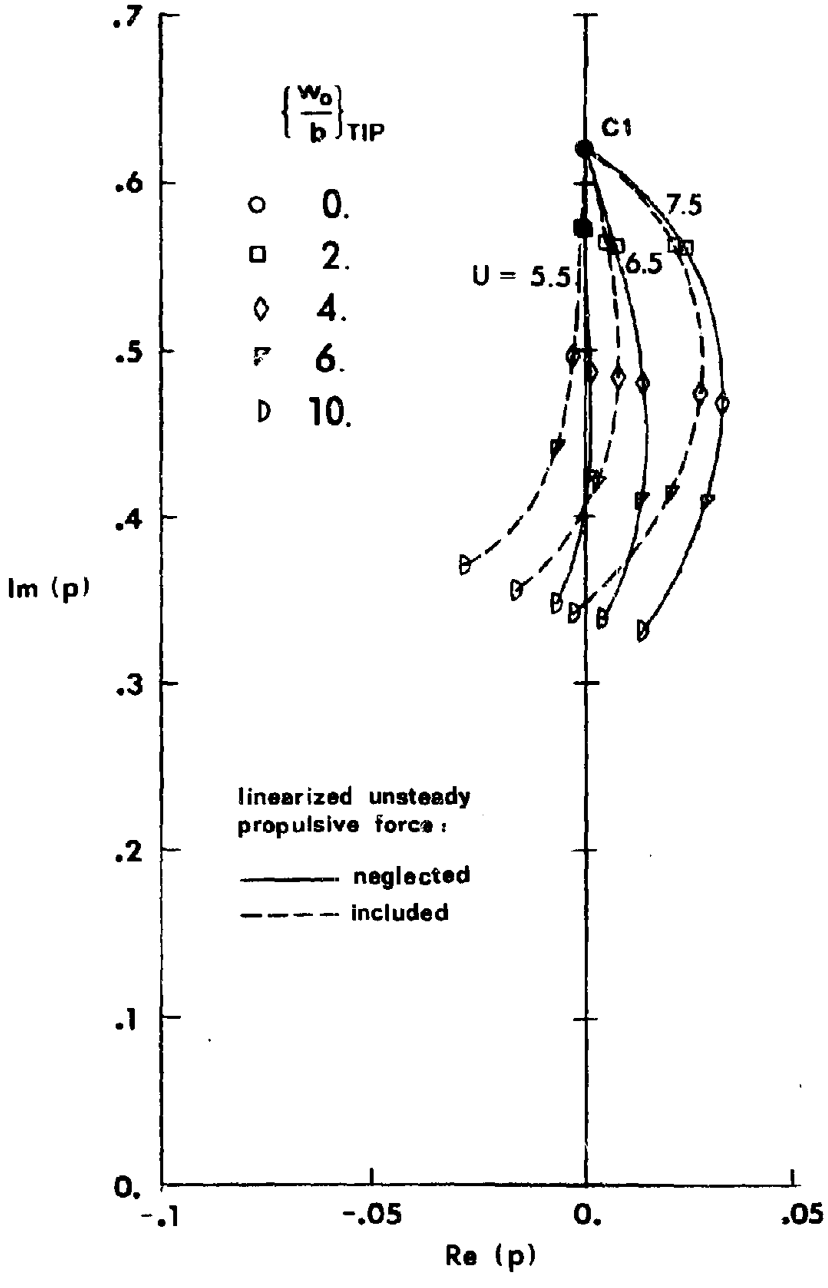

FIGURE 6-37 Effect of Allowing for Unsteady Leading Edge Suction Upon the Constant Speed Branches of Fig. 20

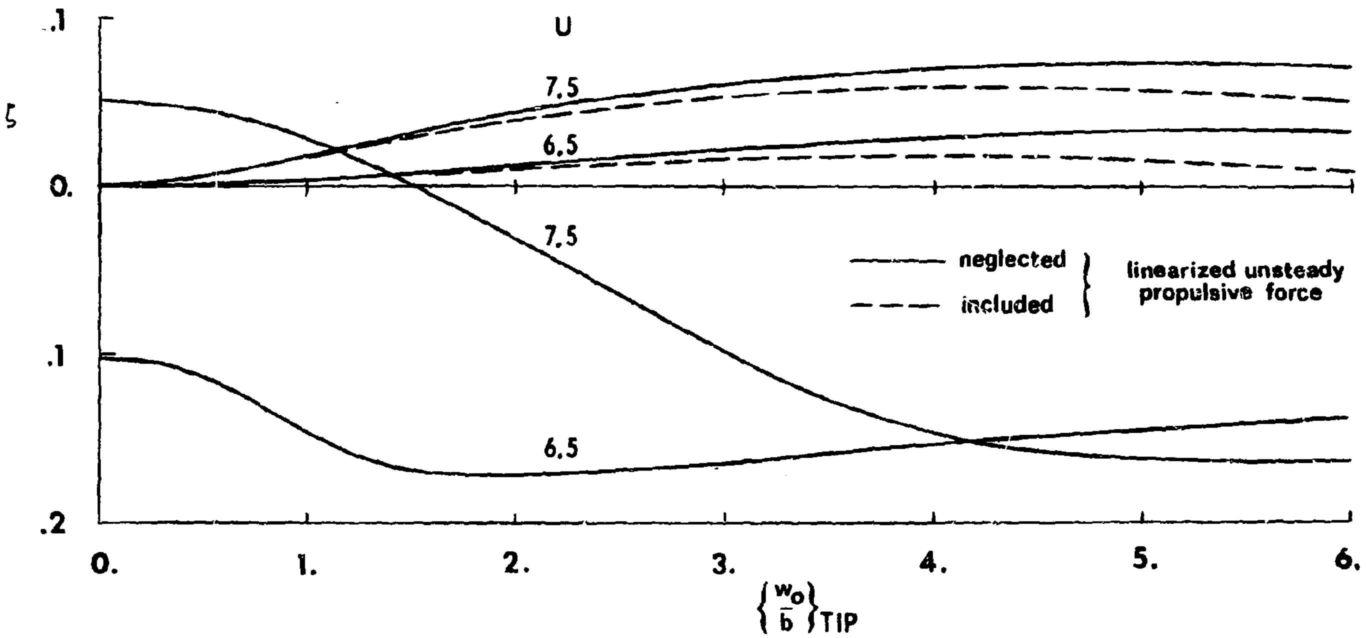

FIGURE 6-38 Damping Ratio of the Branches in Fig. 6-37, with the High Frequency Constant-Speed Branches in Fig. 6-20 Added

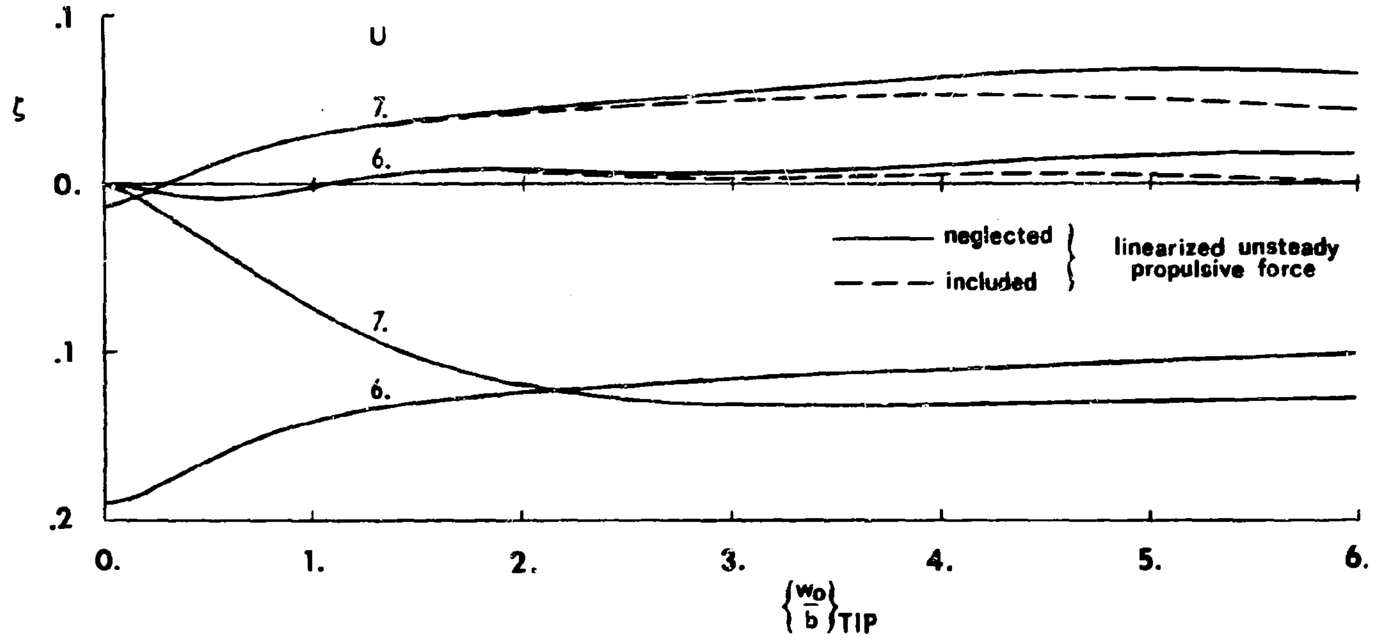

FIGURE 6-39 Damping Ratio of Constant-Speed Branches in Fig. 6-24, With the Effect of Allowing for Unsteady Leading Edge Suction Also Shown

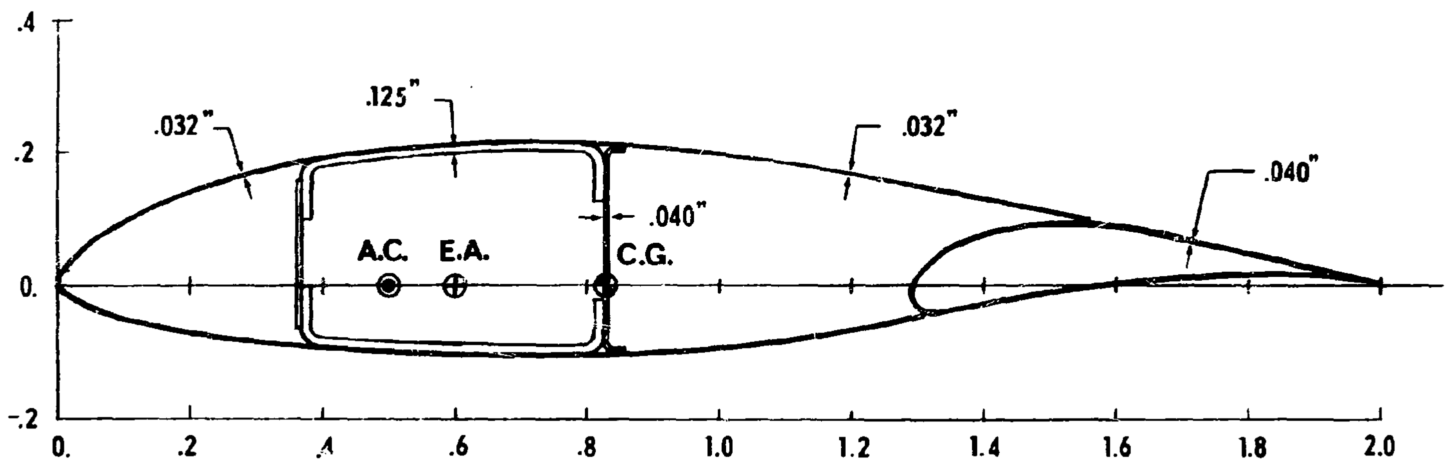

FIGURE 6-40 Typical Wing Section of Gemini Sailplane Used to Determine the Six Dimensionless Parameters, Construction is Aluminum of Indicated Thickness, Dimensions are in Feet

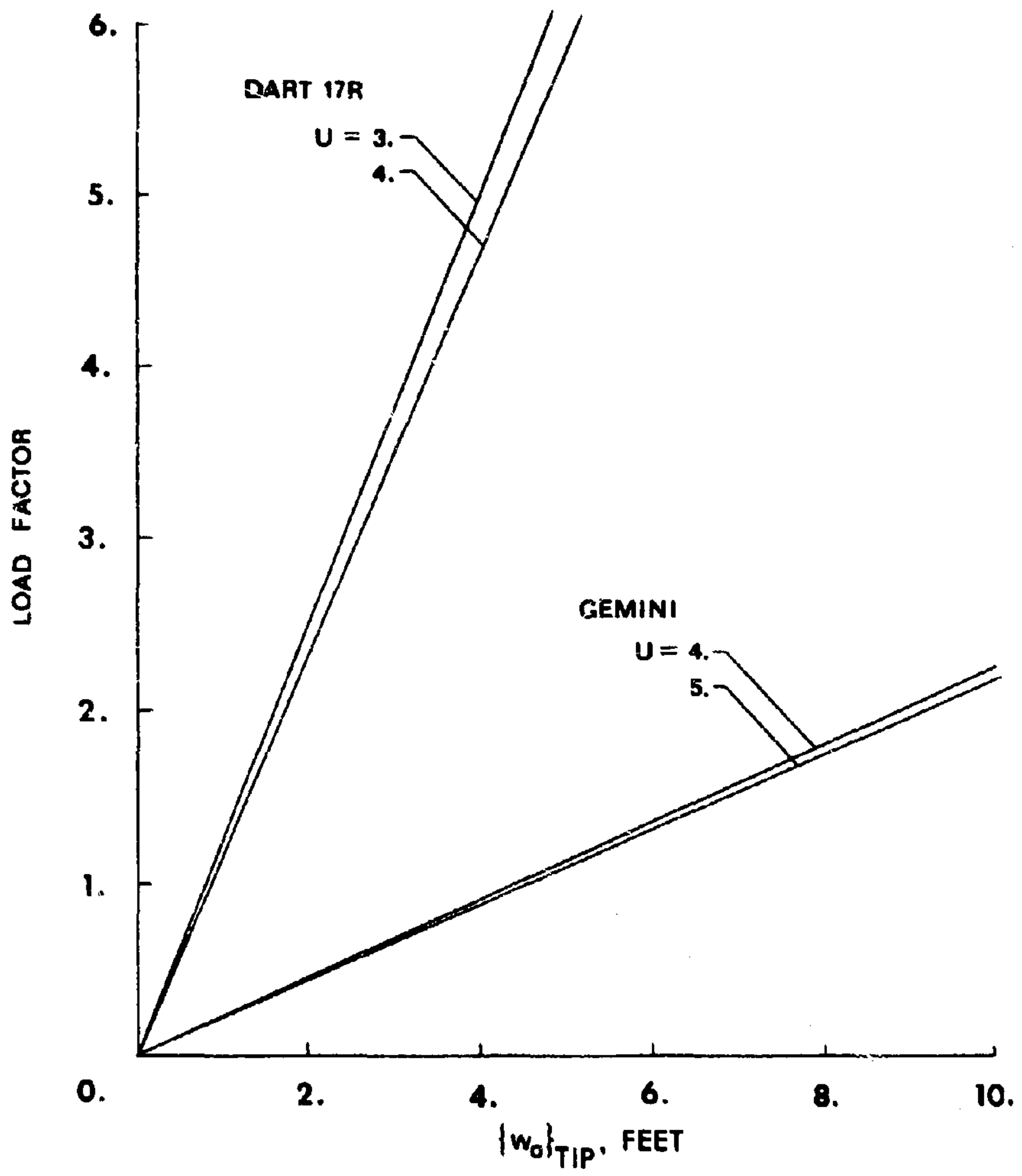

FIGURE 6-41 Comparison of Vertical Bending Deflections of the Two Sailplane Wing Models for Given Steady Load Factor

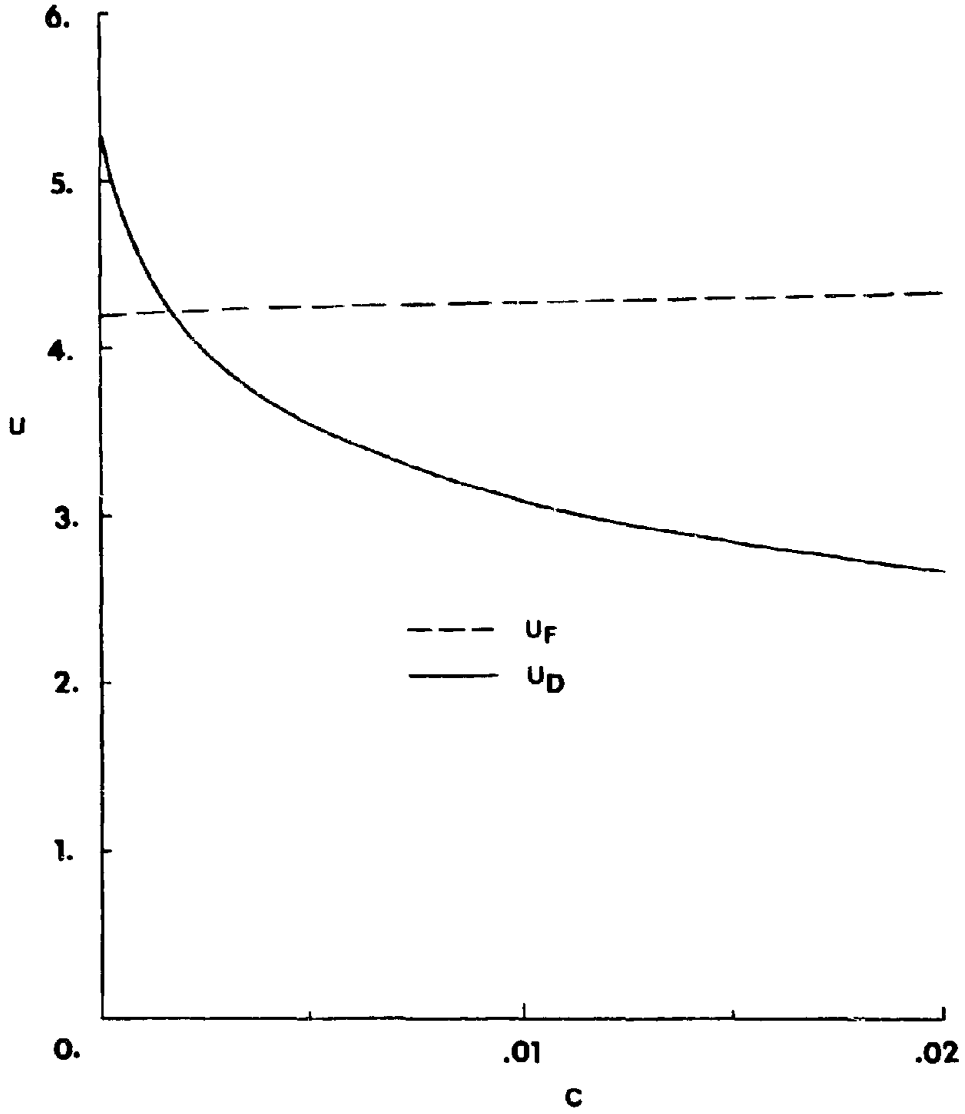

FIGURE 6-42 Effect of Steady Drag on Divergence and Zero-Lift Flutter Speeds of the Dart 17R Model

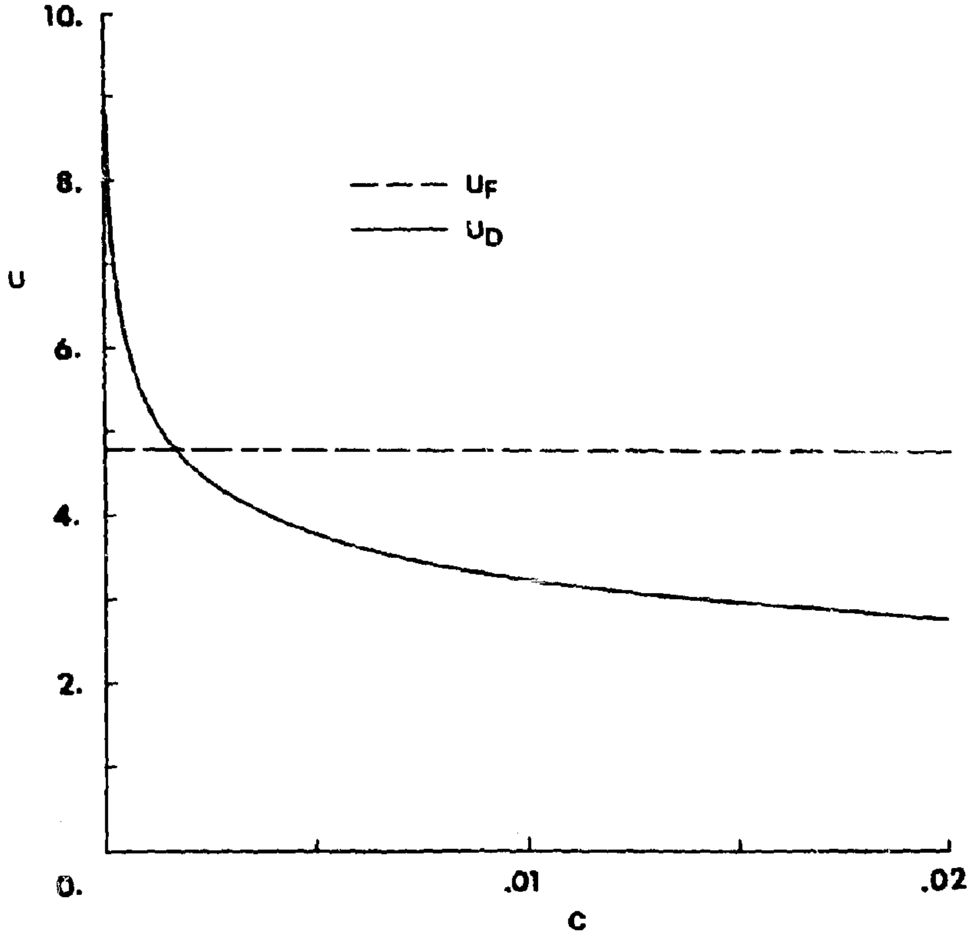

FIGURE 6-43 Effect of Steady Drag on Divergence and Zero-Lift Flutter Speeds of the Gemini Model

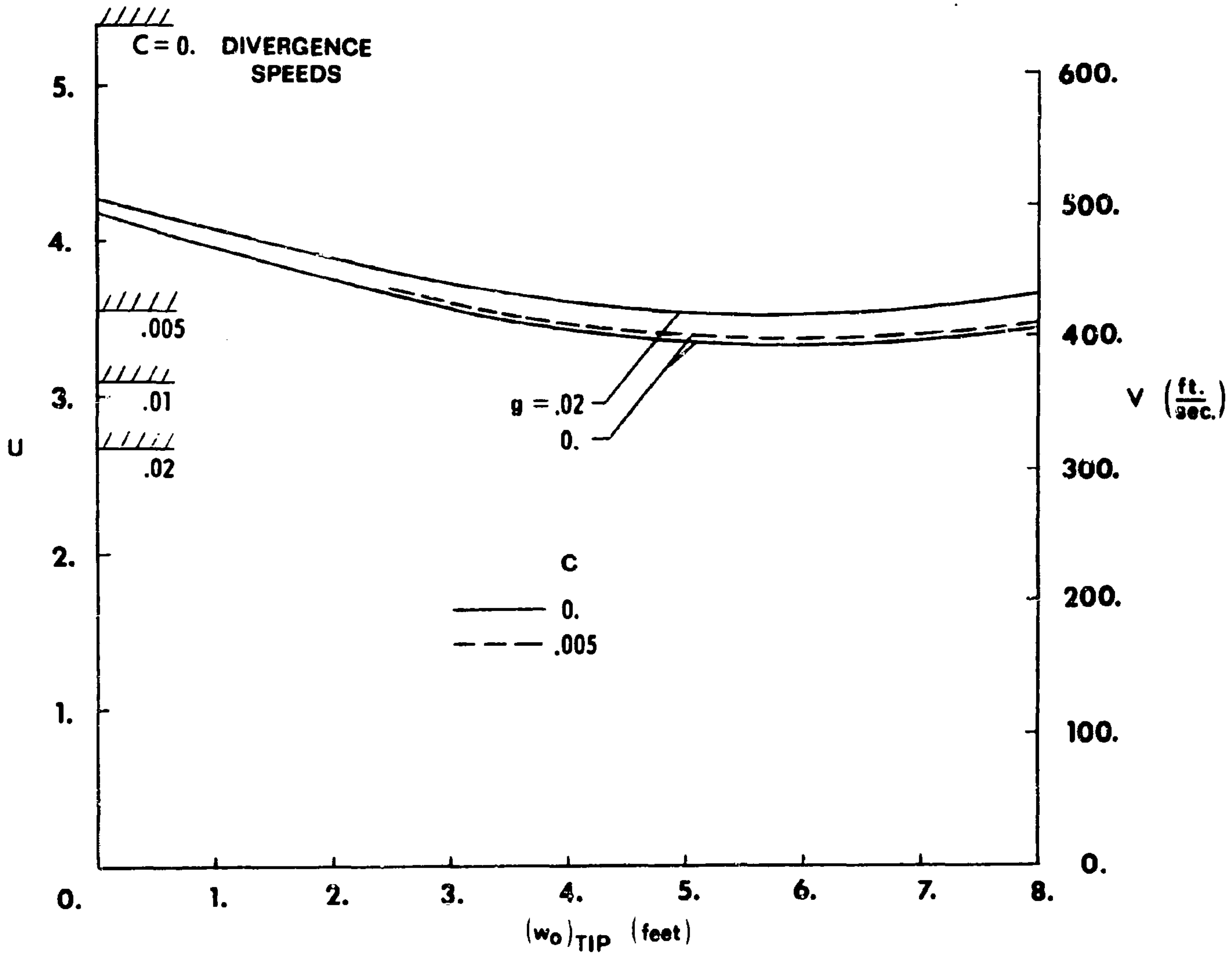

FIGURE 6-44 Stability Boundary For the Dart 17R Model

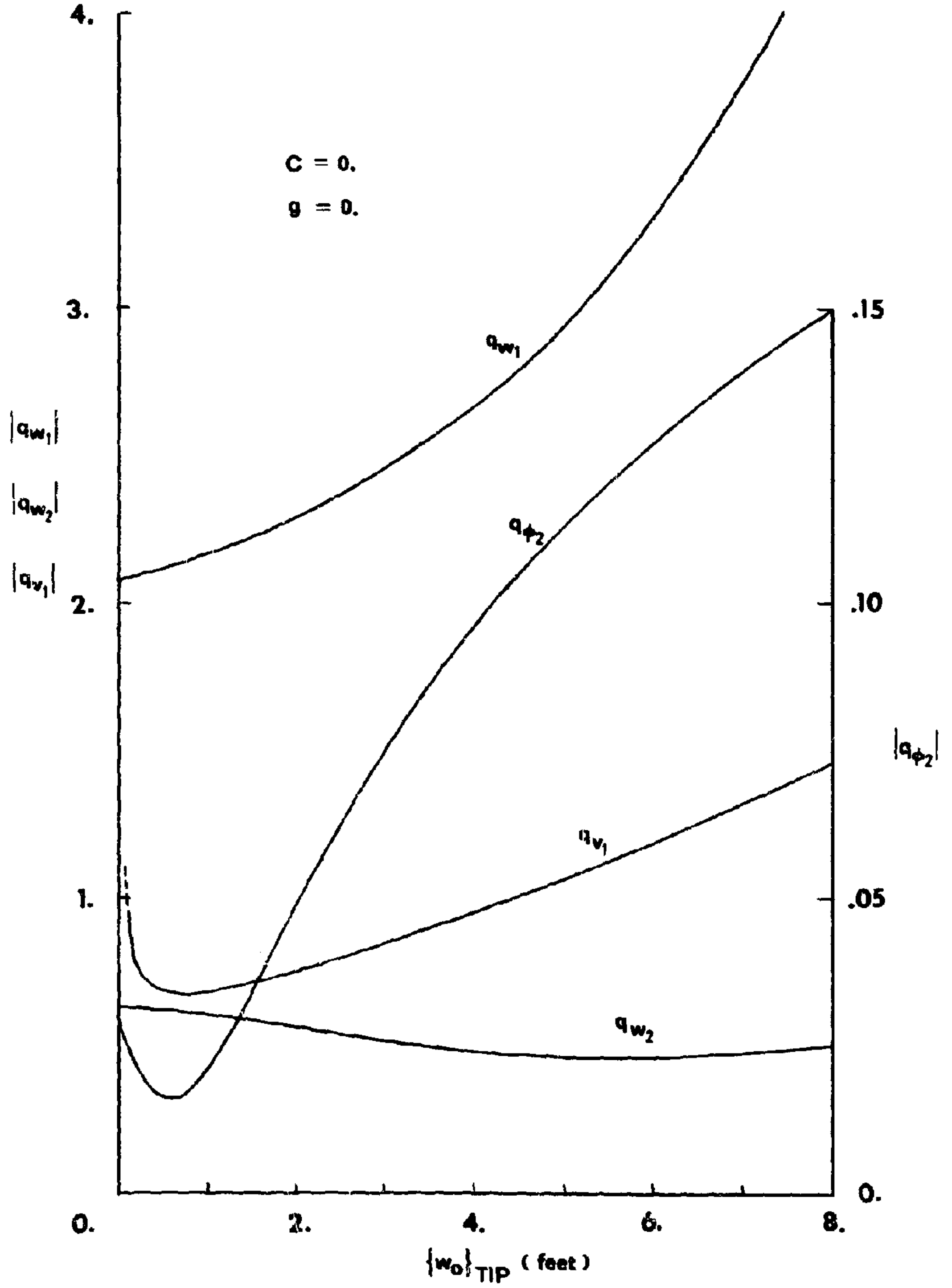

FIGURE 6-45(a) Dart 17R Flutter Mode Shape Amplitudes, Normalized to $|q_{\phi_1}|$

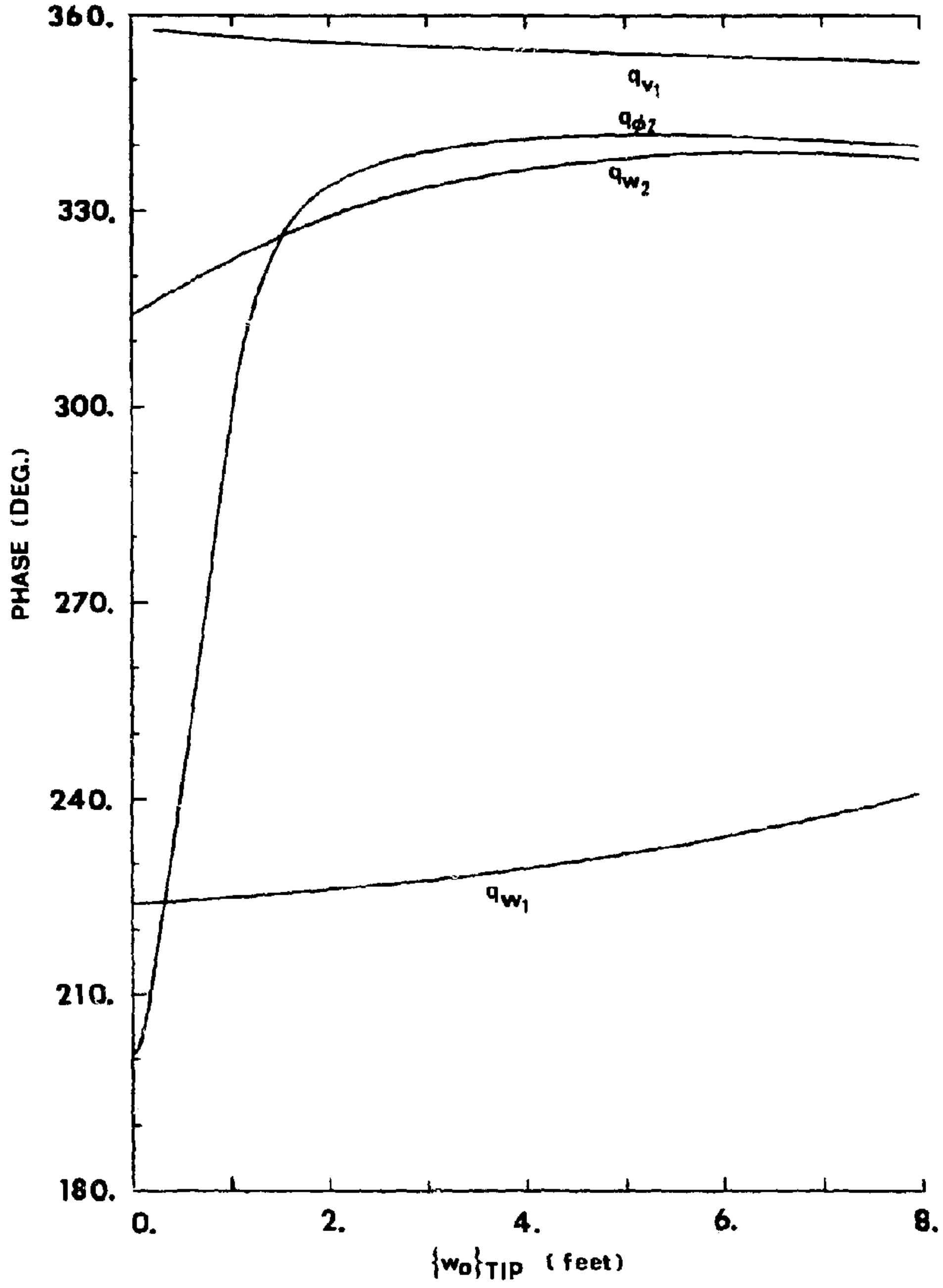

FIGURE 6-45(b) Dart 17R Flutter Mode Shape Phase Angles for Zero Phase of q_{ϕ_1}

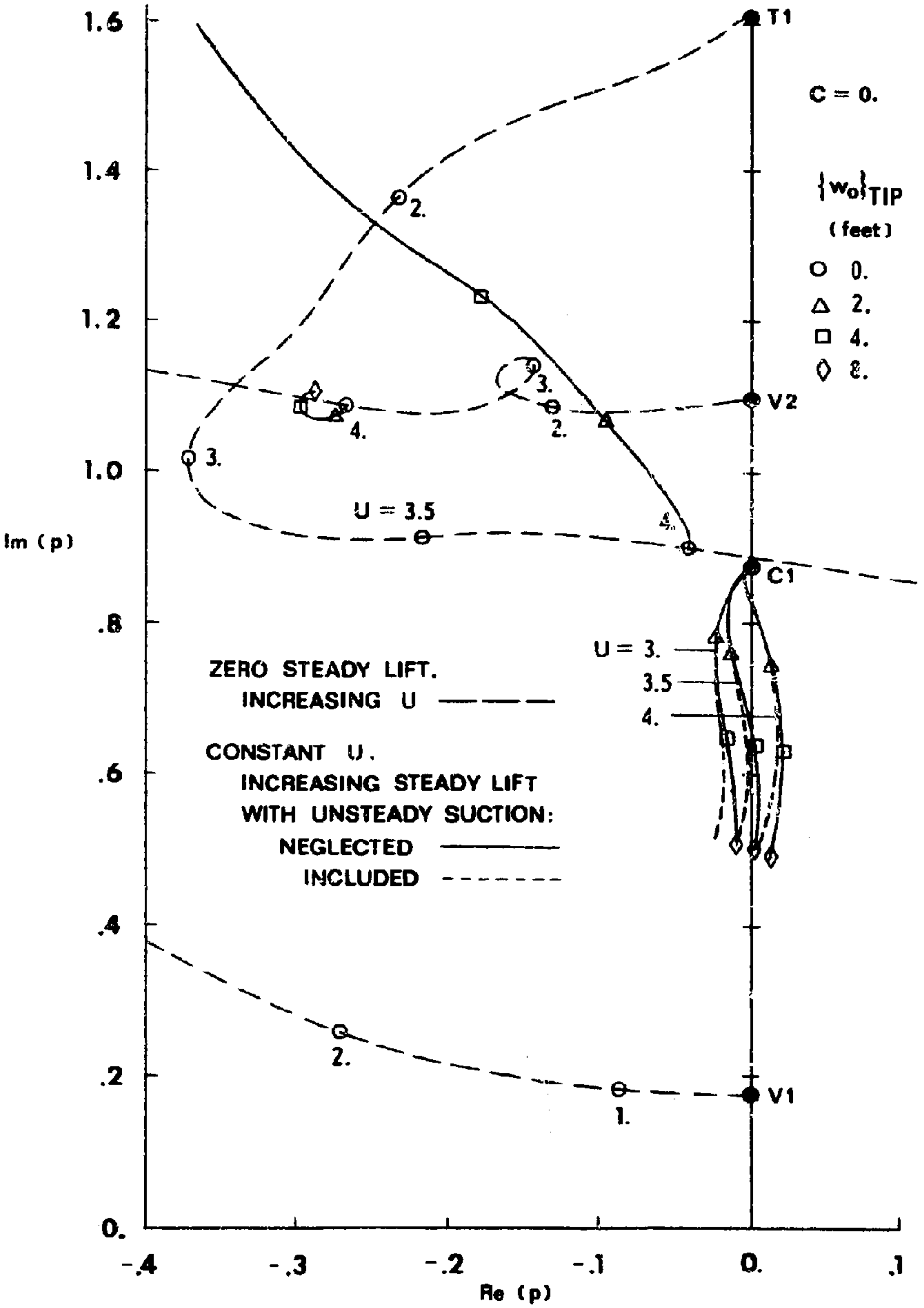

FIGURE 6-46 Locus of Roots for True Aeroelastic Modes, Dart 17R Model

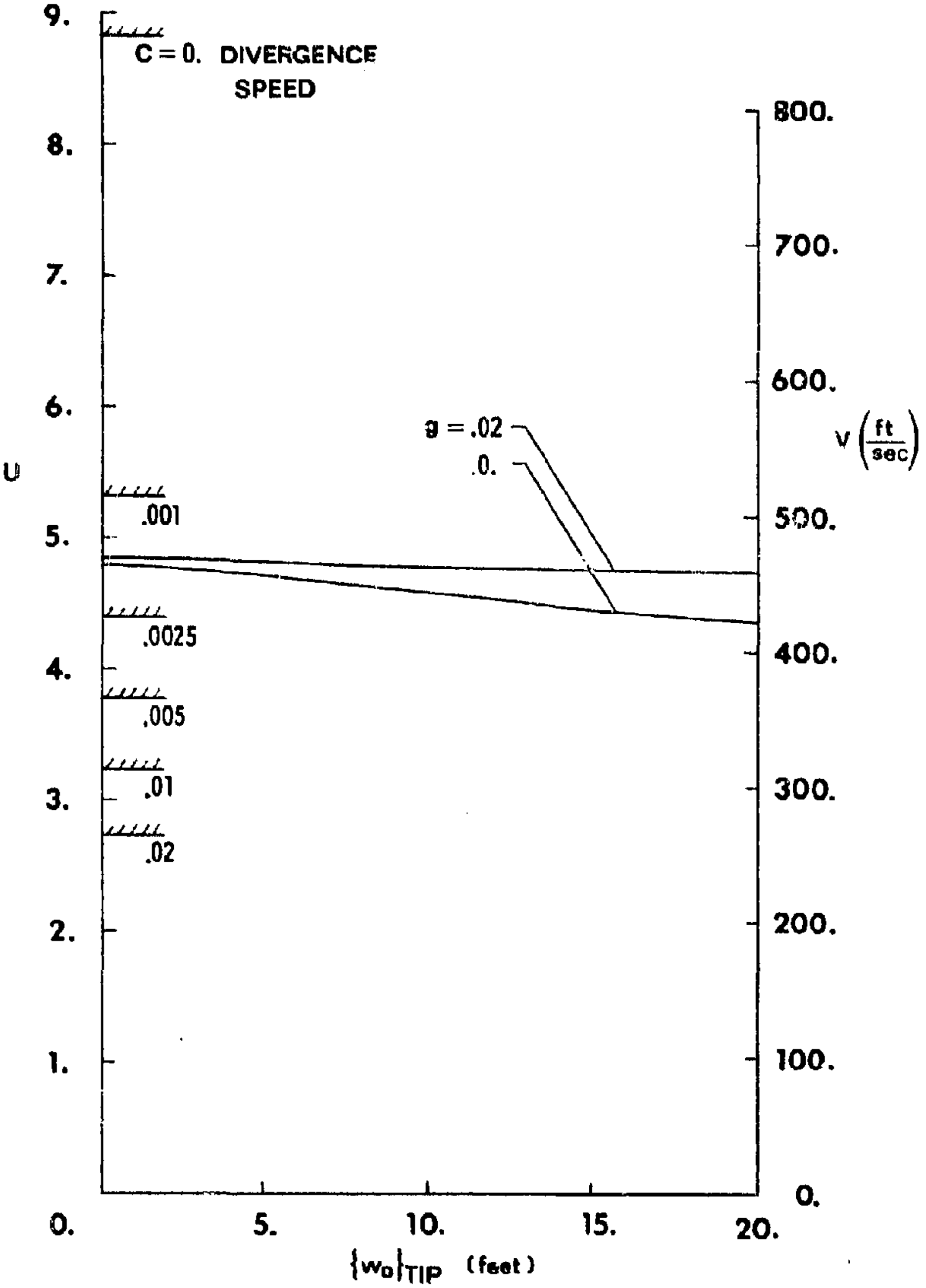

FIGURE 6-47 Stability Boundary for the Gemini Model

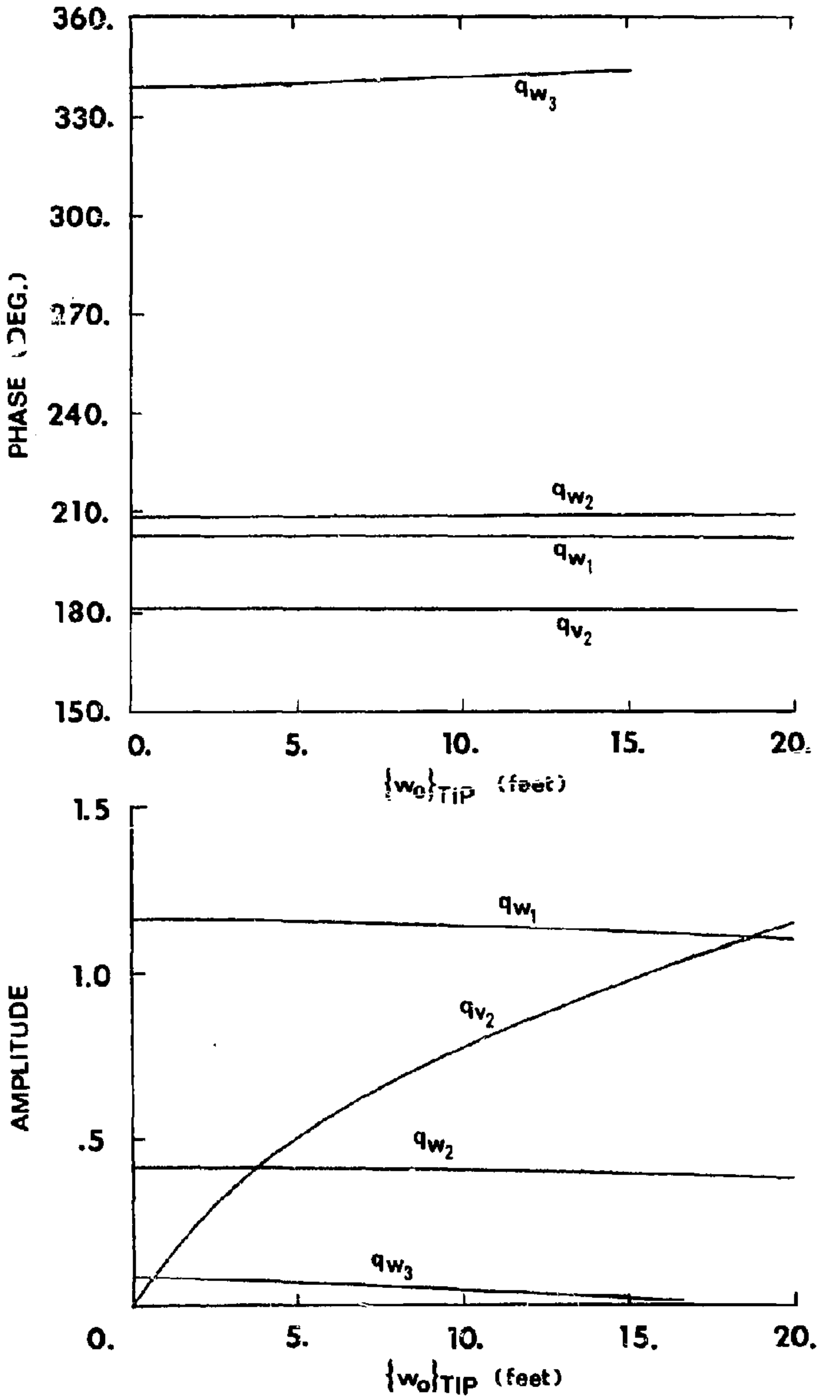

FIGURE 6-48 Flutter Mode Shape Amplitudes and Phase Angles for the Gemini Model, for Unit Amplitude and Zero Phase of q_{ϕ_1}

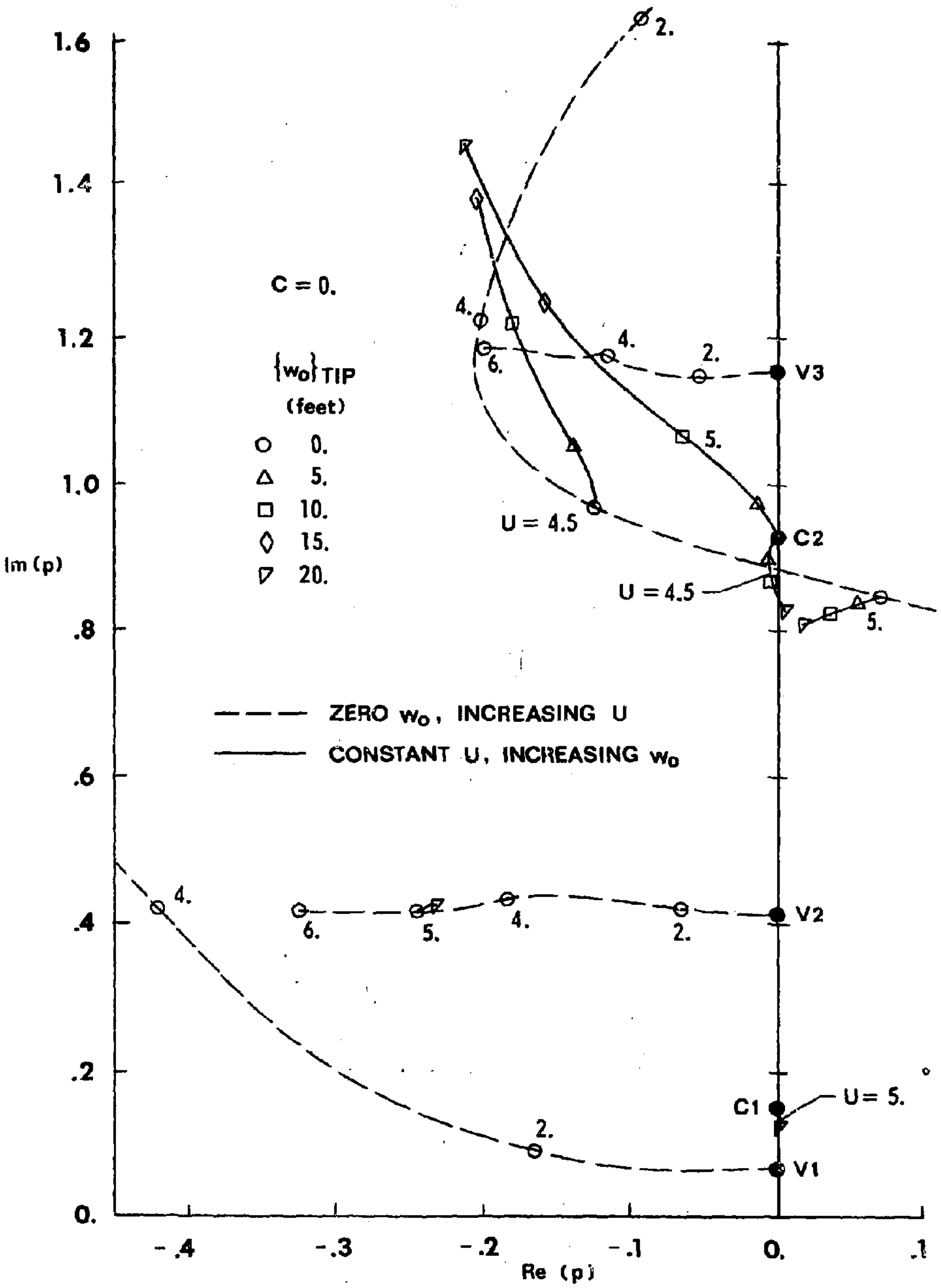

FIGURE 6-49 Locus of Roots for True Aeroelastic Modes, Gemini Model

Chapter VII

FLUTTER VELOCITY USING AIRLOADS FROM THREE-DIMENSIONAL SUBSONIC AERODYNAMIC THEORY

A. Inclusion of Three-Dimensional Airloads

The influence of steady deformations and chordwise forces upon dynamic stability of the uniform cantilever wing has been examined in Chapter VI using lifting airloads predicted by incompressible steady and unsteady strip-theory. This approximate modeling of the aerodynamic loads made possible their convenient numerical computation for any convergent, neutral, or divergent oscillations of interest. As a result, the iterative solution schemes of Chapters IV and V could be developed and a variety of wing configurations could be analyzed efficiently.

The accuracy with which the incompressible strip theory results approximate the three-dimensional compressible flow situation is next explored by extension to subsonic three-dimensional lifting airloads. The simple harmonic flutter solution method described in Chapter IV is accordingly modified to use subsonic three-dimensional steady and oscillating unsteady aerodynamic loads calculated separately by the computer program written by Rowe, et al. (Ref. 18). Results are then found which demonstrate that the phenomena discussed in Chapter VI still occur after three-dimensional aerodynamics are introduced. The role of unsteady potential chordwise loads in flutter is investigated as is the effect of compressibility. Since the use of externally computed air loads requires a more cumbersome solution method, only enough results are sought to provide direct comparison with the incompressible strip-theory calculations.

The Rowe computer program solves the pressure-downwash integral equation (Ref. 24) for compressible flow about a steady or oscillating planform. The kinematic downwash boundary condition for each structural mode is enforced by collocation, at a set of user-specified points, of the downwash distributions associated with an assumed series of pressure functions. For this application seven collocation chords are specified having five collocation points per chord. Six elastic structural modes are input-- three in vertical bending and three in torsion. The three torsion modes are defined for $A = .1$ (lateral displacements depend on elastic axis location). A thorough description of the theoretical aspects of the subsonic kernel function program is provided in Ref. 18, and the programming details are documented in Ref. 19. Its capability for modeling trailing- and leading-edge control surfaces is not required in the present application.

The unsteady potential chordwise forces can be deduced from program output, as follows. For each structural mode and its downwash the program calculates the complex amplitude of an associated distributed lifting pressure difference on the rectangular planform, which in dimensionless form for the jth mode is, per unit q_j having steady or simple harmonic time dependence,

$$(7\text{-}1) \qquad \Delta Cp_j(x,y) = \frac{\Delta P_j(x,y)}{\frac{1}{2}\rho V^2} = \frac{8\sqrt{\ell^2-y^2}}{\ell} \sum_{\nu=1}^{\bar{N}} \sum_{\mu=1}^{\bar{M}} a_{\nu\mu}^{(j)} f^{(\nu)}(y) g^{(\mu)}(x)$$

Here $a_{\nu\mu}^{(j)}$ are coefficient multipliers of the series expansion of pressure on the planform, which can be listed in the program output. The assumed spanwise pressure distributions are

(7-2) $$f^{(\nu)}(y) = \frac{\sin(2\nu-1)\Phi}{\sin\Phi} \quad , \nu = 1,2,3,\ldots\bar{N}$$

(7-3) $$\Phi = \cos^{-1}(\frac{y}{\ell})$$

$\bar{N}$ = number of downwash chords on semispan

The assumed chordwise pressure distributions, dependent upon x only for a rectangular planform, are

(7-4) $$g^{(\mu)}(x) = \begin{cases} \cot\frac{\theta}{2} & \mu = 1 \\ \sin(\mu-1)\theta & \mu = 2,3,4,\ldots\bar{M} \end{cases}$$

(7-5) $$\theta = \cos^{-1}(-\frac{x}{b})$$

$\bar{M}$ = number of downwash points on a downwash chord

where x is measured aft from the midchord.

The resultant chordwise component of potential airloads, acting in the positive x direction, can be expressed as

(7-6) $$D_p(y;t) = -\tfrac{1}{2}\rho V^2 \int_{-b}^{b} \Delta C_p(x,y;t) \frac{\partial z_s}{\partial x}(x,y;t)dx - F_s(y;t)$$

The first term represents the x-component of the force, which is normal to the deflected chord, second term contains the contribution of leading-edge suction. It is an idealization of linearized theory, which is supposed to approximate the actual effects of low pressure acting around a curved leading edge.

Steady and unsteady parts of the pressure and mean-surface chordwise slope can be separated:

$$(7\text{-}7) \qquad \Delta C_p(x,y;t) = \Delta C_{p_o}(x,y) + \Delta C_{p_1}(x,y;t)$$

$$(7\text{-}8) \qquad \frac{\partial z_s}{\partial x}(x,y;t) = -\,\phi_o(y) - \phi_1(y;t)$$

The first term of (7-6) will then contain a steady part, a linear unsteady part, and a nonlinear part, as follows:

$$(7\text{-}9) \qquad D_p(y;t) = \tfrac{1}{2}\rho V^2 \int_{-b}^{b} \Delta C_{p_o}\, \phi_o \, dx$$
$$+ \tfrac{1}{2}\rho V^2 \int_{-b}^{b} (\Delta C_{p_o}\, \phi_1 + \Delta C_{p_1}\, \phi_o) dx$$
$$+ \tfrac{1}{2}\rho V^2 \int_{-b}^{b} \Delta C_{p_1}\, \phi_1 \, dx - F_s(y,t)$$

The suction force likewise can be separated. The leading-edge inverse-square-root pressure singularity strengths for steady and unsteady flow can be defined,

$$(7\text{-}10) \qquad C_{F_o}(y) \equiv \frac{V}{4} \lim_{x \to -b} [-\sqrt{x+b}\; \Delta C_{p_o}(x,y)]$$

$$(7\text{-}11) \qquad C_{F_1}(y;t) \equiv \frac{V}{4} \lim_{x \to -b} [-\sqrt{x+b}\; \Delta C_{p_1}(x,y;t)]$$

From equations (5-9) and (5-10), the leading edge suction force in terms of the vorticity singularity is

$$(7\text{-}12) \qquad F_s(y;t) = \sqrt{1-M_a^2}\, \frac{\Pi}{4}\, \rho [\lim_{x \to -b} (\sqrt{x+b}\; \gamma(x,y;t))]^2$$

where the effect of compressibility is now included with the $\sqrt{1-M_a^2}$ factor (deduced from Eq. 12-1 of Ref. 26). Vorticity and pressure discontinuity distributions in the vicinity of the leading edge are related by (Ref. 23, Eq. (5-93))

$$(7\text{-}13) \qquad \Delta C_p(x,y;t) = -\frac{2\gamma}{V}(x,y;t)$$

The suction force in terms of the leading edge pressure singularity is, therefore,

$$\begin{aligned}(7\text{-}14) \qquad F_s(y;t) &= \sqrt{1-M_a^2}\,\Pi\rho\{\frac{V}{4}\lim_{x\to -b}[-\sqrt{x+b}\,\Delta C_p(x,y;t)]\}^2 \\ &= \sqrt{1-M_a^2}\,\Pi\rho\{c_{F_o}(y) + c_{F_1}(y;t)\}^2 \\ &= \sqrt{1-M_a^2}\,\Pi\rho[c_{F_o}^2 + 2c_{F_o}c_{F_1} + c_{F_1}^2] ,\end{aligned}$$

where (7-7), (7-10), and (7-11) have been used. Equations (7-9) and (7-14) suggest that chordwise forces do affect both the steady displacement solution and the linearized unsteady stability problem.

Actual computation of the suction force contributions can be accomplished through program output of the series coefficients $a_{\nu\mu}^{(j)}$. Insertion of (7-1) into (7-10) and (7-11), for the jth mode, leads to the steady and unsteady leading-edge singularity strengths

$$(7\text{-}15) \qquad c_{F_o}^{(j)}(y) = -2V[\frac{\sqrt{\ell^2-y^2}}{\ell}\sum_{\nu=1}^{\bar{N}} a_{\nu 1}^{(j)} f^{(\nu)}(y)]\sqrt{b}$$

$$(7\text{-}16) \qquad c_{F_1}^{(j)}(y) = -2V[\frac{\sqrt{\ell^2-y^2}}{\ell}\sum_{\nu=1}^{\bar{N}} a_{\nu 1}^{(j)} f^{(\nu)}(y)]\sqrt{b}$$

Here, in taking the limit $x \to -b$, only the $\mu = 1$ chordwise pressure distribution terms from (7-4) remain since

(7-17) $$\lim_{x \to -b} [\sqrt{x+b}\; g^{(\mu)}(x)] = \begin{cases} \sqrt{b} & \mu = 1 \\ 0 & \mu > 1 \end{cases}$$

The single summations that define the modal spanwise leading-edge pressure singularity strength can be arranged for computational purposes

(7-18) $$F_j^{\circ}(y) = \frac{\sqrt{\ell^2-y^2}}{\ell} \sum_{\nu=1}^{\bar{N}} a_{\nu 1_o}^{(j)} \; f^{(\nu)}(y)$$

(7-19) $$F_j(y) = \frac{\sqrt{\ell^2-y^2}}{\ell} \sum_{\nu=1}^{\bar{N}} a_{\nu 1_1}^{(j)} \; f^{(\nu)}(y)$$

This notation, together with summation over all modes, allows the total singularity strengths (7-10) and (7-11) to be computed by

(7-20) $$C_{F_o}(y) = -\, 2V\sqrt{b} \sum_j F_j^{\circ}(y) q_j^{\circ}$$

(7-21) $$C_{F_1}(y,t) = -\, 2V\sqrt{b} \sum_j F_j(y) \; q_j(t)$$

Insertion of (7-20) and (7-21) into (7-14) gives for the suction force

(7-22) $$F_s(y,t) = 4\Pi\rho V^2 b \sqrt{1-M_a^2} \; \{[\sum_\nu F_\nu^{\circ}(y) q_\nu^{\circ}]^2$$

$$+ 2 \sum_\nu \sum_j F_\nu^{\circ}(y) q_\nu^{\circ} \; q_j e^{i\omega t} F_j(y)$$

$$+ [\sum_j F_j(y) \; q_j e^{i\omega t}]^2\}$$

The notation of (7-18) and (7-19) is next adjusted to identify the specific structural modes involved. For the steady problem a rigid pitching mode must be used to solve for pressures and loads due to airplane angle of attack, and its associated singularity strength parameter is denoted as F°_{α}. For the jth elastic torsion mode $F^{\circ}_{\phi_j}$ is used; of course, the vertical bending modes introduce no steady lifting loads. Unsteady, leading-edge-singularity strength parameters for the jth elastic torsion and bending modes are specified by F_{ϕ_j} and F_{w_j}. respectively. The computational form of (7-22) is then

$$(7\text{-}23) \qquad \begin{aligned} F_s(y;t) = 4\Pi\rho V^2\sqrt{1-M_a^2}\, \{ & [F^{\circ}_{\alpha}\alpha + \sum_{\nu=1}^{n} F^{\circ}_{\phi_\nu}\, q^{\circ}_{\phi_\nu}]^2 \\ & + 2\sum_{j=1}^{n} [F^{\circ}_{\alpha}\alpha + \sum_{\nu=1}^{n} F^{\circ}_{\phi_\nu}\, q^{\circ}_{\phi_\nu}] F_{w_j} \frac{q_{w_j}}{b}\, e^{i\omega t} \\ & + 2\sum_{j=1}^{n} [F^{\circ}_{\alpha}\alpha + \sum_{\nu=1}^{n} F^{\circ}_{\phi_\nu}\, q^{\circ}_{\phi_\nu}] F_{\phi_j}\, q_{\phi_j}\, e^{i\omega t} \\ & + [(\sum_{j=1}^{n} F_{w_j} \frac{q_{w_j}}{b} + \sum_{j=1}^{n} F_{\phi_j}\, q_{\phi_j}) e^{i\omega t}]^2 \} \end{aligned}$$

The x-component of the ΔCp-force, as indicated in (7-9), must also be expressed in a form which permits computation. Insertion of the modal quantities

$$(7\text{-}24) \qquad \phi_o = \sum_{\nu=1}^{n} f_{\phi_\nu}\, q^{\circ}_{\phi_\nu}$$

$$(7\text{-}25) \qquad \Delta Cp_o = \Delta Cp^{\circ}_{\alpha}\alpha + \sum_{\nu=1}^{n} \Delta Cp^{\circ}_{\phi_\nu}\, q^{\circ}_{\phi_\nu}$$

$$(7\text{-}26) \qquad \phi_1 = \sum_{j=1}^{n} f_{\phi_j}\, q_{\phi_j}$$

$$(7\text{-}27) \qquad \Delta Cp_1 = \sum_{j=1}^{n} \Delta Cp_{w_j} \frac{q_{w_j}}{b} + \sum_{j=1}^{n} \Delta Cp_{\phi_j}\, q_{\phi_j}$$

into (7-9) leads to

$$(7\text{-}28)\qquad D_p(y;t) = \tfrac{1}{2}\rho V^2\{[\sum_{\nu=1}^{n} \int_{-b}^{b} \Delta Cp^{\circ}_{\alpha}\, f_{\phi_\nu}\, dx\, \alpha\, q^{\circ}_{\phi_\nu}$$

$$+ \sum_{\mu=1}^{n} \sum_{\nu=1}^{n} \int_{-b}^{b} \Delta Cp^{\circ}_{\phi_\mu}\, f_{\phi_\nu}\, dx\, q^{\circ}_{\phi_\mu}\, q^{\circ}_{\phi_\nu}] + [\sum_{i=1}^{n} \sum_{\nu=1}^{n} \int_{-b}^{b} \Delta Cp_{w_i}\, f_{\phi_\nu}\, dx\, q^{\circ}_{\phi_\nu}\, \frac{q_{w_i}}{b}$$

$$+ \sum_{i=1}^{n} \sum_{\nu=1}^{n} \int_{-b}^{b} \Delta Cp_{\phi_i}\, f_{\phi_\nu}\, dx\, q^{\circ}_{\phi_\nu}\, q_{\phi_i}$$

$$+ \sum_{i=1}^{n} \int_{-b}^{b} \Delta Cp^{\circ}_{\alpha}\, f_{\phi_i}\, dx\, \alpha\, q_{\phi_i} + \sum_{i=1}^{n} \sum_{\nu=1}^{n} \int_{-b}^{b} \Delta Cp^{\circ}_{\phi_\nu}\, f_{\phi_i}\, dx\, q^{\circ}_{\phi_\nu}\, q_{\phi_i}]e^{i\omega t}$$

$$+ [\sum_{i=1}^{n} \sum_{j=1}^{n} \int_{-b}^{b} \Delta Cp_{w_i}\, f_{\phi_j}\, dx\, \frac{q_{w_i}}{b}\, q_{\phi_j}$$

$$+ \sum_{i=1}^{n} \sum_{j=1}^{n} \int_{-b}^{b} \Delta Cp_{\phi_i}\, f_{\phi_j}\, dx\, q_{\phi_i}\, q_{\phi_j}]e^{2i\omega t} - F_s(y;t)$$

where steady, linear unsteady, and nonlinear unsteady terms in the generalized displacements are grouped together.

The chordwise integrals in (7-28) involving the steady and unsteady modal pressures can be computed at any spanwise station by taking advantage of the Rowe program's capability to compute sectional generalized forces. Program output is of the form

$$(7\text{-}29)\qquad Q^{s}_{ij}(y) = \int_{-b}^{b} \Delta Cp_j(x,y) H_i(x,y) dx$$

where the deflection mode shape $H_i(x,y)$ for all integrals in (7-28) will be $f_{\phi_i}(y)$.

The nonlinear modal equations (4-9) for steady displacements must be modified by substitution of the steady compressible lifting airloads in place of the strip theory loads (4-3). Inclusion of the steady parts of (7-28) and (7-23) will account for the induced drag caused by the three-dimensionality of the flow. Generalized forces which will appear in equations (4-9a) and (4-9c) are to be computed directly, but the generalized forces for the chordwise bending equations (4-9b) involve the chordwise forces described above and must be calculated separately. These preliminary calculations require the pressure coefficients $a_{\nu\mu}^{(j)}$ and sectional generalized forces Q_{ij}^{s} obtained from Rowe program output. Program output of generalized forces is of the form

$$Q_{ij} = \int_{0}^{\ell} \int_{-b}^{b} \Delta Cp_j(x,y) H_i(x,y) \; dx \; dy \tag{7-30}$$

where $H_i(x,y)$ is the ith modal displacement and $\Delta Cp_j(x,y)$ the pressure distribution per unit q_j .

Rederivation of (4-9) with three-dimensional subsonic steady airloads produces the following nonlinear system:

$$\Pi^4 N_j^4 \frac{MPi_\alpha}{U^2} \frac{q_{w_j}^{\circ}}{b} - (\tau-1) \frac{MPi_\alpha}{U^2} \Big[\sum_{\mu=1}^{n} \sum_{\nu=1}^{n} H_{\nu j\mu} \, q_{\phi_\nu}^{\circ} \, \frac{q_{v_\mu}^{\circ}}{b} - \sum_{\mu=1}^{n} \sum_{\nu=1}^{n} \sum_{i=1}^{n} R_{ij\mu\nu} q_{\phi_\mu}^{\circ} \, q_{\phi_\nu}^{\circ} \, \frac{q_{w_i}^{\circ}}{b} \Big] - \frac{b}{2\Pi\ell} \Big[Q_{j,o}^{\bullet} \alpha + \sum_{\nu=1}^{n} Q_{j,\nu+2n}^{\bullet} q_{\phi_\nu}^{\circ} \Big] = 0 \tag{7-31a}$$

$$
\begin{aligned}
\text{(7-31b)}\quad & \Pi^4 N_j^4 \frac{\tau \mathrm{MPi}_\alpha}{U^2}\frac{q^\circ_{v_j}}{b} - (\tau-1)\frac{\mathrm{MPi}_\alpha}{U^2}\Big[\sum_{\nu=1}^{n}\sum_{\mu=1}^{n} H_{\nu\mu j}\, q^\circ_{\phi_\nu}\frac{q^\circ_{w_\mu}}{b} \\
& + \sum_{\nu=1}^{n}\sum_{\mu=1}^{n}\sum_{i=1}^{n} R_{ij\mu\nu}\, q^\circ_{\phi_\nu}\, q^\circ_{\phi_\mu}\frac{q^\circ_{v_i}}{b}\Big] \\
& - \frac{1}{2\Pi\ell}\sum_{\nu=1}^{n}\int_0^\ell \Big[\int_{-b}^{b}\Delta Cp^\circ_\alpha\, dx\Big] f_{\phi_\nu}(y) f_{v_j}(y)\, dy\, q^\circ_{\phi_\nu}\,\alpha \\
& - \frac{1}{2\Pi\ell}\sum_{\mu=1}^{n}\sum_{\nu=1}^{n}\int_0^\ell \Big[\int_{-b}^{b}\Delta C\dot{p}^\circ_{\phi_\mu}(x,y)\, dx\Big] f_{\phi_\nu}(y) f_{v_j}(y)\, dy\, q^\circ_{\phi_\mu}\, q^\circ_{\phi_\nu} \\
(1 \le j \le n)\quad & + 4\sqrt{1-M^2}\,\Big\{\int_0^\ell (F^\circ_\alpha)^2 f_{v_j}\, dy + 2\sum_{\nu=1}^{n}\int_0^\ell F^\circ_\alpha F^\circ_{\phi_\nu} f_{v_j}\, dy\,\alpha\, q^\circ_{\phi_\nu} \\
& + \sum_{\mu=1}^{n}\sum_{\nu=1}^{n}\int_0^\ell F^\circ_{\phi_\mu} F^\circ_{\phi_\nu} f_{v_j}\, dy\, q^\circ_{\phi_\mu}\, q^\circ_{\phi_\nu}\Big\} = 0
\end{aligned}
$$

$$
\begin{aligned}
\text{(731c)}\quad & \tfrac{1}{2}\Pi^2 (j-\tfrac{1}{2})^2 \frac{\mathrm{Mi}_\alpha}{U^2} q^\circ_{\phi_j} + (\tau-1)\frac{\mathrm{MPi}_\alpha}{U^2}\Big[\sum_{\nu=1}^{n}\sum_{\mu=1}^{n}\sum_{i=1}^{n} R_{\mu\nu j i}\frac{q^\circ_{w_\nu}}{b}\frac{q^\circ_{w_\mu}}{b} q^\circ_{\phi_i} \\
& - \sum_{\nu=1}^{n}\sum_{\mu=1}^{n}\sum_{i=1}^{n} R_{\mu\nu j i}\frac{q^\circ_{v_\mu}}{b}\frac{q^\circ_{v_\nu}}{b} q^\circ_{\phi_i} - \sum_{\mu=1}^{n}\sum_{\nu=1}^{n} H_{j\nu\mu}\frac{q^\circ_{v_\nu}}{b}\frac{q^\circ_{v_\mu}}{b}\Big] \\
& - \frac{b}{2\Pi\ell}\Big[\underset{\sim}{Q}^\circ_{j+2n,o}\,\alpha + \sum_{\nu=1}^{n}\underset{\sim}{Q}^\circ_{j+2n,\nu+2n}\, q^\circ_{\phi_\nu}\Big] = 0
\end{aligned}
$$

In (7-31) the notation $\underset{\sim}{Q}^\circ_{i,j}$ refers to the steady generalized forces computed directly by the Rowe program. Here 2n+1 structural modes must be used to compute generalized forces: n in vertical bending, n in elastic torsion, and one rigid pitching mode.

Computation of the chordwise load terms in (7-31b) quickly becomes an unwieldy task as n is increased, because of the profusion of numerical integrations that become necessary (for n = 3 there would be 75 integrations). In order to avoid extensive labor but still retain the most significant effects of the potential chordwise forces, the following simplifying assumptions are adopted. First, integrals appearing in the first $(j=1)$ chordwise equation of (7-31b) only are retained. Second, only the pressure distribution and slope of the first of the elastic torsion modes are kept; terms containing $\Delta Cp^{\circ}_{\phi_{\mu}}$ or $f_{\phi_{\mu}}$ for $\mu > 1$ are dropped. Similarly, all terms containing $F^{\circ}_{\phi_{\mu}}$ for $\mu > 1$ are removed. This approach should preserve the first-order effect of steady chordwise potential forces, yet only five numerical spanwise integrations will be required.

Actual computation of the remaining integrals

$$\int_0^{\ell} [\int_{-b}^{b} \Delta Cp^{\circ}_{\alpha}(x,y)dx] f_{\phi_1}(y) f_{v_1}(y) dy$$

$$\int_0^{\ell} [\int_{-b}^{b} \Delta Cp^{\circ}_{\phi_1}(x,y)dx] f_{\phi_1}(y) f_{v_1}(y) dy$$

is done by direct calculation of the integrals over x as sectional generalized forces with the Rowe program at eleven spanwise stations. The spanwise integration is then carried out numerically. For the three integrals

$$\int_0^{\ell} [F^{\circ}_{\alpha}(y)]^2 f_{v_1}(y) dy$$

$$\int_0^{\ell} F^{\circ}_{\alpha}(y) F^{\circ}_{\phi_1}(y) f_{v_1}(y) dy$$

$$\int_0^{\ell} [F^{\circ}_{\phi_1}(y)]^2 f_{v_1}(y) dy$$

the summations implied by (7-18) are first made. This step is followed by spanwise numerical integration.

The nonlinear solution scheme described in Appendix C was straightforwardly adapted to compute steady deflections in subsonic three-dimensional flow from (7-31). Since spanwise induction introduces coupling among the torsional modal equations, solution for linear displacements as an initial estimate becomes an $n x n$ linear matrix problem.

Equation (4-12) remains as the $3n \times 3n$ linear unsteady modal system for stability about the steady equilibrium position. It now requires the generalized force matrix to be expressed for three-dimensional unsteady compressible flow. As for the steady case, the generalized forces relating pressures and displacements in the vertical bending and torsion modes can be computed directly by the Rowe program, with reduced frequency and Mach number specified. Direct insertion into (4-12a) and (4-12c) is accomplished by the simple substitution, for generalized forces $Q_{j,i}$ and $\mathcal{Q}_{j,i}$ relating the same two modes,

$$Q_{j,i} = \frac{b}{2\Pi \ell k^2} \mathcal{Q}_{j,i} \qquad (7-32)$$

Even more so than for the steady airloads, complete inclusion of all linear unsteady potential chordwise terms introduces a profusion of integrals. Formally, the linear unsteady terms which appear in (7-28) and (7-23) enter into generalized forces, computation of which involves spanwise integrations of the terms' products with f_{v_j}. Practically, simplifying assumptions of the type made for the steady chordwise terms have been made to keep the number of numerical integrations at a manageable level. Accordingly, only the first chordwise equation of (4-12b) will retain the chordwise force terms. Furthermore, only the chordwise force integrals containing pressure contributions and displacements for the q_{ϕ_1}, q_{w_1}, and q_{w_2} degrees of freedom will be kept. (Justification of this approximation is based on the flutter behavior observed in Chapter VI, which revealed little participation by the remaining vertical bending and torsion modes.) The remaining linear unsteady terms from (7-23) and (7-28) are

$$
\begin{aligned}
(7\text{-}33) \qquad D_p(y;t) \cong\ & \tfrac{1}{2}\rho V^2 \Big\{ \int_{-b}^{b} \Delta Cp_{w_1}\, f_{\phi_1}\, dx\; q^{\circ}_{\phi_1} \frac{q_{w_1}(t)}{b} \\
& + \int_{-b}^{b} \Delta Cp_{w_2}\, f_{\phi_1}\, dx\; q^{\circ}_{\phi_1} \frac{q_{w_2}(t)}{b} + \int_{-b}^{b} \Delta Cp_{\phi_1}\, f_{\phi_1}\, dx\; q^{\circ}_{\phi_1}\, q_{\phi_1}(t) \\
& + \int_{-b}^{b} \Delta Cp^{\circ}_{\alpha}\, f_{\phi_1}\, dx\; \alpha\, q_{\phi_1}(t) + \int_{-b}^{b} \Delta Cp^{\circ}_{\phi_1}\, f_{\phi_1}\, dx\; q^{\circ}_{\phi_1}\, q_{\phi_1}(t) \Big\} \\
& + 8\Pi\rho V^2 \sqrt{1-M_a^2}\, \Big\{ F^{\circ}_{\alpha} F_{w_1}\, \alpha \frac{q_{w_1}(t)}{b} + F^{\circ}_{\alpha} F_{w_2}\, \alpha \frac{q_{w_2}(t)}{b} \\
& + F^{\circ}_{\alpha} F_{\phi_1}\, \alpha\, q_{\phi_1}(t) + F^{\circ}_{\phi_1} F_{w_1}\, q^{\circ}_{\phi_1} \frac{q_{w_1}(t)}{b} \\
& + F^{\circ}_{\phi_1} F_{w_2}\, q^{\circ}_{\phi_1} \frac{q_{w_2}(t)}{b} + F^{\circ}_{\phi_1} F_{\phi_1}\, q^{\circ}_{\phi_1}\, q_{\phi_1}(t) \Big\}
\end{aligned}
$$

The generalized force matrix terms for inclusion in (4-12b) are then found to be

$$
\begin{aligned}
(7\text{-}34) \qquad Q_{1+n,1} =\ & \frac{b}{2\Pi k^2 \ell} \int_0^{\ell} \Big[\int_{-b}^{b} \Delta Cp_{w_1}(x,y)\, dx \Big] f_{\phi_1}(y)\, f_{v_1}(y)\, dy\; q^{\circ}_{\phi_1} \\
& - \frac{8b}{k^2 \ell} \sqrt{1-M_a^2}\, \Big\{ \int_0^{\ell} F^{\circ}_{\alpha}(y) F_{w_1}(y)\, f_{v_1}(y)\, dy\, \alpha + \int_0^{\ell} F^{\circ}_{\phi_1} F_{w_1} f_{v_1}\, dy\; q^{\circ}_{\phi_1} \Big\}
\end{aligned}
$$

(7-34)
con't

$$
\begin{aligned}
Q_{1+n,2} &= \frac{b}{2\pi k^2 \ell} \int_0^{\ell} [\int_{-b}^{b} \Delta Cp_{w_2}(x,y)\,dx] f_{\phi_1}(y) f_{v_1}(y)\,dy\; q^{\circ}_{\phi_1} \\
&\quad - \frac{8b}{k^2 \ell} \sqrt{1-M_a^2} \{ \int_0^{\ell} F^{\circ}_{\alpha} F_{w_2} f_{v_1}\,dy\; \alpha + \int_0^{\ell} F^{\circ}_{\phi_1} F_{w_2} f_{v_1}\,dy\; q^{\circ}_{\phi_1} \} \\
Q_{1+n,1+2n} &= \frac{b}{2\pi k^2 \ell} \{ \int_0^{\ell} [\int_{-b}^{b} \Delta Cp^{\circ}_{\alpha}\,dx] f_{\phi_1} f_{v_1}\,dy\; \alpha \\
&\quad + \int_0^{\ell} [\int_{-b}^{b} \Delta Cp^{\circ}_{\phi_1}\,dx] f_{\phi_1} f_{v_1}\,dy\; q^{\circ}_{\phi_1} + \int_0^{\ell} [\int_{-b}^{b} \Delta Cp_{\phi_1}\,dx] f_{\phi_1} f_{v_1}\,dy\; q^{\circ}_{\phi_1} \} \\
&\quad - \frac{8b}{k^2 \ell} \sqrt{1-M_a^2} \{ \int_0^{\ell} F^{\circ}_{\alpha} F_{\phi_1} f_{v_1}\,dy\; \alpha + \int_0^{\ell} F^{\circ}_{\phi_1} F_{\phi_1} f_{v_1}\,dy\; q^{\circ}_{\phi_1} \}
\end{aligned}
$$

All remaining $Q_{j+n,i}$ terms in (4-12b) will be zero.

For a given reduced frequency, computation of these generalized forces involves program output for both oscillating and steady flow conditions. Sectional generalized forces and pressure series coefficients output by the Rowe program are used, in the same manner described above for steady chordwise loads, to compute (7-34). Integrals for oscillating flow, of course, are complex. Nine complex spanwise numerical integrations are needed for each k, whereas 126 would have been required without the simplifying approximations. Two real integrations in $Q_{1+n,1+2n}$ involving steady pressures also appear in the steady displacement solution.

B. Flutter Calculation Procedure and Results

Inclusion of subsonic three-dimensional (3-D) airloads eliminates a serious flaw of the strip theory loads used to obtain all Chapter VI results. This was the approximate spanwise load distribution, which is most inaccurate near the tip. Leading-edge suction has been included in the same manner as the Chapter V, Section D, analysis of 2-D flow. An effect which was neglected in the strip theory case, that of the x-component of the resultant pressure force normal to the deformed chord (cf. Eqs. (5-18) to (5-20) is now retained. It is accounted for by the chordwise terms which are computed with sectional generalized forces. The influence of induced drag upon both steady deformations and flutter stability should now be implicitly included by the modeling of chordwise loads. Two parameters which must be specified in addition to those mentioned in Chapter IV, in order to define a specific wing are the aspect ratio $(\frac{\ell}{b})$ and Mach number.

The Chapter IV stability calculation method has been modified to accept the subsonic 3-D steady and unsteady airloads derived in Section A. Since these airloads are now externally generated, iteration of the reduced frequency to find neutrally damped eigenvalues is no longer feasible. Generalized forces have to be computed beforehand, both for steady flow and for oscillatory flow at preselected reduced frequencies. Computation of steady displacements for a given angle of attack and flight speed is accomplished as before, now based on Equations (7-31). Then for each of the preselected reduced frequencies, the previously calculated generalized forces (7-32) and (7-34) are input, the eigenvalue determinant (4-19) is assembled, and complex eigenvalues are determined. For each of these there are an associated speed and damping as shown by (2-25) and (2-27). The speed and damping of each flutter mode are then plotted for all k, and a neutrally-damped speed U_F is determined by graphical interpolation. The procedure is repeated with a newly estimated U_e ; with care, U_e and U_F can be matched with sufficient accuracy after two such steps.

The expense in computer time to execute the Rowe program and the additional effort required to prepare the chordwise loads make it desireable to use as few as possible k values. Fortunately, all U vs. g interpolation graphs proved to be quite smooth. Flutter speeds accurate to three significant digits (sufficient) were reliably obtained.

The moderate-aspect-ratio wing whose stability boundary for 2-D airloads appears in Fig. 6-7 has been re-analyzed using 3-D incompressible aerodynamic theory. Figure 7-1 shows the results, compared with the 2-D flutter calculations. The curve marked "100% suction" was computed with the complete system (4-12), (7-32), and (7-34) whereas that marked "0% suction" was found by repeating the analysis after removal of all terms containing the singularity strength parameters $\bar{F}_{\phi_1}$ etc. in (7-34). This latter result thus represents the effects of forces normal to the deflected airfoil chord only in the dynamic equations. The coupling of fore-and-aft bending motions into flutter by the leading edge suction forces is therefore absent in the "0% suction" case.

The 2-D stability boundary involves the aerodynamic loads of (4-18), which actually do not account for suction. The effect of modeling the suction force, as derived in Section C of Chapter V, is shown by Figs. 6-35 and 6-36. These plots suggest that, if a stability boundary had been determined with suction accounted for, the 2-D curve in Fig. 7-1 would show less influence of steady deformation and would not drop below $U = 7$. The solid, 3-D curve does, of course, account for suction.

Comparison between the 2-D and 3-D flutter speeds is also made more difficult because they involve different steady aerodynamics. In order to minimize differences of this kind, the steady tip deflection was judged to be the best common measure of steady airload effects.

Inspection of Fig. 7-1 affirms that the influence of steady deformations upon flutter is not just governed by elastic bending-torsion coupling but is also sensitive to the manner in which the potential aerodynamic loads are applied to the fore-and-aft degree of freedom. Even though the chordwise force components represent tilting of a relatively large, approximately vertical resultant force vector, they are seen to have a significant stabilizing influence. This conclusion follows from comparing the "100% suction" and "0% suction" curves. Any analysis of this type will obviously be sensitive to the way in which chordwise forces are accounted for.

The influence of compressibility is next explored by repeating the foregoing calculations with airloads computed for Mach numbers of .6 and .8 . Results are shown in Fig. 7-2. Strictly speaking, this procedure involves an inconsistency, since Mach number is held fixed while velocity is freely varied. The type of calculations required to model properly a wing at high subsonic speeds would require iterative matching of Mach number and speed U_F for a given flight altitude. This refinement is deemed to be excessively costly in both computer time and effort. Nevertheless, the results of Fig. 7-2 provide interesting qualitative information on Mach number effects.

As M_a is increased, the decrease in flutter speed with steady deformation for the "0% suction" case becomes less pronounced. The results for "100% suction" show less sensitivity to Mach number. In either case, no adverse effects due to compressibility upon flutter of a lifting wing are revealed, other than those associated with a modest decrease in U_F with increasing M_a .

When extending this analysis to higher subsonic Mach numbers, it must be remembered that the only aerodynamic loads being included are those which arise from inviscid, first-order, small perturbation steady and unsteady theory for planar lifting surfaces. Induced drag is present, as discussed above, but all chordwise forces which arise from either direct viscous shears or from modifications to the pressure distribution due to the presence of a boundary layer are not modeled. Yet viscous effects of this type become increasingly more pronounced as flight speeds approach the transonic regime and/or as mean angle of attack is increased.

The chordwise laods associated with direct viscous shear should not contain a significant unsteady component, at least at the lower reduced frequencies encountered here. It is expected that they will produce a steady drag force aligned with the airfoil section. By contrast, the chordwise potential loads represent the horizontal component of a relatively large resultant circulatory lift vector. Tilting of this vector can introduce unsteady chordwise loads of considerable magnitude. Indeed their importance in aeroelastic stability is suggested by comparison of the 100% and 0% suction curves in the figures.

Since viscous shear should cause a predominantly steady drag loading, qualitative information regarding its effect on flutter can be inferred from the strip theory studies of Chapter VI involving the drag parameter

C. For example, no substantial alteration of the dependence of flutter speed upon steady lift should be expected from including this additional drag term. The effect of unsteady viscous contributions to aeroelastic stability has not been considered anywhere in this investigation. The mere prediction of unsteady viscous chordwise loads is still regarded as an open question for experimental and analytical research, especially when turbulent boundary layers are involved.

As a final case, the large-aspect-ratio example of Fig. 6-13 has been reanalyzed. Aspect ratio is fixed at 20 and Mach number at 0. Results are shown in Fig. 7-3. Interestingly, the zero-lift flutter speeds for 2-D and 3-D flows are nearly the same; of course, strip theory is expected to be more accurate for the larger aspect ratio.

The difference between the 2-D and 3-D (with suction) stability boundaries is actually deceiving, since (as already mentioned) the 2-D results do not contain the improved modeling of the suction force from Chapter V. Figures (6-37) and (6-38) suggest the stabilizing effect which introducing suction would have upon the 2-D curve in Fig. 7-3. The key observation here is that the same type of instability, involving substantial participation of the fore-and-aft bending degree of freedom observed for 2-D aerodynamic loads, is still observed after 3-D aerodynamics are introduced. Also the influence of steady deformation upon flutter speed remains appreciable. Removal of the unsteady suction terms decreases stability, much as was observed for $\mathcal{R} = 10$ in Fig. 7-1. Points on the stability boundary for $\alpha < .005$ could not be found reliably because of the extremely light damping in this region; approximate curves are shown by dashed lines.

In conclusion, the results found in this chapter seem to confirm that the phenomena analyzed extensively in Chapter VI are still observed when the strip theory airloads are replaced by airloads from 3-D aerodynamic theory. Furthermore, the role of chordwise forces due to leading edge suction has been found to increase the aeroelastic stability of a wing undergoing steady deformation due to lift.

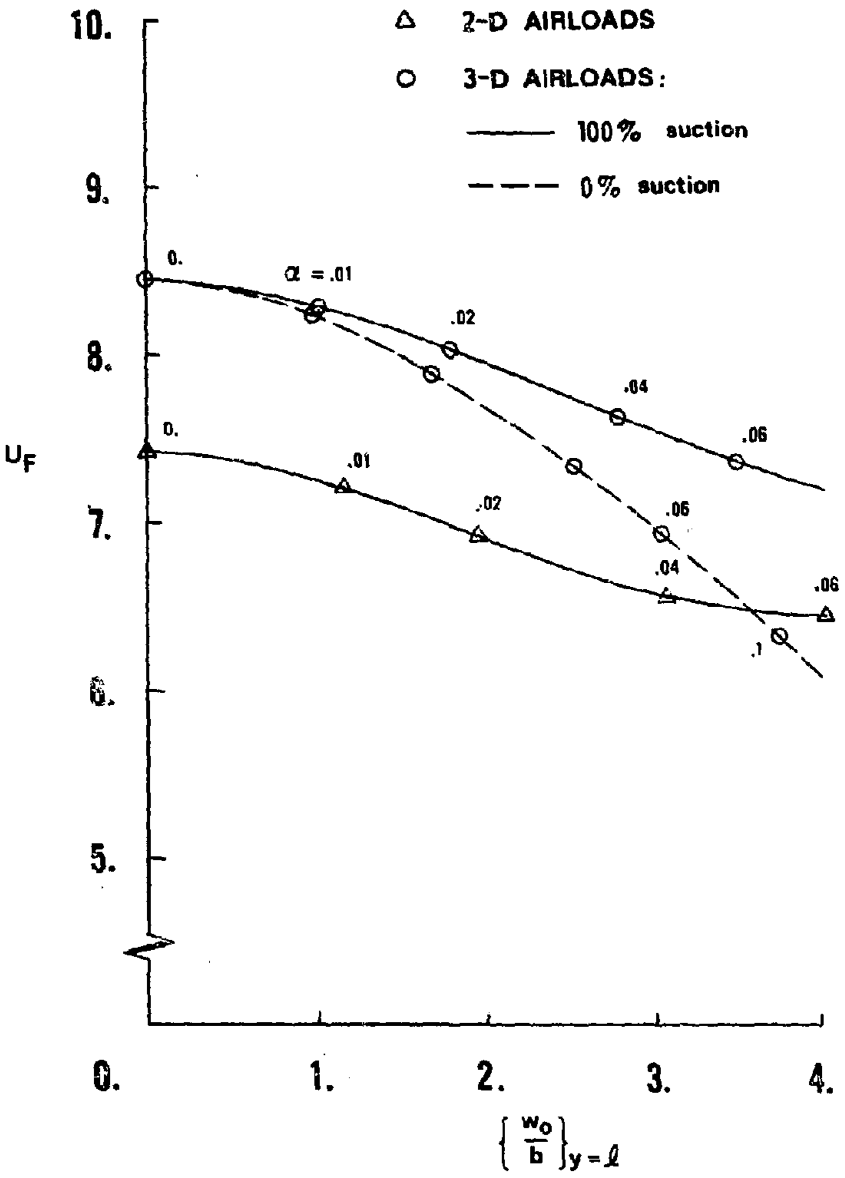

FIGURE 7-1 Flutter Speeds as Influenced by Steady Deformation, Moderate-Aspect-Ratio Example of Fig. 6-7 with Æ = 10 and $M_a = 0$

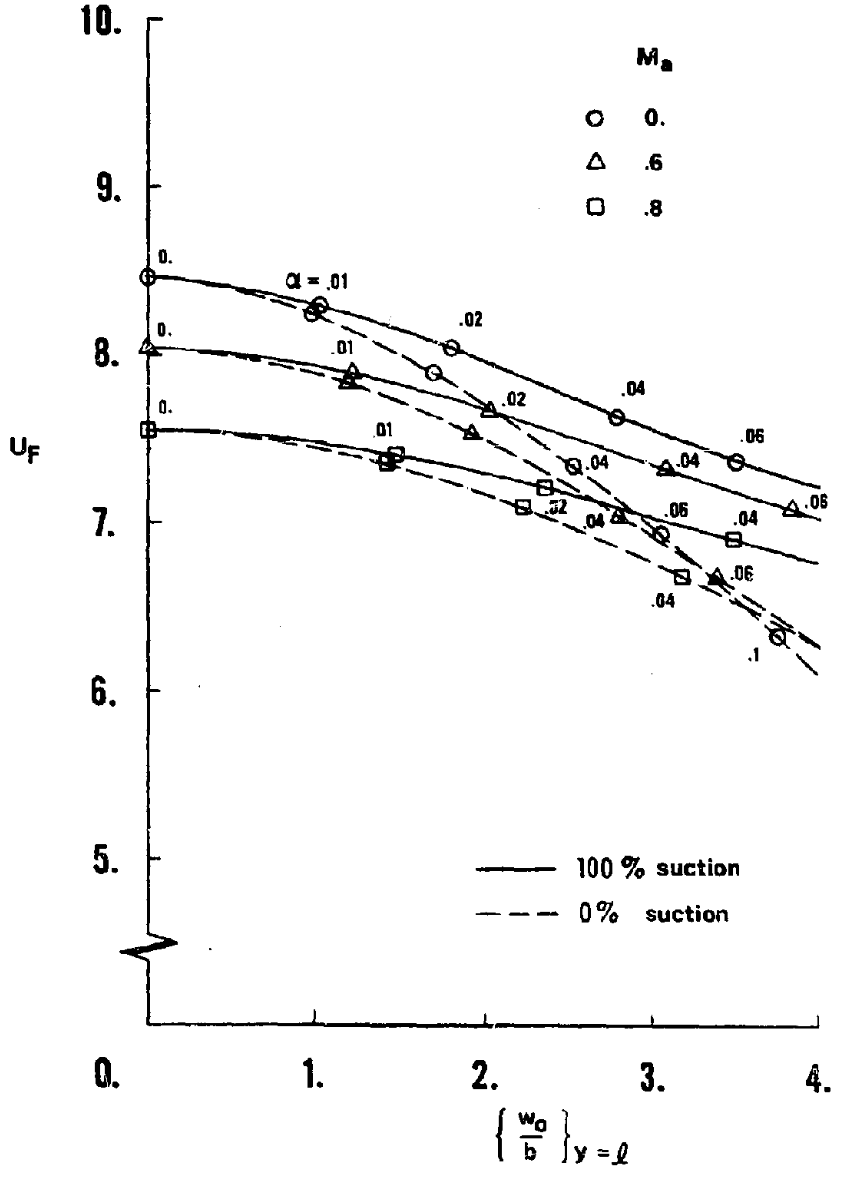

FIGURE 7-2 Flutter Speeds as Influenced by Steady Deformation at Three Mach Numbers; Wing of Fig. 7-1

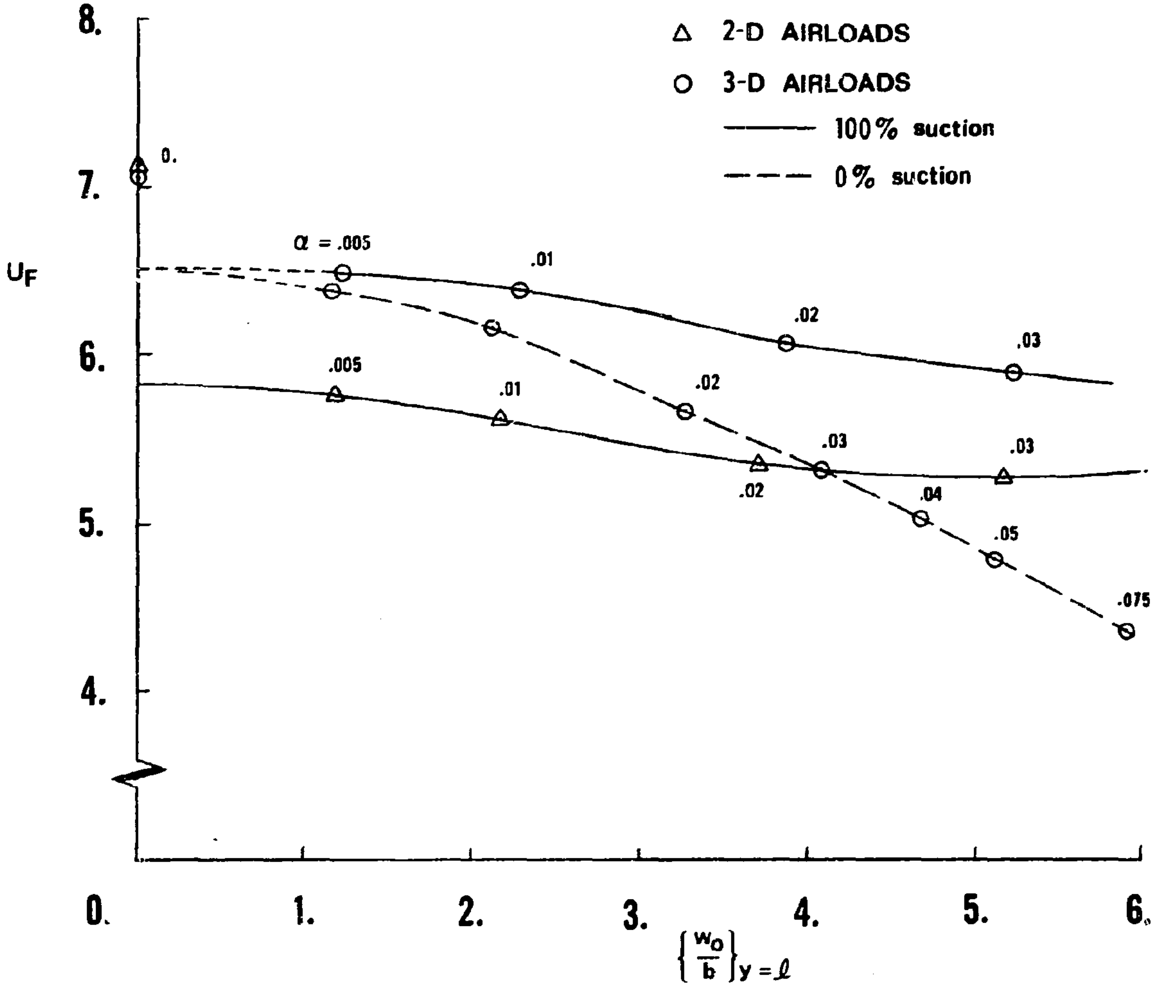

FIGURE 7-3 Flutter Speeds as Influenced by Steady Deformation; Large-Aspect-Ratio Example of Fig. 6-13 with $\mathcal{R}$ = 20 and $M_a = 0$

Chapter VIII

CONCLUSIONS AND RECOMMENDATIONS

The following conclusions are drawn from the variety of results obtained in this investigation.

1) The influence of steady drag on flutter speed changes from favorable to unfavorable as aspect ratio is increased. The frequency of the second transverse bending mode decreases, tending toward the fundamental bending-torsion flutter frequency, as aspect ratio is increased.

2) The prediction of the influence of steady drag upon flutter is not substantially altered when steady deformations due to lift are considered. The major effect of steady drag is to reduce divergence speed, especially for large aspect ratios.

3) When a wing has such a large aspect ratio that its fundamental fore-and-aft bending frequency is less than the frequency of bending-torsion flutter at zero steady lift, an instability associated with chordwise bending occurs. The critical speeds are lower than the zero-lift flutter speed when any steady lifting deformation is present. This type of flutter can disappear at small steady deflections when realistic structural damping is introduced, but for reasonably large displacements it can still occur.

4) Steady deformations decrease flutter speed and flutter frequency. The effect is most pronounced when the fundamental fore-and-aft bending frequency is near the zero-lift bending-torsion flutter frequency.

5) The aeroelastic phenomena predicted using incompressible strip-theory airloads are also observed when three-dimensional, compressible subsonic airloads are employed.

6) The inclusion of unsteady leading-edge suction forces moderates the predicted decrease in flutter speed due to steady lifting deformations.

7) In subsonic compressible flow, with unsteady potential chordwise forces, there seem to be only slight adverse effects of M_a on flutter when steady deformations are present.

One of the predictions of this study is that a high performance sailplane undergoing a limit load factor pullout from a dive could encounter flutter or divergence at lower speeds than might be anticipated from a conventional aeroelastic analysis. The increased steady drag which accompanies higher C_L would reduce the divergence speed considerably, while the deformation of the flexible high-aspect-ratio wings would change the dynamic aeroelastic stability as well.

The present analysis could be refined still further. Nonlinear aerodynamic effects deserve further attention. Higher mean angles of attack would lead to increased importance of the turbulent boundary layer, culminating in separation (stall), which will alter the stabilizing contribution found due to leading-edge suction in attached flow.

Vehicles intended to operate at the higher subsonic or low transonic speeds (certain RPV's or missiles could still be designed with the straight wings considered here) are expected to encounter various phenomena which could greatly affect the chordwise loads. Viscous shear, boundary layer modification of the flow, and thickness effects with the appearance of shocks will all modify the aeroelastic behavior.

Finally, the transonic and supersonic flow regimes, where drag loads are considerably larger than at subcritical speeds, remain largely uninvestigated. In these ranges different structural and aerodynamic configurations are likely to be involved.

Appendix A

THE ASSUMED MODES

1. Bending

The natural mode shapes and frequencies in bending of a uniform beam of length ℓ are found by seeking homogeneous simple harmonic solutions of

$$EI_x w'''' + m\ddot{w} = 0$$

Letting

$$w = W e^{i\omega t}$$

the general solution is

$$W = A_1 \sin \sqrt{\frac{\omega}{a}}\, y + A_2 \cos \sqrt{\frac{\omega}{a}}\, y + A_3 \sinh \sqrt{\frac{\omega}{a}}\, y + A_4 \cosh \sqrt{\frac{\omega}{a}}\, y$$

where $a^2 = \frac{EI_x}{m}$

Application of the bending boundary conditions

$$W(0) = W'(0) = W''(\ell) = W'''(\ell) = 0$$

results in a trancendental equation for the natural frequency eigenvalues

$$\cos \sqrt{\frac{\omega}{2}}\, \ell = - \frac{1}{\cosh \frac{\omega}{a}\, \ell}$$

which are for vertical bending

$$\text{(A-1)} \qquad \omega_{w_i} = \Pi^2 N_i^2 \frac{1}{\ell^2} \sqrt{\frac{EI_x}{m}} \qquad i = 1,2,3,\ldots$$

The trancendental numbers N_i for $1 \leq i \leq 5$ are

$$
\text{(A-2)} \qquad
\begin{aligned}
N_1 &= 0.596864162695 \\
N_2 &= 1.494175614274 \\
N_3 &= 2.500246946168 \\
N_4 &= 3.499989319849 \\
N_5 &= 4.500000461516
\end{aligned}
$$

and the corresponding eignevectors yield the vertical bending natural modes

$$
\text{(A-3)} \qquad f_{w_i} = \left[\left(\frac{\sin N_i\Pi - \sinh N_i\Pi}{\cosh \Pi N_i + \cos \Pi N_i}\right)(\sinh \Pi N_i\tilde{y} - \sin \Pi N_i\tilde{y}) + \cosh \Pi N_i\tilde{y} - \cos \Pi N_i\tilde{y}\right]
$$

expressed in orthonormal form so that

$$
\int_0^1 f^2_{w_i}(\tilde{y})d\tilde{y} = 1
$$

The modal property B_i in the steady equations (4-9) is related to the modal integral

$$
\text{(A-4)} \qquad \int_0^1 f_{w_i} dy = -\frac{2}{N_i\Pi}\left[\frac{\sin \pi N_i - \sinh \pi N_i}{\cosh \pi N_i + \cos \pi N_i}\right] \equiv -\frac{B_i}{2}
$$

Fore-and-aft bending natural modes f_{v_i} are the same as in (A-3), however the natural frequencies are

$$
\text{(A-5)} \qquad \omega_{v_i} = \Pi^2 N_i^2 \frac{1}{\ell^2}\sqrt{\frac{EI_z}{m}} = \sqrt{\tau}\,\omega_{w_i}
$$

The f_{w_i} are illustrated in Fig. A-1 for $1 \leq i \leq 5$.

2. Torsion

Natural mode shapes and frequencies in torsion are simply

$$f_{\phi_j} = \sin \Pi(j-\tfrac{1}{2})\tilde{y} \qquad \text{(A-6)}$$

$$\omega_{\phi_j} = \Pi(j-\tfrac{1}{2}) \frac{1}{\ell} \sqrt{\frac{GI_d}{J}} \qquad \text{(A-7)}$$

which result from the elementary Sturm-Liouville problem for torsion of a uniform rod. These modes are not normalized since

$$\int_0^1 f_{\phi_j}^2 (\tilde{y})d\tilde{y} = \tfrac{1}{2}$$

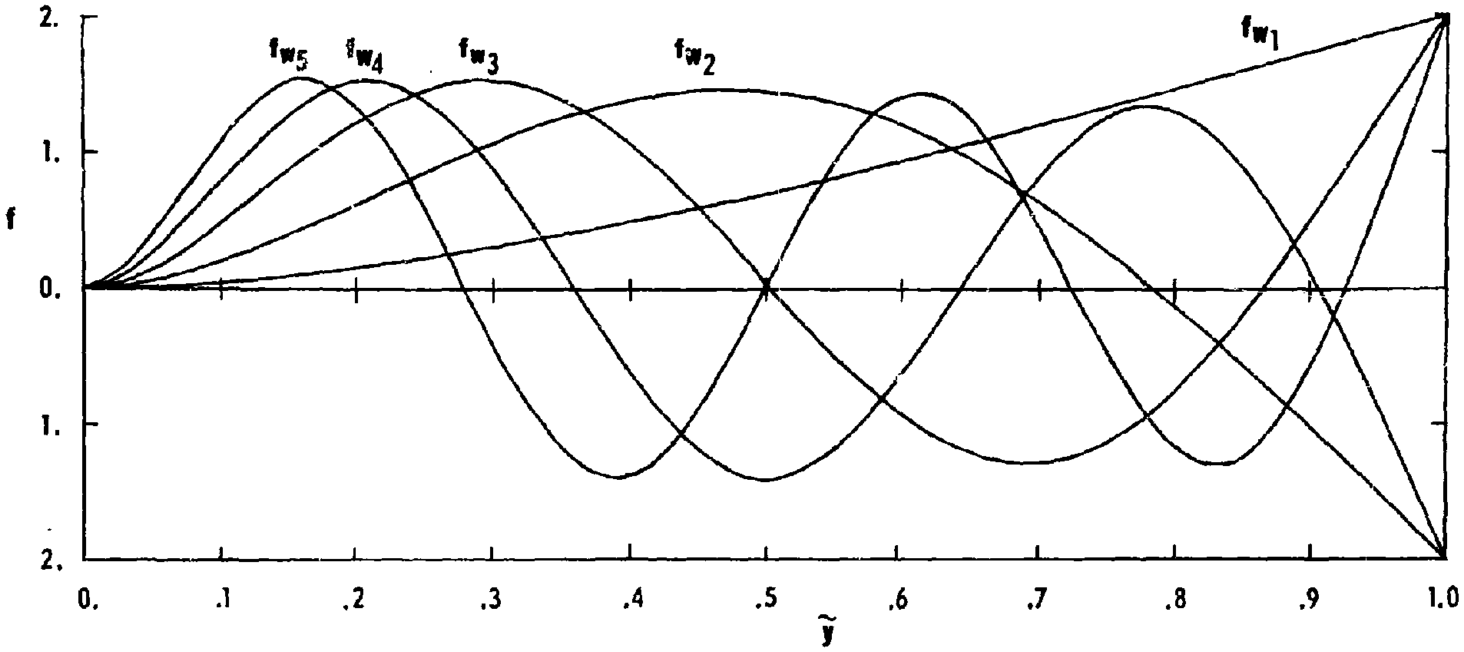

FIGURE A-1 Assumed Bending-Mode Shapes

Appendix B

CALCULATION OF MODIFIED BESSEL FUNCTIONS

The modified Bessel functions $K_o(\bar{s})$ and $K_1(\bar{s})$ appearing in the expression (5-1) for the generalized Theodorsen function can be computed by using the following ascending power series expansions, drawn from Abramowitz and Stegun (Ref. 26, Equations 9.6.10, 9.6.11, and 9.6.13).

$$\text{(B-1)} \qquad I_\nu(\bar{s}) = (\tfrac{1}{2}\bar{s})^\nu \sum_{j=0}^{\infty} \frac{(\tfrac{1}{4}\bar{s}^2)^j}{j!\,\Gamma(\nu+j+1)}$$

$$\text{(B-2)} \qquad K_o(\bar{s}) = -\{\ell n(\tfrac{1}{2}\bar{s}) + \gamma_e\} I_o(\bar{s})$$

$$+ \frac{\tfrac{1}{4}\bar{s}^2}{(1!)^2} + (1+\tfrac{1}{2})\frac{(\tfrac{1}{4}z^2)^2}{(2!)^2} + (1+\tfrac{1}{2}+\tfrac{1}{3})\frac{(\tfrac{1}{4}z^2)^3}{(3!)^2} + \ldots$$

$$\text{(B-3)} \qquad K_1(\bar{s}) = \tfrac{1}{2}(\tfrac{1}{2}\bar{s})^{-1} + \ell n(\tfrac{1}{2}\bar{s}) I_1(\bar{s})$$

$$- \tfrac{1}{2}(\tfrac{1}{2}\bar{s}) \sum_{j=o}^{\infty} \{\psi(j+1) + \psi(j+2)\} \frac{(\tfrac{1}{4}\bar{s}^2)^j}{j!(j+1)!}$$

where

$$\Gamma(\nu + 1) = \nu!$$

$$\psi(1) = -\gamma_e$$

$$\psi(\nu) = -\gamma_e + \sum_{j=1}^{\nu-1} j^{-1} \quad , \quad \nu \geq 2$$

$$\gamma_e = 0.5772156649\ldots \qquad \text{(euler's constant)}$$

No convergence difficulties with the power series expansions were encountered over the range of $\bar{s}$ that occurred in this investigation.

Simple harmonic airloads involving the Theordorsen function of reduced frequency $C(k)$ were computed by the same procedure, simply by the substitution $\bar{s} = 0 + ik$.

Appendix C

SOLUTION FOR NONLINEAR STEADY DISPLACEMENTS

With the vector of generalized displacements defined as

$$(\text{C-1}) \qquad \underset{\sim}{q}^{\circ} = \{q^{\circ}_{w_1},\ldots,q^{\circ}_{w_n},q^{\circ}_{v_1},\ldots,q^{\circ}_{v_n},q^{\circ}_{\phi_1},\ldots,q^{\circ}_{\phi_n}\}^T$$

the nonlinear equations (4-9) can be expressed,

$$(\text{C-2}) \qquad \underset{\sim}{F}(\underset{\sim}{q}^{\circ}) = 0$$

where

$$(\text{C-3}) \qquad \underset{\sim}{F} = \{F_{w_1},\ldots F_{w_n},F_{v_1},\ldots,F_{v_n},F_{\phi_1},\ldots,F_{\phi_n}\}^T$$

Let an initial estimate $\underset{\sim}{q}^{\circ}_{(o)}$ be found by solving the linear steady equations (4-20), then linearize $\underset{\sim}{F}$ about $\underset{\sim}{q}^{\circ}_{(o)}$ by first-order Taylor series,

$$(\text{C-4}) \qquad \underset{\sim}{F}(\underset{\sim}{q}^{\circ}) = F(\underset{\sim}{q}^{\circ}_{(o)}) + [J(\underset{\sim}{q}^{\circ}_{(o)})](\underset{\sim}{q}^{\circ} - \underset{\sim}{q}^{\circ}_{(o)}) + \text{H.O.T.}$$

The Jacobian matrix J contains partial derivatives of the F's with respect to the q°'s evaluated at $\underset{\sim}{q}^{\circ}_{(o)}$; its elements are shown in Fig. C-1. Equation (C-4) can be used to solve for $(\underset{\sim}{q}^{\circ}_{(1)} - \underset{\sim}{q}^{\circ}_{(0)})$ by the linear approximation

$$(\text{C-5}) \qquad \underset{\sim}{F}(\underset{\sim}{q}^{\circ}_{(o)}) + [J(\underset{\sim}{q}^{\circ}_{(o)})](\underset{\sim}{q}^{\circ}_{(1)} - \underset{\sim}{q}^{\circ}_{(o)}) = 0$$

and the first iteration solution is

$$(\text{C-6}) \qquad \underset{\sim}{q}^{\circ}_{(1)} = (\underset{\sim}{q}^{\circ}_{(1)} - \underset{\sim}{q}^{\circ}_{(o)}) + \underset{\sim}{q}^{\circ}_{(o)}$$

This process is repeated until satisfactory convergence is achieved, with the general jth step given by

$$(\text{C-7}) \qquad [J(\underset{\sim}{q}^{\circ}_{(j)})](\underset{\sim}{q}^{\circ}_{(j+1)} - \underset{\sim}{q}^{\circ}_{(j)}) = -\underset{\sim}{F}(\underset{\sim}{q}^{\circ}_{(j)})$$

$$\underset{\sim}{q}^{\circ}_{(j+1)} = (\underset{\sim}{q}^{\circ}_{(j+1)} - \underset{\sim}{q}^{\circ}_{(j)}) + \underset{\sim}{q}^{\circ}_{(j)}$$

In practice, more than four or five iterations rarely were required, for cases near static divergence speeds.

$$J_{j,i} = \frac{\partial F_{w_j}}{\partial q^\circ_{w_i}} = \Pi^4 N_j^4 \frac{MPi_\alpha}{bU^2} \delta_{ij} + (\tau-1) \frac{MPi_\alpha}{bU^2} \sum_{\mu=1}^{n} \sum_{\nu=1}^{n} R_{ij\mu\nu}\, q^\circ_{\phi_\mu} q^\circ_{\phi_\nu}$$

$$J_{j,i+n} = \frac{\partial F_{w_j}}{\partial q^\circ_{v_i}} = -\frac{MPi_\alpha}{bU^2} (\tau-1) \sum_{\nu=1}^{n} H_{\nu ji}\, q^\circ_{\phi_\nu}$$

$$J_{j,i+2n} = \frac{\partial F_{w_j}}{\partial q^\circ_{\phi_i}} = -(\tau-1) \frac{MPi_\alpha}{U^2} \left[\sum_{\mu=1}^{n} H_{ij\mu} \frac{q^\circ_{v_\mu}}{b} - 2 \sum_{\mu=1}^{n} \sum_{\nu=1}^{n} R_{\nu j\mu i}\, q^\circ_{\phi_\mu} \frac{q^\circ_{w_\nu}}{b} \right] - 2I_{ij}$$

$$J_{j+n,i} = \frac{\partial F_{v_j}}{\partial q^\circ_{w_i}} = -\frac{MPi_\alpha}{bU^2} (\tau-1) \sum_{\nu=1}^{n} H_{\nu ij}\, q^\circ_{\phi_\nu}$$

$$J_{j+n,i+u} = \frac{\partial F_{v_j}}{\partial q^\circ_{v_i}} = \tau\Pi^4 N_j^4 \frac{MPi_\alpha}{bU^2} \delta_{ij} - (\tau-1) \frac{MPi_\alpha}{bU^2} \sum_{\nu=1}^{n} \sum_{\mu=1}^{n} R_{ij\mu\nu}\, q^\circ_{\phi_\nu} q^\circ_{\phi_\mu}$$

$$J_{j+n,i+2n} = \frac{\partial F_{v_j}}{\partial q^\circ_{\phi_i}} = -(\tau-1) \frac{MPi_\alpha}{U^2} \left[\sum_{\mu=1}^{n} H_{i\mu j} \frac{q^\circ_{w_\mu}}{b} + 2 \sum_{\mu=1}^{n} \sum_{\nu=1}^{n} R_{\nu j\mu i}\, q^\circ_{\phi_\mu} \frac{q^\circ_{v_\nu}}{b} \right] + 2\alpha I_{ij}$$

$$J_{j+2n,i+n} = \frac{\partial F_{\phi_j}}{\partial q^\circ_{v_i}} = (\tau-1) \frac{MPi_\alpha}{bU^2} \left[-2 \sum_{\mu=1}^{n} \sum_{\nu=1}^{n} R_{\mu i\nu j} \frac{q^\circ_{v_\mu}}{b} q^\circ_{\phi_\nu} - \sum_{\nu=1}^{n} H_{j\nu i} \frac{q^\circ_{w_\nu}}{b} \right]$$

$$J_{j+2n,i+2n} = \frac{\partial F_{\phi_j}}{\partial q^\circ_{\phi_i}} = \left(\tfrac{1}{2}\Pi^2 (j-\tfrac{1}{2})^2 \frac{Mi_\alpha}{U^2} - A\right)\delta_{ij}$$

$$+ (\tau-1) \frac{MPi_\alpha}{U^2} \left[\sum_{\nu=1}^{n} \sum_{\mu=1}^{n} R_{\mu\nu ji} \frac{q^\circ_{w_\nu}}{b} \frac{q^\circ_{w_\mu}}{b} - \sum_{\nu=1}^{n} \sum_{\mu=1}^{n} R_{\mu\nu ji} \frac{q^\circ_{v_\mu}}{b} \frac{q^\circ_{v_\nu}}{b} \right]$$

$$\delta_{ij} = \begin{cases} 1 & (i=j) \\ 0 & (i \neq j) \end{cases}$$

$$(1 \leq i \leq n)\ ,\ (i \leq j \leq n)$$

FIGURE C-1 Elements of the Jacobian Matrix

REFERENCES

1. Petre, A. and H. Ashley, "Drag Effects on Wing Flutter," *J. of Aircraft*, Vol. 13, No. 10, October 1976, pp. 755-763.

2. Petre, A., *Teoria Aeroelasticitatii-Statica*, Editura Academiei Republicii Socialiste Romania, Bucharest, 1966.

3. Petre, A., "L'effet de la résistance à l'avancement sur la vitesse critique du flutter," *Proceedings Sixth International Congress of the Aeronautical Sciences*, Munich, September 1968.

4. Hoff, N., *The Analysis of Structures*, John Wiley and Sons, New York, 1956.

5. Bisplinghoff, R.L. and Ashley, H., *Principles of Aeroelasticity*, John Wiley and Sons, New York, 1962.

6. Houbolt, J.C. and Brooks, G.W., "Differential Equations of Motion for Combined Flapwise Bending, Chordwise Bending, and Torsion of Twisted, Nonuniform Rotor Blades," NACA Report No. 1346, 1958.

7. Hodges, D.H., and Dowell, E.H., "Nonlinear Equations of Motion for the Elastic Bending and Torsion of Twisted Nonuniform Rotor Blades," NASA TN D-7818, 1974.

8. Irwin, C.A.K. and P.R. Guyett, "The Subcritical Response and Flutter of a Swept Wing Model," Tech. Rept. 65186, RAE, Farnborough, U.K., August 1965.

9. Goland, M. and Luke, Y.L., "A Study of the Bending-Torsion Aeroelastic Modes for Aircraft Wings," *J. Aero. Sci.*, Vol. 16, No. 7, July 1949, pp. 389-396.

10. Jones, R.T., "Operational Treatment of the Non-Uniform Lift Theory to Airplane Dynamics," NACA TN 667, 1938.

11. Edwards, J.W., "Unsteady Aerodynamic Modeling and Active Aeroelastic Control," SUDAAR 504, February 1977.

12. von Kármán, T. and Burgers, J.M., General Aerodynamic Theory -- Perfect Fluids, Vol. II of Aerodynamic Theory, div. E, W.F. Durand, ed., Julius Springer (Berlin), 1935.

13. Greenberg, J.M., "Some Considerations on an Airfoil in an Oscillating Stream," NACA TN 1372, August 1947.

14. Garrick, I.E., "Propulsion of a Flapping and Oscillating Airfoil," NACA Report No. 567, May 1936.

15. Welch, A., Welch, L., and Irving, F., New Soaring Pilot, Butler and Tanner Ltd., London, 1968.

16. Marsden, D.J., "Gemini-- A Variable Geometry Sailplane," AIAA, MIT, and SSA 2nd International Symposium on the Technology and Science of Low Speed and Motorless Flight, Cambridge, Mass., September 11-13, 1974.

17. Goetz, R.C., "Divergence of Some All-Movable Control Surfaces Including Drag Loadings," NASA TN D-4793, October 1968.

18. Rowe, W.S., Redman, M.D., Ehlers, F.E., and Sebastian, J.D., "Prediction of Unsteady Aerodynamic Loadings Caused by Leading Edge and Trailing Edge Control Surface Motions in Subsonic Compressible Flow-- Analysis and Results," NASA CR-2543, 1975.

19. Redman, M.C. and Rowe, W.S., "Prediction of Unsteady Aerodynamic Loadings Caused by Leading Edge and Trailing Edge Control Surface Motions in Subsonic Compressible Flow-- Computer Program Description," NASA CR-132634, May 1975.

20. Novozhilov, V.V., Foundations of the Nonlinear Theory of Elasticity, Translated edition by Graylock Press, Rochester, New York, 1953.

21. Sears, W.R., "Operational Methods in the Theory of Airfoils in Non-Uniform Motion", J. of the Franklin Inst., Vol. 230, No. 1, July 1940, pp. 95-111.

22. Milne, R.D., "Asympotic Solutions of Linear Stationary Integro-Differential Equations," A.R.C.R. & M. 3548, July 1966.

23. Bisplinghoff, R.L., Ashley, H., and Halfman, R.L., Aeroelasticity, Addison-Wesley, Reading, Mass. 1955.

24. Watkins, C.E., Runyan, H.L., and Woolston, D.S., "On the Kernel Function of the Integral Equation Relating the Lift and Downwash Distributions of Oscillating Finite Wings in Subsonic Flow," NACA Rep. 1234.

25. Jones, R.T. and Cohen, D., High Speed Wing Theory, Princeton Aeronautical Paperback No. 6, Princeton University Press, Princeton, 1960.

26. Handbook of Mathematical Functions (ed. by Abramowitz and Stegun), Dover, New York, 1965.

27. Johnson, Wayne, "Dynamics of Tilting Proprotor Aircraft in Cruise Flight," NASA TN D-7677, May 1974.

SECURITY CLASSIFICATION OF THIS PAGE (When Data Entered)

12 REPORT DOCUMENTATION PAGE

READ INSTRUCTIONS
BEFORE COMPLETING FORM

1. REPORT NUMBER AFOSR-TR 78-0856
2. GOVT ACCESSION NO.
3. RECIPIENT'S CATALOG NUMBER
4. TITLE (and Subtitle) EFFECT OF CHORDWISE FORCES AND DEFORMATIONS AND DEFORMATIONS DUE TO STEADY LIFT ON WING FLUTTER.
5. TYPE OF REPORT & PERIOD COVERED 9 INTERIM rept., 1 Apr 77 – 31 Mar 78.
6. PERFORMING ORG. REPORT NUMBER
7. AUTHOR(s) WILLIAM NEWSOME BOYD
8. CONTRACT OR GRANT NUMBER(s) 15 AFOSR-74-2712, NGL-05-020-243
9. PERFORMING ORGANIZATION NAME AND ADDRESS
STANFORD UNIVERSITY
AERONAUTICS AND ASTRONAUTICS DEPARTMENT
STANFORD, CA 95305
10. PROGRAM ELEMENT, PROJECT, TASK AREA & WORK UNIT NUMBERS
2307A1
61102F
11. CONTROLLING OFFICE NAME AND ADDRESS
AIR FORCE OFFICE OF SCIENTIFIC RESEARCH/NA
BLDG 410
BOLLING AIR FORCE BASE, D C 20332
12. REPORT DATE 11 Dec 77
13. NUMBER OF PAGES 263 12 260
14. MONITORING AGENCY NAME & ADDRESS(if different from Controlling Office)
15. SECURITY CLASS. (of this report) UNCLASSIFIED
15a. DECLASSIFICATION/DOWNGRADING SCHEDULE
16. DISTRIBUTION STATEMENT (of this Report)

Approved for public release; distribution unlimited.

17. DISTRIBUTION STATEMENT (of the abstract entered in Block 20, if different from Report)

16 2307 17 A1

18. SUPPLEMENTARY NOTES

14 F-DAAH-508

19. KEY WORDS (Continue on reverse side if necessary and identify by block number)

AEROELASTICITY	FLUTTER
STATIC STABILITY	WING FLUTTER
DYNAMIC STABILITY	FLUTTER SPEED
CHORDWISE FORCE	LEADING-EDGE SUCTION
LARGE ASPECT RATIO WINGS	

20. ABSTRACT (Continue on reverse side if necessary and identify by block number)

This investigation explores the effects of chordwise forces and deformations and steady-state deformation due to lift on the static and dynamic aeroelastic stability of a uniform cantilever wing. Results of this analysis are believed to have practical applications for high-performance sailplanes and certain RPV's. The airfoil cross section is assumed to be symmetric and camber bending is neglected. Motions in vertical bending, fore-and-aft bending, and torsion are considered. A differential equation model is developed, which included the nonlinear elastic bending-torsion coupling that accompanies even moderate deflections. A linearized expansion in small time-dependent deflections is made

DD FORM 1473, 1 JAN 73 EDITION OF 1 NOV 65 IS OBSOLETE

UNCLASSIFIED
SECURITY CLASSIFICATION OF THIS PAGE (When Data Entered)

about a steady flight condition. The stability determinant of the linearized system then contains coefficients that depend on steady displacements. Loads derived from two-dimensional incompressible aerodynamic theory are used to obtain the majority of the results, but cases using three-dimensional subsonic compressible theory are also studied The stability analysis is carried out in terms of the dynamically uncoupled natural modes of vibration of the uniform cantilever. Dynamic stability in the case of incompressible strip-theory airloads is determined in two ways. One is the "V-g method" familiar to aeroelasticians. When steady deformations are present this method requires an iterative matching of flutter speeds with estimated speed. The second approach involves determination of the complex eigenvalues of the aeroelastic modes at any desired flight condition. The aerodynamic loads are expressed in terms of the generalized Theodorsen function; eigenvalues of the aeroelastic system are located with a gradient search technique. The effect of steady drag on flutter of nonlifting wings using incompressible strip-theory is studied and shown to correlate with previously known results. Next, the influence of steady lifting deformations on flutter is investigated, and flutter modes are found that involve fore-and-aft bending motions. The significance of unsteady leading edge suction forces, which are predicted by the two-dimensional incompressible aerodynamic theory, is then examined. Two idealized examples based upon existing sailplanes are analyzed. Steady drag loads lower the flutter speed for larger aspect ratios but increase it for aspect rotios less than a certain value. Divergence speed is more sensitive to steady drag, and for very high aspect rotio wings it can fall below the bending-torsion flutter speed. Steady deformations due to lift always decrease the flutter speed by an amount dependent upon the aspect ratio and the fore-and aft bending stiffness. Leading-edge suction forces increase flutter speed. Three-dimensional steady and unsteady airloads are introduced into the V-g flutter analysis scheme, and for a Mach number of zero the role of steady lifting deformations and unsteady leading-edge suction forces is more accurately determined. The behavior predicted using strip theory loads is again observed, and the suction forces are confirmed to contribute a significant stabilizing effect. Furthe calculations using high subsonic Mach numbers reveal only mild effects due to compressibility (disregarding unsteady cordwise loads of viscous origin).